

# Biophysical principles underlying binaural coincidence detection: Computational approaches



Dissertation

zur Erlangung des Grades eines Doktors der Naturwissenschaften  
an der Fakultät für Biologie  
der Ludwig-Maximilians-Universität München

vorgelegt von

Simon Lehnert

München, 30. Juni 2015

Erstgutachter und Betreuer: Prof. Dr. Christian Leibold  
Zweitgutachter: Prof. Dr. Benedikt Grothe

Tag der Abgabe: 30.06.2015  
Tag der mündlichen Prüfung: 24.11.2015





Meiner Familie.



# Table of contents

<b>Summary</b> .....	<b>3</b>
<b>Zusammenfassung</b> .....	<b>9</b>
<b>1. Introduction</b> .....	<b>15</b>
<b>1.1. The auditory brainstem with a focus on binaural processing</b> .....	<b>15</b>
1.1.1. From sound to a signal in the auditory nerve.....	15
1.1.2. The cochlear nucleus.....	16
1.1.3. The superior olivary complex.....	17
1.1.4. The lateral lemniscus and the inferior colliculus.....	19
1.1.5. Two localization cues in the horizontal plane.....	20
1.1.6. Encoding of ITDs in the MSO.....	22
1.1.7. The MSO from a biophysical perspective.....	26
<b>1.2. Action potential initiation</b> .....	<b>29</b>
1.2.1. History of the action potential.....	29
1.2.2. Modeling a neuronal membrane with Hodgkin-Huxley equations.....	31
1.2.3. The morphology of myelinated axons.....	34
1.2.4. Action potential initiation in cortical neurons.....	35
<b>1.3. Aims of this thesis</b> .....	<b>37</b>
<b>2. Action Potential Generation in an Anatomically Constrained Model of Medial Superior Olive Axons</b> .....	<b>41</b>
<b>3. Glycinergic inhibition tunes coincidence detection in the auditory brainstem</b> .....	<b>59</b>
<b>4. Tonotopic organization of the hyperpolarization-activated current (I<sub>h</sub>) in the mammalian medial superior olive</b> .....	<b>83</b>
<b>5. Discussion</b> .....	<b>99</b>
<b>5.1. The site of action potential initiation in central neurons</b> .....	<b>101</b>
<b>5.2. The role of Kv1 channels in the context of coincidence detection in the MSO</b> .....	<b>114</b>
<b>5.3. The role of glycinergic inhibition in mammalian ITD processing</b> .....	<b>119</b>

<b>5.4. Concluding remarks and outlook.....</b>	<b>126</b>
<b>References.....</b>	<b>129</b>
<b>List of abbreviations.....</b>	<b>161</b>
<b>List of publications.....</b>	<b>163</b>
<b>Acknowledgments.....</b>	<b>165</b>
<b>Curriculum vitae.....</b>	<b>167</b>
<b>Eidesstattliche Erklärung.....</b>	<b>169</b>
<b>Erklärung.....</b>	<b>169</b>
<b>Author contributions.....</b>	<b>171</b>

## Summary

Spatial hearing is crucial to the survival of a wide range of animal species. The ability to localize a sound source plays a decisive role for many situations and tasks, for example predation, navigation, and reproduction. Spatial hearing is also important for humans, for example, it contributes to the ability to focus on a conversation with another person in a cocktail party situation and provides additional guidance in visually confusing situations. In the mammalian brain, auditory space is computed from various monaural and binaural features which are extracted from the perceived sound in specialized neurons and nuclei in the auditory brainstem. Low-frequency sound sources in the horizontal plane can be localized using interaural time differences (ITDs), which arise when a sound reaches the ear closer to the sound source earlier than the opposite ear. Owing to the traveling speed of sound through the air of around 340 m/s and the limited ear-to-ear distance of particularly small mammals, ITDs are in the magnitude of at most a few hundreds of microseconds. Consequently, the detection of such minute arrival time differences requires exceptional temporal precision which is unique in the mammalian nervous system. The first structure in the mammalian brain that generates sensitivity to ITDs is the medial superior olive (MSO). MSO neurons receive fast excitatory inputs from both ears that are phase-locked to the fine structure of the sound and thus faithfully carry the information of the sound's arrival times to the two ears. Additionally, the MSO receives phase-locked inhibitory inputs from both ears. In keeping with their demanding temporal task, MSO cells show remarkable features. To discriminate ITDs with a temporal resolution of few tens of microseconds mature MSO neurons exhibit a membrane time constant of only a few hundred microseconds, making them up to a hundred times faster than most cortical neurons. The high speed of the MSO neurons' membrane dynamics is based on a strong expression of low-threshold potassium channels (Kv1) and hyperpolarization-activated channels (HCN) on the somatodendritic membrane that generate a strong current leak, causing the membrane potential to rapidly return to its equilibrium. As a consequence, the integration time window of MSO neurons is very short, making MSO neurons extremely fast coincidence detectors.

The exceptional temporal precision necessary to successfully detect minute ITDs has drawn considerable attention on MSO neurons and the microcircuitry they are embedded in. Although numerous insights into the properties of the somatic membrane, the phase-locked inputs, and the two sub-threshold channels in mature and developing MSO neurons have been gained, many questions regarding these neurons are still insufficiently investigated or heavily debated. Three of those questions, each of which was treated in a separate study, are addressed in this thesis: (1) the excitability and action potential generation of MSO neurons, in Chapter 2; (2) the role of glycinergic inhibition in the coincidence detection in Chapter 3; and (3) the role of HCN channels in the integration of inputs from different frequency channels, in Chapter 4. Each of these studies is comprised of an experimental and a computational part. The author of this thesis contributed to the computational part of the studies, the experiments were performed by experimental collaborators (see Author Contributions). In the following, the questions of the studies are outlined, and the results are briefly summarized.

The first study (Chapter 2) treats the excitability and action potential (AP) initiation of MSO neurons. It is generally assumed that the site of AP initiation is located in the axon initial segment (AIS). In most cortical neurons, which exhibit membrane time constants ranging from several to tens of milliseconds, the soma is capable of providing a stable current source to the AIS, such that AP initiation is facilitated. Owing to the very fast membrane speed of MSO neurons, such a requirement is not met. In MSO neurons, two strong sub-threshold conductances mediated by Kv1 and HCN channels, cause the soma of MSO neurons to constitute a tremendous current sink to the AIS. Furthermore, strong phase-locked synaptic inputs at rates up to 2 kHz lead to the further opening of the sub-threshold channels, intensifying the current sink effect of the soma. How, under these difficult circumstances, MSO neurons generate APs and even generate sustained firing rates of up to 100 Hz, as observed *in vivo*, is a mystery. To investigate this question, an extensive computational study was conducted, aided by immunohistochemical and electrophysiological experiments. The immunohistochemical stainings showed that MSO neurons exhibit particularly thin axons (0.66 microns in diameter) and a length of the first myelinated segment of 100 microns. Using the obtained morphological parameters a biophysical model of an MSO neuron with a detailed axon was created. We found that the AIS was well isolated from the leaky soma and capable of generating

APs, in line with the current textbook view of AP initiation obtained from notably more excitable neurons. However, when simulating high-frequency naturalistic input trains, a growing portion of action potentials started to become initiated in more distal axonal segments, the first nodes of Ranvier, while the AIS was merely capable of producing sub-threshold responses. These results indicate that MSO neurons might not have a distinct site of AP initiation but rather that the AP generation is established by an interaction of the proximal axon (AIS and the first nodes of Ranvier) as a whole, depending on stimulus frequency and intensity. The reasons behind this phenomenon were found to be the strong somatic current sink to the AIS that is intensified by higher frequency inputs and additional inhibition. Furthermore, the inactivation of sodium channels in the AIS caused by the temporal summation of high-frequency excitatory inputs was identified to modulate the site of AP initiation. We speculate that our results for MSO neurons could also apply to other leaky neurons in the central nervous system as well as more excitable neurons during strong synaptic bombardment, challenging the current textbook view of the AIS being the singular site of AP initiation. Moreover, our results show that it is the axon which maintains the neuron's excitability in situations where the soma is not excitable. Thus, it follows that to investigate the firing behavior of particularly leaky neurons, a single compartment model is not sufficient.

The study in Chapter 3 focuses on the role of phase-locked glycinergic inhibition in the tuning of the coincidence detection performed in the MSO. *In vivo* recordings assessing the ITD sensitivity have shown that MSO neurons respond best to sounds arriving from the contralateral side. Blocking glycinergic inhibitory inputs *in vivo* reduces this bias and shifts the best response towards zero ITD (corresponding to a sound arriving from straight ahead), indicating that inhibition is involved in the tuning of the neuron's ITD sensitivity. Moreover, masking the phase-locked endogenous inhibition by tonically applying glycine *in vivo*, it was found that the ITD sensitivity bias vanished, suggesting that a specific timing of the inhibitory inputs relative to the corresponding excitatory inputs is necessary to tune ITD sensitivity. To investigate the role of precisely-timed inhibition in tuning the coincidence detection in the MSO, as well as to quantify relative timing conditions of inhibitory inputs that would explain *in vivo* results, a thorough *in vitro* study of MSO neurons was performed. It was found that precisely-timed inhibitory inputs are indeed capable of shifting the ITD sensitivity of MSO neurons, and specific

relative timing conditions for inhibitory inputs with respect to the excitation that can explain *in vivo* data were identified. The tuning of coincidence detection by inhibition showed to be robust against synaptic jitter and temporal summation of the inputs during stimulus trains. In a computational model, which was constrained to fit the membrane and response kinetics found *in vitro*, we were able to reproduce the results found in the slice. Moreover, the computational model allowed us to establish that an active Kv1-current further facilitates the inhibition-enforced effects.

The third study (Chapter 4) was concerned with HCN channels largely expressed in MSO neurons. Membrane properties, such as the input resistance and time constant, are tuned to the specific function a neuron implements. Cortical neurons, for example layer 5 pyramidal cells, integrate their inputs over several milliseconds and thus exhibit longer time constants. On the other hand, the coincidence detection of MSO neurons requires small time constants to maintain temporal precision. However, even within the same class of neurons differences in membrane properties were found, for example to support different input frequencies like in the auditory system. Most nuclei of the auditory system, like the MSO, are tonotopically arranged, i.e. there is a spatial gradient within the nucleus where lower to higher frequency sounds are processed. In the MSO, the dorsal part processes lower- and the ventral part processes higher-frequency sounds. It is thus interesting to investigate whether membrane and channel properties in MSO neurons are differentially distributed along the dorsoventral axis. Therefore, an *in vitro* study of MSO neurons was performed, aided by computational modeling. The *in vitro* recordings revealed that the amplitude of the HCN current ( $I_h$ ) varied systematically along the dorsoventral axis. Higher  $I_h$  current densities and faster kinetics were observed for ventral MSO neurons compared to their dorsal counterparts. This difference in  $I_h$  was also reflected in lower input resistances and time constants of ventral neurons. Also, ventral neurons showed smaller half-widths and less temporal summation in response to a 100 Hz train of simulated inhibitory events. To examine possible mechanisms underlying these differences of synaptic integration along the dorsoventral axis, biophysical models of prototypical dorsal and ventral MSO neurons were created, by adjusting the kinetics of the incorporated HCN channel model according to the voltage-clamp data of  $I_h$  in dorsal and ventral MSO cells. Using these cell models we demonstrated that an interplay of the ventrally larger  $I_h$  currents and fast-activating Kv1

channels facilitates the processing of higher frequency inhibitory inputs with less temporal summation in ventral neurons. This result indicates that the larger  $I_h$  helps to counteract higher frequencies of inhibitory inputs keeping the membrane potential close to the action potential threshold.



## Zusammenfassung

Räumliches Hören ist für eine breite Vielfalt von Tierspezies überlebenswichtig. Für viele Aufgaben und Situationen, wie beispielsweise die Beutejagd, die Navigation und die Fortpflanzung, spielt die Fähigkeit eine Schallquelle zu lokalisieren eine entscheidende Rolle. Räumliches Hören ist auch für den Menschen wichtig, so trägt es, zum Beispiel, in einer Cocktail Party Situation dazu bei, sich auf ein Gespräch mit einer anderen Person konzentrieren zu können und bietet darüber hinaus auch eine Orientierungshilfe in visuell unübersichtlichen Situationen. Im Säugerhirn wird der akustische Raum mithilfe verschiedener monauraler und binauraler Eigenschaften berechnet, welche von speziellen Neuronen und Hirnkernen aus dem wahrgenommenen Klang extrahiert werden. Tieffrequente Schallquellen können auf der horizontalen Ebene geortet werden, indem sogenannte interaurale Laufzeitdifferenzen (interaural time differences; ITDs) ausgewertet werden. Diese entstehen, da der Schall das zur Schallquelle nähere Ohr früher erreicht als das gegenüberliegende Ohr. Aufgrund der Schallgeschwindigkeit in Luft von etwa 340 Meter pro Sekunde, sowie des begrenzten Ohrenabstandes von, insbesondere, kleinen Säugern, sind diese ITDs in einer Größenordnung von höchstens einigen hundert Mikrosekunden. Die Detektion dieser winzigen Laufzeitdifferenzen erfordert daher eine außerordentliche zeitliche Präzision, wie sie im gesamten Nervensystem von Säugern einzigartig ist. Die erste Hirnstruktur, die eine Sensitivität für ITDs erzeugt, ist die mediale obere Olive (medial superior olive; MSO). Die Neurone der MSO erhalten schnelle exzitatorische Eingangssignale von beiden Ohren. Diese synaptischen Eingangssignale erreichen die MSO jeweils zu einer bestimmten Phase der Feinstruktur des Klanges (auch genannt: phasen-gekoppelt) und bewahren somit die Information über die Ankunftszeiten des Klanges an beiden Ohren. Zusätzlich zu den exzitatorischen Eingängen erhalten MSO Neurone phasen-gekoppelte hemmende (inhibitorische) Eingänge. MSO Neurone weisen, ihrer zeitlich anspruchsvollen Aufgabe entsprechend, einige bemerkenswerte Eigenschaften auf. Um ITDs mit einer zeitlichen Auflösung von nur wenigen zehn Mikrosekunden unterscheiden zu können, verfügen MSO Neurone über eine Membranzeitkonstante von nur wenigen hundert Mikrosekunden. Damit ist die Membran von MSO Neuronen um

bis zu einhundert Mal schneller als die der meisten kortikalen Neuronen. Dieser hohen Geschwindigkeit der Membrandynamik liegt eine hohe Expression von niedrige-schwelligen Kalium-Kanälen (Kv1 Kanäle) und Hyperpolarisations-aktivierten, durch zyklische Nukleotide modulierten, Kation-Kanälen (hyperpolarization-activated and cyclic nucleotide-gated; HCN Kanäle) in der somatodendritischen Membran zugrunde, welche einen starken Leckstrom erzeugen und somit eine schnelle Repolarisation der Membran zum Equilibrium hin verursachen. Aufgrund dieses Umstandes ist das Zeitfenster, in welchem eine Integration der Eingangssignale stattfindet, besonders klein und MSO Neurone extrem schnelle Koinzidenzdetektoren.

Die bemerkenswert hohe zeitliche Präzision, die notwendig ist um erfolgreich winzige ITDs zu detektieren hat beachtliche Aufmerksamkeit auf MSO Neurone sowie den neuronalen Schaltkreis, in welchem sie eingebettet sind, gezogen. Zwar konnten bereits zahlreiche Erkenntnisse über die Membraneigenschaften des Somas, die phasengekoppelten Eingangssignale und der zwei unterschwelligen Ionenkanäle in erwachsenen, sowie sich in der Entwicklung befindlichen, MSO Zellen bereits errungen werden. Viele Fragen MSO Neurone betreffend sind jedoch noch sehr wenig untersucht oder stark umstritten. In dieser Arbeit werden drei solcher Fragestellungen, jede in einer separaten Studie, behandelt: (1) die Erregbarkeit und Aktionspotential-Generierung von MSO Zellen, in Kapitel 2; (2) die Rolle der glyzinerger Inhibition bei der Koinzidenzdetektion, in Kapitel 3; und (3) die Rolle der HCN Kanäle bei der Integration von Eingangssignalen aus verschiedenen Frequenzkanälen, in Kapitel 4. Jede dieser Studien besteht aus einem experimentellen, sowie einem theoretischen Teil. Der Autor dieser Doktorarbeit trug jeweils zum theoretischen Teil der Studien bei, der experimentelle Teil wurde von Experimentatoren durchgeführt (siehe Author Contributions). Im Folgenden werden die Fragestellungen der Studien erläutert, sowie die Ergebnisse kurz zusammengefasst.

Die erste Studie (Kapitel 2) behandelt die Erregbarkeit sowie die Generierung von Aktionspotentialen in MSO Neuronen. Es wird allgemein angenommen, dass Aktionspotentiale von Neuronen im Axon nah am Zellkörper – im sogenannten „axon initial segment“ oder kurz AIS – erzeugt werden. Die meisten kortikalen Neurone weisen eine Membranzeitkonstante von einigen, bis zu mehreren zehn Millisekunden auf. Dieser Umstand begünstigt die Erzeugung von Aktionspotentialen, da hier der

Zellkörper dieser Neurone dem AIS eine stabile Stromquelle liefert. Aufgrund der äußerst geringen Membranzeitkonstante, ist diese Voraussetzung für MSO Neurone nicht gegeben. In MSO Neuronen ist sogar genau das Gegenteil der Fall: zwei stark exprimierte unter-schwellige Ionenkanaltypen im Soma (Kv1 und HCN) erzeugen einen enormen transmembranen Leckstrom. Damit stellt das Soma von MSO Neuronen eine immense Stromsenke für das AIS dar. Ein weiteres Problem stellen die starken synaptischen Eingänge der MSO Neurone dar, welche effektiv die Kv1 und HCN Kanäle noch weiter öffnen und somit den Effekt der Stromsenke sogar noch intensivieren. Wie MSO Neurone, unter diesen schwierigen Umständen, Aktionspotentiale, geschweige denn die *in vivo* gemessenen Feuerraten von bis zu 100 Hz erzeugen können, ist völlig unklar. Um diese Frage zu untersuchen, wurde, unterstützt von immunohistochemischen und elektrophysiologischen Experimenten, eine umfangreiche computergestützte theoretische Studie erstellt. Bei den immunohistochemischen Färbungen wurde entdeckt, dass MSO Zellen Axone mit einem besonders geringen Durchmesser von nur 0.66 Mikrometern, sowie eine Länge des ersten myelinisierten Abschnittes von etwa 100 Mikrometern, aufweisen. Basierend auf diesen morphologischen Daten wurde ein biophysikalisches Modell eines MSO Neurons mit seinem Axon erstellt. In unseren Simulationen konnten wir zeigen, dass das AIS von MSO Neuronen elektrisch gut vom Zellkörper isoliert ist und somit imstande ist Aktionspotentiale zu generieren. Dies stimmt überein mit der heutigen Lehrbuchmeinung bezüglich Neuronen, welche eine deutlich bessere Erregbarkeit als MSO Neurone zeigen. Stimuliert man jedoch mit hochfrequenten naturalistischen synaptischen Inputs, so beginnt das neuronale Modell Aktionspotentiale mehr und mehr in distaleren axonalen Segmenten – den ersten Ranvier'schen Schnürringen – zu erzeugen, während das AIS nur noch unter-schwellige Antworten generieren kann. Diese Resultate zeigen auf, dass in MSO Neuronen möglicherweise kein einzelner, eindeutiger Ort für die Erzeugung von Aktionspotentialen verantwortlich ist, sondern vielmehr ein Zusammenwirken verschiedener proximaler Segmente des Axons (dem AIS und den ersten Ranvier'schen Schnürringen). Dieses Zusammenwirken zeigte sich im Modell durch die Stimulusfrequenz und -intensität beeinflussbar. Als Ursachen dieses Phänomens wurde der Zellkörper als starke Stromsenke für das AIS identifiziert, welches durch höherfrequente und hemmende Eingänge weiter intensiviert wird.

Darüber hinaus stellte sich heraus, dass durch die Aufsummierung von hochfrequenten erregenden Eingängen, Natriumkanäle, besonders im AIS, inaktivieren, wodurch der Ort der AP Erzeugung im Axon moduliert wird. Wir vermuten, dass sich unsere Resultate bezüglich MSO Zellen auch auf weitere weniger gut erregbare Zelltypen erweitern lassen. Auch stellt sich die Frage, ob sich unsere Ergebnisse nicht auch auf gut erregbare Neurone, etwa wenn sie einem starken synaptischen Bombardement ausgesetzt sind, anwenden lassen. Im Falle einer positiven Antwort, würde dies die derzeitige Lehrbuchmeinung des AIS als einzigen Ort der AP Erzeugung im Axon in Zweifel ziehen. Unter dem Strich legen unsere Ergebnisse dar, dass es das Axon ist, welches die Erregbarkeit des Neurons erhält, wenn der Zellkörper in manchen Situationen besonders schlecht erregbar ist. Daraus folgt auch, dass eine Untersuchung des Feuerverhaltens von besonders undichten Neuronen mittels eines Punktneuronmodells nicht ausreichend ist.

Die Studie in Kapitel 3 befasst sich mit der Rolle der glyzineren Inhibition auf die Justierung der Koinzidenzdetektion in der MSO. In Messungen der ITD Sensitivität *in vivo* wurde gefunden, dass MSO Neurone die höchste Antwortrate für Geräusche zeigen, welche aus kontralateraler Richtung kommen. Wird die glyzinerge Inhibition blockiert, verschwindet diese Präferenz und die beste Antwortrate von MSO Neuronen verschiebt sich Richtung 0 ITD (welches einer Geräuschquelle direkt von vorn entsprechen würde). Dieses Resultat deutet stark darauf hin, dass glyzinerge Inhibition die ITD Sensitivität in der MSO beeinflusst. Indem man durch eine tonische Applikation von Glyzin die endogenen hemmenden Eingangssignale maskierte, konnte man darüber hinaus *in vivo* zeigen, dass Inhibition allein nicht ausreicht, um die kontralaterale Präferenz der MSO Neurone zu erzeugen. Vielmehr gibt dieses Resultat Hinweise darauf, dass ein bestimmtes Timing der hemmenden Eingangssignale relativ zu den exzitatorischen Eingangssignalen notwendig ist um die kontralaterale Präferenz der MSO Neurone zu erklären. In dieser Studie soll die Rolle einer präzise getimten Inhibition bei der Justierung der Koinzidenzdetektion in MSO Neuronen untersucht werden. Dabei sollen auch konkrete Zeitbedingungen für die inhibitorischen Eingänge relativ zur Exzitation bestimmt werden, welche die *in vivo* Resultate erklären können. Um dieser Frage auf den Grund zu gehen wurde eine umfassende *in vitro* Studie an MSO Neuronen angefertigt. Dabei wurde gefunden, dass eine zeitlich gut abgestimmte

Inhibition tatsächlich in der Lage ist die Koinzidenzdetektion von MSO Neuronen zu justieren und die *in vivo* Resultate zu erklären. Des Weiteren stellte sich heraus, dass die Einstellung der Koinzidenzdetektion mithilfe der Inhibition robust war gegenüber synaptischem Jitter und zeitlicher Summation der Eingangssignale, wenn Folgen von Stimuli präsentiert wurden. In einem Computermodell, welches auf den *in vitro* gemessenen Eigenschaften der Zellmembran und der Eingänge basierte, waren wir in der Lage die *in vitro* gemessenen Ergebnisse zu reproduzieren. Schließlich konnten wir im Modell zeigen, dass ein aktiver Kv1-Kanal die durch die Inhibition induzierten Effekte unterstützt.

Die dritte Studie (Kapitel 4) in dieser Arbeit beschäftigt sich mit den in MSO Zellen stark exprimierten HCN Kanälen. Zellmembraneigenschaften, wie der Eingangswiderstand und die Zeitkonstante, sind angepasst auf die Funktion, die ein Neuron implementiert. Neurone der Großhirnrinde, wie etwa die Pyramidalzellen der Lamina V, summieren ihre Eingangssignale über mehrere Millisekunden hinweg auf und weisen somit längere Zeitkonstanten auf. Auf der anderen Seite benötigt die Koinzidenzdetektion, die MSO Zellen durchführen, sehr kleine Membranzeitkonstanten, um die zeitliche Präzision sicherzustellen. Auch innerhalb eines Zelltyps wurden Unterschiede in den Membraneigenschaften gefunden, etwa im auditorischen System, um die Verarbeitung verschiedener Frequenzen zu erleichtern. Die meisten Hirnkerne im auditorischen System, auch die MSO, sind tonotop angeordnet. Das bedeutet, dass innerhalb eines Hirnkernes ein Gradient existiert entlang welchem tiefe bis hin zu hohen Frequenzen verarbeitet werden. In der MSO werden tieffrequente Signale im dorsalen Teil und hochfrequente Signale im ventralen Teil verarbeitet. Es ist daher von großem Interesse, ob sich Membran- und Ionenkanaleigenschaften entlang der dorsoventralen Achse der MSO unterscheiden. Um dies zu untersuchen wurde eine *in vitro* Studie durchgeführt, unterstützt von Computersimulationen. *In vitro* konnte dabei gezeigt werden, dass sich, in der Tat, die Amplitude des Stromes, welcher durch die HCN Kanäle fließt ( $I_h$ ), entlang der dorsoventralen Achse systematisch verändert. Darüber hinaus wurde gezeigt, dass  $I_h$  im ventralen Abschnitt höhere Stromdichten und schnellere Kinetiken aufwies als im dorsalen Abschnitt der MSO. Diese Unterschiede fanden ihre Entsprechung auch im niedrigeren Eingangswiderstand und kleineren Zeitkonstante der MSO Zellen im ventralen Teil. Auch zeigten die Neurone im

ventralen Teil der MSO schmalere Antworten und weniger zeitliche Aufsummierung als Reaktion auf eine 100 Hz Folge von inhibitorischen Eingangssignalen. Im theoretischen Teil der Studie wurde untersucht, welche Mechanismen diesen Unterschieden in der synaptischen Integration dorsaler und ventraler Zellen zu Grunde liegen. Dazu wurde jeweils ein Modell einer prototypischen dorsalen und ventralen MSO Zelle angefertigt, indem die jeweiligen HCN Kanäle angepasst wurden auf die durchschnittlich in dorsalen und ventralen Zellen gemessenen Kanalkinetiken. Im Ergebnis konnten wir in unseren Simulationen zeigen, dass ein Zusammenspiel des ventral stärkeren  $I_h$  mit schnellen Kv1 Kanälen es ventralen MSO Zellen ermöglicht höhere Raten inhibitorischer Eingänge, bei geringerer zeitlicher Aufsummierung, zu verarbeiten im Vergleich zu dorsalen Neuronen. Dieses Ergebnis zeigt auf, dass der größere  $I_h$  im ventralen Teil dabei helfen kann, den putativ höherfrequenten hemmenden Eingangssignalen entgegenzuwirken und damit das Membranpotential näher an der Schwelle für Aktionspotentiale zu halten.

# 1. Introduction

## 1.1. The auditory brainstem with a focus on binaural processing

### 1.1.1. From sound to a signal in the auditory nerve

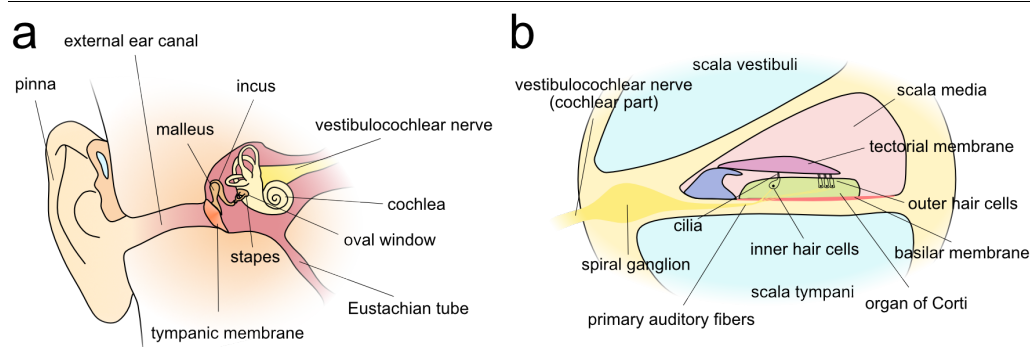


**Figure 1.** Human ear and cochlea. (a) Ear cross section. (b) Cochlea cross section.

Sound is a pressure wave which propagates through compressible media, such as air. When a sound reaches the ear (Figure 1a), it passes the external ear canal and induces a vibration of the tympanic membrane. This vibration causes the three middle ear ossicles (malleus, incus and stapes) to oscillate. The stapes connect to the cochlea through the oval window. The cochlea can be described as a coil-, or snail-shaped<sup>1</sup> fluid-filled tube subdivided into three chambers: the scala tympani, the scala media, and the scala vestibuli (Figure 1b). The movements of the stapes transduce the sound waves from the outer air to the cochlear fluids and hence manifest the sound as a traveling wave of the basilar membrane which separates the scala media from the scala tympani. The basilar membrane varies in width and stiffness along its longitudinal axis and thus has different resonance properties from its base to its apex. While the thin and stiff base shows the largest membrane deflection for high-frequency sounds, the broader and more flexible apex responds most to low-frequency sounds (von Békésy, 1947). This spectral analysis defines the cochleotopic structure and functionally yields a tonotopic organization, which is preserved throughout the auditory system. Located on the basilar membrane is the organ of Corti which incorporates the inner hair cells (IHCs). The heads of the IHCs develop a hair-like structure, the cilia, which themselves are connected to the tectorial

<sup>1</sup> hence the name “cochlea”, a latin word, derived from the greek κόχλος, the snail or the snail shell.

membrane. The motion of the basilar membrane induces a shearing force between the IHCs and the tectorial membrane that opens mechanosensitive channels in the cilia. The resulting ionic influx changes the membrane potential of the corresponding hair cells and thus transforms the mechanically transmitted sound into an electrical signal. Membrane depolarization of the IHCs results in action potentials (APs) being generated in the peripheral processes of type I spiral ganglion cells which synapse at the base of the IHCs. The axons of the spiral ganglion cells (called the primary auditory fibers) then establish the cochlear part of the vestibulocochlear nerve.

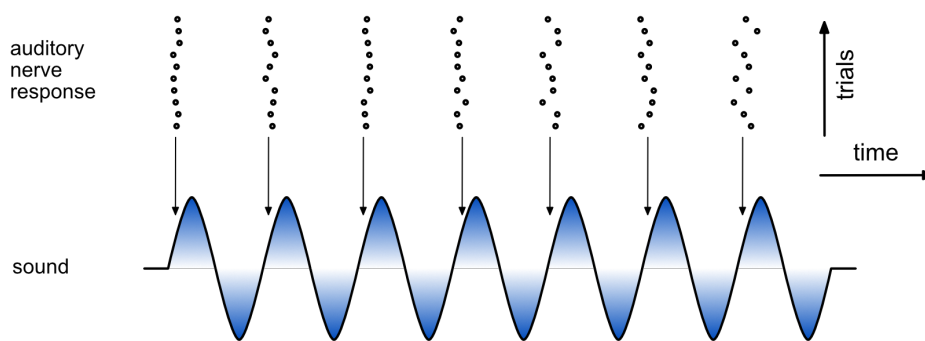


**Figure 2.** Schema displaying the phase-locked response of the auditory nerve to a presented pure tone sound. Circles (at the top) indicate action potentials generated in the auditory nerve in response to the sound (at the bottom) for different trials. For each cycle of the sound, an arrow points toward the (average) phase the firing of the auditory nerve is restricted to in this illustration.

An important temporal feature of the APs elicited at this stage is that they are generated at a specific phase of the sinusoidal voltage deflections of the IHC (phase-locked; Galambos and Davis, 1943; also see Figure 2). The fact that the APs are generated in a phase-locked manner is inevitable for the high-resolution temporal processing in downstream nuclei as will be discussed in Section 1.1.7. This thesis covers the binaural nucleus of the MSO and will henceforth focus on the nuclei of the ascending auditory pathway that are relevant for binaural processing.

### 1.1.2. The cochlear nucleus

As the primary auditory fibers enter the cochlear nucleus complex, they synapse with mainly four different cell types in the cochlear nuclei: the bushy cells in the anterior ventral cochlear nucleus (AVCN), the octopus cells in the posterior ventral cochlear nucleus (PVCN), the multipolar cells in the ventral cochlear nucleus (VCN) and the

stellate cells in the dorsal cochlear nucleus (DCN). Each of these cell groups encodes different auditory informations and thus initiates a different pathway of auditory processing. From a binaural viewpoint, the most important cells in the cochlear nucleus are the bushy cells in the AVCN. The bushy cells can be divided into two sub-groups: the spherical and the globular bushy cells (SBCs and GBCs, respectively). Both cell types receive inputs mediated by large synapses from the type I spiral ganglion cells. For SBCs these synapses are especially large, called endbulbs of Held. Owing to these sizable synapses most action potentials carried by the primary auditory fibers result in APs in the bushy cells, thus preserving the responses of the primary auditory fibers (Joris et al., 1994a,b).

### 1.1.3. The superior olivary complex

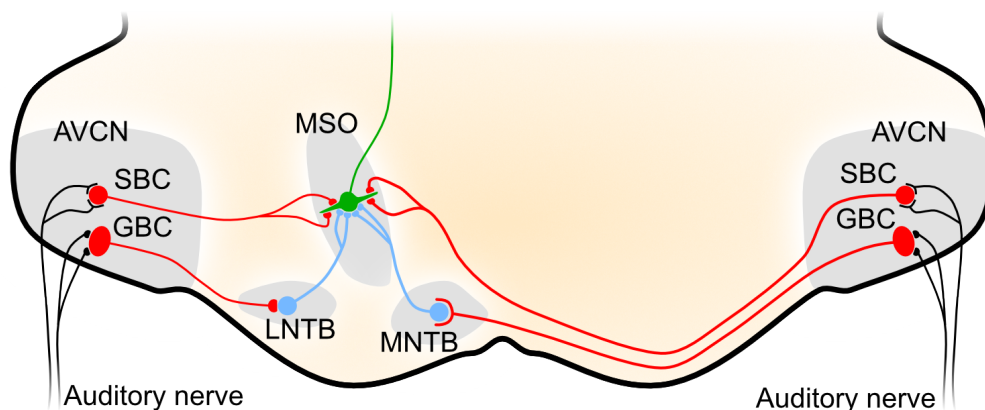


**Figure 3.** The medial superior olive (MSO) and its upstream nuclei.

The superior olivary complex (SOC) is comprised of several major nuclei: the lateral and medial superior olive (LSO and MSO) and the lateral and medial nucleus of the trapezoid body (LNTB and MNTB). These nuclei receive most of their synaptic inputs from the spherical and globular bushy cells in the AVCN. Furthermore, the major nuclei of the SOC are surrounded by various other nuclei, called periolivary nuclei, one of them being the superior periolivary nucleus (SPN), located dorsal to the MNTB (Webster, 1992; Schwartz, 1992).

The LNTB receives excitatory inputs from the ipsilateral GBCs, while the MNTB

receives excitatory inputs from the contralateral GBCs (Tolbert et al., 1982; Friauf and Ostwald, 1988; Kuwabara et al., 1991; Smith et al., 1991; Thompson and Schofield, 2000; also see Figure 3, and Section 1.1.7. for more details).

The MSO is located laterally to the MNTB (Figure 3). The principal neurons of the MSO are arranged on the dorsoventral axis and exhibit stereotypical bilateral dendrites extending along the mediolateral axis (Ramón y Cajal, 1909; Stotler, 1953; Schwartz, 1992; Grothe, 2000). The neurons of the MSO (and the LSO) are the first to be innervated from both ears and thus are the first to process binaural information in the mammalian brain. The principal cells of the MSO receive glutamatergic excitatory inputs from both, the ipsi- and contralateral AVCN (Stotler, 1953; Warr, 1966; Clark, 1969; Perkins, 1973; Lindsey, 1975; Cant and Casseday, 1986). Additionally they receive inhibitory inputs from the ipsilateral LNTB (Cant and Hyson, 1992; Kuwabara and Zook, 1992; Spirou and Berrebi, 1996) and MNTB (Spangler et al., 1985; Banks and Smith, 1992). Both inhibitory inputs are glycinergic (Adams and Mugnaini, 1990; Spirou and Berrebi, 1997). Recently, a GABAergic inhibitory input to the MSO, arising from a disynaptic feedback loop via the superior periolivary nucleus (SPN), has been identified (Stange et al., 2013). For an overview of the MSO and its upstream nuclei see Figure 3.

The LSO is located laterally to the MSO (Figure 3). The LSO receives excitatory inputs from the ipsilateral AVCN and inhibitory inputs from contralateral site relayed via the ipsilateral MNTB (Spangler et al., 1985; Cant and Casseday, 1986; Matsubara, 1990; Sanes, 1990; Kuwabara et al., 1991).

In the literature, the two main binaural response types of MSO and LSO neurons are commonly referred to as EE (excitatory-excitatory) and EI (excitatory-inhibitory), respectively – where the two letters describe the predominant ipsilateral and contralateral inputs (Grothe et al., 2010).

#### 1.1.4. The lateral lemniscus and the inferior colliculus

The lateral lemniscus (LL) extends from the lower pontine tegmentum and is the main auditory tract that connects the SOC to the inferior colliculus (Webster, 1992; Schwartz, 1992). It contains axons from both the cochlear nuclei and the SOC. Three different cell types that infiltrate the LL give rise to the three lemniscal nuclei: the ventral, intermediate and dorsal nucleus of the lateral lemniscus (VNLL, INLL and DNLL). While the VNLL and INLL are monaural (Covey, 1991, Yavuzoglu, 2010), the DNLL responds best to binaural inputs. The DNLL receives glutamatergic excitatory connections from the ipsilateral MSO and contralateral LSO, as well as glycinergic inhibitory inputs from the ipsilateral LSO (Adams, 1979; Glendenning et al., 1981 and 1992; Glendenning and Masterton, 1983; Aitkin and Shuck, 1985; Shneiderman, 1988, Saint-Marie et al., 1989; Saint Marie and Baker, 1990). Also, the DNLL projects to its contralateral counterpart with GABAergic connections via the commissure of Probst (Adams and Mugnaini, 1984; Thompson et al., 1985; Moore and Moore, 1987; Shneiderman et al., 1988).

The largest auditory structure in the brainstem is established by the inferior colliculus (IC). The IC is located in the midbrain dorsal to the LL. It is comprised of three subdivisions, the central nucleus (ICC), the dorsal cortex and the external cortex. The IC receives multi-modal inputs from a vast number of different nuclei and brain regions, some of the auditory being: the LL, the medial geniculate nucleus and the auditory cortex. Furthermore, the nuclei of the SOC innervate the IC in different ways. The IC receives excitatory projections from the ipsilateral MSO and contralateral LSO and inhibitory connections from the ipsilateral LSO (Adams, 1979; Glendenning and Masterton, 1983; Aitkin and Shuck, 1985; Saint Marie et al., 1989; Saint Marie and Baker, 1990). Like the DNLL, the IC sends projections to its contralateral counterpart (Moore and Goldberg, 1963; Brunso-Bechtold et al., 1981). The neurons of the ICC, which receive most of their inputs from the LL seem to be involved in binaural computation, since many of them are ITD-sensitive (Rose et al., 1966).

Both, the DNLL and the ICC have proven to provide a comparably easy-to-access read-

out of the MSO and LSO regarding ITD-related data (Rose et al., 1966; Kuwada and Yin, 1983; Yin and Kuwada, 1983a,b; Caird and Klinke, 1987; McAlpine et al., 1998 and 2001; Siveke et al., 2006, 2007 and 2012).

### 1.1.5. Two localization cues in the horizontal plane

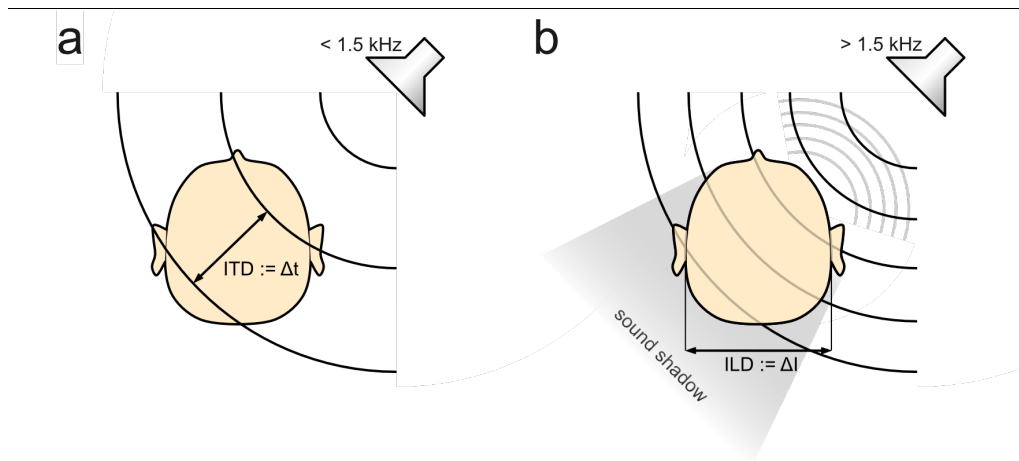


**Figure 4.** Two localization cues in the horizontal plane: (a) interaural time difference (ITD), (b) interaural level difference (ILD). See text for further description. Reproduced similar to Grothe et al. (2010).

A sound source which is not located exactly in front (or behind) of a listener will give rise to arrival time and level differences at the two ears (for review see Grothe et al., 2010). These two differences are the physical cues for the horizontal localization of a sound source, and are called interaural time differences (ITDs) and interaural level differences (ILDs).

ITDs arise since sound waves arrive at the ear closer to the sound source first, then propagate along the listener's head and ultimately, only microseconds later, reach the opposite ear (Figure 4a). The physiologically relevant range of ITDs, or the maximally possible ITD, depends on the listener's ear-to-ear distance, as well as the size and shape of the head. For the mongolian gerbil (*Meriones unguiculatus*), which is the animal model underlying all performed studies in this thesis, the maximum ITD is around  $\pm 135 \mu\text{s}$  (Maki and Furukawa, 2005). For humans, which exhibit considerably larger heads, the maximum ITD is roughly  $\pm 700 \mu\text{s}$  (Moore, 2012). Relative to the considered hemisphere, positive ITDs thereby indicate that the sound source is located

on the contralateral side, and negative ITDs mean the sound source is on the ipsilateral side. As a sound originating from exactly the front (or behind) reaches both ears at the same time, the resulting ITD is consequently zero. ITDs can be utilized as a localization cue for low-frequency sounds that exhibit a wavelength larger than the ear-to-ear distance. For high-frequency sounds ITDs become ambiguous, since for the usage of ITDs it is imperative to be able to distinguish between the timing of individual cycles of a sound wave. When stimulating with pure tones or stimuli with a sinusoidal structure, it became sensible to sometimes use the notion of interaural phase differences (IPDs) when referring to arrival time differences of sound (Grothe, 2000).

ILDs emerge, when sounds are reflected by the listener's head thus reaching the opposing ear (in the sound shadow) at a lower intensity than the ear facing the sound source (Figure 4b). Since low-frequency sounds are diffracted by the listener's head rather than reflected, ILDs are especially eligible as a localization cue for high-frequency sounds with a wavelength which is shorter than the ear-to-ear distance.

The assignment of localization cues to different frequency bands goes back to the work of Lord Rayleigh (1907) and his “duplex theory”. The duplex theory states that ITDs are used to localize low-frequency sound sources, while ILDs are employed to localize high-frequency sounds sources. The duplex theory was later refined by restricting the range where ITDs are a useful cue for humans to below 1.5 kHz (Sandel et al., 1955; also see Hartmann and Macaulay, 2014). Even though an attribution of both cues to low- (ITD) and high-frequencies (ILD) is generally accurate, it does not tell the whole story. It has been shown that substantial ILDs are also generated when a low-frequency sound source is nearby the listener (Brungart and Rabinowitz, 1999; Shinn-Cunningham et al., 2000). On the other hand, low-frequency components as in the amplitude envelope of high-frequency sounds give rise to utilizable ITDs (Bernstein, 2001; Griffin et al., 2005).

The nuclei concerned with the detection of these localization cues are the MSO and the LSO in the SOC. The principal cells of the MSO have been found to be ITD sensitive in a variety of mammals (for example, cat: Galambos et al., 1959; Caird and Klinke, 1983;

Yin and Chan, 1990; dog: Goldberg and Brown, 1969; kangaroo rat: Moushegian et al., 1975; Crow et al., 1978; rabbit: Batra et al., 1997a,b; gerbil: Spitzer and Semple, 1995; Brand et al., 2002; Pecka et al., 2008). In fact, the MSO has shown to be the primary structure for ITD coding in the brain. Albino cats, which present a pronounced atrophy of their MSO nuclei (Conlee et al., 1984 and 1986), show strong behavioural deficits regarding the localization of sound sources in the horizontal plane (Heffner and Heffner, 1987) and a reduced sensitivity to ITDs (Yin et al., 1990). The principal cells of the LSO are mainly sensitive to ILDs (Boudreau and Tsuchiani, 1968; Tollin, 2003), however low-frequency LSO neurons have also shown to be ITD-sensitive (Tollin and Yin, 2005).

### 1.1.6. Encoding of ITDs in the MSO

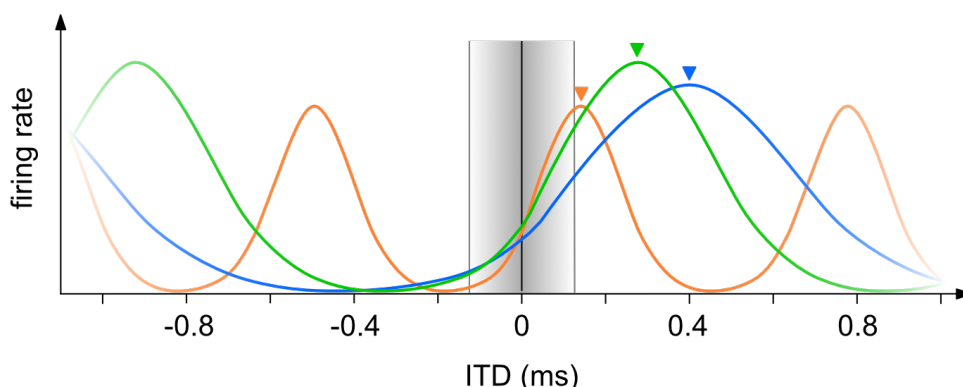
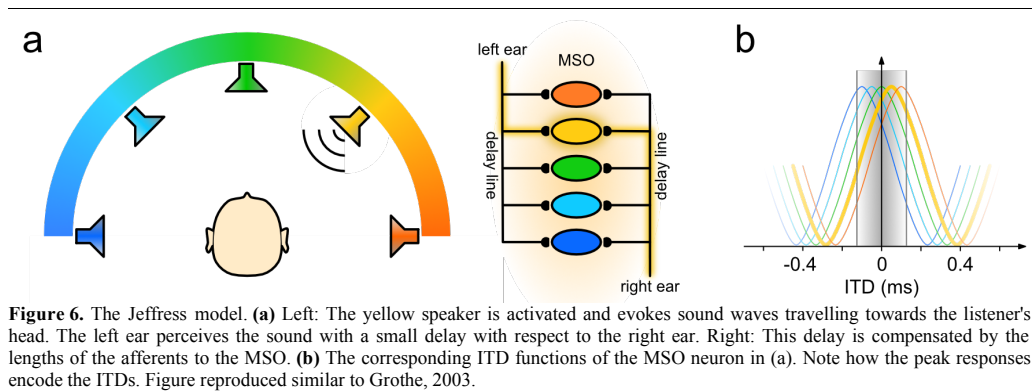


**Figure 5.** Schema of a typical response of a gerbil MSO cell to pure tones at different ITDs. Colors indicate different stimulus frequencies (green = best frequency (BF), orange (>BF), blue (<BF)). Arrow heads indicate the corresponding best ITD. Note the preference for positive ITDs as observed *in vivo*. The shaded area indicates the physiologically relevant range for ITDs (in this example the range between  $\pm 135 \mu\text{s}$  corresponding to the head size of a gerbil). Note how the slopes of the ITD functions are within the physiological range, establishing a rate code of ITDs.

The principal cells of the MSO are sensitive to ITDs, i.e. their firing rate is substantially modulated by the ITDs of a sound stimulus (Rose et al, 1966; Goldberg and Brown, 1969; Yin and Chan, 1990; Brand et al., 2002). The firing rate of a cell as a function of ITDs is called the ITD function (Figure 5). The ITD to which the cell responds with the highest firing rate is called the best ITD. When stimulated with a pure tone and a range of artificially generated ITDs that exceeds the length of several cycles of the tone, the ITD-function shows multiple peaks and troughs (Figure 5; Goldberg and Brown, 1969; Yin and Chan, 1990). The distance between these peaks then represents the period of

the presented pure tone. MSO neurons can discriminate ITDs with a resolution of tens of microseconds (Lesica et al., 2010).



The underlying mechanism of this ITD sensitivity is generally accepted to be a coincidence detection of the two phase-locked excitatory inputs coming from the two ears (Jeffress, 1948, Yin and Chan 1990; also see Figure 2 and 3). In 1948, Lloyd Alexander Jeffress proposed a theoretical model of how ITDs can be analyzed and processed by coincidence detectors in the auditory system. His theory assumes that excitatory inputs are conveyed to target coincidence detector neurons via afferent axons of systematically varying lengths (called “delay lines”) in order to compensate for the arrival time differences of sound at the two ears (Figure 6a, right). Consequently, it suggests that for every frequency channel a map of the horizontal auditory space is created with individual neurons encoding one specific ITD by its peak rate, thus establishing a peak-coding strategy (Jeffress, 1948; also see Figure 6b). This intriguing hypothesis was heavily investigated particularly to find anatomical evidence for the delay line structure. Indeed, in the avian counterpart of the MSO, the nucleus laminaris (NL), evidences of systematic length variations of NL afferents and a systematic representation of best ITDs were found (Rubel and Parks, 1975; Sullivan and Konishi, 1986; Carr and Konishi, 1990). Although indications for a putative delay-line type of structure of excitatory MSO afferents in mammals were found (Smith et al., 1993; Beckius et al., 1999, but see Karino et al., 2010), recent studies incorporating *in vivo* data of the MSO and its downstream neurons in the DNLL and IC provide several reasons to challenge the Jeffress theory (McAlpine et al., 2001; Brand et al., 2002; Hancock and Delgutte, 2004; Siveke, et al., 2006; Pecka et al., 2008; for review: Grothe

et al., 2010). The main arguments in opposition of the Jeffress theory applying to the MSO are now elaborated on further.

First, for the Jeffress model to apply one would expect to see a homogeneous distribution of best ITDs over the physiological range to properly encode azimuthal space by a peak-coding strategy (Figure 6b). Even though for the data of Yin and Chan (1990) one could argue the distribution of best ITDs in the physiological range to be rather homogeneous, more recent studies show that there exists a strong bias towards positive ITDs, rendering the best ITDs to be mostly outside the physiological range (McAlpine et al., 2001; Brand et al., 2002; Hancock and Delgutte, 2004; Siveke, et al., 2006; Pecka et al., 2008; van der Heijden et al., 2013). Furthermore, low-frequency tuned neurons show markedly larger and more widespread best ITDs compared to high-frequency neurons, i.e. the best ITD and its variability is strongly dependent on the best frequency<sup>2</sup> (BF) of the neuron (McAlpine et al., 2001). This circumstance renders the steepest part of the ITD function's slope to be inside of the physiological range (illustrated in Figure 5). Taken together, this strongly indicates that, at the very least for small mammals, instead of a peak-coding strategy, a population rate coding strategy is more plausible for the MSO.

Second, there is considerable evidence that MSO neurons receive strong phase-locked inhibitory inputs, mediated by the ipsilateral LNTB and MNTB (Clark, 1969; Perkins, 1973; Wenthold et al., 1987; Cant, 1991; Cant and Hyson, 1992; Kuwabara and Zook, 1992; also see Section 1.1.3.). While early studies already speculated that inhibition might play a role in ITD detection (Rose et al., 1966; Yin and Kuwada, 1983), the extent to which it influences the encoding of ITDs is still a matter of debate (for reviews, see Grothe, 2003; Joris and Yin, 2006; Grothe et al., 2010 and 2014). *In vivo* recordings of the gerbil MSO show that blocking the glycinergic inhibitory inputs with strychnine removes the preference for positive ITDs and shifts the best ITD to zero (Brand et al., 2002; Pecka et al., 2008). This finding unveils the crucial role of the phase-locked inhibition in tuning the coincidence detection of MSO neurons and contradicts the pure excitatory coincidence detection mechanism the Jeffress model

---

<sup>2</sup> The stimulus frequency to which the neuron shows the largest firing rate.

proposes.

The third reason to challenge the Jeffress model is regarding the characteristic phase (CP) and characteristic delay (CD) of a cell. In 1966, Rose and colleagues defined the CD as the ITD to which the cell responds with the same relative amplitude over different stimulation frequencies (Rose et al., 1966). Since then, several studies used the notion of a CD, identifying the CD of a cell by visual inspection (for example: Brugge et al., 1969, 1970, 1973; Geisler et al., 1969; Stillman 1971). The lack of an appropriate objective measure of CD prompted Yin and Kuwada to provide a simple method to statistically determine whether a cell shows a CD (Yin and Kuwada, 1983). To do so, they plotted the best IPD versus the stimulation frequency and fitted a linear function to this data by linear regression. The slope of this fit function establishes the CD of the cell. The CP of the cell, which is defined as the IPD at which the CD occurs, can be obtained by evaluating the fit function at zero (Figure 7).

When we now consider the EE type coincidence detector neurons of the MSO to be driven by purely excitatory inputs, and being innervated by delay-line-type afferents according to the Jeffress scheme, we would expect the best ITD to be invariant with respect to the stimulation frequency. Thus, the CD of such a neuron would show at the peak firing rate and the CP would be zero. At the other extreme, when we observe an EI neuron which receives excitatory inputs from the ipsilateral side and inhibitory ones from the contralateral side, we would expect the troughs of the ITD functions to be invariant with respect to the stimulation frequency. We would expect to see the best ITDs to occur when these two inputs are maximally out of phase and thus the CP of such a neuron to be around 0.5 cycles. However, several older (Goldberg and Brown, 1969; Rose et al., 1966; Stillman, 1971) and newer (Batra et al., 1997a,b; Pecka et al., 2008) *in vivo* studies have shown that the CPs are by no means restricted to 0 or 0.5 only, but assume a variety of values between 0 and 0.5 CP. This observation indicates

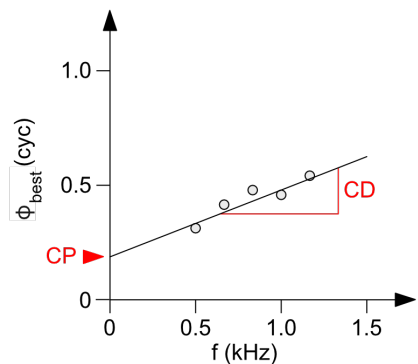


**Figure 7.** Determining the characteristic delay (CD) and characteristic phase (CP) of an MSO neuron. Circles indicate exemplary best phases (IPDs) of an MSO neuron given a pure tone stimulus presented at five different frequencies (abscissa). The line represents the linear regression of these five data points.

that the ITD sensitivity seems to be not only generated by a pure time delay as suggested by the Jeffress model, but additionally incorporates a phase delay which cannot be explained by that model. Such a phase delay could arise from the well established strong phase-locked inhibitory inputs and their timing relative to the corresponding excitatory inputs (see Discussion, Subchapter 5.3).

### 1.1.7. The MSO from a biophysical perspective

The discrimination of minute discrepancies in arrival time of incoming signals is a physiologically demanding task. To establish the sensitivity to these sub-millisecond arrival time differences of the inputs, two major prerequisites must be met. First, appropriately brief synaptic inputs have to reliably transport the exquisite temporal information of the incoming sound. Second, the cell must only integrate these precisely timed synaptic inputs over a very small time window to distinguish between tens of microseconds in arrival time difference.

The first requirement is addressed by the circumstance that MSO neurons receive some of the most temporally precise inputs in the whole central nervous system. Inside the ITD frequency domain, the auditory nerve fibers (ANFs) generate action potentials which are highly synchronized to a specific phase of the sinusoidal signal in the IHCs (Galambos and Davis, 1943; Kiang et al., 1965; Rose et al., 1967). These phase-locked discharges build the temporal fundament of the ITD-detection in the MSO for two reasons. First, they reliably carry the temporal information of incoming sounds at each ear. Second, they are preserved throughout the whole ITD-detection circuitry up to the MSO. The SBCs, that directly mediate the excitatory inputs to the MSO, as well as the GBCs, which innervate the MNTB and LNTB in the inhibitory pathway to the MSO, have shown phase-locking at an even higher degree of precision than that of the ANFs (Spirou et al., 1990; Smith et al., 1991; Joris et al., 1994a,b; McLaughlin et al., 2008; Rhode, 2008; Lorteije et al., 2009; Recio-Spinoso, 2012). The MNTB itself was found to be exceptionally well-suited for temporarily precise computation, for it receives its inputs through the largest synapse in the brain, the calyx of Held. The mere size and the massive vesicle release of the calyx of Held ensures that a presynaptic AP results in an

AP in the MNTB neuron at a very small synaptic delay and thus preserves the phase-locked response (Smith et al., 1998; Paolini et al., 2001; Kopp-Scheinpflug et al., 2003; Hermann et al., 2007; McLaughlin et al., 2008; Englitz et al., 2009; Kopp-Scheinpflug et al., 2011; Borst and Soria van Hoeve, 2012; Roberts et al., 2014). Even though the incoming excitatory synapses to the LNTB are smaller, the intrinsic physiology of LNTB neurons has also shown to be well capable of phase-locking at input frequencies of 600 Hz or higher and thus deliver rapid and temporarily precise inhibition to the MSO (Roberts et al., 2014). The principal cells of the MSO also phase-lock to pure tone stimuli themselves (Galambos et al., 1959; Goldberg and Brown, 1969; Crow et al., 1978; Yin and Chan, 1990; Spitzer and Semple, 1995; Batra et al., 1997a; Brand et al., 2002; Pecka et al., 2008), thereby showing a higher degree of phase-locking to favorable ITDs than at unfavorable ones (Goldberg and Brown, 1969; Crow et al., 1978; Caird and Klinke, 1983; Yin and Chan, 1990; Spitzer and Semple, 1995; Batra et al., 1997a,b).

Aside from the temporal precision of their arrival times, the synaptic inputs to the MSO principal cells are also some of the fastest regarding their time course in the whole brain. The time constant of excitatory inputs is only around 0.3 milliseconds and the time constant of inhibitory inputs ranges around 1.5 milliseconds (Couchman et al., 2010).

To fulfill the second condition, the principal neurons of the MSO exhibit an exceptionally small membrane time constant of only around 350  $\mu$ s (Scott et al., 2005; Couchman et al., 2010). The very fast membrane kinetics are a result of the unusually low input resistance of MSO neurons of only about 5 Mohm at rest (Scott et al., 2005; Couchman et al., 2010), which is based on the high expression of two sub-threshold channels: a hyperpolarization-activated and cyclic nucleotid-gated channel (HCN or just h-channel) and a low-voltage activated potassium channel (Kv1, sometimes also called KLT or K-LVA). The corresponding currents ( $I_h$  and  $I_{Kv1}$ ) differ drastically in their kinetics and polarity and thus operate on different time scales and serve different purposes.

$I_{Kv1}$  is a fast-activating and slow-inactivating outward current mediated by potassium

ions. Its voltage-dependent activation time constant averages around 1 millisecond (at 35°C, Mathews et al., 2010). The channels to conduct  $I_{Kv1}$  are encoded by the Kv1 (or KCNA) gene subfamily. Due to the sensitivity to DTX-K (dendrotoxin-K; specific Kv1.1 blocker) the heteromeric Kv1-channels in the MSO have shown to contain member 1 (KCNA1, Kv1.1) as a subunit (Svirskis et al., 2002; Scott et al., 2005; Mathews et al., 2010). As a byproduct of the immunohistochemical stainings in Chapter 2, a substantial expression of Kv1.2 in the soma could be observed (Chapter 2, Figure 2). In the MSO, Kv1-channels have shown to sharpen the integration time window and half-width of EPSPs and thus to substantially improve the temporal resolution of coincidence detection (Scott et al., 2005, Mathews et al., 2010). Furthermore, Kv1 channels have been identified to have a share in the attenuation of axonally initiated action potentials in the soma which therefore do not interfere with synaptic integration (Scott et al., 2007). Apart from the MSO (Smith, 1995), Kv1-channels are also found in various nuclei of the auditory brainstem, for example in the VCN (Manis and Marx, 1991), the MNTB (Brew and Forsythe, 1995), the LSO (Barnes-Davies et al., 2004), where they contribute to the phasic AP firing pattern (i.e. a singular or very few APs at the onset of a depolarizing step, as opposed to repetitive (tonic) firing). The role of Kv1 channels in the MSO is discussed in more detail in Subchapter 5.2.

In contrast,  $I_h$  is a slow (time constant of tens to hundreds of milliseconds) non-selective cation current, which is activated on hyperpolarization (Biel et al., 2009; Wahl-Schott and Biel, 2009).  $I_h$  is carried by sodium and potassium ions (Pape, 1996). Since the usual sub-threshold membrane potential yields a much larger driving force for sodium as opposed to potassium ions, this current is strongly mediated by the influx of sodium ions and thus causes the membrane potential to depolarize (Biel et al., 2009). HCN channels are encoded by four genes (HCN1-4). Immunofluorescence labeling in the MSO has identified HCN1 and HCN4 to be the primary underlying subunits in the principal cells; HCN1 being the most expressed subunit (Koch et al., 2004; Khurana et al., 2012). The half-activation potential and activation time constant of  $I_h$  is modulated by intracellular levels of cAMP (Biel et al., 2009; Wahl-Schott and Biel, 2009; Khurana et al., 2012). HCN channels primarily based on HCN1 are usually activated for more depolarized voltages, showing the fastest time constant and being least sensitive to

modulation by cAMP. On the other hand, HCN channels based on HCN4 are the exact opposite, i.e. they are opening for more hyperpolarized membrane voltages, gating slowly and are strongly sensitive to cAMP (Wahl-Schott and Biel, 2009). In MSO neurons  $I_h$  is contributing to the large resting conductance and thus the fast membrane time constant (Khurana et al., 2011).

Kv1 and HCN channels should not be only considered separated from each other. On the contrary, it is the balanced co-expression of these two adversatively activating channels which sets the membrane resting potential. Also, since both channels are already open at rest to a significant extent, they mediate the large resting conductance of MSO cells and thus their exceptionally low input resistance (Scott et al., 2005; Mathews et al., 2010; Khurana et al., 2012). The dynamic interplay of Kv1 and HCN channels in the MSO has shown to maintain the temporal resolution of coincidence detection (Khurana et al., 2011).

MSO neurons are not fast, high-resolution coincidence detectors from the outset. Studies in gerbils have shown that the principal cell's membrane properties undergo drastic changes in the first weeks after hearing onset (in gerbil: postnatal day 12 (P12); Scott et al., 2005; Khurana et al., 2012). Underlying these changes are an increase of channel expression and/or modulatory factors of Kv1 and HCN channels, causing a substantial upregulation of  $I_{Kv1}$  and  $I_h$ . The upregulation of these sub-threshold currents entails a dramatic decrease of input resistance and membrane time constant and thus a significant shortening of the integration time window (Scott et al., 2005; Khurana et al., 2012).

## **1.2. Action potential initiation**

### **1.2.1. History of the action potential**

The history of the discovery of the action potential goes back to (and is strongly associated with) the foundations of modern electrophysiology. At the end of the 18<sup>th</sup> century, Luigi Aloisio Galvani discovered that dissected legs of frogs began to twitch

when hit by an electrical spark (Galvani, 1791; Hoff, 1936; Piccolino, 1997). It was Galvani's finding that led to the invention of the first electric battery by Alessandro Volta, a professor at the university of Pavia (Volta, 1800; Piccolino, 2000). Following Galvani's work, Carlo Matteucci, an Italian physicist and professor at the university of Pisa, found that injured muscles generated a direct current between the cut and intact surface (Moruzzi, 1996; Seyfarth, 2006). Inspired by Matteucci's work, the German physician Emil du Bois-Reymond reproduced the experiments in muscles and nerves, which led him to the discovery of the action potential (AP; du Bois-Reymond, 1843; du Bois-Reymond, 1848; Moruzzi, 1996). A few years later, du Bois-Reymond's colleague and friend, Hermann von Helmholtz was the first to measure the conduction velocity of action potentials in a dissected sciatic nerve of a frog<sup>3</sup> (von Helmholtz, 1850; Hoff and Geddes, 1960; Piccolino, 1998; Schmidgen, 2011). Julius Bernstein, who among others studied medicine under Emil du Bois-Reymond and later worked as an assistant to Hermann von Helmholtz in the beginning of his scientific career, developed a hypothesis today known as the “membrane theory” which he published in 1902 and refined in 1912 (Bernstein, 1902 and 1912). His work was mainly focused on the origin of the resting potential and action potentials in the nerve. Bernstein suggested that the negative resting potential is established by the permeability of the membrane to potassium ions while being impermeable to other ions. As potassium ions move through the membrane of the cell they would carry positive charge outside, leaving an excess of negative charge inside the cell when the electrochemical equilibrium sets in. An action potential in Bernstein's view would occur when the membrane suddenly becomes permeable to all ions, called the “membrane breakdown”, once the internal potential is sufficiently raised by, for example, electrical stimulation or the arrival of another action potential. He suggested that once the membrane breakdown happens, the membrane potential would jump to zero giving rise to an action potential.

---

3 Helmholtz reported that the conduction time of an impulse propagating through the nerves (50 to 60 millimeter in length, kept at 2 – 6 °C) measured from 0.0014 to 0.002 seconds, which translates to a velocity of around 25 to 43 meters per second (von Helmholtz, 1850; Hoff and Geddes, 1960).

In 1939, Ken Cole and Howard Curtis confirmed Bernstein's theory by showing that the membrane permeability increases during an AP in squid axons (Cole and Curtis, 1939). In the same year Alan Lloyd Hodgkin and Andrew Fielding Huxley found that an action potential (starting at a negative membrane potential) in the giant squid axon substantially overshoot 0 mV by tens of millivolts, inducing a polarity change of the membrane potential, which was a contrast to Bernstein's theory of a mere “breakdown” of the membrane potential (Hodgkin and Huxley, 1939; Huxley, 2002). Ten years later, Hodgkin and Bernard Katz published a result of what they found to be the reason for this overshoot: the massive increase of the membrane permeability during an action potential was mainly mediated by an increase of permeability to sodium ions, which marked another milestone in the understanding of AP generation (Hodgkin and Katz, 1949). Using voltage-clamp recordings Hodgkin, Katz and Huxley then demonstrated the dependence of sodium and potassium permeability on

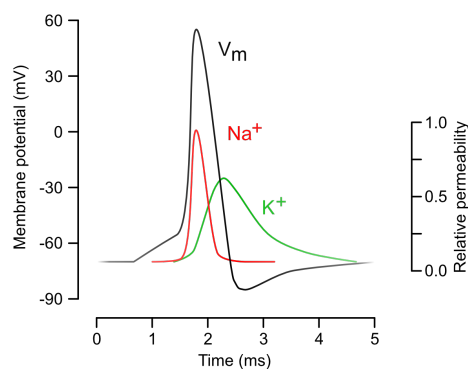


**Figure 8.** The action potential and the involved conductances. Voltage deflection of the neuronal membrane (black), underlying sodium (red) and potassium (green) conductances. Figure reproduced similar to Hodgkin and Huxley (1952d).

voltage and time (Hodgkin, Huxley and Katz 1952, Hodgkin and Huxley 1952a,b,c; Figure 8) which ultimately led to the quantitative description the generation of the action potential, today well-known as the Hodgkin-Huxley model (Hodgkin and Huxley 1952d; also see Section 1.2.2.).

The model of Hodgkin-Huxley assumes the existence of distinct channels for sodium and potassium ions in the membrane which can assume the states “open”, “closed” and “inactivated”. This hypothesis was confirmed by Erwin Neher and Bert Sakmann who were able to show the different conductance states of individual ion channels using their newly invented patch-clamp technique (Neher and Sakmann, 1976; Neher, Sakmann and Steinbach, 1978; Neher and Sakmann, 1992; Sakmann and Neher, 1995).

### 1.2.2. Modeling a neuronal membrane with Hodgkin-Huxley equations

To investigate the different questions of this thesis biophysical modeling of MSO

neurons is performed using differential equation systems that are based on the Hodgkin-Huxley equations (Hodgkin and Huxley 1952d). In this section a brief description is given on how a neuronal membrane is modeled following the Hodgkin-Huxley paradigm.

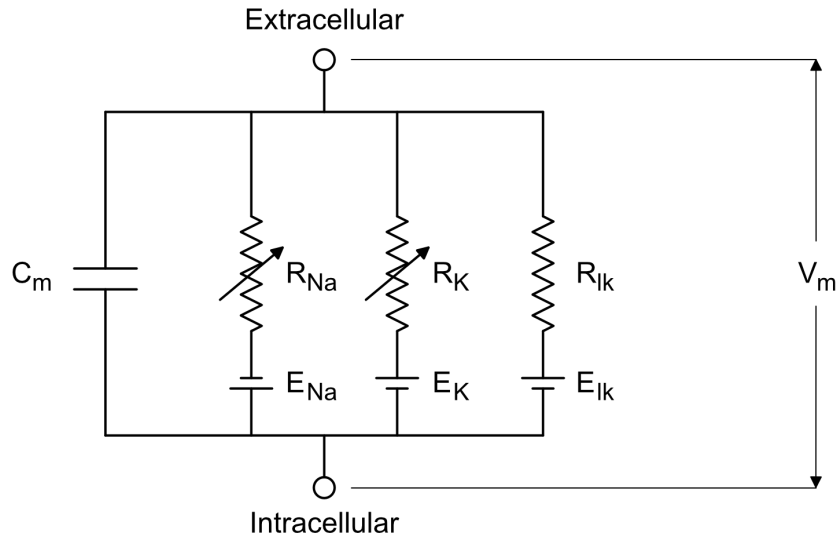


**Figure 9.** Equivalent electrical circuit of a membrane patch as proposed in Hodgkin and Huxley (1952d). The membrane is modeled by a capacitor with capacitance  $C_m$  giving rise to the membrane potential  $V_m$ . Resistors ( $R_{Na}$ ,  $R_K$ ,  $R_{lk}$ ) indicate the voltage-dependent permeabilities of sodium and potassium ions and the passive leak through the neuronal membrane. The electrochemical gradients are mimicked by batteries ( $E_{Na}$ ,  $E_K$ ,  $E_{lk}$ ).

The Hodgkin-Huxley model regards the excitable neuronal membrane as an electrical RC circuit where the membrane itself is modeled by a capacitor and the transmembrane ion channels by resistors (Figure 9). The gating of voltage-sensitive ion channels is modeled by two types of gating particles, which represent the activation and inactivation of the channel. The gating particles are thereby modeled by the first order differential equation

$$\frac{da}{dt} = \frac{a_\infty(V) - a(V)}{\tau(V)}, \quad (1)$$

whereby  $a_\infty$  represents the voltage-dependent steady-state activation (or inactivation) of the channel, and  $\tau$  is the voltage-dependent time constant of the respective gating particle. The transmembrane current  $I$  flowing through a population of channels of the given kinetics can then be described by

$$I = g a^x b^y (V - E). \quad (2)$$

The number  $g$  denotes the maximum conductance of the channels per specified area of the putative channel population in the membrane. The activation of the channel is modeled by  $a$  and the inactivation is modeled by  $b$ , both according to Equation 1. The variables  $x$  and  $y$  represent the number of the respective gating particles and  $E$  denotes the reversal potential of the channel. If a channel does not inactivate,  $b$  is set to 1 or omitted. Considering the classical Hodgkin-Huxley model of an excitable membrane, incorporating sodium, potassium and unspecified passive leak, the temporal evolution of the membrane potential can be given by

$$C \frac{dV}{dt} = I_{ext} - \overbrace{g_{Na} m^3 h (V - E_{Na})}^{I_{Na}} - \overbrace{g_K n (V - E_K)}^{I_K} - \overbrace{g_{lk} (V - E_{lk})}^{I_{lk}} . \quad (3)$$

The constant  $C$  represents the capacitance of the neuronal membrane viewed as a capacitor.  $I_{Na}$ ,  $I_K$ , and  $I_{lk}$  describe the ionic currents flowing through the sodium, potassium and leak channels, respectively.  $I_{ext}$  represents an external current which is injected to stimulate the membrane patch.

In case of a multi-compartmental cable model (as is used in Chapter 2), Equation 3 has to be extended by an axial current. If  $V_i$  denotes the voltage of the  $i$ -th segment, the axial current  $I_{ax}$  linking the  $i$ -th segment of the cable to its neighbors can be described by

$$I_{ax}^i = \frac{V_{i-1} - V_i}{R_{ax}^{i-1,i}} + \frac{V_{i+1} - V_i}{R_{ax}^{i+1,i}} , \quad (4)$$

where  $R_{ax}$  denotes the axial resistance between the  $i$ -th compartment and its respective neighbors (see the Chapter 2, Materials and Methods).

In the past decades a large number of voltage-sensitive channels in miscellaneous neurons were identified, including different types of sodium, potassium, calcium and hyperpolarization-activated unspecific cation channels. Using voltage-clamp recordings, the activation kinetics of these channels were extracted which allowed to generate biophysical models of various neuronal types adapting the Hodgkin-Huxley equations accordingly. For a thorough treatment of biophysical modeling using Hodgkin-Huxley

equations (among other models), see Izhikevich, 2007 and Koch, 1999.

### 1.2.3. The morphology of myelinated axons

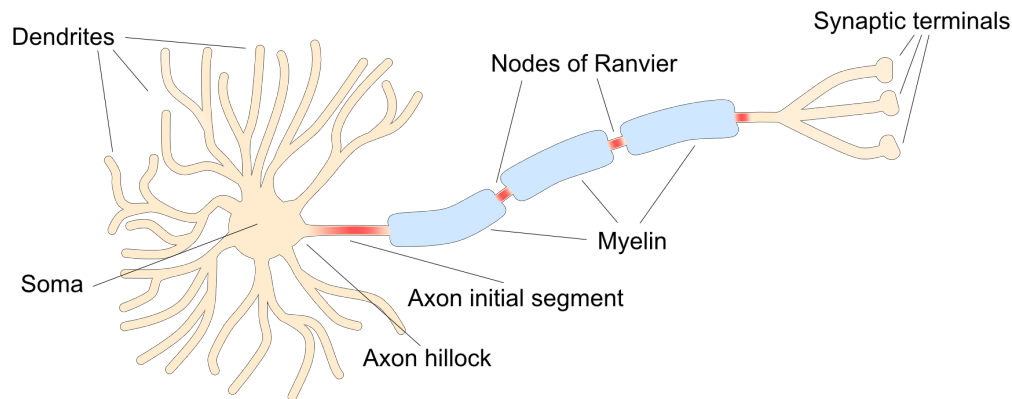


**Figure 10.** Cartoon of a neuron with its axon. Regions of high sodium channel densities are indicated in red.

The axon is a relatively thin process mostly emerging from the soma or proximal dendrite of a neuron. The axon conducts electrical impulses away from the cell forming the main transmission structure in the nervous system. Myelinated axons (Figure 10) can be divided into the proximal unmyelinated part, the axon initial segment (AIS), and an extended myelinated part. The most proximal part of the AIS is called the axon hillock, which initiates the axonal process by tapering its diameter down to only a few microns forming a conical shape. The AIS expresses a high density of sodium channels. The myelinated part which is much longer than the AIS can branch extensively forming collaterals. It thus constitutes the major part of the axon. In the central nervous system the myelination arises from oligodendrocytes which wrap their processes around axons providing them with an insulation called the myelin sheath. The myelination is periodically interrupted by the nodes of Ranvier. Like the AIS, the nodes of Ranvier exhibit a high sodium channel density which, in concert with the low membrane capacitance provided by the myelin-sheath, enables a fast transmission of APs in a reproductory fashion called saltatory conduction. The most distal part of the axon (or collaterals) forms unmyelinated branches and culminates in the synaptic terminals which connect the presynaptic cell to the postsynaptic cells.

#### 1.2.4. Action potential initiation in cortical neurons

The integration of synaptic inputs in central neurons generally concludes with the generation of all-or-nothing impulses – the action potentials (APs; for detailed review, see: Stuart et al., 1997b; Bean, 2007; Debanne et al., 2011). Once generated, APs are transmitted by the axon which synapses on other neurons and thus conveys the information encoded by the AP rate and pattern. A growing number of evidences indicates that also the shape of the AP waveform itself encodes information, modulating the transmitter release at the synapses (Geiger and Jonas, 2000; Kole et al., 2007, reviews: Debanne, 2004; Debanne et al., 2011). Since the site of AP initiation in a neuron is the location where a putative modulation of neuronal output could take place most efficiently, as well as to better understand how inputs are ultimately translated into output signals, it is of particular interest to investigate where neurons generate their action potentials.

Seminal work of the 1950s marked the starting point of AP initiation site investigation, when, investigating spinal motoneurons, AP initiation was already suggested to occur in the axon (Coombs et al., 1957; Fatt, 1957; Fuortes et al., 1957; also see Eccles, 1964; Llinás, 1988). In contrast to these early influential studies growing evidence on active sodium and calcium conductances in dendrites of several central neuron types indicated that APs could be initiated in the dendrites (Spencer and Kandel, 1961; Wong et al., 1979; Turner et al., 1989; Pockberger, 1991; Regehr et al., 1992 and 1993). Inspired by these findings, several studies employing simultaneous somatodendritic patch-clamp recordings were prepared to test the hypotheses of axonal or dendritic AP initiation in the following years. It was found that for neurons in the cortex, cerebellum, and further brain structures the APs are initiated in the axon and then are subsequently backpropagated into the soma and dendrites (Stuart and Häusser, 1994; Stuart and Sakmann, 1994; Häusser et al., 1995; Spruston et al., 1995; Bischofberger, et al., 1997; Stuart et al, 1997a). In some cases, however, upon particularly strong synaptic stimulation, it was found that dendrites can also elicit regenerative responses mediated by sodium and calcium channels which can precede the somatic AP (Stuart et al., 1997a; Golding, Spruston, 1998; Rancz et al., 2006). A breakthrough which finally

allowed to pinpoint the AP initiation site was achieved only a couple of years ago with the progress of existing, or the employment of new recording methods. Results from whole-cell (Williams et al., 1999; Shu et al., 2006; Kole et al., 2007 and 2008, Schmidt-Hieber, et al., 2008) and loose-patch recordings (Raastad et al., 2003; Meeks, et al., 2005; Clark, et al., 2005; Boudkkazi et al., 2007; Atherton et al., 2008), as well as the usage of voltage-sensitive dyes (Palmer, et al., 2006; Foust et al., 2010, Palmer et al., 2010, Popovic et al., 2011) and sodium imaging (Kole et al., 2008; Bender et al., 2009; Fleidervish et al., 2010) further corroborated that action potentials are initiated in the axon. Moreover, it was found that in most neurons with myelinated axons, AP initiation was identified to take place in the distal part of the axon initial segment (AIS; Khaliq et al., 2005; Khaliq et al., 2006; Palmer et al., 2006; Shu et al., 2007; Atherton et al., 2008; Yu et al., 2008; Foust et al., 2010; Palmer et al., 2010).

Section 5.1 of this thesis provides an extensive discussion about action potential initiation in central neurons, including the methods involved, and our results (of Chapter 2) in the context of the current state of scientific knowledge.

### **1.3. Aims of this thesis**

This thesis is subdivided into three individual studies, presented in Chapter 2, 3, and 4, investigating the excitability, the role of the glycinergic inhibition in the tuning of coincidence detection, channel properties and synaptic integration along the tonotopic axis in the principal cells of the MSO. Each of these studies is comprised of an experimental and a computational part. The author of this thesis contributed to the computational part of the studies; the experiments were performed by experimental collaborators (see Author Contributions). A detailed statement of the author's contributions to the individual studies can be found at the end of the thesis (see Author Contributions). Before the results are presented (Chapter 2, 3, and 4), the introduction is briefly summarized and the aims of each study, as well as our approaches to reach these aims, are outlined.

The medial superior olive (MSO) is a nucleus in the mammalian auditory brainstem. MSO neurons are the first to receive binaural inputs and encode arrival time differences of sounds at the two ears by means of coincidence detection. These arrival time differences, called interaural time differences (ITDs), are in the magnitude of only microseconds, and represent the major cue for localizing low-frequency sounds in the horizontal plane. The extreme temporal precision required to discriminate these minute ITDs has been subject to a large number of studies over the past several decades investigating the MSO and its upstream microcircuitry. It was found that the ITD detection circuitry includes some of the fastest and temporally most accurate axons and synapses in mammalian anatomy, that convey phase-locked excitatory and inhibitory inputs to MSO neurons, and preserves the ITDs in the earlier stages prior to the MSO. Moreover, it has been demonstrated that the principal neurons of the MSO themselves exhibit some of the fastest membrane kinetics in the mammalian central nervous system. Underlying this speed are strong transmembrane conductances mediated by low-threshold potassium channels (Kv1 channels) and hyperpolarization-activated cyclic nucleotide-gated channels (HCN channels) which are expressed in the MSO

neuron's somatodendritic membrane and drastically decrease the membrane time constant and input resistance of MSO neurons.

### **Study 1 (Chapter 2)**

While the increased membrane conductance mediated by Kv1 and HCN channels is essential for the exceptional temporal precision of the MSO neuron's coincidence detection, it is problematic for the neuron's excitability, since the strong transmembrane leak renders the somatodendritic membrane to constitute a tremendous current sink to the axon initial segment, the typical site of action potential initiation, thus impeding the generation of action potentials (APs). How, under these difficult circumstances, MSO neurons are capable of generating action potentials and even produce sustained high firing rates, as has been observed *in vivo*, is unclear. To investigate this question, we conducted a thorough computational study, aided by immunohistochemical and electrophysiological experiments. We created a biophysical model of an MSO neuron and its axon based on anatomical data that has been obtained analyzing the morphology of MSO axons. Using temporally extended naturalistic conductance trains we assessed how the firing probability is influenced by morphological and electrical parameters of the model. Also, the firing threshold's dependence on input frequency was investigated in simulations, as well as in MSO neurons *in vitro*. Furthermore, we developed a sophisticated algorithm that allowed us to determine the site of AP initiation for each AP elicited during trains of synaptic stimuli, for a variety of input rates, morphological and electrical parameters of the model. Monitoring electrical membrane properties and channel activation during stimulation enabled us to identify mechanisms that keep the neuron excitable, as well as that modulate the site of AP initiation.

### **Study 2 (Chapter 3)**

*In vivo* recordings demonstrated that MSO neurons generally respond best to positive (i.e. contra-leading) ITDs. Moreover, it has been shown that blocking the glycinergic inputs to MSO neurons *in vivo* shifts the peak of the ITD function towards zero, providing direct evidence that inhibition tunes the ITD sensitivity of MSO neurons. As a consequence, a model (here referred to as inhibition model) was developed that proposes a mechanism how a precisely-timed phase-locked inhibition is able to tune the

coincidence detection such that the preference for positive ITDs can be explained. The fundamental principle of the inhibition model is that precisely-timed inhibitory inputs shift the peak timing of excitatory inputs on each side, thereby influencing the timing of best coincidence. Several studies challenged the hypothesis of glycinergic inhibition being capable to tune coincidence detection of MSO neurons in the way the inhibition model proposes. Also, the inhibition model lacks thorough experimental testing under physiologically relevant conditions, in particular to quantify its efficacy as well as the specific relative timing conditions of inhibitory inputs that could explain *in vivo* data. The aim of the second study is to investigate these questions, thereby also addressing arguments recently brought up against the inhibition model. To do so, an extensive *in vitro* study in acute auditory brainstem slices of adult gerbils was performed, aided by computational modeling. To base the quantitative analysis on realistic synaptic kinetics, the time courses of excitatory and inhibitory synaptic conductances (ESPGs and IPSPs) were extracted in voltage-clamp experiments. To assess the magnitude of the inhibition-enforced peak shifts, these ESPGs and IPSPs were used as templates to inject them into the soma in conductance-clamp covering a broad parameter space of arrival times of inhibitory inputs relative to the excitatory inputs. To test the robustness of the inhibition-induced effects, these experiments were repeated for a wide range of physiologically relevant parameters, such as different synaptic kinetics, arrival time jitter, as well as for trains of inputs. To assess the impact of these peak shifts on coincidence detection, AP probability was determined in a supra-threshold setting. We created a biophysical model of an MSO neuron that was constrained to fit the membrane and response properties of the MSO neurons measured *in vitro*. This model allowed us to corroborate the *in vitro* findings as well as to investigate the impact of the fast-activating K<sub>v</sub>1 channels on the inhibition-enforced effects by adjusting the activation parameters of the channel.

### **Study 3 (Chapter 4)**

The MSO is tonotopically organized. Low-frequency sounds are thereby processed in the dorsal part of the nucleus, whereas higher frequencies are processed in the ventral part. The hyperpolarization-activated currents mediated by HCN channels substantially contribute to the tuning of membrane properties, hence to the temporal precision of

MSO neurons. The goal of this study is to investigate the putative differences of HCN currents along the tonotopic axis, in particular in the context of integration of inhibitory input trains at different frequencies. To investigate this question, *in vitro* experiments in acute auditory brainstem slices were performed, aided by computational modeling. Voltage-clamp measurements were conducted to determine putative differences of HCN current properties and membrane properties along the dorsoventral axis of the MSO. To investigate whether differences in the integration of inhibitory inputs along the dorsoventral axis exist, previously recorded inhibitory post-synaptic currents (IPSCs) were injected in trains at a rate of 100 Hz into dorsal as well as ventral MSO neurons, using a current-clamp setup. The responses to these injected IPSC trains were analyzed to determine the half-widths and the temporal summation. We developed two computational models of MSO neurons that were constrained to fit the HCN and membrane properties of an average dorsal and ventral MSO neuron, respectively. Using the models we determined the temporal summation in response to inhibitory input trains at different frequencies, assuming dorsal and ventral neurons receiving phase-locked inhibition at different rates. Finally, by manipulating the channel properties of HCN and Kv1 channels in the computational models, we are able to identify a mechanism how an interplay of HCN channels and fast-activating Kv1 channels facilitates the processing of inhibitory inputs at higher rates in ventral neurons.

## **2. Action Potential Generation in an Anatomically Constrained Model of Medial Superior Olive Axons**

Published in The Journal of Neuroscience (2014).

**Reference:** Lehnert S, Ford MC, Alexandrova O, Hellmundt F, Felmy F, Grothe B, Leibold C. Action potential generation in an anatomically constrained model of medial superior olive axons. *J Neurosci* 34: 5370–5384, 2014.

### **Author Contributions:**

List of authors: Simon Lehnert (SL), Marc C. Ford (MCF), Olga Alexandrova (OA), Franziska Hellmundt (FH), Felix Felmy (FF), Benedikt Grothe (BG), and Christian Leibold (CL).

Individual contributions: SL and CL, conception and design of the study, SL designed and generated the computational model, performed all simulations and analyzed the resulting data, SL and CL interpreted the results of the modeling; MCF and OA, designed and performed the immunohistochemical experiments, MCF and OA analyzed the immunohistochemical data; FF designed the electrophysiological experiments, FH and FF performed the electrophysiological experiments and analyzed the data; SL prepared all figures, except Figure 2, which was made by MCF. SL wrote the initial draft of the manuscript, MCF wrote the immunohistochemical part of the manuscript. FF, BG and CL contributed to various parts of the manuscript. SL, MCF, FF, BG and CL critically revised the manuscript. All authors approved the final version of the manuscript.



# Action Potential Generation in an Anatomically Constrained Model of Medial Superior Olive Axons

Simon Lehnert,<sup>1</sup> Marc C. Ford,<sup>1,2</sup> Olga Alexandrova,<sup>1</sup> Franziska Hellmundt,<sup>1,2</sup> Felix Felmy,<sup>1,3</sup> Benedikt Grothe,<sup>1</sup> and Christian Leibold<sup>1</sup>

<sup>1</sup>Department Biology II, <sup>2</sup>Graduate School of Systemic Neurosciences, and <sup>3</sup>Department Biology I, BioImaging Zentrum, Ludwig-Maximilians-Universität München, D-82152 Planegg-Martinsried, Germany

Neurons in the medial superior olive (MSO) encode interaural time differences (ITDs) with sustained firing rates of >100 Hz. They are able to generate such high firing rates for several hundred milliseconds despite their extremely low-input resistances of only few megohms and high synaptic conductances *in vivo*. The biophysical mechanisms by which these leaky neurons maintain their excitability are not understood. Since action potentials (APs) are usually assumed to be generated in the axon initial segment (AIS), we analyzed anatomical data of proximal MSO axons in Mongolian gerbils and found that the axon diameter is <1  $\mu\text{m}$  and the internode length is  $\sim 100 \mu\text{m}$ . Using a morphologically constrained computational model of the MSO axon, we show that these thin axons facilitate the excitability of the AIS. However, for ongoing high rates of synaptic inputs the model generates a substantial fraction of APs in its nodes of Ranvier. These distally initiated APs are mediated by a spatial gradient of sodium channel inactivation and a strong somatic current sink. The model also predicts that distal AP initiation increases the dynamic range of the rate code for ITDs.

**Key words:** action potential; axon; coincidence detection; interaural time difference; sound localization

## Introduction

The generation of action potentials (APs) is widely assumed to take place in the axon initial segment (AIS). Evidence for this assumption stems predominantly from cortical pyramidal neurons and cerebellar Purkinje neurons using simultaneous somatic and axonal whole-cell recordings (Stuart and Sakmann, 1994; Stuart et al., 1997; Kole et al., 2007; Shu et al., 2007) and voltage-sensitive dye imaging (Palmer and Stuart, 2006; Foust et al., 2010; Palmer et al., 2010; Popovic et al., 2011). At rest, these neurons have relatively high input resistances of 10–200 M $\Omega$ , allowing them to integrate synaptic inputs over several milliseconds. Thus, during depolarizing stimuli, the soma generally serves as a strong and temporarily stable current source for the AIS. In neurons with very low input resistances of 2–5 M $\Omega$ , the mechanisms of AP initiation have not yet been studied in such great detail. In those cells, the membrane time constants are too short to allow the soma to serve as a temporarily stable current source. Conversely, the soma might even act as a current sink to the AP generating zone and therefore increases the AP threshold at the AIS.

In the present study, we investigated AP generation in neurons of very low input resistance, the principal cells of the medial superior olive (MSO). These neurons have membrane time constants in the range of only a few hundreds of microseconds and input resistances as low as 5 M $\Omega$  (Scott et al., 2005; Couchman et al., 2010). The MSO is a binaural nucleus in the ascending auditory pathway. MSO neurons encode the azimuthal position of low-frequency sounds via differences in the time of arrival at the two ears by their firing rate (Goldberg and Brown, 1969; Yin and Chan, 1990; Fitzpatrick et al., 1997; Brand et al., 2002) with a precision of only a few tens of microseconds. This exquisite temporal precision of binaural coincidence detection is partly achieved by the fast membrane time constants of neurons resulting from the high expression of low-voltage-activated potassium channels and hyperpolarization-activated cation channels (Svirskis et al., 2002; Koch et al., 2004; Scott et al., 2005; Mathews et al., 2010; Baumann et al., 2013), both of which are already open at rest. Despite the resulting low input resistance, these neurons can fire at high rates of  $\sim 100$  Hz and more. The mechanisms by which this is possible are still unresolved.

In this article, we address the question of how AP generation is accomplished in leaky neurons using a computational model of MSO neurons with axonal morphology based on new detailed morphometric data. Our simulations show that, despite the leaky soma, the AIS remains electrotonically isolated and retains its ability to generate APs. However, we also identified conditions under which the APs are initiated at the nodes of Ranvier. This distal initiation of APs increases the dynamic range of the rate code of interaural time differences (ITDs).

Received Sept. 20, 2013; revised March 5, 2014; accepted March 8, 2014.

Author contributions: S.L., M.C.F., O.A., F.F., B.G., and C.L. designed research; S.L., M.C.F., O.A., F.H., and F.F. performed research; S.L., M.C.F., O.A., F.H., and F.F. analyzed data; S.L., M.C.F., F.F., B.G., and C.L. wrote the paper.

This work was supported by the German Research Foundation via the Collaborative Research Center 870 and the Elisabeth and Helmut Uhl Stiftung.

The authors declare no competing financial interests.

Correspondence should be addressed to Christian Leibold, Computational Neuroscience, Department Biology II, Ludwig-Maximilians-University Munich, Grosshaderner Strasse 2, D-82152 Planegg-Martinsried, Germany. E-mail: leibold@bio.lmu.de.

DOI:10.1523/JNEUROSCI.4038-13.2014

Copyright © 2014 the authors 0270-6474/14/345370-15\$15.00/0

## Materials and Methods

### General

All experiments were performed according to institutional guidelines, and national and regional laws; it was approved by the Regierung von Oberbayern (AZ55.2-1-54-2531-105-10). All results are given as the mean  $\pm$  SEM.

### Retrograde labeling of MSO cells

Mongolian gerbils (*Meriones unguiculatus*) of either sex [ $n = 4$ ; postnatal day 29 (P29) to P31] were anesthetized with pentobarbital (2 mg/kg body weight) and intracardially perfused with ice-cold Ringer's solution containing 0.1% heparin. After decapitation, the brainstem was removed from the skull under ice-cold dissection solution comprising the following (in mM): 125 NaCl, 2.5 KCl, 1 MgCl<sub>2</sub>, 0.1 CaCl<sub>2</sub>, 25 glucose, 1.25 NaH<sub>2</sub>PO<sub>4</sub>, 25 NaHCO<sub>3</sub>, 0.4 ascorbic acid, 3 myo-inositol, and 2 pyruvic acid (all chemicals were from Sigma-Aldrich). For retrograde labeling of MSO cells, the brainstem was sectioned along the posterior–anterior axis until the MSO, lateral superior olive, and superior paraolivary nucleus (SPN) were clearly visible. Borosilicate glass micropipettes with a tip diameter of 10–15  $\mu$ m were filled with a 10% solution of tetramethylrhodamine dextran (3000 molecular weight; Invitrogen) and visually guided to the SPN. Cells were labeled by applying 2–4 electroporation pulse trains (50 ms, 50 V, 10 Hz; modified from previous studies; Ford et al., 2009). Subsequently, the explants were transferred to a chamber containing oxygenated incubation solution (same as incubation solution, but containing 2 mM instead of 0.1 mM CaCl<sub>2</sub>) and incubated at room temperature for 90 min. Thereafter, brainstems were immersion fixed at room temperature overnight in 4% paraformaldehyde solution.

### Immunohistochemistry

Brainstems were sectioned transversally (80–120  $\mu$ m slice thickness), rinsed in PBS, and transferred to blocking solution containing 1% bovine serum albumin, 2% Triton X-100, and 0.1% saponin in PBS. Multiple-immunofluorescence labeling was performed with the following primary antibodies: ankyrin G (sc-28561; rabbit; 1:500; Santa Cruz Biotechnology), Kv1.2 (75-008 clone K14/16; mouse; 1:500; NeuroMab), microtubule-associated protein 2 (CH22103; chicken polyclonal; 1:1000; Neuromics), and myelin basic protein (ab7349; rat monoclonal; 1:20; abcam). The incubation time (4°C) for primary antibodies was 3 d. After incubation with secondary antibodies (1–2 d; 4°C) and rinsing in PBS, sections were mounted with Vectashield mounting medium.

### Confocal microscopy

Confocal images were acquired with a TCS SP5-2 confocal laser-scanning microscope (Leica Microsystems) equipped with HCX PL APO 63 $\times$ /numerical aperture 1.3 glycerol objective. Fluorochromes were excited at 405, 488, 561, 594, and 633 nm for aminoethylcoumarin acetate, DyLight488, tetramethylrhodamine dextran, Alexa Fluor 594, and DyLight649, respectively. The emission filters for these fluorochromes were set to (in the same order) 410–460, 510–550, 565–585, 605–625, and 640–760 nm. For each optical section the images were collected sequentially for four to five fluorochromes. Stacks of 8-bit grayscale images were obtained with axial distances of 290 nm between optical sections and a pixel size of 120.4 nm. To obtain an improved signal-to-noise ratio, each section image was averaged from five successive scans. After stack acquisition, the Z chromatic shift between color channels was corrected. RGB stacks, montages of RGB optical sections, and maximum-intensity projections were assembled into tables by using ImageJ 1.37k plugins and Photoshop version 8.0.1 (Adobe Systems) software.

### Morphometry

Morphometric measurements were made from overlapping image stacks of MSO principal cells. Using the ImageJ 1.37k paint-brush tool, individual axons of MSO cells filled with tetramethylrhodamine dextran were manually labeled by following single axons subsequently through each optical section of the confocal stack (Werth et al., 2008; for dendrites, see Couchman et al., 2010). Afterward, the neighboring axons were digitally deleted. We refer to this method as digital extraction. The same axon was identified in the neighboring overlapping confocal stacks and digitally extracted. AISs and nodes of Ranvier were identified on the basis

of ankyrin G/Kv1.2 antibody staining. AIS and internode lengths were measured in three dimensions in confocal stack images using the ImageJ 1.37k Sync Measure 3D tool. AIS and internodal axon diameters were measured at the positions defined by ankyrin G and Kv1.2 labeling (see Fig. 2B) in maximum-intensity projections of image stacks based on tetramethylrhodamine dextran labeling. The mean diameter of the first internode was averaged from measurements at several (10–29) different positions between the outer borders of the juxtaparanodes (see Fig. 2B, K3 and K6).

### Electrophysiology

Experimental procedures were as described in Couchman et al. (2010). In brief, Mongolian gerbils of either sex of P60–P80 were anesthetized with isoflurane. Brains were removed after decapitation, and 110- $\mu$ m-thick horizontal brainstem slices were taken with a VT1200S vibratome (Leica) in dissection solution containing the following (in mM): 50 sucrose, 25 NaCl, 27 NaHCO<sub>3</sub>, 2.5 KCl, 1.25 NaH<sub>2</sub>PO<sub>4</sub>, 3 MgCl<sub>2</sub>, 0.1 CaCl<sub>2</sub>, 25 glucose, 0.4 ascorbic acid, 3 myo-inositol, and 2 Na-pyruvate, pH 7.4 when bubbled with 95% O<sub>2</sub> and 5% CO<sub>2</sub>. Slices were incubated in recording solution (same as slice solution but with 125 mM NaCl, no sucrose, and 2 mM CaCl<sub>2</sub> and 1 mM MgCl<sub>2</sub>) at 36°C for 45 min, bubbled with 5% CO<sub>2</sub> and 95% O<sub>2</sub>.

Incubated slices were placed into a recording chamber attached to a BX51WI microscope (Olympus) equipped with a custom-made gradient contrast illumination and continuously perfused with recording solution kept at 34–36°C by a Warner Instruments heating system. MSO neurons were visualized at 60 $\times$  magnification with a Retiga 2000 DC camera (Till Photonics/FEI Munich). Current-clamp whole-cell recordings were performed using an EPC10/2 amplifier (HEKA Elektronik) on visually identified MSO neurons with electrode resistances of  $\sim$ 3 M $\Omega$ . Access resistance was estimated in voltage-clamp after break in and was bridge balanced to 100% in current-clamp mode. The internal recording solution consisted of the following (in mM): 145 K-gluconate, 4.5 KCl, 15 HEPES, 2 Mg-ATP, 2 K-ATP, 0.3 Na<sub>2</sub>-GTP, 7.5 Na<sub>2</sub>-phosphocreatine, 5 K-EGTA, pH 7.2. The liquid junction potential was corrected on-line with an estimated value of 17 mV.

### Computational modeling

Based on the morphometric analysis, a multicompartmental model was created to study the generation of APs in MSO principal cells. The model consists of one large somatic compartment that combines the somatic and dendritic membrane surface (Ashida et al., 2007). The model focuses on the axonal morphology, since APs are generally assumed to be generated there. The axon model consisted of an unmyelinated AIS followed by an extensive myelinated part that was periodically interrupted by 21 nodes of Ranvier. Figure 1A shows a schematic drawing of the first segments of the model up to the fourth node of Ranvier (R4). The AIS was further subdivided into a tapering part (tAIS) and a constant part (cAIS), resembling the actual geometry of the AIS. The voltages of the compartments followed a Hodgkin–Huxley-type equation as follows:

$$C_m \frac{dV}{dt} = - (I_{Na} + I_{KHT} + I_{KLT} + I_h + I_{lk} + I_{syn} + I_{axial} + I_{ext}),$$

where  $I_{ext}$  is the external current, and the ohmic transmembrane currents are as follows:

$$I_x(V) = g_x a_x^m b_x^n (V - E_x).$$

Here,  $C_m$  is the membrane capacitance,  $g_x$  is respective peak conductances,  $a_x$  and  $b_x$  are the gating variables, and  $m$  and  $n$  are the respective cooperativities. The dynamics of the gating variables are modeled according to first-order kinetics, as follows:

$$\frac{da}{dt} = \frac{a_\infty - a}{\tau_a} \quad \text{and} \quad \frac{db}{dt} = \frac{b_\infty - b}{\tau_b}$$

where  $a_\infty$  and  $b_\infty$  are the steady-state activation functions, and  $\tau_a$  and  $\tau_b$  are the voltage-dependent time constants.

The axial current for the  $i$ th compartment is defined as follows:

$$I_{\text{axial}}^i = \frac{V_{i-1} - V_i}{R_{\text{axial}}^{i-1,i}} + \frac{V_{i+1} - V_i}{R_{\text{axial}}^{i+1,i}},$$

in which  $R_{\text{axial}}$  denotes the axial resistance between the  $i$ th compartment and its respective neighboring compartments. The axial resistance results from the geometry of the axonal segment (diameter and length) as well as the specific axial resistivity of  $100 \Omega\text{cm}$ , which is in the range of usually assumed values (Mainen et al., 1995; Mainen and Sejnowski, 1996; Shu et al., 2007).

The specific model for the sodium channel was taken from Scott et al. (2010) with a reversal potential for sodium of 69 mV and a modified conductance density in the axon of  $4 \text{ nS}/\mu\text{m}^2$  to fit the firing threshold of our current-clamp measurements (see Fig. 4). We chose the somatic sodium conductance density to be  $0.2 \text{ nS}/\mu\text{m}^2$ , a value 20-fold smaller than that in the axon and reflecting the low sodium channel density found in MSO principal cell somata (Scott et al., 2010). The high-threshold potassium channel was modeled according to Rothman and Manis (2003) without a slow activation variable and only at the soma since it had only little effect in the axon. The low-threshold potassium channel (KLT) was modeled according to (Mathews et al., 2010) and was present in the soma and all unmyelinated axonal compartments. The potassium reversal potential was set to  $-90 \text{ mV}$ . The hyperpolarization-activated cation channel gives rise to a somatic hyperpolarization (h)-activated cation current ( $I_h$ ), which was modeled using the kinetics measured in dorsal MSO neurons (Baumann et al., 2013), with a reversal potential of  $-35 \text{ mV}$ . The resting potential of  $-68 \text{ mV}$  and the somatic input resistance of  $5 \text{ M}\Omega$  were set by adjusting the peak conductances of KLT and h current. The somatic surface was set to  $8750 \mu\text{m}^2$ , such that we get a somatodendritic capacitance of  $70 \text{ pF}$  (Rautenberg et al., 2009), assuming a specific capacitance of  $0.8 \mu\text{F}/\text{cm}^2$  (Gentet et al., 2000; Shu et al., 2007). As a consequence, the somatic membrane time constant is  $350 \mu\text{s}$ , which closely resembles the measured membrane time constants *in vitro* (Scott et al., 2005; Couchman et al., 2010). The specific myelin conductance per lamella was set to  $0.1 \mu\text{F}/\text{cm}^2$  (McIntyre et al., 2002, 2004). Together with a g-ratio of 0.7 and an assumed myelin periodicity of  $16 \text{ nm}$  (Agrawal et al., 2009), our standard model exhibits nine myelin lamellae. Thus, we obtain a specific capacitance of the myelin sheath of  $0.0111 \mu\text{F}/\text{cm}^2$ , similar to the value of  $0.01 \mu\text{F}/\text{cm}^2$  used in Kuba et al. (2006) for axons of nucleus laminaris (NL) neurons. Some computational studies of axons use specific capacitances per lamella that are significantly higher; however, they compensate for this by a larger number of myelin lamellae. Using a substantially larger myelin capacitance (e.g., three times or higher) would cause propagation failures of generated APs in our model, a result that would contradict the secure propagation of APs known from MSO principal neurons (Scott et al., 2007). This matching of an experimental finding argues in favor of our parameter choice. The validity of the parameter choice is further supported by our physiological measurements of firing thresholds for onset-like responses in Figure 4.

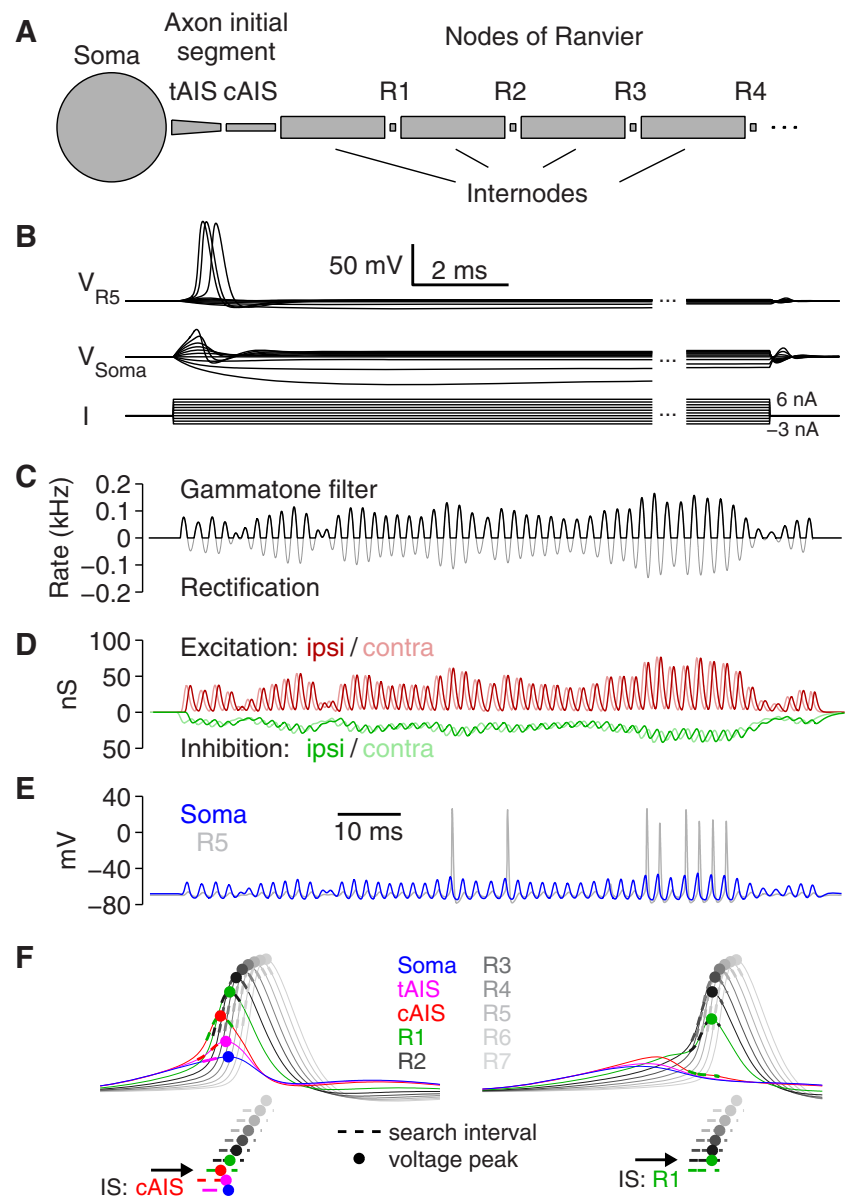


**Figure 1.** Computational model. **A**, Schematic drawing of the first segments from the soma to R4 of the MSO model neuron. The AIS is subdivided into two compartments: the tAIS and the cAIS. **B**, Voltage response in different compartments (top, R5; middle, soma) to current injections at the soma (bottom). **C**, **D**, The input conductances were obtained from noise that is filtered by a gammatone filter with a center frequency of 500 Hz (gray) and half-wave rectified (**C**, black). The trace from **C** is transformed into conductance inputs by convolution with excitatory (ipsilateral, dark red; contralateral, light red) and inhibitory (ipsilateral, green; contralateral, light green) synaptic kernels (**D**; see Materials and Methods). **E**, Voltage responses of the soma (blue) and R5 (light gray) of the model when driven with the conductance trains depicted in **D**. **F**, The AP initiating segment (IS, black arrow) is derived from the voltage traces at the individual compartments (color coded segments: blue, soma; pink, tAIS; red, cAIS; green, R1; dark gray to light gray, R2–R7). Example traces show a cAIS-generated (left) and an R1-generated (right) AP. Dashed traces indicate the search intervals of duration  $L$  that are defined by the voltage peak (dot) of the downstream segment (see Materials and Methods). The voltage peak that occurs earliest in time defines the SIS.

A detailed account of the geometrical and electrical features of the model is given in Tables 1 and 2, respectively.

In response to somatic current injections, the neuron model exhibits typical onset behavior (Fig. 1*B*; i.e., it fires only one AP; Scott et al., 2005; Couchman et al., 2010) at the onset of the depolarizing pulse. The AP amplitude at the soma resembles physiologically measured values of  $\sim 10 \text{ mV}$  (Scott et al., 2005; Couchman et al., 2010), whereas, at the nodes of Ranvier, the APs exhibit usual amplitude values of  $\sim 100 \text{ mV}$ .

**Table 1. Geometrical parameters of the model**

Parameters	Values
Soma/somatodendritic compartment	
Area	8750 $\mu\text{m}^2$
Axon initial segment (tapering part)	
Length	10 $\mu\text{m}$
Large diameter	1.64 $\mu\text{m}$
Small diameter	0.66 $\mu\text{m}$
Axon initial segment (constant part)	
Length	10 $\mu\text{m}$
Diameter	0.66 $\mu\text{m}$
Internodes	
Length	100 $\mu\text{m}$
Inner diameter	0.66 $\mu\text{m}$
Outer diameter	0.948 $\mu\text{m}$ (corresponding to a g-ratio of 0.7),
Myelin lamellae	9 (corresponding to a myelin periodicity of 16 nm)*
Node(s) of ranvier	
Length	1 $\mu\text{m}$
Diameter	0.66 $\mu\text{m}$

\*From Agrawal et al. (2009).

**Table 2. Maximum conductances of voltage-gated channels**

Channels	Soma	tAIS	cAIS	Internodes	Nodes
gNa	0.2	4	4	0	4
gKHT	0.1	0	0	0	0
gKLT	1.55	1.55	1.55	0	1.55
gh	0.02	0.02	0.02	0	0
gIk	0.0005	0.0005	0.0005	0.0002	0.05

Data are in nS/ $\mu\text{m}^2$ .

Since ongoing synaptic bombardment under *in vivo* conditions increases the leakiness of the neuron, we decided to study AP generation using a temporally extended naturalistic stimulus that resembles the periodicity of a cochlear channel with a specific center frequency. Our stimuli were generated using bandpass-filtered white noise  $n(t)$  (Fig. 1C) that was linearly filtered (convolved) with a gammatone kernel, as follows:

$$f(t) = t^4 e^{-\gamma t} \cos(t\omega_c),$$

with  $\gamma(\omega_c) = 24.7(4.37 \times \omega_c/(2\pi) + 1)$  in kilohertz (Glasberg and Moore, 1990) and the center frequency  $\omega_c/(2\pi)$  in kilohertz. The filter output was half-wave rectified and normalized to yield a spike probability function with a mean AP rate  $R$  (200 Hz) during the stimulus length  $l = 300$  ms. The resulting input train was then multiplied with a factor  $S$ , which we call the stimulus intensity, and afterward convolved with double-exponential functions  $G_{\text{exc}}$  and  $G_{\text{inh}}$ , which we created to resemble electrophysiologically measured synaptic kinetics for excitatory and inhibitory synaptic activity (Couchman et al., 2010):

$$G_{\text{exc}}(t) = g_{\text{exc}} \frac{(1 - e^{-t/1.0})^{1.3} e^{-t/0.27}}{\max((1 - e^{-t/1.0})^{1.3} e^{-t/0.27})}$$

$$\text{and}$$

$$G_{\text{inh}}(t) = g_{\text{inh}} \frac{(1 - e^{-t/0.4}) e^{-t/1.6}}{\max((1 - e^{-t/0.4}) e^{-t/1.6})}.$$

Here,  $g_{\text{exc}} = 37$  nS and  $g_{\text{inh}} = 57$  nS are the peak conductances of single fibers (Couchman et al., 2010), and time  $t$  is considered in milliseconds. Examples for such synaptic conductance trains are shown in Figure 1D. Unless mentioned otherwise, we used two inhibitory inputs based on the same stimulus wave form; one advances the excitatory inputs by 0.6 ms and one lags them by 0.11 ms (see Impact of distal AP initiation on ITD coding; Leibold, 2010). Apart from the simulations in which the inhibitory inputs are essential (see Figs. 5M, 8), all simulations were performed with only excitatory inputs activated.

### Neuron model with dendrites

To test the robustness of our findings in a model with dendrites, we performed simulations (see Fig. 8) in a model variant in which two identical dendrites (five compartments each) were added to the soma. Excitatory synapses were placed at the dendrites (ipsilateral inputs at the lateral dendrite, contralateral inputs at the medial dendrite), and inhibitory synapses were restricted to the soma (Kapfer et al., 2002). The parameters of the dendritic model were chosen such that the basic characteristics at the soma (input resistance, resting potential, capacitance, and EPSP kinetics) matched that of the model with a single somatodendritic compartment and hence the physiological data from Scott et al. (2005) and Couchman et al. (2010). Most importantly, the length of each of the dendrites was 200  $\mu\text{m}$ , with a constant diameter of 5  $\mu\text{m}$ . The somatic surface was reduced to 2467  $\mu\text{m}^2$ , such that the total cell surface remained at 8750  $\mu\text{m}^2$ , which is equal to the model with only one somatodendritic compartment. The geometrical length of the dendritic compartments appears slightly longer than that observed in MSO neurons (Rautenberg et al., 2009), since we did not take into account branching of dendrites but had to match the overall cell surface for comparability.

In the dendritic compartments, sodium channels were omitted (Scott et al., 2010), and thus the sodium density of the remaining somatic compartment was scaled up such that the total sodium conductance matched that of the simpler model with only one somatodendritic compartment. The conductance of the low-threshold potassium channels decayed exponentially along the dendrites with a length constant of 74  $\mu\text{m}$  (Mathews et al., 2010). The peak conductance at the somatic compartment was thereby identical to that of the simpler model. The conductance of the h current was chosen to follow the same gradient along the dendrite to keep the local balance of the two channels. Finally, the input resistance and resting potential of the model with dendrites were matched to those of the simpler model by adjusting the peak conductances of the h current and the passive leak current.

### Analysis of simulations

In our simulations, APs during ongoing stimulation were often not detectable in the soma (Fig. 1E). However, at more distal locations in the axon, the amplitude and kinetic differences of subthreshold responses and APs are much larger, and, thus, at the more distal axonal compartments these two cases are very easy to separate by a simple amplitude threshold.

**Initiating segment.** Since the MSO model is described by a system of coupled differential equations, the generation of an AP necessarily requires the interplay of all compartments. The question of where an AP is generated thus can only be answered by a phenomenological criterion. This phenomenological AP-initiating segment was identified as follows (Fig. 1F). First, a stimulus evoked AP was defined by a voltage threshold criterion in R7 at which AP and no AP events are clearly separable. Second, we inspected the voltage trace at the axonal nodes of Ranvier and the AIS going from distal to proximal, and identified the segment-specific AP times via the voltage peaks (above  $-50$  mV) that occurred within a certain time interval of duration  $L$  around the voltage peak in the (previous) downstream node. The duration  $L$  of this time interval is determined by  $L = 5.33 \lambda$ , where  $\lambda$  is the impulse conduction time from node to node for a strong current stimulus delivered at rest, which elicits a clear AIS AP. The window is asymmetrically aligned to the previous voltage peak such that the preceding part is three times longer than the part following the voltage peak. The factor 5.33 allows for a slower AP propagation of the AIS and near-threshold stimuli. Within the set of all detected voltage peaks, the earliest in time defines the AP initiation segment. This algorithm has been tested against a variety of simple threshold and phase space criteria, and has proven to give more reliable results for different axonal morphologies and different input parameters, even for extremely fast voltage deflections.

In simulations in which we tested higher somatic input resistances (see Fig. 5L), the somatic AP was strongly influencing the voltage trace in the AIS, which made it difficult to identify a clear AIS voltage peak. We therefore identified the AIS AP as the first drop of the voltage derivative below 50 V/s, identifying a shoulder in the voltage deflection.

In few cases (see Fig. 6) during orthodromic propagation does the AP amplitude initially decrease before increasing again in the more distal

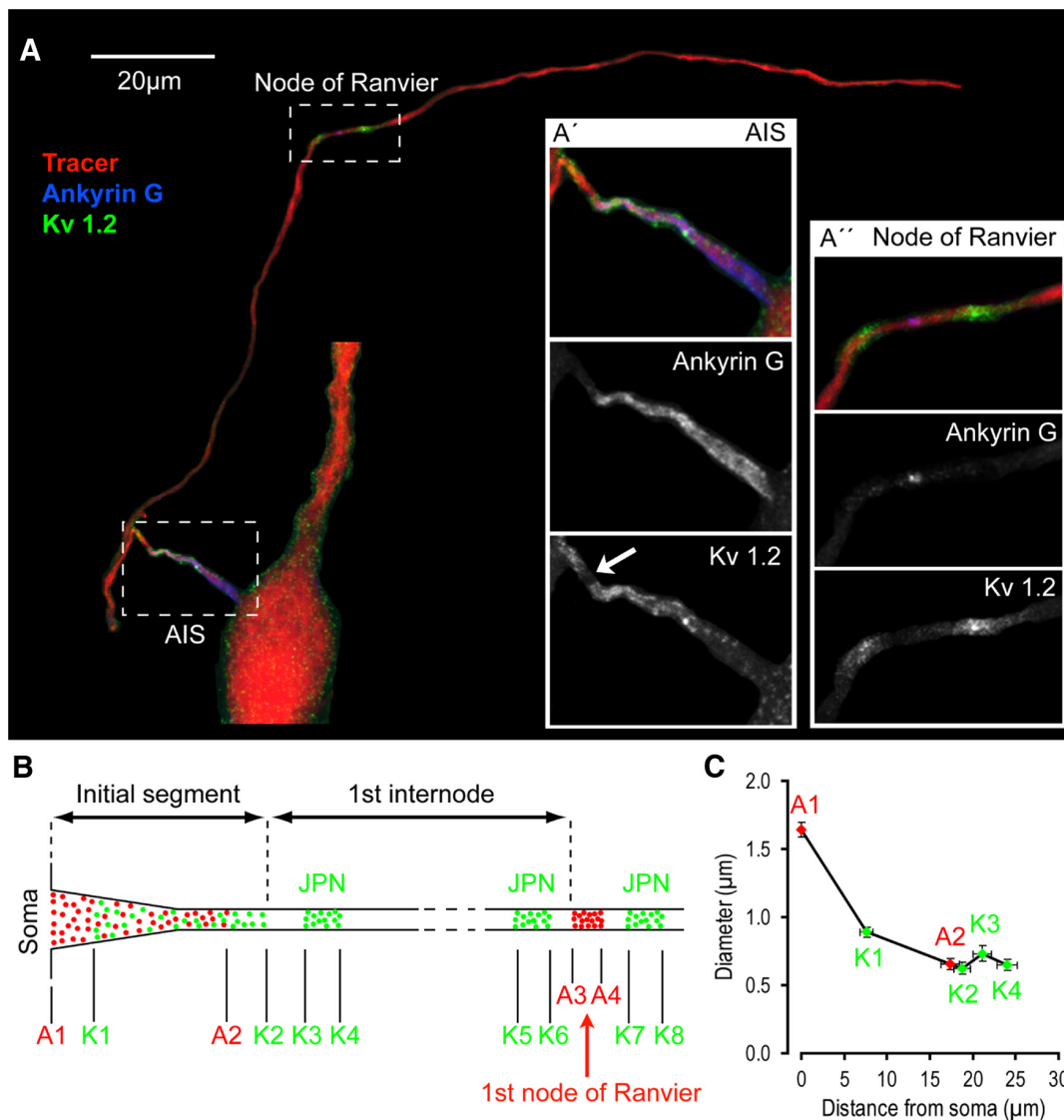


**Figure 2.** Morphometry of the AIS and first internodal segments in MSO neurons. **A**, Retrogradely labeled MSO neuron after digital extraction from the surrounding area. Insets **A'** and **A''** show magnifications of the AIS and first node of Ranvier, respectively. **B**, Schematic of the proximal axon segment comprising the AIS, the first internode, and the first node of Ranvier, illustrating the positions where measurements were made. Red and green dots indicate the distribution of ankyrin G and Kv1.2 immunolabeling in the AIS and axon. A1–A4 and K1–K8 indicate the borders of ankyrin G- and Kv1.2-positive domains, respectively. JPN, Juxtaparanodes. **C**, Mean diameter of the AIS at various positions plotted as a function of the mean distance from the soma. Diameter and distance measurements were made at the positions indicated in **B**. Error bars show the SEM.

axonal segments. Such APs were also labeled as being distally initiated, even though they would have been an AIS AP according to the time-window criterion.

**Relative slope during ongoing conductance trains.** To identify the input features that are most predictive for spiking, we placed particular emphasis on current amplitude and the relative current slope (derivative divided by amplitude). We chose relative slope because the derivative of any oscillating function linearly scales with the amplitude of the input, and, thus, without such normalization, dependencies on slopes are confounded by amplitude effects. To determine the relative derivative of the input current in Figure 7, *G* and *H*, we normalized by the amplitude of a high-pass-filtered version (fourth-order Butterworth filter with a cutoff of one-third of the stimulation frequency) of the input current rather than by the actual amplitude itself. This was necessary to obtain the actual local relative slope for each cycle and not a distorted value caused by the temporal summation of the input currents of high-frequency stimuli.

#### ITD coding

To assess how well the responses of the model neuron resolve an ITD  $\tau$ , we computed the Fisher information  $I(\tau)$ , assuming a Gaussian distribution of AP counts. From at least 90 repetitions of a 300 ms stimulus, we obtained the mean AP count (tuning curve)  $\mu(\tau)$  and its variance  $v(\tau)$ , and calculated the Fisher information as follows:

$$I(\tau) = \frac{\mu'(\tau)^2}{v(\tau)} + \frac{1}{2} \left( \frac{v'(\tau)}{v(\tau)} \right)^2$$

## Results

### Morphometry of the AIS and proximal axon

Using a combination of retrograde tracing of MSO neurons and immunohistochemical labeling of ankyrin G and Kv1.2 channels, a detailed morphometric analysis of the AIS and proximal axon of

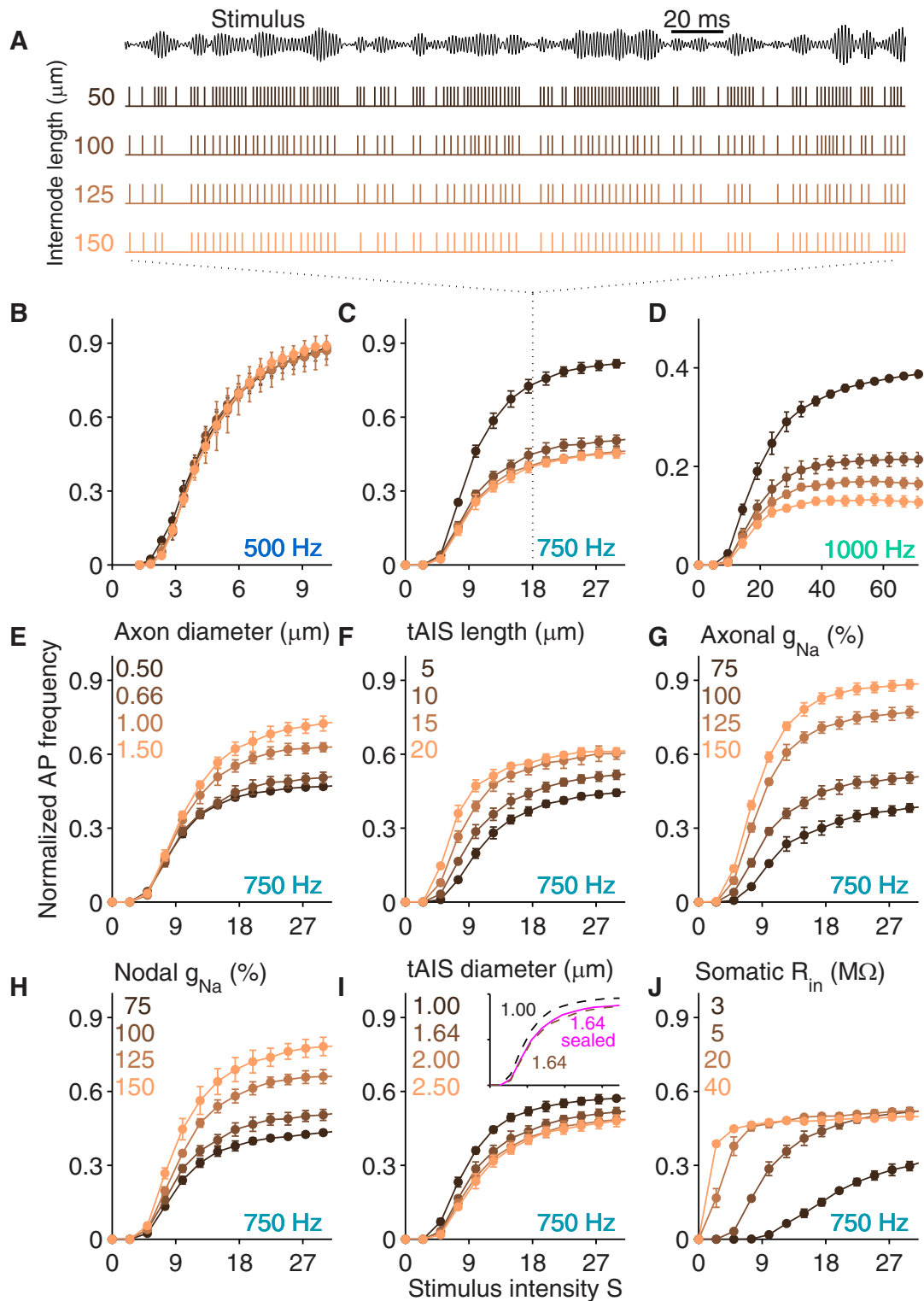


**Figure 3.** Input/output functions of the model. **A**, Spike trains were simulated for bandpass stimuli (top trace) of duration 300 ms. The four spike trains are derived from the same (frozen noise) stimulus with a center frequency of 750 Hz and intensity  $S = 18$  (as indicated by dotted lines) and internode lengths as indicated by colors. **B–J**, Graphs depict firing probabilities for different (color-coded) morphological parameters and sodium conductances and for increasing stimulus intensities  $S$  (see Materials and Methods). Parameters that were varied are internode length (color-coded) and center frequency (**B–D**), axonal diameter (**E**), length of the AIS tapering part (**F**), peak sodium conductance in all unmyelinated parts of the axon (**G**), peak sodium conductance in the nodes of Ranvier (**H**), proximal diameter of the AIS tapering part (**I**), and somatic input resistance (**J**). Inset in **I** compares relative AP frequencies of two control traces (with different tAIS diameter) from **I** to a model where all subthreshold transmembrane conductances were removed from the tAIS (pink trace, sealed).

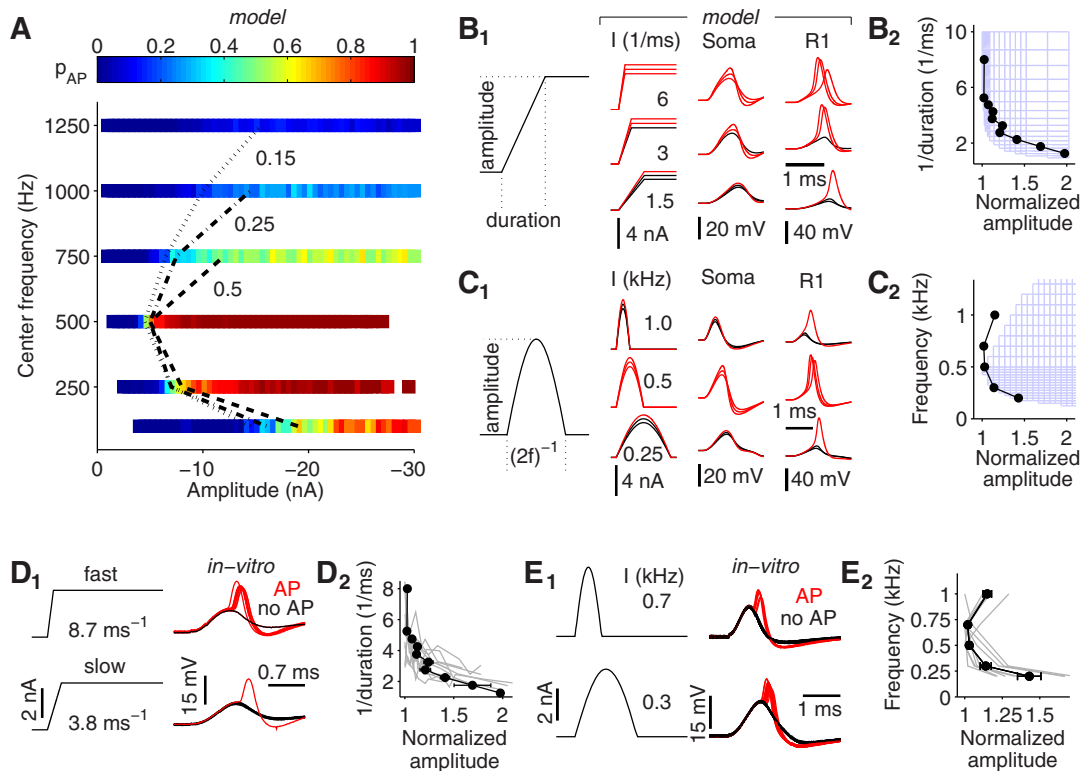


**Figure 4.** Frequency-dependent AP threshold. **A**, Firing probability (color coded) of the model cell as a function of center frequency and cycle amplitude for ongoing inputs. Iso-probability contours are shown for firing probabilities of 15% (dotted trace), 25% (dot-dashed trace), and 50% (dashed trace). **B<sub>1</sub>**, Ramp stimulus (left) and raw data of the simulation for three different ramp durations (right). Black and red traces indicate subthreshold and AP responses, respectively. **B<sub>2</sub>**, Light blue mesh shows parameter region that evoked an AP response. *In vitro* threshold is overlaid as a black line (see **D**). **C**, same as **B**, for half-wave-rectified sine stimuli. **D**, **E**, *In vitro* results. **D<sub>1</sub>**, Stimuli (left) and current-clamp traces (right) for the ramp stimulus experiment. **D<sub>2</sub>**, Threshold curves from individual neurons (gray traces) and their average (black,  $n = 12$ , same as in **B<sub>2</sub>**). **E**, same as **D**, but for half-wave-rectified sine stimuli *in vitro* ( $n = 8$ ). The data of **B–E** were normalized to the smallest amplitude that elicited an AP response in the specific cell. Error bars show the SEM.

12 MSO neurons was performed (Fig. 2A). Our immunostainings revealed that the AIS consisted of a  $17.3 \pm 1.1\text{-}\mu\text{m}$ -long ankyrin G-positive domain emerging directly from the soma and a  $11.2 \pm 0.6\text{-}\mu\text{m}$ -long Kv1.2-positive domain starting at  $7.6 \pm 0.7\text{-}\mu\text{m}$  distal from the soma in the labeled axons (Fig. 2A,B). Diameter measurements indicated that the AIS consisted of the tAIS and the cAIS. On average, the diameter of the AIS decreased from  $1.6 \pm 0.1\text{-}\mu\text{m}$  at the soma (position A1) to  $0.6 \pm 0.1\text{-}\mu\text{m}$  at the position K2, as defined in Figure 2, B and C. The length of the AIS (measured from A1 to K2; Fig. 2B) ranged from 14.0 to  $24.0\text{-}\mu\text{m}$  ( $18.8 \pm 1.0\text{-}\mu\text{m}$ ). Adjacent to the AIS was a  $2.3 \pm 0.2\text{-}\mu\text{m}$ -long segment devoid of ankyrin G and Kv1.2 labeling, which we interpret as the paranodal (or para-AIS) region, where myelin is anchored to the axon (Duflocq et al., 2011; Fig. 2A', arrow). The paranodal region was followed by a  $2.9 \pm 0.5\text{-}\mu\text{m}$ -long Kv1.2-positive domain representing the juxtapanode (or juxtapanode-AIS). The first node of Ranvier was identified based on its typical arrangement of two juxtapanodal Kv1.2-positive domains that were separated from the nodal ankyrin G domain through unlabeled paranodes (Fig. 2A'). The length of the first internode ranged from  $\sim 50$  to  $\sim 150\text{-}\mu\text{m}$  ( $100.4 \pm 9.1\text{-}\mu\text{m}$ ), and its mean diameter (Fig. 2B,C, measured at several positions between the two juxtapanodal borders K3 and K6) was  $0.7 \pm 0.1\text{-}\mu\text{m}$ . These axonal parameters were used to constrain a computational model of the MSO neuron (Table 1).

### Input–output functions

We first determined how the AP frequency of our computational neuron model is influenced by the parameters that we assumed to be most crucial for axonal excitability (AP threshold), i.e., the morphological parameters internode length, axonal diameter, proximal diameter, and tAIS length; and the electrical properties density of sodium channels in the unmyelinated axonal segments and somatic input resistance (Fig. 3). We tested how much the influence of these excitability parameters on AP probability depended on the center frequency of the bandpass stimuli (see Materials and Methods) and found that for center frequencies of  $\leq 500\text{ Hz}$  all of the axonal parameters had little influence on spiking probability (Fig. 3A–D, example of internode length). For higher stimulus frequencies, the axonal parameters had distinct influences on the input–output functions. As we increased the internode length, the spiking probability generally decreased (Fig. 3A–D), which can be attributed to a reduction of the axial current flow. Geometrical alterations that increase the axonal sodium conductance (while keeping the channel density constant) mostly result in an increase of the firing rate. This increase could be observed in simulations with altered axonal diameters [keeping a constant ratio of 0.7 between the inner (axon) and outer (myelin) diameter of the internode]. The firing rate also increased with axonal diameter (Fig. 3E), reflecting the corresponding increase of the number of sodium channels. Also an increase of the length of the tAIS led to a higher AIS sodium

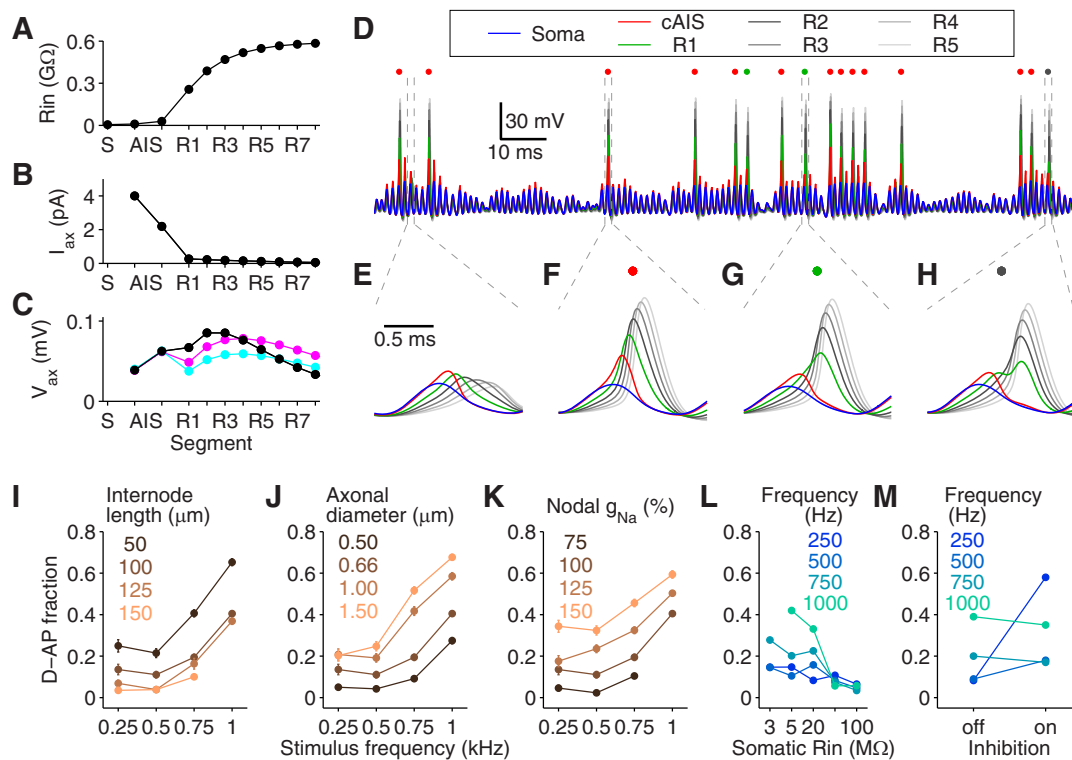


**Figure 5.** Distal AP initiation. **A–C**, Local input resistance (**A**), axial current (**B**), and  $V_{ax}$  (**C**) in the different model compartments for the standard parameters (black traces), the model with shorter internode lengths of 50  $\mu\text{m}$  (magenta traces), and thicker axonal diameter of 1.5  $\mu\text{m}$  (cyan traces). **D**, Exemplary voltage traces in different compartments (colors as indicated). Filled colored circles show the AP-initiating segment for each suprathreshold response (see legend). **E–H**, Example events (from **D**) for subthreshold response (**E**), and evoked APs generated in the AIS (**F**), R1 (**G**), and R2 (**H**). **I–K**, Fraction of distally initiated APs (D-AP; for a fixed AP probability of 15%), with varying internode length (**I**), axonal diameter (**J**), and sodium conductance in the nodes of Ranvier (**K**). **L**, Fraction of distally initiated APs for different somatic input resistances. **M**, Fraction of distally initiated APs without and with inhibition for several input frequencies.

conductance and an increasing firing probability (Fig. 3F). In line with these findings, a direct increase in the sodium conductance in unmyelinated axonal compartments (Fig. 3G,H) also facilitated AP probabilities. However, a different effect was observed when the proximal diameter of the tAIS was decreased, which also decreased the amount of sodium conductance but, interestingly, increased AP frequency (Fig. 3I). This indicates that in addition to the total local sodium conductance excitability of the axon also profits from an increased electrotonic isolation from the leak currents in the soma. This interpretation was corroborated by the following two additional sets of simulations: (1) an increase of the tAIS input resistance by removing all tAIS subthreshold conductances from the equation had almost no effect on firing probability (Fig. 3I, inset); and (2) increasing the somatic input resistance (by multiplicative scaling of the peak conductances of KLT channel and h current, keeping a constant resting potential) strongly enhanced AP frequency (Fig. 3J). The MSO soma thus acts as a strong current sink for the AIS, and, hence, the axon excitability crucially depends on rather small changes of the somatic current reaching the axon.

### Frequency-dependent threshold

Since the firing probabilities strongly depended on the center frequency of the inputs (Fig. 3), we performed a more systematic analysis of the frequency dependence of excitability of our computational neuron model and corroborated these data by *in vitro* measurements of MSO cells. The frequency dependence of MSO firing probability in the model was determined for a large range of bandpass stimuli with center frequencies ranging from 100 to

1250 Hz and varying stimulation intensities (Fig. 4A). This allows the assessment of the firing thresholds of MSO neurons with respect to both the shape (frequency content) and the amplitude of the input currents. The lowest current thresholds were observed at  $\sim 500$  Hz. For higher as well as lower input frequencies, more excitatory drive was necessary to reach a certain firing probability.

To better understand the dependence of AP initiation on the input kinetics, we simulated two onset stimulation paradigms using brief current stimuli applied at rest. First, we applied a ramp stimulus for which we could independently vary amplitude and ramp duration (Fig. 4B<sub>1</sub>). The ramp duration was assumed to serve as a proxy for stimulus shape (frequency) during the ongoing bandpass stimulation. The firing probabilities (Fig. 4B<sub>2</sub>) obtained with these stimuli very well explained the behavior observed for low-frequency bandpass inputs, which effectively implements a slope threshold (Golding and Oertel, 2012); that is, the neuron fires in response to a specific speed of membrane depolarization that is rather independent of amplitude. Such behavior has been previously described in octopus cells (Ferragamo and Oertel, 2002), in the vestibular pathway (Beraneck et al., 2007) and the MSO (Jercog et al., 2010), and is generally attributed to the fast kinetics of the KLT channels, which are further opening only for slow stimuli and cannot generate such additional leaks for fast-rising stimuli. The high-frequency behavior of our threshold profile, however, could not be modeled using the simple ramp stimuli. We therefore also applied half-wave-rectified sine waves (Fig. 4C<sub>1</sub>). Here again, both the low- and the high-frequency increase of threshold amplitudes was observed

(Fig. 4C<sub>2</sub>). Thus, the threshold amplitude for high frequencies crucially depends on the duration of the stimulus. This indicated that the high-frequency part of the threshold curve reflects the limit imposed by the charging of the membrane capacitor for regimes in which the membrane voltage rises too quickly to open the low-threshold potassium channels (Jercog et al., 2010). These modeling results were verified physiologically using whole-cell current-clamp recordings using the same stimuli as in the model (see Materials and Methods). From the recorded data obtained with the ramp stimuli, the AP probability was fitted by a sigmoid for each ramp duration as a function of the amplitude using at least 10 consecutive trials. The amplitude at which the fit was at 50% AP probability was defined as the threshold. The physiologically obtained threshold curves qualitatively matched the modeling results for the ramp-current stimuli (Fig. 4B<sub>2</sub>, superimposed black trace, *D*) with less firing for slow-input ramps and secure responses for faster ramps. For the half-wave-rectified sine stimuli, threshold amplitudes were obtained by manual testing (Fig. 4C<sub>2</sub>, superimposed black trace, *E*) and also qualitatively matched the simulations with the lowest firing threshold for medium frequencies and less firing for low and high frequencies. From these simulations and experiments, we concluded that the threshold behavior observed during ongoing stimulation is functionally very similar to that in onset-like stimulus paradigms with single current pulses.

### Site of AP initiation

Although AP initiation might be functionally similar under onset and ongoing stimulus conditions, the underlying mechanisms may be different, since, owing to the temporal summation of the inputs, the ongoing stimulation sets the cell membrane into a state that is very different from resting conditions (e.g., because of steady-state activation of channels and changes in input resistance). We therefore investigated AP initiation during ongoing stimulation in greater detail. In particular, we were interested in the contributions of the different cellular (somatic and axonal) compartments to the generation of APs.

A first assessment of the local excitability of the model neuron was derived from local input resistance measurements, using small hyperpolarizing current pulses (amplitude,  $-100$  pA for 300 ms) that were consecutively injected into the soma, the cAIS, and the nodes of Ranvier of our model at rest (Fig. 5A, black trace). Here, the input resistance was derived from the peak of the voltage responses and not the steady-state component to obtain a measure for the instantaneous susceptibility of the local membrane. In our model, the peak conductance parameters were chosen such that the somatic input resistance was fixed at 5 M $\Omega$  (Scott et al., 2005; Couchman et al., 2010). With the standard parameter settings (Tables 1 and 2), the AIS had two (tAIS, 9.7 M $\Omega$ ) to six times (cAIS, 28.5 M $\Omega$ ) the input resistance of the soma. Further distally in the axon, the R1 showed a 50-fold increase of input resistance (256.5 M $\Omega$ ). We next applied a current pulse of 1 nA at the soma while at the same time extracting the peak of the axial current in the respective axonal segments (Fig. 5B, black trace). The portion of this current that spread from the

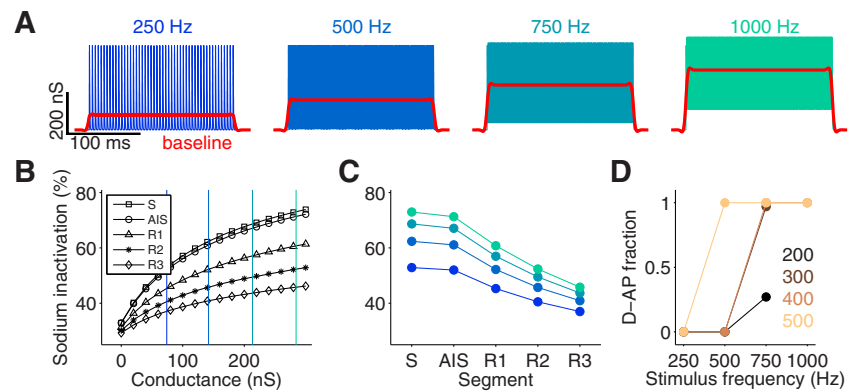


**Figure 6.** High input frequencies cause sodium channel inactivation in the somatic and proximal axonal membranes. **A**, Periodic synaptic conductances with a peak value of 400 nS for center frequencies of 250, 500, 750, and 1000 Hz. Red traces are obtained by low-pass filtering the voltage traces (cutoff frequency, 100 Hz). **B**, Steady-state sodium channel inactivation measured in different model compartments for increasing excitatory conductances. **C**, Steady-state sodium channel inactivation for traces (color coded) in **A** in different compartments. **D**, Fraction of distally initiated APs (D-APs) for input traces in **A** with different conductance peak values (color coded; in nS).

soma into the AIS was only 0.4% (4 pA), with further attenuation at the R1 (0.3 pA). Multiplying the axial current by the local input resistance yields a measure that can be interpreted as the axonally mediated voltage amplitude ( $V_{ax}$ ). This voltage amplitude was further used as an estimate for the local excitability. The axially mediated voltage amplitude was maximal at the second and third nodes of Ranvier (Fig. 5C, black trace). Thus, in contrast to the classical model of AP initiation at the AIS, the second and third nodes appear to be more excitable, indicating that the more distal compartments play an important role in axon excitability in leaky neurons.

A detailed analysis of AP times in the individual compartments revealed that the site of AP initiation was indeed not restricted to the AIS (Fig. 5D–H). Although many APs were initiated in the AIS (Fig. 5F, I–K), 5–60% (depending on input conditions) of the APs first crossed the detection threshold (see Materials and Methods) at the first (Fig. 5G) or even the second (Fig. 5H) node of Ranvier, while the AIS showed a response similar to the subthreshold case (Fig. 5E). The amplitudes of the somatic and AIS APs were relatively small, independent of where they were generated, and underwent subsequent amplification by the nodes of Ranvier as they orthodromically propagated along the axon (Fig. 5F–H).

To further elucidate the mechanisms of this distal AP initiation, we quantified its occurrence under our naturalistic ongoing input paradigm for different morphological parameters. For purely excitatory inputs, the fraction of distally initiated APs over AIS APs increased with stimulus frequency (Fig. 5I–L). For shorter internodes (Fig. 5I) and thicker axonal diameter (Fig. 5J), more distal APs were observed. This is because the resulting increased axial conductance allows the stimulus-evoked potential to propagate further along the axon and is also illustrated by the peak of the  $V_{ax}$  located at more distal regions of the axon in both conditions (Fig. 5C, cyan and magenta traces). Consistently, a higher nodal sodium conductance increased the fraction of distally initiated APs as well, because APs could be more easily initiated at the nodes (Fig. 5K).

A major factor influencing distal AP initiation for inputs at all center frequencies is the somatic input resistance. The prevalence of distal AP initiation is strongly reduced with the increase of input resistance of the soma (Fig. 5L). Hence, distal spiking

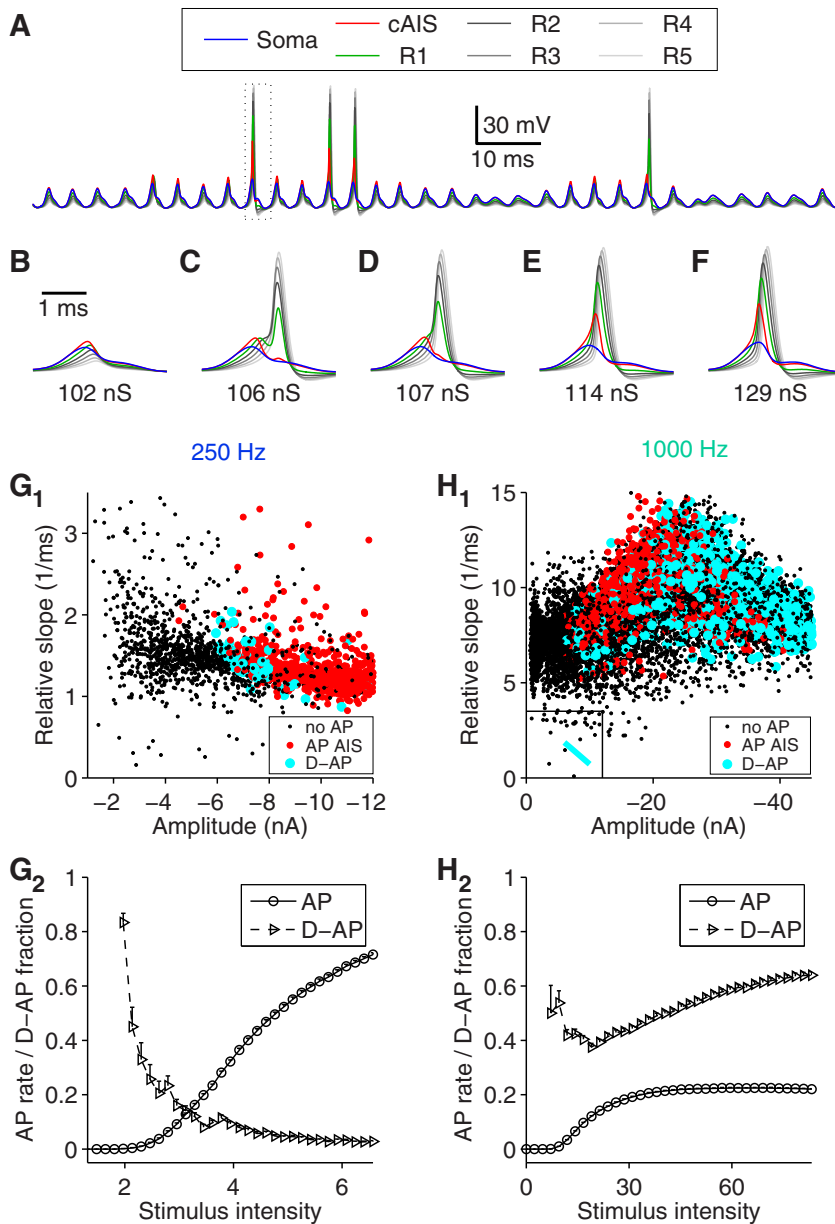


**Figure 7.** Function of distal AP initiation. **A**, Example voltage traces for a stimulus with center frequency 250 Hz. The box indicates a cycle that was further investigated for different excitatory peak conductance values. **B–F**, The selected stimulus cycle evolves from a subthreshold response (**B**), via a distally initiated AP (**C, D**), to an AP initiated in the AIS (**E, F**). **G<sub>1</sub>**, Model responses to input trains with a center frequency of 250 Hz generate a broad range of cycle amplitudes and relative derivatives (see Materials and Methods). Each dot corresponds to a cycle within the input train. Black, Subthreshold response; red, AP response initiated in the AIS; cyan, AP response initiated in a node of Ranvier (D-AP). **G<sub>2</sub>**, Firing rate and fraction of distally initiated APs for increasing excitatory synaptic conductances and an input with 250 Hz center frequency. **H<sub>1</sub>**, Same as **G<sub>1</sub>** for an input with a center frequency of 1000 Hz. The cyan line in the box is a linear fit to the distally initiated APs from **G<sub>1</sub>**. **H<sub>2</sub>**, Same as **G<sub>2</sub>** but for inputs with 1000 Hz center frequency.

should be particularly prevalent in leaky neurons that receive fast-fluctuating inputs such as in the MSO.

Since MSO neurons not only receive excitatory inputs but also strong phase-locked inhibitory inputs via the medial and lateral trapezoid body, we also performed simulations with excitatory and inhibitory inputs. In these simulations, the frequency dependence of the site of AP initiation is less clear (Fig. 5M). On the one hand, the fraction of distally initiated APs also increased with frequency for center frequencies of >500 Hz. On the other hand,

for a low center frequency of 250 Hz, inhibition also generated large amounts of distal AP initiation. This already indicates that distal AP initiation may result from a variety of different mechanisms, particularly also those that add to the somatic current sink.

### Distal AP initiation for high-frequency inputs

The steady-state approach to axonal excitability (Fig. 5A–C) disregards contributions from the dynamics of the ion channels. To understand whether such dynamic properties of the neuron model also contribute to distal AP initiation, we used strictly periodic synaptic (conductance) input trains of different frequencies (Fig. 6A). Temporal summation of the synaptic inputs generated a conductance plateau that increased with frequency as revealed by low-pass filtering (Fig. 6A, second-order Butterworth low-pass filter with a cutoff frequency of 100 Hz, red traces). We then applied these average conductance values as a constant conductance to the cell and measured the corresponding steady-state sodium channel inactivation at the soma, the AIS, and the first three nodes of Ranvier (Fig. 6B). This revealed that a larger average conductance generally caused more sodium channel inactivation. Moreover, the conductance level was highest at the soma and decreases along the axon. Thus, a regime of a high-frequency input generates a persistent depolarization of the membrane with a larger fraction of inactivated sodium channels at the proximal axonal membranes than at the distal segments (Fig. 6C). As a result, this leads to a larger fraction of distal AP initiation with increased input frequency (Fig. 6D).

### Influence of distal AP initiation on the firing threshold

To understand the functional relevance of distal AP initiation, we next investigated which input properties are particularly amenable to evoke distal APs during ongoing stimulation (Fig. 2B–D). We therefore repeatedly stimulated the neuron model with identical input trains for consecutively increasing mean synaptic conductances. Figure 7A–F shows an exemplary stimulus cycle for which, with increasing conductance, the voltage profile along the axon transitions from a completely subthreshold response (Fig. 7B) over an AP being initiated at the nodes of Ranvier (Fig. 7C,D) to an AP generated at the AIS (Fig. 7E,F). From these examples, it seemed that distal AP initiation is particularly prevalent at the AP threshold.

To further evaluate the threshold property of distal AP initiation, we ran the simulations using excitatory bandpass inputs of

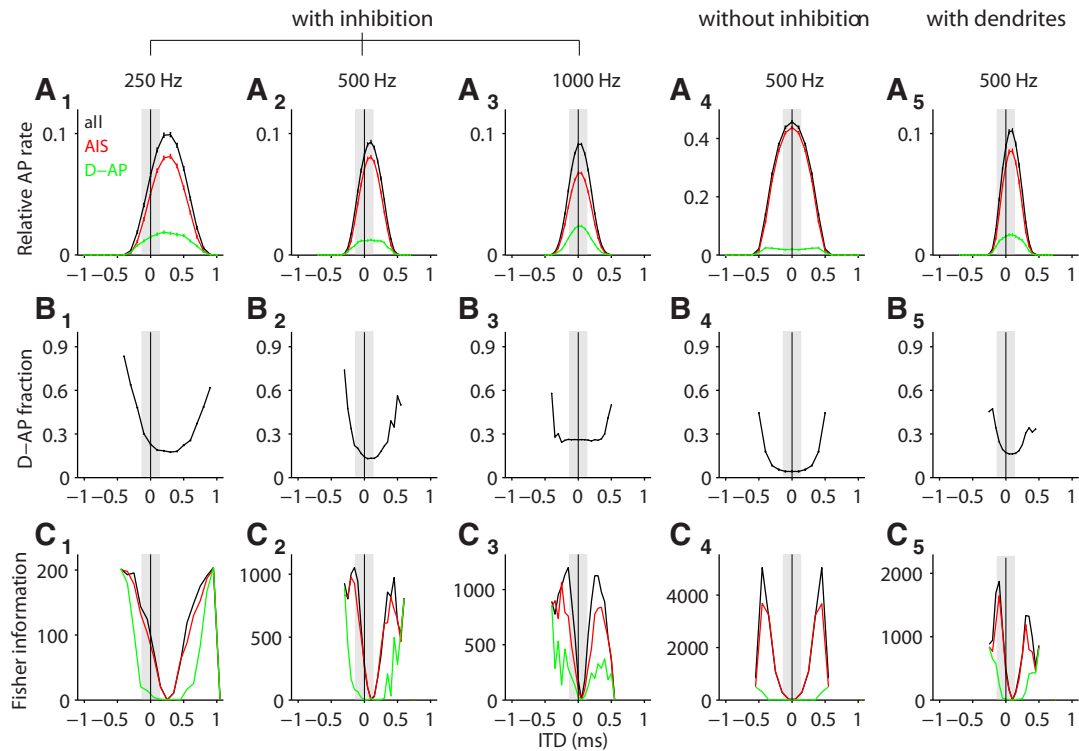


**Figure 8.** Representation of auditory space. **A**, ITD tuning curves (more specifically noise delay functions; black) for input trains of 250, 500, and 1000 Hz center frequency, a purely excitatory model, and a model with dendrites (both receiving input with 500 Hz center frequency). Tuning curves without distally initiated APs are depicted in red, and tuning curves with only distally initiated APs are depicted in green. Gray bar indicates the physiological range of ITDs for gerbils. **B**, Fraction of distally initiated APs (D-APs) of the tuning curves from **A**. **C**, Fisher information (in  $\text{kHz}^2$ , stimulus duration 300 ms) of the tuning curves (and the respective distal and AIS parts) from **A**.

different center frequencies and amplitudes. For a low-frequency input with a center frequency of 250 Hz, the rate of distally initiated APs was highest right at the border between no APs and AIS APs (Fig. 7*G*<sub>1</sub>, *G*<sub>2</sub>). The orientation of this border was diagonal in amplitude–frequency space and qualitatively matched the AP boundaries from Figure 4 (Fig. 7*G*<sub>1</sub>). For 1000 Hz, the distribution of AIS APs and distally initiated APs is different (Fig. 7*H*<sub>1</sub>, *H*<sub>2</sub>). There, the boundary between AP firing and no firing was approximately vertical, indicating that the cell effectively implemented an amplitude threshold being insensitive to the slope of the input current (Fig. 7*H*<sub>1</sub>). Moreover, for 1000 Hz center frequency, distal AP initiation could no longer be seen as a threshold effect. In fact, after an initial dip for low amplitudes, the overall fraction of distally initiated spikes rose with input amplitude (Fig. 7*H*), which is in line with the dependence of the fraction of distally initiated APs on sodium inactivation from Figure 6.

In conclusion, distal AP initiation seems to have two effects. (1) If the sodium channels were only slightly inactivated, the cell is able to fire in response to smaller stimulus amplitudes than without distal initiation of APs. (2) If the sodium channels are largely inactivated (as in the case of temporally summed high-frequency input), distal AP initiation allows the cell to keep up high firing rates for high-frequency stimuli with large stimulus amplitudes.

#### Impact of distal AP initiation on ITD coding

The above findings have important consequences for the firing behavior of MSO cells *in vivo*. We simulated ITD tuning functions using our ongoing input paradigm with synaptic conductances derived from bandpass-filtered noise. Mimicking phase-locked au-

ditary activity from the two ears, we split up the synaptic inputs into two channels with distinct temporal disparity for the putative ipsilateral and contralateral excitatory synapses, which, disregarding possible additional cochlear and transmission delays, we interpret as an ITD. We assumed that the cell also received phase-locked inhibitory input from both ears (from the medial and lateral nuclei of the trapezoid body) and used the inhibitory synapses to generate a maximum shift in best ITD (Brand et al., 2002; Leibold and van Hemmen, 2005; Pecka et al., 2008; Leibold, 2010). For bandpass input with a center frequency of 250 and 500 Hz, the contralateral inhibition was advanced compared with excitation by 0.8 ms, whereas the ipsilateral inhibition was delayed with respect to excitation by 0.11 ms. For these low center frequencies of the input, the model generated a rate code of ITD (Fig. 8*A*<sub>1</sub>, *A*<sub>2</sub>) in which firing at low rates was relatively more supported by distally initiated APs (Fig. 8*B*<sub>1</sub>, *B*<sub>2</sub>). This becomes obvious if one computes Fisher information as a means to assess the ITD resolution of the neuronal responses (Fig. 8*C*). Fisher information (resolution) is particularly high at the slopes of the tuning curves. In line with the high fractions of distally initiated APs at low firing rates (Fig. 8*B*), distally initiated APs also contribute a particularly large amount of information at these low rate regimes. Although, for the present definition of ITDs, these low rate parts are largely outside the physiological range (Fig. 8, gray bars), they might still become physiologically relevant if additional bilaterally asymmetric cochlear, axonal, or cellular delays exist that shift the tuning curves in parallel to the ITD axis.

To achieve the maximal peak shift for bandpass input with a center frequency of 1000 Hz, we set the contralateral inhibition to lead the excitation by 0.5 ms. The situation was very similar to

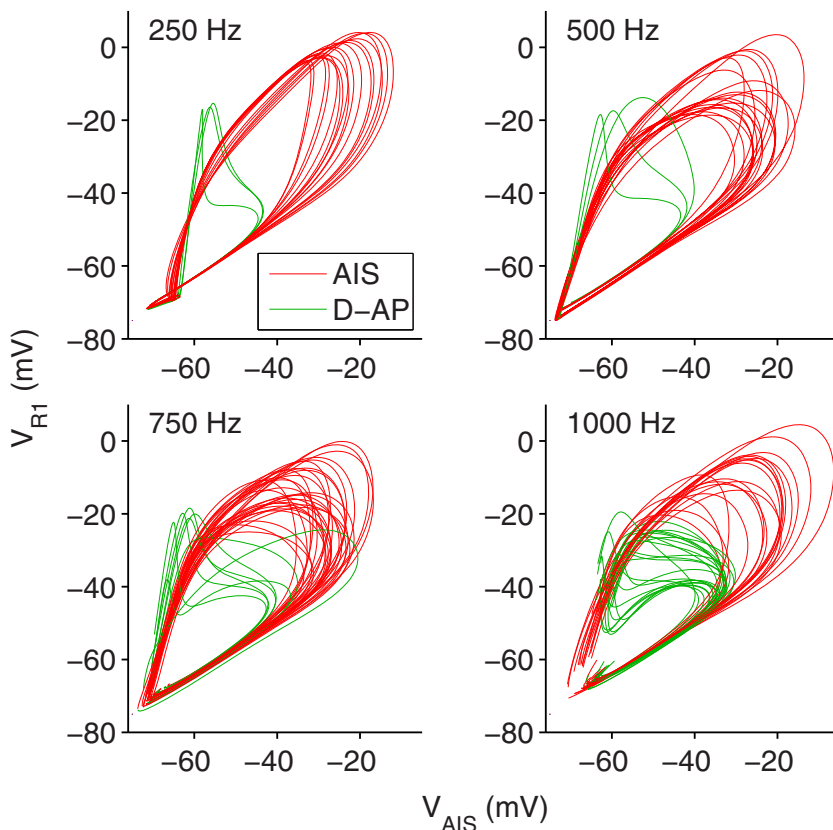


**Figure 9.** Is there a discrete site of AP initiation? AIS voltage vs voltage at the first node of Ranvier during AP firing for inputs with different center frequencies (as indicated). Red traces are APs identified as AIS APs by the algorithm described in Figure 1F. Green traces are APs classified as distally initiated (D-AP).

those for the two lower center frequencies, only that the best ITD, in contrast to *in vivo* findings (Brand et al., 2002), was close to the midline (Fig. 8A<sub>3</sub>), and the code was mediated by distal AP initiation to an even larger extent (Fig. 8B<sub>3</sub>). Also Fisher information was particularly high for distally initiated APs, even within the physiological range without any additional asymmetric delays (Fig. 8C<sub>3</sub>). Thus, the realistically slow decaying inhibition (exponential decay with a time constant of 1.6 ms; Magnusson et al., 2005; Couchman et al., 2010) could well account for the observed peak shifts of low-frequency cells in gerbils, whereas it (at least alone) does not do so for frequencies of ~1 kHz and beyond (Pecka et al., 2008).

As a control, we ran the simulations without inhibitory inputs (Fig. 8A<sub>4</sub>, B<sub>4</sub>, C<sub>4</sub>) which resulted in a best delay of zero. In this case, distally initiated APs were less prevalent. We thus conclude that distal AP initiation is an important mode of AP generation, particularly in the high-frequency channels but also in low-frequency channels with phase-locked inhibition.

In a final set of simulations, we tested how robust our findings are in a model that includes dendrites (Fig. 8A<sub>5</sub>, B<sub>5</sub>, C<sub>5</sub>). MSO neurons typically have two dendrites, a lateral one receives ipsilateral excitatory input fibers and a medial one targeted by contralateral excitatory input fibers. We adjusted the model such that all basic physiological properties matched those of the simpler model and, hence, the published electrophysiological data (Scott et al., 2005; Couchman et al., 2010). The tuning curves and distal AP fractions from this extended model were almost identical to that of the simpler model. We thus con-

clude that the additional dendritic current sinks do not influence the excitability of the neuron beyond their contribution to the basic physiological parameters (input resistance, resting potential, and EPSP shape).

## Discussion

In this study, we used naturalistic synaptic conductance trains to investigate AP initiation in a model of binaural coincidence detector neurons in the MSO, featuring a detailed axonal morphology. Modeling as well as electrophysiology showed that MSO cells incorporate temporal filtering properties such that they were easiest to excite for an input frequency of ~500 Hz. In contrast to current theories, the site of AP generation was not restricted to the AIS but varied depending on the spectral composition of the input. Further distally initiated APs (at the nodes of Ranvier) occurred close to the AP threshold in low-frequency channels, particularly in the presence of inhibition, as well as for strong stimulation in the high-frequency channels. Mechanistically, distal AP initiation at low frequencies was mediated by a strong somatic current sink, whereas for high frequencies it resulted from a stronger sodium channel inactivation in the AIS than in the distal axon. Importantly, in both cases, the ability of the neuron to generate APs in more distal axonal segments increased the dynamic range of firing rates. Distal AP initiation thereby

facilitates the resolution of the rate code of ITDs in the cell (Skottun, 1998).

Our model simulations show that AP initiation cannot be viewed to generally occur at one specific site, but rather the proximal axonal segments act as a whole during this process. This is because the axial transport of charge particularly strongly determines the excitability of neighboring axonal segments (Baranauskas et al., 2013). To support the idea of distributed AP generation on a phenomenological level, we compared the trajectories of AIS APs and distally initiated APs plotting AIS voltage against voltage at the first node of Ranvier (Fig. 9). Although, on average, we see a clear distinction between the trajectories of the AIS and distally initiated APs, for higher stimulus frequencies the two sorts of trajectories form a continuum. This means that for some APs it is valid to assign a single site of initiation, but for others (Fig. 9, close to the border between red and green traces) it is rather difficult. A further argument in favor of spatially distributed AP generation is that the distribution of AP initiation sites in our model also depends on stimulus frequency, with high frequencies giving rise to more distal spiking (Fig. 5I). This finding is consistent with previous reports about layer 5 pyramidal neurons revealing that the first node of Ranvier facilitates high-frequency (>100 Hz) burst firing and reduces the somatic AP threshold by 5 mV (Kole, 2011). In summary, these results suggest that for high-frequency inputs, AP initiation of MSO cells indeed results from a spatially distributed and collective mechanism,

whereas for low-frequency inputs APs are rather generated at a distinct site.

Our computational model explains the small AP amplitudes observed *in vivo* (Yin and Chan, 1990) and *in vitro* (Scott et al., 2007; Couchman et al., 2010). However, the specific choice of parameters is crucial to further justify the model results. Whereas most of the parameters are closely tied to the existing MSO literature and the new morphometric data presented in this article, specifically the sodium conductances have not yet been determined experimentally in MSO axons. We have set the axonal sodium conductance density such that the firing threshold (70–110 nS) for a single excitatory synaptic conductance stimulus fits our current-clamp measurements (Couchman et al., 2010). Moreover, the axonal sodium conductance density of  $4 \text{ nS}/\mu\text{m}^2$  used in the model lies within the range of values reported for cortical pyramidal neuron AISs ( $2.5 \text{ nS}/\mu\text{m}^2$ , Kole et al., 2008) and has been used in several other studies ( $7.5 \text{ nS}/\mu\text{m}^2$ , Shu et al., 2007;  $4.5 \text{ nS}/\mu\text{m}^2$ , Spirou et al., 2008). In our standard parameter set, we decided to use the same sodium channel density for all unmyelinated axonal compartments (the AIS and the nodes of Ranvier). This simplification rather leads to an underestimation of distal AP initiation (Fig. 5K). Assuming a higher sodium channel density in the nodes of Ranvier than in the axon initial segment, as shown by immunogold electron microscopy in cortical pyramidal cells (Lorincz and Nusser, 2010), relatively decreases the excitability of the AIS, thereby increasing the fraction of distally initiated APs.

In the analog ITD circuitry of birds, axonal processing has also been shown to be functionally important (Kuba et al., 2006; Ashida et al., 2007). In NL cells receiving phase-locked inputs up to 3 kHz, the AP initiation zone (clustering of sodium channels) of the AIS is located substantially more distal compared with the low-frequency neurons (Kuba et al., 2006). This finding is in line with the present observation of AP initiation moving to more distal parts of the axon for high-frequency stimuli. Compared with MSO principal neurons, which we suggest to have a dynamically changing site of AP initiation, in NL neurons the site of AP initiation seems rather hardwired, which is also supported by a partial myelination of the initial segment (Carr and Boudreau, 1993).

The mechanisms underlying ITD tuning of MSO principal neurons are highly debated (Grothe et al., 2010; Roberts et al., 2013; van der Heijden et al., 2013). Traditionally, ITD processing was thought to rely exclusively on the coincidence detection of excitatory inputs and neuronal ITD representation on the neurons that respond most at their best ITD. This best ITD is determined by the difference of internal delay lines between the ears and the coincidence detector neuron (Jeffress, 1948). While in the bird systems this concept still seems to constitute the core mechanism underlying ITD maps (Ashida and Carr, 2011), the situation in mammals is less clear. In brainstem and midbrain, the best ITDs change with stimulus frequency inconsistently with the assumption of a solely temporal conduction delay (i.e., they exhibit a so-called characteristic phase; Yin and Chan 1990, Agapiou and McAlpine, 2008, Siveke et al., 2012). Furthermore, blockade of glycinergic transmission *in vivo* shifted the best ITD of MSO neurons toward zero (Brand et al., 2002), hence arguing for a distinct effect of inhibitory inputs on the timing and shape of the excitatory potentials (Brand et al., 2002; Pecka et al., 2008) and providing a putative explanation for the frequency-dependent best ITDs (Leibold, 2010). Although it has been assumed that, given its slow kinetics, inhibition alone cannot account for a substantial shift of the best ITD (Jercog et al., 2010; Day and Semple,

2011; Roberts et al., 2013), our present modeling results show that inhibition has the potential to generate shifts as large as the physiological ITD range of gerbils ( $\sim 130 \mu\text{s}$ ), at least for frequencies  $< 500 \text{ Hz}$ . This, of course, does not exclude further mechanisms like cochlear or axonal delays (Schroeder, 1977; Shamma et al., 1989; Joris et al., 2006; Day and Semple, 2011) and morphological (Zhou et al., 2005; but see Rautenberg et al., 2009) or physiological (Jercog et al., 2010; but see Roberts et al., 2013) asymmetries. A further argument against a contribution of fast inhibition to the shift of best ITDs stems from recent *in vivo* whole-cell recordings (van der Heijden et al., 2013), which state a lack of obvious hyperpolarizing IPSPs. Because of the slow inhibitory time constant, our simulations show that during an ongoing stimulus IPSPs indeed do not show up as isolated potentials (Fig. 1D) but nevertheless influence the phase of the monaurally induced oscillations sufficiently to induce a shift of best ITDs (even for 1 kHz, although not much).

Beyond the auditory brainstem, fast and leaky cell membranes have also been reported in cortical pyramidal cells during massive synaptic bombardment such as in high-conductance states [Paré et al., 1998 (who reported input resistances as low as  $4 \text{ M}\Omega$ )] and sharp wave ripple events (Bähner et al., 2011). Under both conditions, the cells show extensive spiking activity *in vivo* (Csicsvari et al., 1999; Steriade, 2001). It is thus tempting to speculate that distal AP initiation contributes to firing as well by allowing the somatic current sink to decouple from the axonal AP-generating zones in a context-dependent manner (Vladimirov et al., 2013).

## References

- Agapiou JP, McAlpine D (2008) Low-frequency envelope sensitivity produces asymmetric binaural tuning curves. *J Neurophysiol* 100:2381–2396. [CrossRef Medline](#)
- Agrawal D, Hawk R, Avila RL, Inouye H, Kirschner DA (2009) Internodal myelination during development quantitated using x-ray diffraction. *J Struct Biol* 168:521–526. [CrossRef Medline](#)
- Ashida G, Carr CE (2011) Sound localization: Jeffress and beyond. *Curr Opin Neurobiol* 21:745–751. [CrossRef Medline](#)
- Ashida G, Abe K, Funabiki K, Konishi M (2007) Passive soma facilitates submillisecond coincidence detection in the owl's auditory system. *J Neurophysiol* 97:2267–2282. [CrossRef Medline](#)
- Bähner F, Weiss EK, Birke G, Maier N, Schmitz D, Rudolph U, Frotscher M, Traub RD, Both M, Draguhn A (2011) Cellular correlate of assembly formation in oscillating hippocampal networks *in vitro*. *Proc Natl Acad Sci U S A* 108:E607–616. [CrossRef Medline](#)
- Baranauskas G, David Y, Fleidervish IA (2013) Spatial mismatch between the  $\text{Na}^+$  flux and spike initiation in axon initial segment. *Proc Natl Acad Sci U S A* 110:4051–4056. [CrossRef Medline](#)
- Baumann VJ, Lehnert S, Leibold C, Koch U (2013) Tonotopic organization of the hyperpolarization-activated current (I<sub>h</sub>) in the mammalian medial superior olive. *Front Neural Circuits* 7:117. [CrossRef Medline](#)
- Beraneck M, Pfanzelt S, Vassias I, Rohregger M, Vibert N, Vidal PP, Moore LE, Straka H (2007) Differential intrinsic response dynamics determine synaptic signal processing in frog vestibular neurons. *J Neurosci* 27:4283–4296. [CrossRef Medline](#)
- Brand A, Behrend O, Marquardt T, McAlpine D, Grothe B (2002) Precise inhibition is essential for microsecond interaural time difference coding. *Nature* 417:543–547. [CrossRef Medline](#)
- Carr CE, Boudreau RE (1993) An axon with a myelinated initial segment in the bird auditory system. *Brain Res* 628:330–334. [CrossRef Medline](#)
- Couchman K, Grothe B, Felmy F (2010) Medial superior olivary neurons receive surprisingly few excitatory and inhibitory inputs with balanced strength and short-term dynamics. *J Neurosci* 30:17111–17121. [CrossRef Medline](#)
- Csicsvari J, Hirase H, Czurkó A, Mamiya A, Buzsáki G (1999) Oscillatory coupling of hippocampal pyramidal cells and interneurons in the behaving rat. *J Neurosci* 19:274–287. [Medline](#)
- Day ML, Semple MN (2011) Frequency-dependent interaural delays in the

- medial superior olive: implications for interaural cochlear delays. *J Neurophysiol* 106:1985–1999. [CrossRef Medline](#)
- Duflocq A, Chareyre F, Giovannini M, Couraud F, Davenne M (2011) Characterization of the axon initial segment (AIS) of motor neurons and identification of a para-AIS and a juxtapara-AIS, organized by protein 4.1B. *BMC Biol* 9:66. [CrossRef Medline](#)
- Ferragamo MJ, Oertel D (2002) Octopus cells of the mammalian ventral cochlear nucleus sense the rate of depolarization. *J Neurophysiol* 87:2262–2270. [CrossRef Medline](#)
- Fitzpatrick DC, Batra R, Stanford TR, Kuwada S (1997) A neuronal population code for sound localization. *Nature* 388:871–874. [CrossRef Medline](#)
- Ford MC, Grothe B, Klug A (2009) Fenestration of the calyx of Held occurs sequentially along the tonotopic axis, is influenced by afferent activity, and facilitates glutamate clearance. *J Comp Neurol* 514:92–106. [CrossRef Medline](#)
- Foust A, Popovic M, Zecevic D, McCormick DA (2010) Action potentials initiate in the axon initial segment and propagate through axon collaterals reliably in cerebellar Purkinje neurons. *J Neurosci* 30:6891–6902. [CrossRef Medline](#)
- Gentet LJ, Stuart GJ, Clements JD (2000) Direct measurement of specific membrane capacitance in neurons. *Biophys J* 79:314–320. [CrossRef Medline](#)
- Glasberg BR, Moore BC (1990) Derivation of auditory filter shapes from notched-noise data. *Hear Res* 47:103–138. [CrossRef Medline](#)
- Goldberg JM, Brown PB (1969) Response of binaural neurons of dog superior olivary complex to dichotic tonal stimuli: some physiological mechanisms of sound localization. *J Neurophysiol* 32:613–636. [Medline](#)
- Golding NL, Oertel D (2012) Synaptic integration in dendrites: exceptional need for speed. *J Physiol* 590:5563–5569. [CrossRef Medline](#)
- Grothe B, Pecka M, McAlpine D (2010) Mechanisms of sound localization in mammals. *Physiol Rev* 90:983–1012. [CrossRef Medline](#)
- Jeffress LA (1948) A place theory of sound localization. *J Comp Physiol Psychol* 41:35–39. [CrossRef Medline](#)
- Jercog PE, Svirskis G, Kotak VC, Sanes DH, Rinzel J (2010) Asymmetric excitatory synaptic dynamics underlie interaural time difference processing in the auditory system. *PLoS Biol* 8:e1000406. [CrossRef Medline](#)
- Joris PX, Van de Sande B, Louage DH, van der Heijden M (2006) Binaural and cochlear disparities. *Proc Natl Acad Sci U S A* 103:12917–12922. [CrossRef Medline](#)
- Kapfer C, Seidl AH, Schweizer H, Grothe B (2002) Experience-dependent refinement of inhibitory inputs to auditory coincidence-detector neurons. *Nat Neurosci* 5:247–253. [CrossRef Medline](#)
- Koch U, Braun M, Kapfer C, Grothe B (2004) Distribution of HCN1 and HCN2 in rat auditory brainstem nuclei. *Eur J Neurosci* 20:79–91. [CrossRef Medline](#)
- Kole MH (2011) First node of Ranvier facilitates high-frequency burst encoding. *Neuron* 71:671–682. [CrossRef Medline](#)
- Kole MH, Letzkus JJ, Stuart GJ (2007) Axon initial segment Kv1 channels control axonal action potential waveform and synaptic efficacy. *Neuron* 55:633–647. [CrossRef Medline](#)
- Kole MH, Ilschner SU, Kampa BM, Williams SR, Ruben PC, Stuart GJ (2008) Action potential generation requires a high sodium channel density in the axon initial segment. *Nat Neurosci* 11:178–186. [CrossRef Medline](#)
- Kuba H, Ishii TM, Ohmori H (2006) Axonal site of spike initiation enhances auditory coincidence detection. *Nature* 444:1069–1072. [CrossRef Medline](#)
- Leibold C (2010) Influence of inhibitory synaptic kinetics on the interaural time difference sensitivity in a linear model of binaural coincidence detection. *J Acoust Soc Am* 127:931–942. [CrossRef Medline](#)
- Leibold C, van Hemmen JL (2005) Spiking neurons learning phase delays: how mammals may develop auditory time-difference sensitivity. *Phys Rev Lett* 94:168102. [CrossRef Medline](#)
- Lorincz A, Nusser Z (2010) Molecular identity of dendritic voltage-gated sodium channels. *Science* 328:906–909. [CrossRef Medline](#)
- Magnusson AK, Kapfer C, Grothe B, Koch U (2005) Maturation of glycinergic inhibition in the gerbil medial superior olive after hearing onset. *J Physiol* 568:497–512. [CrossRef Medline](#)
- Mainen ZF, Sejnowski TJ (1996) Influence of dendritic structure on firing pattern in model neocortical neurons. *Nature* 382:363–366. [CrossRef Medline](#)
- Mainen ZF, Joerges J, Huguenard JR, Sejnowski TJ (1995) A model of spike initiation in neocortical pyramidal neurons. *Neuron* 15:1427–1439. [CrossRef Medline](#)
- Mathews PJ, Jercog PE, Rinzel J, Scott LL, Golding NL (2010) Control of submillisecond synaptic timing in binaural coincidence detectors by K(v)1 channels. *Nat Neurosci* 13:601–609. [CrossRef Medline](#)
- McIntyre CC, Richardson AG, Grill WM (2002) Modeling the excitability of mammalian nerve fibers: influence of afterpotentials on the recovery cycle. *J Neurophysiol* 87:995–1006. [Medline](#)
- McIntyre CC, Grill WM, Sherman DL, Thakor NV (2004) Cellular effects of deep brain stimulation: model-based analysis of activation and inhibition. *J Neurophysiol* 91:1457–1469. [CrossRef Medline](#)
- Palmer LM, Stuart GJ (2006) Site of action potential initiation in layer 5 pyramidal neurons. *J Neurosci* 26:1854–1863. [CrossRef Medline](#)
- Palmer LM, Clark BA, Gründemann J, Roth A, Stuart GJ, Häusser M (2010) Initiation of simple and complex spikes in cerebellar Purkinje cells. *J Physiol* 588:1709–1717. [CrossRef Medline](#)
- Paré D, Shink E, Gaudreau H, Destexhe A, Lang EJ (1998) Impact of spontaneous synaptic activity on the resting properties of cat neocortical pyramidal neurons *In vivo*. *J Neurophysiol* 79:1450–1460. [Medline](#)
- Pecka M, Brand A, Behrend O, Grothe B (2008) Interaural time difference processing in the mammalian medial superior olive: the role of glycinergic inhibition. *J Neurosci* 28:6914–6925. [CrossRef Medline](#)
- Popovic MA, Foust AJ, McCormick DA, Zecevic D (2011) The spatio-temporal characteristics of action potential initiation in layer 5 pyramidal neurons: a voltage imaging study. *J Physiol* 589:4167–4187. [CrossRef Medline](#)
- Rautenberg PL, Grothe B, Felmy F (2009) Quantification of the three-dimensional morphology of coincidence detector neurons in the medial superior olive of gerbils during late postnatal development. *J Comp Neurol* 517:385–396. [CrossRef Medline](#)
- Roberts MT, Seeman SC, Golding NL (2013) A mechanistic understanding of the role of feedforward inhibition in the mammalian sound localization circuitry. *Neuron* 78:923–935. [CrossRef Medline](#)
- Rothman JS, Manis PB (2003) The roles potassium currents play in regulating the electrical activity of ventral cochlear nucleus neurons. *J Neurophysiol* 89:3097–3113. [CrossRef Medline](#)
- Schroeder MR (1977) New viewpoints in binaural interactions. In: *Psychophysics and physiology of hearing* (Evans EF, Wilson JP, eds), pp 455–467. New York: Academic.
- Scott LL, Mathews PJ, Golding NL (2005) Posthearing developmental refinement of temporal processing in principal neurons of the medial superior olive. *J Neurosci* 25:7887–7895. [CrossRef Medline](#)
- Scott LL, Hage TA, Golding NL (2007) Weak action potential backpropagation is associated with high-frequency axonal firing capability in principal neurons of the gerbil medial superior olive. *J Physiol* 583:647–661. [CrossRef Medline](#)
- Scott LL, Mathews PJ, Golding NL (2010) Perisomatic voltage-gated sodium channels actively maintain linear synaptic integration in principal neurons of the medial superior olive. *J Neurosci* 30:2039–2050. [CrossRef Medline](#)
- Shamma SA, Shen NM, Gopalaswamy P (1989) Stereausis: binaural processing without neural delays. *J Acoust Soc Am* 86:989–1006. [CrossRef Medline](#)
- Shu Y, Duque A, Yu Y, Haider B, McCormick DA (2007) Properties of action-potential initiation in neocortical pyramidal cells: evidence from whole cell axon recordings. *J Neurophysiol* 97:746–760. [CrossRef Medline](#)
- Siveke I, Leibold C, Schiller E, Grothe B (2012) Adaptation of binaural processing in the adult brainstem induced by ambient noise. *J Neurosci* 32:462–473. [Medline](#)
- Skottun BC (1998) Sound location and neurons. *Nature* 393:531. [CrossRef Medline](#)
- Spirou GA, Chirila FV, von Gersdorff H, Manis PB (2008) Heterogeneous Ca<sup>2+</sup> influx along the adult calyx of Held: a structural and computational study. *Neuroscience* 154:171–185. [CrossRef Medline](#)
- Steriade M (2001) Impact of network activities on neuronal properties in corticothalamic systems. *J Neurophysiol* 86:1–39. [Medline](#)
- Stuart GJ, Sakmann B (1994) Active propagation of somatic action poten-

- tials into neocortical pyramidal cell dendrites. *Nature* 367:69–72. [CrossRef Medline](#)
- Stuart G, Schiller J, Sakmann B (1997) Action potential initiation and propagation in rat neocortical pyramidal neurons. *J Physiol* 505:617–632. [CrossRef Medline](#)
- Svirskis G, Kotak V, Sanes DH, Rinzel J (2002) Enhancement of signal-to-noise ratio and phase locking for small inputs by a low-threshold outward current in auditory neurons. *J Neurosci* 22:11019–11025. [Medline](#)
- van der Heijden M, Lorteije JA, Plauška A, Roberts MT, Golding NL, Borst JG (2013) Directional hearing by linear summation of binaural inputs at the medial superior olive. *Neuron* 78:936–948. [CrossRef Medline](#)
- Vladimirov N, Tu Y, Traub RD (2013) Synaptic gating at axonal branches, and sharp-wave ripples with replay: a simulation study. *Eur J Neurosci* 38:3435–3447. [CrossRef Medline](#)
- Werthat F, Alexandrova O, Grothe B, Koch U (2008) Experience-dependent refinement of the inhibitory axons projecting to the medial superior olive. *Dev Neurobiol* 68:1454–1462. [CrossRef Medline](#)
- Yin TC, Chan JC (1990) Interaural time sensitivity in medial superior olive of cat. *J Neurophysiol* 64:465–488. [Medline](#)
- Zhou Y, Carney LH, Colburn HS (2005) A model for interaural time difference sensitivity in the medial superior olive: interaction of excitatory and inhibitory synaptic inputs, channel dynamics, and cellular morphology. *J Neurosci* 25:3046–3058. [CrossRef Medline](#)



### **3. Glycinergic inhibition tunes coincidence detection in the auditory brainstem**

Published in Nature Communications (2014).

**Reference:** Myoga MH, Lehnert S, Leibold C, Felmy, F, and Grothe B. Glycinergic inhibition tunes coincidence detection in the auditory brainstem. Nat Commun. 5: 3790. doi: 10.1038/ncomms4790.

#### **Author Contributions:**

List of authors: Michael H. Myoga (MHM), Simon Lehnert (SL), Christian Leibold (CL), Felix Felmy (FF), and Benedikt Grothe (BG).

Individual contributions: MHM, CL, FF and BG, conception and design of the study; MHM performed the electrophysiological experiments and analyzed the data. SL generated the computational model, performed the simulations and analyzed the resulting data, SL and CL interpreted the results of the modeling; MHM prepared all figures. MHM, CL, FF and BG wrote the initial draft of the manuscript. All authors critically revised the manuscript. All authors approved the final version of the manuscript.



ARTICLE

Received 10 Oct 2013 | Accepted 2 Apr 2014 | Published 7 May 2014

DOI: 10.1038/ncomms4790

OPEN

# Glycinergic inhibition tunes coincidence detection in the auditory brainstem

Michael H. Myoga<sup>1</sup>, Simon Lehnert<sup>1</sup>, Christian Leibold<sup>1</sup>, Felix Felmy<sup>1,2,\*</sup> & Benedikt Grothe<sup>1,\*</sup>

Neurons in the medial superior olive (MSO) detect microsecond differences in the arrival time of sounds between the ears (interaural time differences or ITDs), a crucial binaural cue for sound localization. Synaptic inhibition has been implicated in tuning ITD sensitivity, but the cellular mechanisms underlying its influence on coincidence detection are debated. Here we determine the impact of inhibition on coincidence detection in adult Mongolian gerbil MSO brain slices by testing precise temporal integration of measured synaptic responses using conductance-clamp. We find that inhibition dynamically shifts the peak timing of excitation, depending on its relative arrival time, which in turn modulates the timing of best coincidence detection. Inhibitory control of coincidence detection timing is consistent with the diversity of ITD functions observed *in vivo* and is robust under physiologically relevant conditions. Our results provide strong evidence that temporal interactions between excitation and inhibition on microsecond timescales are critical for binaural processing.

<sup>1</sup>Division of Neurobiology, Department Biologie II, Ludwig-Maximilians-Universität München, Großhaderner Straße 2, Planegg-Martinsried D-82152, Germany. <sup>2</sup>Bioluminescence Imaging Zentrum, Ludwig-Maximilians-Universität München, Großhaderner Straße 2, Planegg-Martinsried D-82152, Germany. \* These authors contributed equally to this work. Correspondence and requests for materials should be addressed to B.G. (email: grothe@lmu.de).

Coincidence detection of afferent synaptic inputs is a hallmark of neuronal processing. In many brain areas, such as the cerebral cortex and cerebellum, neurons integrate hundreds of synaptic inputs and perform coincidence detection with millisecond resolution. In contrast, neurons in the mammalian brainstem nucleus of the medial superior olive (MSO) integrate relatively few, clearly defined synaptic inputs<sup>1</sup>, but must perform coincidence detection with orders of magnitude higher precision. They detect microsecond differences in the arrival time of low-frequency sounds between the ears (interaural time differences or ITDs)<sup>2</sup> and generate a rate code that represents the location of sounds in the horizontal plane<sup>3</sup>.

MSO neurons generally respond best to contralateral-leading ITDs<sup>4–8</sup>. To allow best coincidence detection of such temporally staggered inputs, the circuit must generate internal delays to compensate for the external delay created by the head. A longer excitatory path length from the contralateral side can explain this phenomenon at the population level, but there is increasing evidence that axonal length disparity<sup>9</sup> alone is insufficient to explain the diversity of preferred ITDs observed *in vivo*<sup>10–13</sup>. Thus, it has become a crucial question how individual neurons within the population are tuned to their specific ITDs<sup>7,14–18</sup>, an answer to which is necessary for a complete understanding of low-frequency sound localization in mammals.

Previous studies found that blocking glycinergic inhibition *in vivo* shifted the peak of ITD functions, providing direct evidence that inhibition is important for ITD tuning<sup>6,7</sup>. As glycinergic inputs to the MSO are extremely fast and precise<sup>1,6,19–23</sup>, a computational model was developed in which the relative arrival time of excitatory and inhibitory inputs tunes neurons to their preferred ITDs by modulating the peak timing of the summated input from each side<sup>7,17,24,25</sup>. However, this model was not rigorously tested under naturally occurring conditions and has been recently challenged<sup>18,26</sup>. In one study, the difference in arrival time between inhibition and excitation was measured *in vitro*. Inhibition was indeed precise and actually preceded excitation, but the average timing condition did not tune ITD functions, and it was concluded that inhibition was not important for ITD tuning<sup>26</sup>. In a second study, ITD functions were determined by juxtacellular and whole-cell recordings *in vivo*, but preceding inhibition as measured *in vitro* could not be detected<sup>8</sup>. Thus, there are now discrepancies between the existing data<sup>6–8,24–26</sup> and confusion regarding the relevance of inhibition for ITD tuning<sup>3,27–29</sup>.

To understand these discrepancies, we systematically re-evaluate the role of precise inhibition in synaptic integration and coincidence detection under well-defined, physiologically relevant conditions using acute brain slices from adult Mongolian gerbils. We find that inhibition indeed tunes coincidence detection in a manner consistent with the original model<sup>6,7,24,28</sup>, but much more dynamically than originally proposed. Moreover, we provide evidence that the specific involvement of inhibition in ITD tuning *in vivo* may not be discernable with currently available techniques. Thus, we expand the framework for the role of inhibition in ITD tuning and provide explanations for the discrepancies in the literature.

## Results

**Inhibition modulates the peak timing of excitation.** Coincidence detection neurons in the MSO are strikingly bipolar in shape (Fig. 1a)<sup>30</sup> and receive bilateral excitatory and inhibitory synaptic inputs (Fig. 1b)<sup>31</sup>. Because synaptic kinetics and input resistance change markedly during development<sup>20,21,32</sup>, we restricted our primary experiments exclusively to mature gerbils of ages postnatal day (P) 60–90. As a basis for our quantitative

re-evaluation of cellular ITD sensitivity, we first extracted the time course of excitatory and inhibitory synaptic conductances (EPSGs and IPSPs, respectively) in a separate set of voltage-clamp experiments (Supplementary Fig. 1). Individual conductance waveforms were then selected and injected as templates into the soma using conductance-clamp to simulate excitatory and inhibitory postsynaptic potentials (EPSPs and IPSPs, respectively), which produced events that largely resembled synaptically evoked responses (Supplementary Fig. 2). This allowed us to investigate precise temporal interactions between excitation and inhibition based on synaptic responses measured in mature tissue.

A fundamental principle of the original inhibitory model of ITD tuning proposes that inhibition modulates the timing of best coincidence by enforcing a shift in the peak timing of excitation on each side<sup>6,7,24,28</sup>. As there is strong evidence that the arrival times of excitatory and inhibitory inputs to the MSO is exquisitely precise<sup>19,33,34</sup>, we determined whether a precisely timed IPSP can shift the peak timing of an EPSP, here arbitrarily designated to the contralateral side (Fig. 1). Inhibitory inputs are predominantly restricted to the soma<sup>35–37</sup>, and thus simulating IPSPs with conductance-clamp is suitable to mimic realistic IPSPs. However, because excitatory inputs predominantly target the dendrites<sup>35</sup> we compared the influence of a single conductance-clamp-simulated (G-inject) IPSP on the peak timing of a synaptically evoked (F-stim) EPSP (Fig. 1c) and a conductance-clamp-simulated EPSP (Fig. 1d) in the same recording. We used an IPSP template with a decay time constant ( $\tau_{\text{IPSP}}$ ) that represented our population average (1.5 ms) and an EPSG template with a decay time constant ( $\tau_{\text{EPSP}}$ ) that generated an EPSP matching the kinetic profile of the synaptically evoked EPSP (0.2–0.3 ms, where 0.3 ms was the average; Supplementary Fig. 2). EPSG and IPSP peak amplitudes were then adjusted to achieve an effective excitation–inhibition (E–I) ratio of 1:1 (see Methods).

Because the actual arrival times of excitation and inhibition to the MSO *in vivo* is not known, we investigated a broad range of relative inhibitory timing conditions ( $\Delta t_{\text{inh}}$ ; Fig. 1e). Indeed we found timing conditions that advanced the peak timing of both the synaptically evoked and conductance-clamp-simulated EPSPs ( $\Delta t_{\text{inh}} = 0.1$  ms, F-stim:  $-62 \pm 8$   $\mu\text{s}$ ; G-clamp:  $-53 \pm 3$   $\mu\text{s}$ ,  $n = 7$ ; Fig. 1f,g, left) and others that delayed the peak of the EPSPs, albeit to a lesser extent ( $\Delta t_{\text{inh}} = -0.6$  ms, F-stim:  $21 \pm 9$   $\mu\text{s}$ ; G-clamp:  $4 \pm 6$   $\mu\text{s}$ ,  $n = 7$ ; Fig. 1f,g, right). The similarity of the timing-dependent peak shifts between synaptically evoked and conductance-clamp-simulated EPSPs ( $\Delta t_{\text{inh}} = 0.1$  ms:  $P = 0.986$ ;  $\Delta t_{\text{inh}} = -0.6$  ms:  $P = 0.647$ , two-way analysis of variance (ANOVA)) indicates that inhibition influences synaptic integration at the soma (Fig. 1h). This was further supported by separate dual-electrode conductance-clamp experiments that revealed no substantial difference in PSP kinetics or the magnitude of inhibition-enforced EPSP peak shifts compared with single-electrode experiments (Supplementary Fig. 3). Taken together, these findings demonstrate that single-electrode conductance-clamp is suitable to investigate precise temporal interactions between excitation and inhibition in MSO neurons. Thus, inhibition can indeed modulate the peak timing of excitation from either side in a bidirectional manner depending on its arrival time relative to excitation. These findings are consistent with the basic predictions of the original inhibitory model<sup>6,7,24,28</sup> as well as recent reports<sup>26</sup>.

**Input speed and balance influence peak shift magnitude.** Conductance-clamp is advantageous over synaptic stimulation in that many parameters can be tested quickly in a single recording.

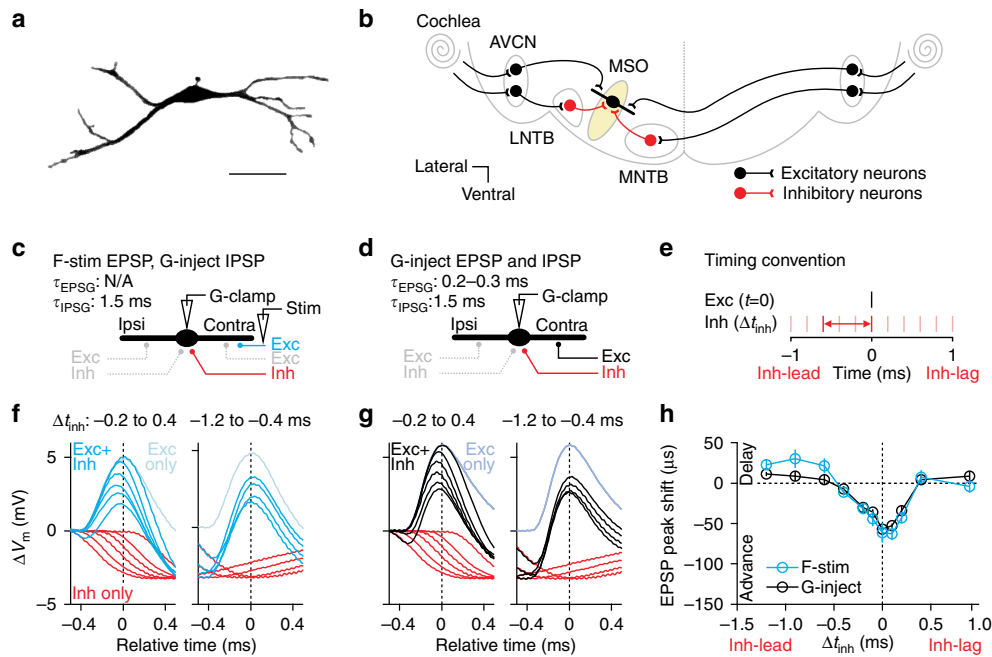


**Figure 1 | Inhibition modulates the timing of excitation.** (a) Fluorescence micrograph of a P60 MSO neuron. Scale bar, 50  $\mu$ m. (b) Schematic of input circuitry to the MSO. Ipsilateral (Ipsi) and contralateral (Contra) glutamatergic inputs from the anteroventral cochlear nuclei (AVCN) target the dendrites. Glycinergic inputs from the lateral and medial nucleus of the trapezoid body (LNTB and MNTB, respectively) target the soma. (c,d) Schematics of configurations for synaptic stimulation of EPSPs (F-stim) while simulating IPSPs (G-inject) with conductance-clamp (G-clamp, c) and simulating both EPSPs and IPSPs with conductance-clamp (d). (e) Timing convention. The onset of Inhibition is timed relative to that of Excitation from one side ( $\Delta t_{inh}$ ), designated as contralateral. Negative values indicate Inhibition leads Excitation (Inh-lead), and positive values indicate Inhibition lags Excitation (Inh-lag). (f,g) Voltage traces for an example recording using configurations in c,d, respectively, aligned in time to the peak of the EPSP alone (light traces). The influence of a precisely timed IPSP (red traces) on EPSP peak timing is visualized as a shifted peak of the composite PSP (dark traces). Traces are separated to illustrate inhibitory timing conditions that enforced a peak advance (left) or delay (right). Traces are also plotted aligned in time to the IPSP in Supplementary Fig. 2e. Resting membrane potential ( $V_{rest}$ ):  $-64$  mV. (h) Average ( $\pm$  s.e.m.) EPSP peak shifts plotted against  $\Delta t_{inh}$  for synaptically evoked (blue) and conductance-clamp-simulated (black) EPSPs. Negative and positive values indicate an EPSP peak advance and delay, respectively.  $\Delta t_{inh} = 0.1$  ms,  $P = 0.986$ ;  $\Delta t_{inh} = -0.6$  ms,  $P = 0.647$ ; two-way ANOVA,  $n = 7$  recordings.

Using this advantage, we investigated a broad parameter space in each neuron to gain insight into the mechanism by which the relative timing of inhibition modulates the peak timing of excitation. For example, this allowed us to test whether the wide range of excitatory and inhibitory input kinetics we observed (Supplementary Fig. 1) is relevant for the efficacy of inhibition-enforced EPSP peak shifts (Fig. 2a–f). Here, we compared representative fast (Fig. 2a,b) and slow (Fig. 2c,d) EPSP and IPSP templates with their average-speed ( $\tau_{EPSPG} = 0.3$  ms,  $\tau_{IPSG} = 1.5$  ms) counterparts (Supplementary Fig. 2), maintaining an E–I ratio of 1:1. Peak shifts were substantially dependent on excitatory input kinetics, where slower excitation ( $\tau_{EPSPG} = 0.5$  ms) was comparably more sensitive to peak shifts in both directions ( $\Delta t_{inh} = 0.1$  ms:  $-92 \pm 12$  versus  $-58 \pm 6$   $\mu$ s,  $P = 0.003$ ;  $\Delta t_{inh} = -0.6$  ms:  $32 \pm 8$  versus  $2 \pm 6$   $\mu$ s,  $P = 0.011$ , two-way ANOVA,  $n = 5$ ; Fig. 2a,c,e). Peak shifts were also sensitive to inhibitory input kinetics, where faster inhibition ( $\tau_{IPSG} = 1.0$  ms) was more effective at enforcing the peak delay ( $\Delta t_{inh} = -0.6$  ms:  $20 \pm 6$ ,  $P = 0.015$ , two-way ANOVA,  $n = 5$ ), but did not substantially impact the peak advance ( $\Delta t_{inh} = 0.1$  ms:  $-62 \pm 8$ ,  $P = 0.925$ , two-way ANOVA,  $n = 5$ ; Fig. 2b,d,f). Thus, although we predominantly use the average-speed EPSP and IPSP throughout the manuscript, slower excitation and faster inhibition will generally enhance the impact of inhibition on excitatory timing.

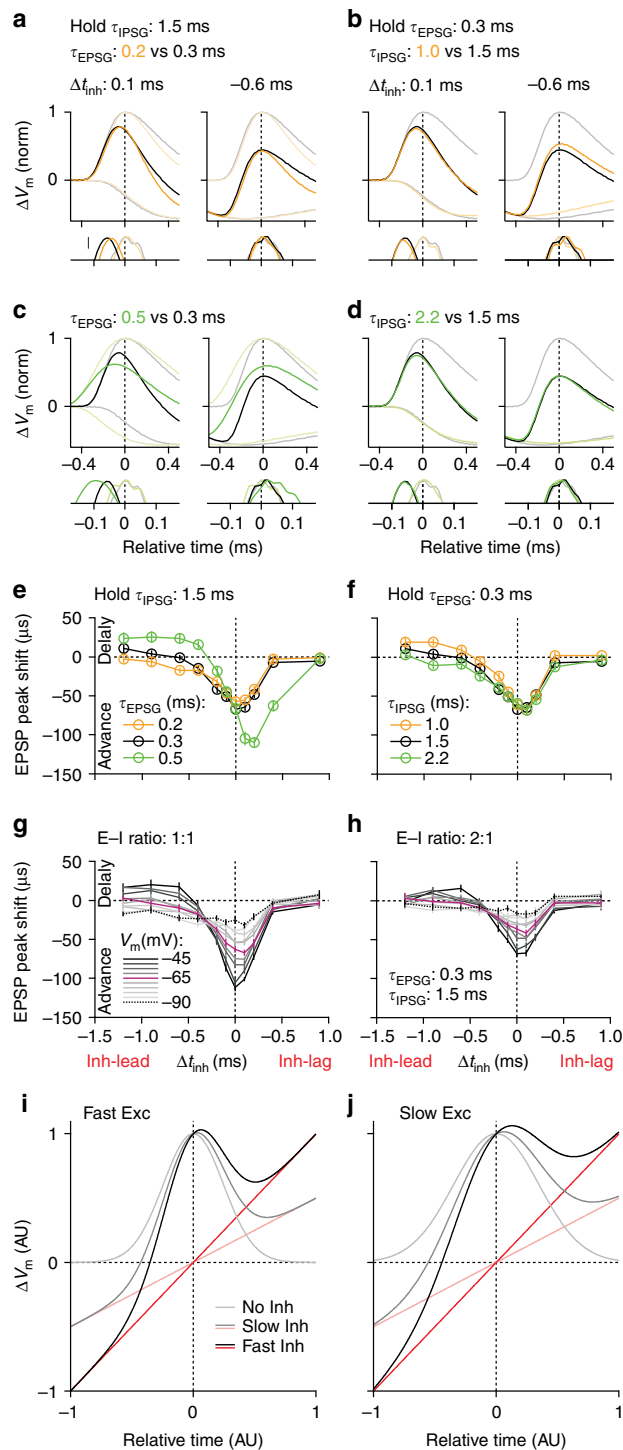
Because inhibition can impose both a shunt and hyperpolarization on the membrane, we next evaluated their independent contributions to EPSP peak shifts (Fig. 2g). Shunting inhibition

was isolated by hyperpolarizing neurons to the set reversal potential for chloride ( $-90$  mV)<sup>20</sup>. This manipulation revealed a peak advance regardless of timing ( $\Delta t_{inh} = 0.1$  ms:  $-32 \pm 4$   $\mu$ s;  $\Delta t_{inh} = -0.6$  ms:  $-23 \pm 4$   $\mu$ s,  $n = 11$ ; Fig. 2g, dotted black). Depolarizing neurons from this point revealed the contribution of hyperpolarization that manifested itself as a biphasic function superimposed on the shunt-induced function. Compared with the median resting potential ( $-65$  mV, Fig. 2g, maroon and Supplementary Fig. 4) more depolarized potentials ( $-45$  mV, black) revealed larger peak shifts in both directions ( $\Delta t_{inh} = 0.1$  ms:  $-101 \pm 3$  versus  $-67 \pm 4$   $\mu$ s,  $P < 0.001$ ;  $\Delta t_{inh} = -0.6$  ms:  $17 \pm 6$  versus  $-10 \pm 5$   $\mu$ s,  $P < 0.001$ , two-way ANOVA,  $n = 11$ ; Fig. 2g). We also doubled the E–I ratio to reduce the relative strength of inhibition and found that peak shifts were proportionally reduced, particularly for the peak advance (at  $-65$  mV,  $\Delta t_{inh} = 0.1$  ms:  $-42 \pm 4$   $\mu$ s,  $P = 0.002$ ;  $\Delta t_{inh} = -0.6$  ms:  $-3 \pm 6$   $\mu$ s,  $P = 0.972$ , two-way ANOVA,  $n = 11$ ; Fig. 2h). Thus, an inhibitory shunt generally advances the peak of an EPSP, but hyperpolarization enforces the bidirectional effect of inhibition on EPSP peak timing, depending on the balance of excitation and inhibition. Here, more depolarized membrane potentials (imposing a larger driving force on IPSPs) and stronger inhibition (relative to excitation) enhance the inhibitory control of excitatory timing.

Because MSO neurons integrate their synaptic inputs linearly<sup>8,26</sup>, these findings can be explained by a simple model (Fig. 2i,j). Here, we schematized an EPSP as a Gaussian function

and the hyperpolarizing profile of an IPSP as a sloped line (in this case the re-depolarizing phase). If we add the line to the Gaussian function, the peak of the summated function is shifted proportionally towards the slope of the line (Fig. 2i). This explains why coincident or slightly lagging inhibition (imposing a negative slope) enforces a peak advance, and why leading inhibition (positive slope) enforces a peak delay. It also illustrates why faster and stronger inhibition (steeper slope) is

more effective at enforcing EPSP peak shifts<sup>22</sup>. Because differences in inhibitory kinetics predominantly influence the slope of the re-depolarizing phase of the IPSP (Supplementary Fig. 2), it further shows why inhibitory kinetics predominantly influenced the peak delay compared to the peak advance. Finally, if we double the Gaussian half-width to mimic a relatively slower EPSP, larger shifts are generated (Fig. 2j). This explains why slower excitation is more sensitive to peak shifts. Thus, inhibitory control of excitatory timing is influenced by factors beyond the relative time of arrival<sup>16,7,22,28</sup>.



**The activity of potassium channels facilitates peak shifts.** Before investigating the consequences of inhibition-enforced EPSP peak shifts on bilateral coincidence detection, we investigated the role of low-threshold potassium channels ( $K_{LTA}$ ) in inhibition-enforced EPSP peak shifts.  $K_{LTA}$  has been implicated in sharpening EPSPs<sup>32,38</sup> and has recently been shown to interact with IPSPs<sup>26</sup>. Simply blocking  $K_{LTA}$  does not allow an assessment of its influence on synaptic integration because  $K_{LTA}$  also maintains the neuron's exquisitely fast membrane time constant in the adult ( $\sim 180 \mu s$ ). To circumvent this pharmacological limitation, we generated a point-neuron model based on our electrophysiological measurements and performed cell-wise fittings of EPSPs and IPSPs that were recorded in conductance-clamp (Fig. 3). The model recapitulated the kinetic profile and amplitude of measured events (Fig. 3a) by altering only a few independent parameters (Fig. 3b,c), demonstrating its accuracy for evaluating synaptic integration. It also successfully recapitulated inhibition-enforced EPSP peak shifts for individual recordings (Fig. 3d) and the entire population (Fig. 3e). To determine whether native  $K_{LTA}$  activity influenced inhibition-enforced EPSP peak shifts, we eliminated the  $K_{LTA}$

**Figure 2 | Input speed and balance influence peak shift magnitude.** (a-d) Normalized (norm) voltage traces for an example recording of inhibition-enforced EPSP peak shifts comparing fast ( $\tau_{EPSG} = 0.2$  ms, a;  $\tau_{IPSG} = 1.0$  ms, b; goldenrod) and slow ( $\tau_{EPSG} = 0.5$  ms, c;  $\tau_{IPSG} = 2.2$  ms, d; chartreuse) speed EPSPs (a,c) and IPSPs (b,d) with their average-speed counterparts ( $\tau_{EPSG} = 0.3$  ms;  $\tau_{IPSG} = 1.5$  ms) for  $\Delta t_{inh} = 0.1$  (left) and  $-0.6$  ms (right). Insets are zooms of the peaks, aligned in amplitude. Inset scale bar (a, bottom), 0.1 mV. Traces are colour-coded as follows: light traces indicate the EPSP and IPSP alone, dark traces indicate the composite PSP. Traces are aligned in time to the peak of the EPSP alone for each kinetic template pair.  $V_{rest} = -62$  mV. (e,f) Average ( $\pm$  s.e.m.) EPSP peak shifts plotted against  $\Delta t_{inh}$  for comparing EPSP ( $\Delta t_{inh} = 0.1$  ms:  $\tau_{EPSG} = 0.2$  ms,  $P = 0.542$ ;  $\tau_{EPSG} = 0.5$  ms,  $P = 0.003$ ;  $\Delta t_{inh} = -0.6$  ms:  $\tau_{EPSG} = 0.2$  ms,  $P = 0.422$ ;  $\tau_{EPSG} = 0.5$  ms,  $P = 0.011$ ) (e); and IPSP ( $\Delta t_{inh} = 0.1$  ms:  $\tau_{IPSG} = 1.0$  ms,  $P = 0.925$ ;  $\tau_{IPSG} = 2.2$  ms,  $P = 0.213$ ;  $\Delta t_{inh} = -0.6$  ms:  $\tau_{IPSG} = 1.0$  ms,  $P = 0.015$ ;  $\tau_{IPSG} = 2.2$  ms,  $P = 0.500$ ) (f) kinetics. Two-way ANOVA,  $n = 5$  recordings. (g,h) Same as in e,f, except the average-speed EPSP and IPSP were used, and the holding potential ( $V_m$ ) was between  $-90$  and  $-45$  mV in 5 mV increments. Compared with the median  $V_{rest} = -65$  mV (maroon; Supplementary Fig. 4b),  $V_m = -45$  mV (black):  $\Delta t_{inh} = 0.1$  ms,  $P < 0.001$ ;  $\Delta t_{inh} = -0.6$  ms,  $P < 0.001$ . The E-I ratio was 1:1 in e, but 2:1 in f. Compared with E-I ratio = 1:1, E-I ratio = 2:1 at  $V_m = -65$  mV:  $\Delta t_{inh} = 0.1$  ms,  $P < 0.001$ ;  $\Delta t_{inh} = -0.6$  ms,  $P = 0.972$ . Two-way ANOVA,  $n = 11$  recordings. (i,j) Model illustrating the mechanism underlying the dynamics of Inh-enforced EPSP peak shifts. Fast and slow EPSPs are modelled as Gaussian functions of comparably narrow (i) and wide (j) half-widths, respectively. Slow, weak (pink) and fast, strong (red) IPSPs are modelled as shallow and steep sloped linear functions, respectively. The EPSP alone is shown in light grey with a peak at  $t = 0$ . The composite PSP is the linear sum of the Gaussian function and the shallow (grey) or steep (black) linear functions. AU, arbitrary units.

activation kinetics, thereby rendering the channel passive. Interestingly, this manipulation did not substantially reduce peak shifts ( $\Delta t_{inh} = 0.1$  ms:  $-66$  versus  $-73$   $\mu$ s;  $\Delta t_{inh} = -0.6$  ms:  $-6$  versus  $-6$   $\mu$ s; Fig. 3f, turquoise). However, optimal model fit parameters (Fig. 3b) supported by measured intrinsic membrane properties (Supplementary Fig. 4) indicate that in contrast to observations in juvenile (P16–19) gerbils<sup>38</sup>  $K_{LTA}$  channels in adult (P60–P90) gerbils are activated at more hyperpolarized potentials ( $V_{0.5} = -73$  mV), thus rendering a larger fraction of them open at rest ( $-65$  mV). Indeed, we found that in contrast to P17 gerbils, the slowing and tightening of the membrane with increasing hyperpolarization (indicating that  $K_{LTA}$  had closed) was not complete, even at  $-90$  mV (Supplementary Fig. 4d,e). Interestingly, depolarizing the activation voltage in the model to levels observed in juvenile gerbils ( $V_{0.5} = -38$  mV)<sup>38</sup> revealed more robust peak shifts, particularly for a peak delay

( $\Delta t_{inh} = 0.1$  ms:  $-90$   $\mu$ s;  $\Delta t_{inh} = -0.6$  ms:  $10$   $\mu$ s; Fig. 3f, black). We also repeated the same protocol using the slow-speed EPSP and found even more pronounced peak delays ( $\Delta t_{inh} = -0.6$  ms:  $55$  versus  $8$   $\mu$ s; Fig. 3g).

To gain insight into the mechanism underlying the facilitation of  $K_{LTA}$  activity on inhibition-enforced EPSP peak shifts, we further evaluated the EPSPs (Fig. 3h,i) and the IPSP (Fig. 3j) produced by the model. When the  $K_{LTA}$  activation voltage was depolarized, both EPSPs and the IPSP amplitudes increased, but only IPSP kinetics were visibly altered.  $K_{LTA}$  gating is fast enough to follow the profile of the IPSP and is thus closed during the hyperpolarizing phase. This naturally moves the membrane potential away from the potassium reversal potential, speeding the re-depolarizing phase, from which our previous experiments would predict larger peak delays (Fig. 2b,f,i)<sup>39</sup>. The observation that the slow-speed EPSP is even more sensitive to  $K_{LTA}$  activity is also consistent with our observation that slower EPSPs are generally more sensitive to peak shifts (Fig. 2c,e,j). Thus,  $K_{LTA}$  activity promotes inhibition-enforced EPSP peak shifts by speeding the decay kinetics of the IPSP, and therefore may have a more influential role in facilitating E–I interactions during development<sup>14,32,38</sup>.

**Inhibition tunes coincidence detection.** We have shown that inhibition can modulate the peak timing of excitation from one side, but it was not known how this influences the integration of bilateral excitation. We therefore evaluated the effect of a precisely timed IPSP on subthreshold PSP summation and supra-threshold action potential probability functions (Fig. 4). Because excitation from both sides have equal strength (Supplementary Fig. 1) and summate linearly at the soma<sup>8,26</sup>, we injected two identical EPSPs at various relative times ( $\Delta t_{exc}$ ) to simulate ITDs *in vitro* (Fig. 4a, see Methods)<sup>25,26</sup>. We then determined whether a single IPSP (timed relative to the contralateral EPSP) could bias the excitatory timing of best PSP summation (PSP sum) or greatest action potential probability (AP prob). For these experiments, it matters at what  $\Delta t_{exc}$  the largest summation or the most action potentials occur and not when they occur, which was the case for previous experiments (Figs 1–3). In the absence of inhibition, these functions peaked near zero (PSP sum:  $3 \pm 2$   $\mu$ s,  $n = 5$ ; Fig. 4b; AP prob:  $7 \pm 3$   $\mu$ s,  $n = 7$ ; Fig. 4c).

Contralateral inhibition modulated coincidence detection timing in a manner consistent with its effects on the peak timing

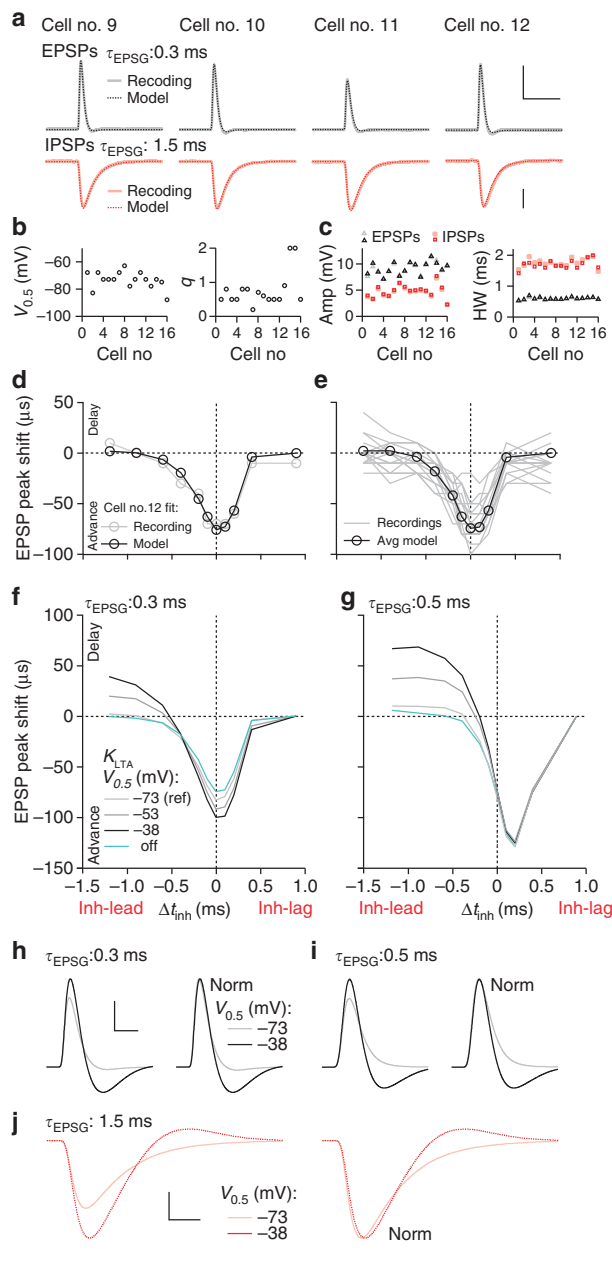


**Figure 3 | The activity of potassium channels facilitates peak shifts.** (a) Example model fittings of EPSPs (top) and IPSPs (bottom) overlaid with corresponding experimentally recorded responses (dotted lines). Scale bars, 5 mV, 5 ms (top) and 2 mV (bottom).  $V_{rest}$ :  $-65$  mV. (b) Half-activation voltage ( $V_{0.5}$ , left) and the multiplicative scaling factor for the activation time constant ( $q$ , right) of the  $K_{LTA}$  values for each cell in the population ( $n = 16$  cells). (c) Comparisons between model-fitted (dark markers) and recorded (light markers) EPSP and IPSP amplitude (Amp, left) and half-width (HW, right). (d) EPSP peak shifts plotted against  $\Delta t_{inh}$  for the model prediction (black) and experimental values (grey) for an example cell fitting. (e) Same as in d, but the prototypical neuron generated from average fit parameters (black) compared with the population of recordings (grey). (f) Same as in d, but the  $K_{LTA}$   $V_{0.5}$  was depolarized from the reference value for the example cell in d ( $-73$  mV, light grey) to  $-53$  (grey) and  $-38$  (black) mV. The activation kinetics of the  $K_{LTA}$  was also slowed by 100-fold to eliminate  $K_{LTA}$  activity (turquoise). (g) Same as in f, but for the slow-speed EPSP. (h–j) Voltage traces of the EPSPs (h,i) and IPSP (j) produced by the model of the cell in (d,f,g) with a  $K_{LTA}$   $V_{0.5}$  of  $-73$  (light traces) or  $-38$  mV (dark traces, left). Normalized (Norm) traces are shown on the right to illustrate differences in kinetics. Scale bars, 5 mV, 1 ms (h,i), and 2 mV, 1 ms (j).

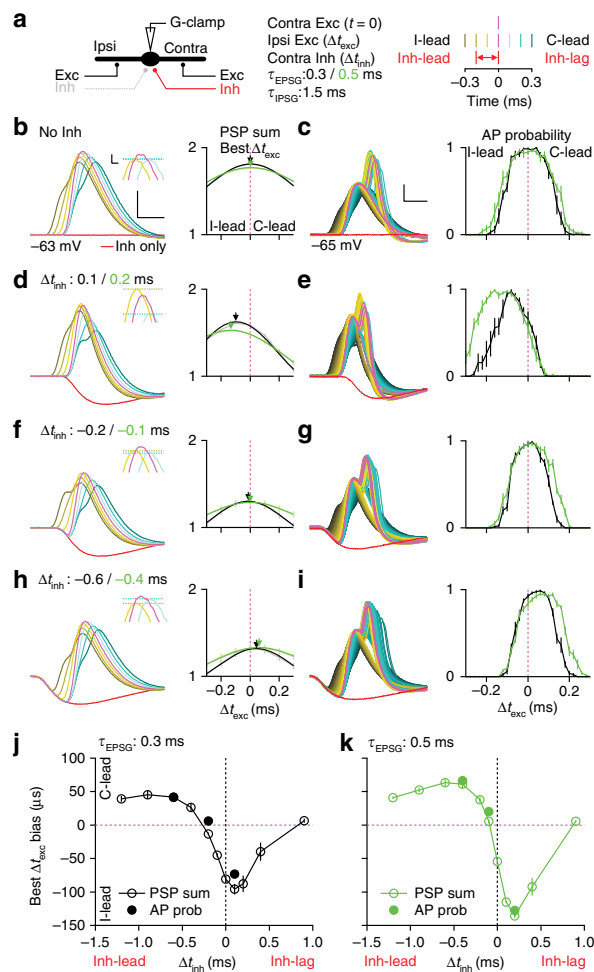


**Figure 4 | Inhibition tunes coincidence detection.** (a) Schematic illustrating three of four inputs examined (left) and timing convention (right). Contralateral Inh and ipsilateral excitation are timed relative to Contra Exc ( $\Delta t_{inh}$  and  $\Delta t_{exc}$ , respectively). (b,d,f,h) Voltage traces for an example recording of a subthreshold PSP summation experiment (left). Traces were generated from the average-speed EPSG and IPSP and are colour-coded to reflect excitatory timing conditions in a. Scale bar, 5 mV, 1 ms. Insets show zooms of the peaks. Summation bias is resolved by comparing the peak amplitudes of the flanking 100  $\mu s$  Ipsilateral-leading (yellow) and contralateral-leading (cyan) traces (horizontal dotted lines) against zero  $\Delta t_{exc}$  (pink). Inset scale bar, 50  $\mu V$ , 0.1 ms. Summated PSP amplitudes (PSP sum, normalized to the response of a single EPSP) are plotted against  $\Delta t_{exc}$  (light) and fitted with Gaussian functions (dark) for experiments using the average- (j) and slow- (k)-speed EPSG (right). Arrows indicate the peak of the function fits (best  $\Delta t_{exc}$ ). Negative and positive  $\Delta t_{exc}$  values indicate Ipsi-leading (I-lead) and Contra-leading (C-lead) conditions, respectively. Contra Inh was absent from (b) or occurred at  $\Delta t_{inh}$  values for average and slow-speed EPSGs that (respectively) advanced (0.1/0.2 ms, d), did not substantially shift (-0.2/-0.1 ms, f) or delayed (-0.6/-0.4 ms, h) the peak of the Contra EPSP. Different  $\Delta t_{inh}$  values are shown for the average and slow-speed EPSGs because these representative effects occurred at different relative timing conditions.  $n = 5$  recordings. (c,e,g,i) Same as in b,d,f,h, except that suprathreshold action potential probability (AP prob) functions were determined. Scale bar, 5 mV, 1 ms;  $n = 8-12$  recordings. (j,k) Best  $\Delta t_{exc}$  ( $\pm$  s.d.) plotted against  $\Delta t_{inh}$  for average- (j) and slow- (k)-speed EPSGs for PSP summation experiments (open markers) and action potential probability experiments (filled markers).

of contralateral excitation. Inhibitory timing conditions that advanced the peak of the contralateral EPSP ( $\Delta t_{inh} = 0.1$  ms) biased subthreshold summation and action potential probability functions towards ipsilateral-leading excitation (PSP sum:  $-96 \pm 8 \mu s$ ,  $n = 5$ ; Fig. 4d; AP prob:  $-73 \pm 2 \mu s$ ,  $n = 7$ ; Fig. 4e). This corresponds to an advanced contralateral EPSP that now summates best with an ipsilateral EPSP that occurs earlier in time. Timing conditions that did not robustly influence the peak timing of the EPSP ( $\Delta t_{inh} = -0.2$  ms) did not substantially bias coincidence detection (PSP sum:  $-11 \pm 2 \mu s$ ,  $n = 5$ ; Fig. 4f; AP prob:  $6 \pm 3 \mu s$ ,  $n = 8$ ; Fig. 4g), consistent with a different study that was performed with synaptic stimulation<sup>26</sup>. However, this timing condition ( $\Delta t_{inh} = -0.2$  ms) did narrow the half-widths of the coincidence detection functions (PSP sum:  $387 \pm 7$  versus  $467 \pm 6 \mu s$ ,  $P < 0.001$ ,  $n = 5$ ; AP prob:  $208 \pm 6$  versus  $221 \pm 8 \mu s$ ,  $P < 0.001$ , two-way ANOVA,  $n = 8$ ), also consistent with the synaptic stimulation experiments<sup>26</sup>. Finally, timing conditions that delayed the peak of the contralateral EPSP ( $\Delta t_{inh} = -0.6$  ms) biased coincidence detection towards contralateral-leading excitation, albeit to a lower extent (PSP sum:  $41 \pm 6 \mu s$ ,  $n = 5$ ; Fig. 4h; AP prob:  $41 \pm 2 \mu s$ ,  $n = 8$ ; Fig. 4i). This corresponds to a delayed contralateral EPSP that now summates best with an ipsilateral EPSP that occurs later in time. Thus, a precisely timed contralateral IPSP can modulate coincidence detection in a bidirectional manner, but only under timing conditions that had not been previously explored<sup>26</sup>.

Because recent *in vivo* recordings of MSO neurons revealed many cases where the EPSP was much slower than our average *in vitro* measurements<sup>8</sup>, we also evaluated the slow-speed EPSG paired with the average-speed IPSP (Fig. 4b–i, k, chartreuse). The peaks of both PSP summation and action potential probability functions were biased comparably further towards ipsilateral-leading ( $\Delta t_{inh} = 0.2$  ms, PSP sum:  $-136 \pm 2 \mu s$ ,  $n = 5$ ; AP prob:  $-127 \pm 3 \mu s$ ,  $n = 7$ ) and contralateral-leading ( $\Delta t_{inh} = -0.4$  ms, PSP sum:  $64 \pm 5 \mu s$ ,  $n = 5$ ; AP prob:  $66 \pm 3 \mu s$ ,  $n = 12$ ) excitation. This is consistent with the observation that slower EPSPs are more sensitive to inhibition-enforced peak shifts (Fig. 2c,e). Importantly, the similarity between the peaks of subthreshold and suprathreshold coincidence detection functions (Fig. 4j,k) indicates that the influence of inhibition on subthreshold summation accurately translates into action potential generation.

**Synaptic jitter enhances peak shifts.** Because MSO neurons can be ITD-sensitive at frequencies between  $\sim 100$  and  $\sim 1,500$  Hz (ref. 48) we returned to our single-side E–I interaction paradigm (Figs 1–3) and evaluated the efficacy of inhibitory modulation of excitatory timing under such naturalistic conditions. Although phase locking is relatively stronger at low frequencies, synaptic inputs are actually more jittered<sup>39</sup>. We therefore challenged our inhibition-enforced EPSP peak shift paradigm with increasing amounts of jitter (Fig. 5). We introduced jitter to four EPSPs and IPSPs with gamma distribution functions of up to 640  $\mu s$  in half-width (Fig. 5a,b). The resulting composite EPSPs and IPSPs revealed a broadening of event kinetics with increasing jitter, but much more pronounced for EPSPs than IPSPs (Fig. 5c). Increasing excitatory jitter alone robustly increased peak shifts in both directions (for 320  $\mu s$  excitatory jitter,  $\Delta t_{inh} = 0.1$  ms:  $117 \pm 8$  versus  $67 \pm 6 \mu s$ ,  $P < 0.001$ ;  $\Delta t_{inh} = -0.6$  ms:  $44 \pm 4$  versus  $6 \pm 3 \mu s$ ,  $P = 0.002$ , two-way ANOVA,  $n = 6$ ; Fig. 5d,e, blue), and increasing inhibitory jitter alone decreased peak shifts (for 320  $\mu s$  inhibitory jitter,  $\Delta t_{inh} = 0.1$  ms:  $-48 \pm 4 \mu s$ ,  $P = 0.023$ ;  $\Delta t_{inh} = -0.6$  ms:  $-5 \pm 3 \mu s$ ,  $P = 0.344$ , two-way ANOVA,  $n = 6$ ; Fig. 5d,e, red). Interestingly, increasing both excitatory and inhibitory jitter resulted in a net increase in peak shifts (for 320  $\mu s$  excitatory plus inhibitory jitter,  $\Delta t_{inh} = 0.1$  ms:  $-95 \pm 9 \mu s$ ,

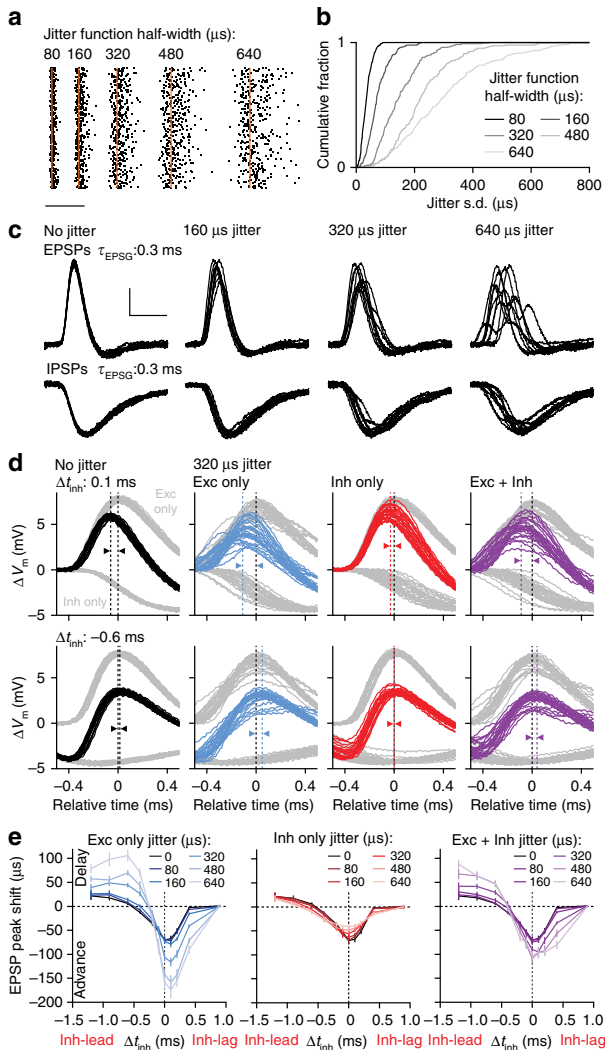


**Figure 5 | Synaptic jitter enhances peak shifts.** (a) Raster plots showing 100 trials of four event onset times jittered with gamma distributions of increasing function half-widths (left to right). Orange line indicates the reference time point (no jitter). Scale bar, 1 ms. (b) Cumulative histogram of the onset timing s.d. for the four jittered events. (c) Ten overlaid voltage traces for an example recording of the resulting composite EPSPs (top) and IPSPs (bottom) generated by jitter functions of increasing half-widths (left to right).  $V_{rest}$ :  $-64$  mV. Scale bar, 2 mV, 1 ms. (d) Voltage traces of 25 trials from the recording in c (from left to right) without jitter, or the 320  $\mu$ s half-width jitter function applied to excitation (Exc) only, inhibition (Inh) only, or Exc and Inh. Inhibitory timing conditions that advanced ( $\Delta t_{inh} = 0.1$  ms, top) and delayed ( $\Delta t_{inh} = -0.6$  ms, bottom) EPSP peak timing are shown. Grey traces show EPSPs and IPSPs alone, and dark traces show composite PSPs, aligned in time to the peak of the EPSP alone for each trial. Dotted vertical lines and arrow heads indicate the average peak shift of all 100 trials in the recording. (e) Average ( $\pm$  s.e.m.) EPSP peak shifts plotted against  $\Delta t_{inh}$  for each jitter function applied to Exc only (left), Inh only (centre) and Exc plus Inh (right). Without jitter, EPSP peak shifts were similar to those in Fig. 1h. Compared with no jitter conditions, introducing EPSP jitter (320  $\mu$ s jitter function half-width) increased peak shifts to  $\sim 200\%$  ( $\Delta t_{inh} = 0.1$  ms,  $P < 0.001$ ;  $\Delta t_{inh} = -0.6$  ms,  $P = 0.002$ ), and introducing IPSP jitter reduced peak shifts to  $\sim 75\%$  ( $\Delta t_{inh} = 0.1$  ms,  $P = 0.023$ ;  $\Delta t_{inh} = -0.6$  ms,  $P = 0.344$ ). Introducing EPSP plus IPSP jitter increased peak shifts to  $\sim 150\%$  ( $\Delta t_{inh} = 0.1$  ms,  $P = 0.014$ ;  $\Delta t_{inh} = -0.6$  ms,  $P = 0.047$ ). Two-way ANOVA,  $n = 6$  recordings.

$P = 0.014$ ;  $\Delta t_{inh} = -0.6$  ms:  $44 \pm 4 \mu$ s,  $P = 0.047$ , two-way ANOVA,  $n = 6$ ; Fig. 5d,e, magenta). Evaluation of individual trials revealed that substantially jittered conditions increase the diversity of peak shift magnitudes (Supplementary Fig. 5). However, the distribution of all trials (Supplementary Fig. 6) shows a trend towards larger peak shifts with equal amounts of excitatory and inhibitory jitter. The ability of excitatory jitter to outcompete the reduction in peak shifts generated by inhibitory jitter can be explained by larger distortion of the EPSP profile compared to the IPSP profile with equivalent amounts of jitter (Fig. 5c), from which our analysis of synaptic kinetics (Fig. 2) predict larger peak shifts. These findings indicate that naturally occurring synaptic jitter enhances inhibition-enforced EPSP peak shifts, despite the degradation of peak timing precision that was recently suggested to diminish its efficacy<sup>8,26</sup>. As ITD tuning at low frequencies has been particularly difficult to explain by axon length disparity<sup>11</sup>, these findings support an especially important role of inhibition for ITD tuning in the low-frequency range<sup>40</sup>.

**Precise inhibition maintains efficacy at high frequencies.** At high frequencies, synaptic jitter is much less, but IPSPs naturally summate<sup>26</sup>. We thus challenged inhibition-enforced EPSP peak shifts with 16 pulse trains at 333, 500 and 800 Hz under timing conditions that produced a large peak advance ( $\Delta t_{inh} = 0.1$  ms) and delay ( $\Delta t_{inh} = -0.6$  ms) (Fig. 6). Despite substantial summation (Fig. 6a, red, and Supplementary Fig. 7), inhibition sustained the ability to advance (Fig. 6b, left) and delay (Fig. 6b, right) EPSP peak timing, even at 800 Hz (for the 16th event,  $\Delta t_{inh} = 0.1$  ms:  $-48 \pm 2 \mu$ s;  $\Delta t_{inh} = -0.6$  ms:  $22 \pm 6 \mu$ s,  $n = 8$ ; Fig. 6b, bottom). Small changes in peak shifts during the train (16th event compared with the first,  $\Delta t_{inh} = 0.1$  ms:  $-70 \pm 4 \mu$ s,  $P < 0.001$ ;  $\Delta t_{inh} = -0.6$  ms:  $18 \pm 4 \mu$ s,  $P = 0.996$ , two-way ANOVA,  $n = 8$ ; Fig. 6c) can be attributed to frequency-dependent interactions between individual IPSPs during the train, which alter their effective relative peak timing (Supplementary Fig. 7). Inhibition-enforced subthreshold PSP summation bias was also similarly maintained at 800 Hz (Supplementary Fig. 8), strengthening the translation from inhibition-enforced EPSP peak shifts to coincidence detection timing. Importantly, at higher frequencies IPSPs cannot be discerned during the train regardless of whether they lead or lag EPSPs (Fig. 6a, bottom and Supplementary Fig. 8a, bottom). This is remarkably consistent with the inability to detect IPSPs from *in vivo* whole-cell recordings<sup>8</sup>. Thus, inhibition maintains its ability to influence EPSP peak timing and synaptic integration at high frequencies, despite undergoing substantial summation that was recently suggested to diminish its efficacy<sup>26</sup>.

**Bilateral inhibition extends the range of tuning.** To this point, we have considered only the influence of one (contralateral) inhibitory pathway on synaptic integration and coincidence detection. However, in the full MSO circuit both ipsilateral and contralateral inhibition are present<sup>31,41</sup>. We therefore examined the additional effect of a second, precisely timed (putative ipsilateral) inhibition in biasing subthreshold PSP summation (Fig. 7a). In these experiments, we timed the ipsilateral IPSP relative to its corresponding EPSP ( $\Delta t_{inhi}$ ) and used the slow-speed EPSPG paired with the average-speed IPSPG to evaluate the extent of inhibitory modulation on synaptic integration under our experimental conditions (Fig. 7b). Importantly, an ipsilateral IPSP will also interact with the contralateral EPSP, but because it is locked in time to the ipsilateral EPSP, the integration of all four synaptic inputs can be conceptually simplified as two composite PSPs from each side that summate linearly at the soma.

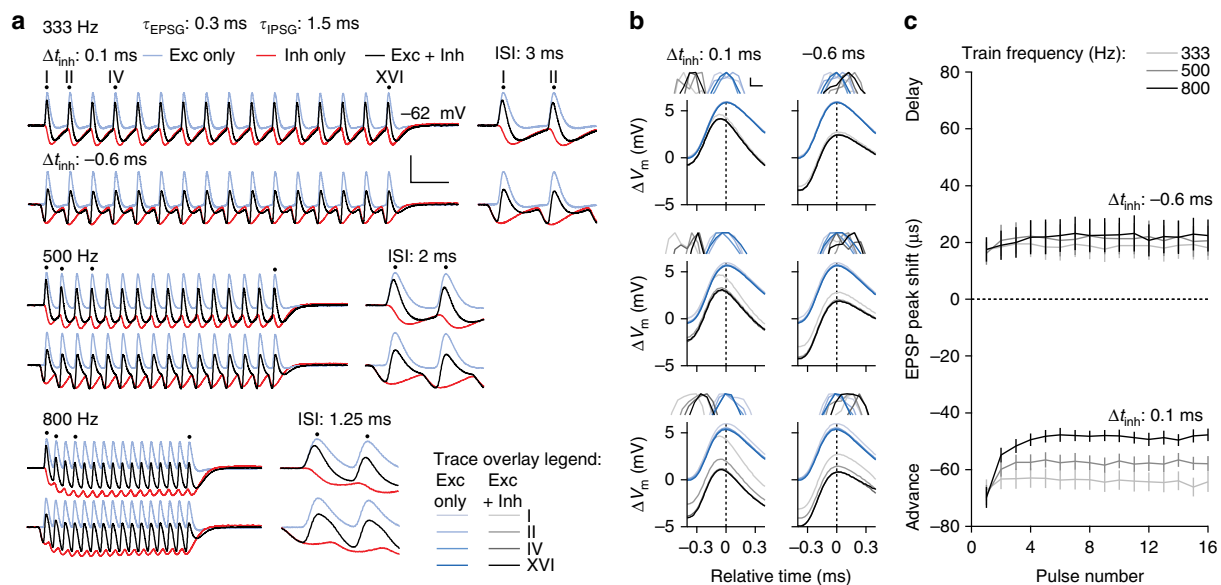


**Figure 6 | Precise inhibition maintains efficacy at high frequencies.** (a) Voltage traces of 16 pulse trains for an example recording of EPSPs (blue), IPSPs (red) and composite PSPs (black) at 333 (top), 500 (middle) and 800 (bottom) Hz. For each frequency, inhibitory timing that enforced an EPSP peak advance ( $\Delta t_{\text{inh}} = 0.1$  ms, upper traces) and delay ( $\Delta t_{\text{inh}} = -0.6$  ms, lower traces) are shown. Dots and numerals above the traces indicate individual events that are further analysed in **b**. Scale bar, 5 mV, 5 ms. The entire train is shown on the left, and a time zoom of the first two events is shown on the right. ISI, inter-stimulus interval. (b) The first, second, fourth and sixteenth event for each train in **a** overlaid for the peak advance (left) and delay (right) conditions, aligned in time to the peak of the EPSP alone. Traces are colour-coded to indicate their position in the train (colour code is indicated in **a**, bottom right). IPSPs are omitted for clarity. Insets above each plot are zooms of the peaks, aligned in amplitude. Inset scale bar, 50  $\mu$ V, 50  $\mu$ s. (c) Average ( $\pm$  s.e.m.) inhibition-enforced EPSP peak shifts plotted against each event in the train for peak advance ( $\Delta t_{\text{inh}} = 0.1$  ms) and delay ( $\Delta t_{\text{inh}} = -0.6$  ms) conditions. At 800 Hz, the 16th event compared with the first:  $\Delta t_{\text{inh}} = 0.1$  ms,  $P < 0.001$ ;  $\Delta t_{\text{inh}} = -0.6$  ms,  $P < 0.001$ ; two-way ANOVA,  $n = 8$  recordings. Independent analyses of EPSP and IPSP trains are shown in Supplementary Fig. 7. Inh, Inhibition.

We started with a pre-existing contralateral inhibition that was timed (now termed  $\Delta t_{\text{inhc}}$ ) to bias ipsilateral-leading excitation ( $\Delta t_{\text{inhc}} = 0.2$  ms:  $-163 \pm 2 \mu$ s,  $n = 7$ ; Fig. 7c–e), produce no bias ( $\Delta t_{\text{inhc}} = -0.1$  ms:  $-2 \pm 4 \mu$ s,  $n = 7$ ; Fig. 7f–h) or bias contralateral-leading excitation ( $\Delta t_{\text{inhc}} = -0.4$  ms:  $71 \pm 7 \mu$ s,  $n = 7$ ; Fig. 7i–k). In each case, the additional ipsilateral IPSP biased the timing of best PSP summation in a manner nearly equal and opposite to that of the contralateral IPSP at each  $\Delta t_{\text{inhc}}$  tested. This is consistent with an ipsilateral IPSP that shifts the peak timing of the ipsilateral EPSP in the same manner as for the contralateral side, which would in fact produce the inverse influence on coincidence detection timing (Fig. 8a). Now considering the temporal integration of all four synaptic inputs, inhibition can bias coincidence detection up to  $220 \pm 10 \mu$ s towards ipsilateral-leading excitation ( $\Delta t_{\text{inhc}} = 0.2$  and  $\Delta t_{\text{inhi}} = -0.4$  ms; Fig. 7e) and up to  $217 \pm 19 \mu$ s towards contralateral-leading excitation ( $\Delta t_{\text{inhc}} = -0.4$  and  $\Delta t_{\text{inhi}} = 0.2$  ms; Fig. 7k). Remarkably, this  $> 400 \mu$ s dynamic range is achieved within a timing window of just 0.6 ms (Fig. 8a). This is important, because even though we do not know what other internal delays may be generated in the circuit, inhibition can provide additional timing shifts that largely span the distribution of gerbil ITD functions recorded *in vivo* (Fig. 8b)<sup>6–8,43</sup>, which has been thus far unsuccessful by axon length disparity-based models of ITD tuning<sup>11</sup>. Interestingly, at timing conditions where inhibition is most capable of influencing coincidence detection, IPSPs would largely be masked by EPSPs, which is compatible with the *in vivo* observation that even at low frequencies IPSPs remained undetected between cycles<sup>8</sup>. Thus, it is tempting to speculate that the strong afterhyperpolarizations following EPSPs recorded *in vivo*<sup>8</sup> reflect the re-depolarization phase of a precisely timed IPSP that occurs nearly concomitant.

## Discussion

We demonstrated that precise inhibition modulates coincidence detection timing in MSO neurons, supporting a crucial role for inhibition in ITD tuning at the cellular level. The cellular basis for the near microsecond discrimination of ITDs, an essential component of the ability to localize sounds in mammals is elusive. As it has recently become clear that axon length disparity alone cannot predict the preferred ITD of individual MSO neurons<sup>11</sup>, several alternative models were proposed<sup>7,14,15</sup>.

The original inhibition-based model was grounded on the finding that blocking glycinergic inhibition *in vivo* shifted contralateral-leading ITD functions towards zero<sup>6–8</sup>. It was thought that a leading contralateral inhibition predominantly mediates this effect by delaying the effective peak timing of contralateral excitation<sup>6,7,24,28</sup>. This mechanism was questioned because it required unusually fast and artificial IPSP kinetics<sup>15</sup> and a level of temporal precision that would be diminished by synaptic jitter and summation<sup>8,26</sup>. We therefore based our re-evaluation on measured, mature synaptic responses (Fig. 1) under challenging temporal conditions (Figs 5 and 6). We found that inhibition was indeed capable of modulating the timing of excitation, but that a leading contralateral inhibition alone only modestly biased coincidence detection timing towards the contralateral-leading side ( $\sim 50 \mu$ s; Fig. 4h,i). However, adding the ipsilateral source of inhibition<sup>31,41</sup>, which has received much less attention, could bias coincidence detection a further  $\sim 150 \mu$ s towards the contralateral-leading side (Fig. 7k). These data strongly support the *in vivo* pharmacological experiments<sup>6,7</sup>, but demonstrate that the precise timing of inhibition from both sides is crucial to explain existing data.

Our rigorous re-evaluation also revealed that inhibitory control over excitatory timing is more diverse than originally proposed.

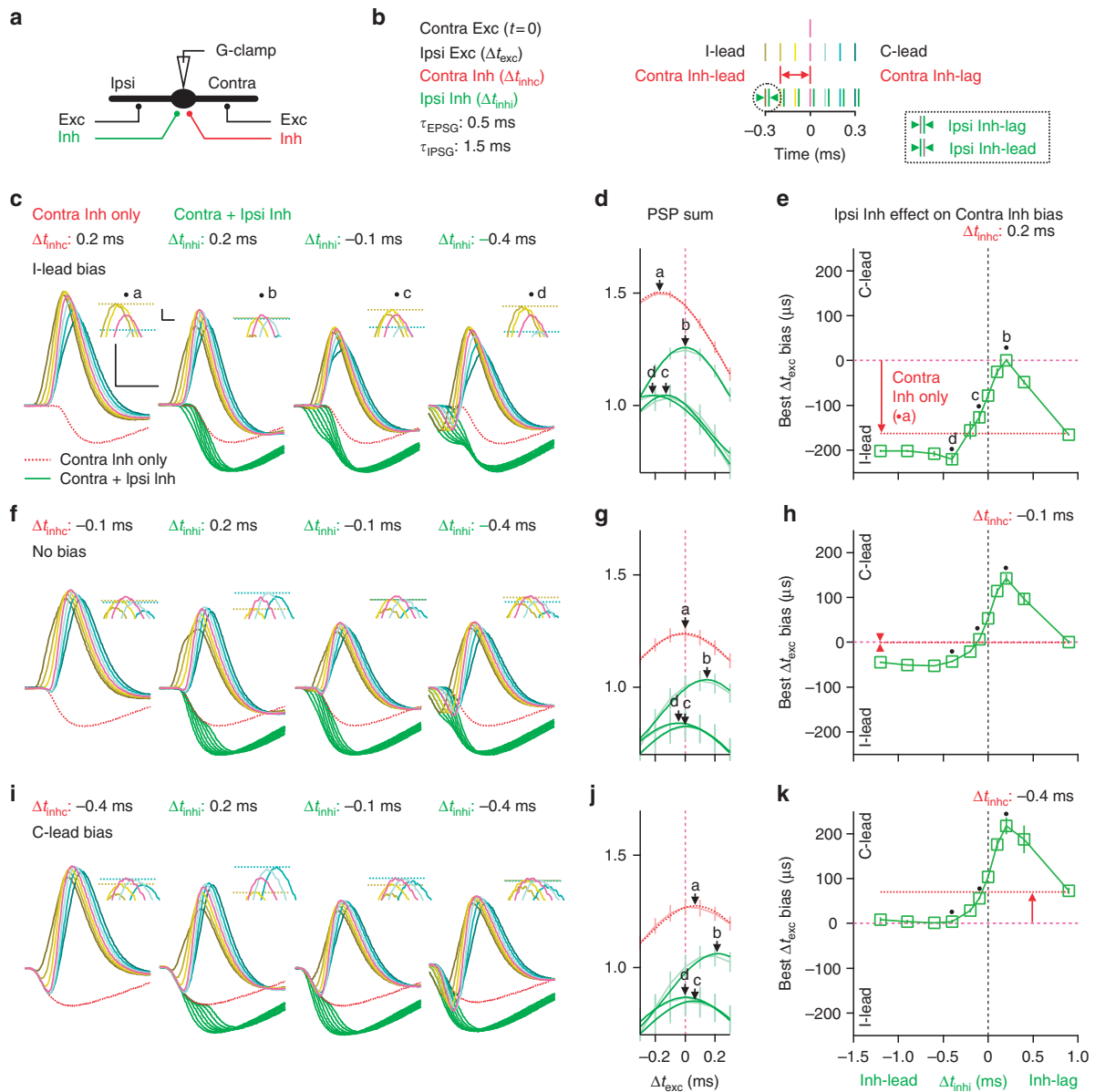


**Figure 7 | Bilateral inhibition extends the range of tuning.** (a,b) Schematic (a) and timing convention (b) for simulating all four synaptic inputs. The slow-speed EPSG was paired with the average-speed IPSG. Note that ipsilateral Inh is timed relative to Ipsilateral excitation (Exc;  $\Delta t_{inhi}$ ), and the relative timing of contralateral Inh is specified here as  $\Delta t_{inhc}$ . (c,f,i) Voltage traces for an example recording showing the effect of an Ipsi IPSP on PSP summation with a pre-existing contralateral IPSP (left panels) timed at  $\Delta t_{inhc}$  to bias PSP summation towards Ipsi-leading Exc (0.2 ms, c), produce no bias ( $-0.1$  ms, f) and bias contralateral-leading Exc ( $-0.4$  ms, i). Scale bar, 5 mV, 1 ms. The composite PSP of all four inputs (three right panels) use Ipsi inhibitory timing that matches each of the contralateral inhibitory timing conditions. Composite PSP traces are colour-coded as in Fig. 4, except the contralateral IPSP traces are dotted red, and the composite contralateral and Ipsi IPSP traces are green. Insets are zooms of the peaks, and dotted lines indicate the peaks of flanking timing conditions around zero  $\Delta t_{exc}$  to illustrate bias (as in Fig. 4b,d,f,h). Letters and dots indicate the timing conditions marked in subsequent analyses. Inset scale bar, 0.5 mV, 0.1 ms. (d,g,j) PSP summation functions of conditions marked in (c,f,e), respectively, (as in Fig. 4b,d,f,h). (e,h,k) Best  $\Delta t_{exc}$  ( $\pm$  s.d.) plotted against Ipsi inhibitory timing (as in Fig. 4j,k, but against  $\Delta t_{inhi}$  for contralateral inhibitory timing that biased Ipsi-leading Exc ( $\Delta t_{inhc} = 0.2$  ms, e), produced no bias ( $\Delta t_{inhc} = -0.1$  ms, h), and biased contralateral-leading Exc ( $\Delta t_{inhc} = -0.4$  ms, k). Dotted red lines and arrows indicate the pre-existing bias enforced by the contralateral Inh alone;  $n = 7$  recordings. Inh, Inhibition.

For example, even small differences in synaptic kinetics (Fig. 2a–f), the driving force on inhibition (Fig. 2g), the balance of excitation and inhibition (Fig. 2g,h), and the activation of  $K_{LTA}$  channels (Fig. 3) markedly influenced the efficacy of inhibition-enforced EPSP peak shifts. Moreover, our investigation of a wide

range of timing parameters revealed conditions that biased best coincidence detection towards the ipsilateral-leading side (Fig. 4d,e) and others that produced no bias at all (Fig. 4f,g). As the actual arrival time of inhibition relative to excitation *in vivo* could be adjusted on a single-neuron basis, inhibition-

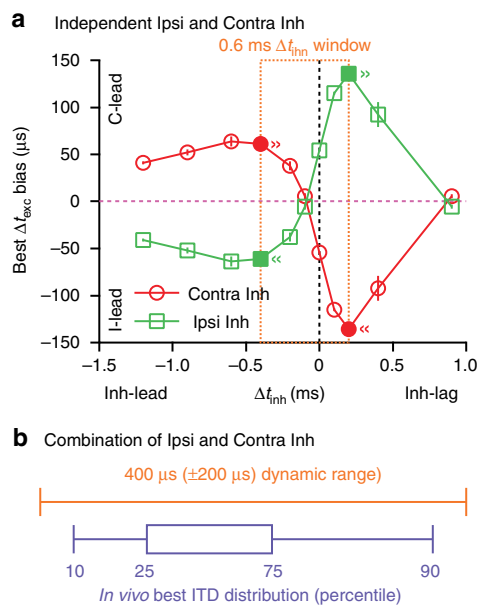


**Figure 8 | Bilateral inhibition can explain ITD tuning *in vivo*.** (a) The independent influence of contralateral (Contra) and ipsilateral (Ipsi) Inh on best  $\Delta t_{exc}$  ( $\pm$  s.d.) plotted against  $\Delta t_{inhc}$  and  $\Delta t_{inhi}$ , respectively. For the Contra Inh, data from Fig. 4k are re-plotted (red circles). To illustrate the near equal and opposite effect of Ipsi Inh on coincidence detection, the data are inverted (green squares). Both Ipsi and Contra Inh can independently influence coincidence detection timing towards the ipsilateral-leading (negative values) and Contra-leading (positive values, light blue shading) sound, depending steeply on their relative arrival timing. The full dynamic range of inhibitory influence on ITD tuning is achieved in a timing window of 0.6 ms (dotted orange box). Ipsilateral and Contra inhibitory timing conditions that maximally bias ipsilateral-leading ( $\Delta t_{inhc} = 0.2$  ms,  $\Delta t_{inhi} = -0.4$  ms) and Contra-leading excitation ( $\Delta t_{inhc} = -0.4$  ms,  $\Delta t_{inhi} = 0.2$  ms) are filled and marked. (b) Comparison between the dynamic range of bilateral Inh on coincidence detection and the diversity of ITD functions observed *in vivo*. The dynamic range is calculated by taking the difference between the combinatorial bias of bilateral Inh under inhibitory timing conditions that are marked in a. Although the magnitude of intrinsic delays in the absence of Inh is not known, the range of bilateral inhibitory control of coincidence detection timing could modulate the preferred ITD of a neuron (best ITD) on an individual basis to an extent that exceeds 80% of the population distribution from previously measured ITD functions *in vivo*<sup>42</sup>. Inh, Inhibition.

enforced ITD tuning *in vivo* may be more diverse than the existing data would suggest<sup>6,7</sup>. This provides a powerful mechanism for tuning individual neurons in the MSO, a central issue that remains unexplained by anatomical specializations<sup>11,41</sup>. Although inhibition is one of several mechanisms that may work in concert to tune neurons to their preferred ITDs, it can accomplish this simply by adjustments or adaptations of synaptic properties<sup>43,44</sup>, a more flexible solution compared with axonal length adjustments<sup>11</sup>. Thus, our findings indicate that the original inhibitory model should be expanded.

Recently, one study evaluated the predictions of the original inhibitory model<sup>26</sup>, specifically whether a leading contralateral inhibition biased ITD functions towards the contralateral side. Although there was already evidence that the inhibitory input pathways are faster compared with their excitatory counterpart<sup>22,23,45</sup>, this was directly evaluated in a thick slice preparation by stimulating the auditory nerve. Inhibition indeed

preceded excitation, but a single IPSP at the average timing condition ( $\Delta t_{inh} = -0.3$  ms) did not tune ITD functions. It was concluded that inhibition, while important for coincidence detection, is not relevant for ITD tuning<sup>26</sup>. Although this study used synaptic stimulation instead of conductance-clamp to generate ITD functions, our findings are in accord, as a similar timing condition ( $\Delta t_{inh} = -0.2$  ms) also did not substantially influence coincidence detection timing (Fig. 4f.g). Importantly, the relative arrival time of excitation and inhibition measured in the study were performed in P15–20 tissue and thus might not represent the fully matured stage of the circuit<sup>26</sup>. Moreover, the measured relative inhibitory timings spanned a range of  $-0.5$  to  $-0.1$  ms<sup>26</sup> and are likely even more diverse *in vivo*, owing to cochlear delays and natural activation of the cochlear nucleus<sup>12,16,46</sup> that are lost in a slice preparation. Therefore, we deliberately made no assumptions about the actual arrival times of excitation and inhibition and indeed found other timing conditions that generated pronounced modulation of coincidence detection timing. Finally, the ipsilateral source of inhibition, which appeared equivalently as strong as the contralateral source, was not previously evaluated in modulating coincidence detection<sup>26</sup>. Our present results indicate that the ipsilateral source of inhibition may be in fact crucial to ITD tuning, and thus future studies are required to elucidate the role of its substantial input to the MSO.

The role of synaptic inhibition in the MSO remains a topic of intense debate<sup>27–29</sup>. A second recent study investigated ITD tuning *in vivo* using whole-cell recordings. A pronounced leading inhibition could not be detected<sup>8</sup>, contradicting the *in vitro* measurements. It was nevertheless reasoned from the lack of detection that the temporal precision of inhibition was not sufficient to tune ITD functions. In contrast, our findings demonstrate that inhibitory modulation of excitatory timing is in fact resilient to synaptic jitter (Fig. 5) and summation (Fig. 6). More importantly, under timing conditions where inhibition is most effective at influencing coincidence detection timing (Fig. 8a), IPSPs would be masked by EPSPs on each cycle. Even if inhibition could be detected between cycles at low frequencies, its interaction with excitation during high-frequency activity would mask its presence, regardless of its relative timing (Fig. 6a and Supplementary Fig. 8). Unfortunately, as currently available *in vivo* electrophysiological techniques are insufficient to resolve excitatory and inhibitory events independently<sup>8</sup>, the exact arrival time of excitation and inhibition to MSO neurons remains unknown. The manner in which inhibition tunes ITD functions *in vivo* thus remains an open question.

The scope of inhibitory mechanisms that modulate ITD coding extends far beyond the precise modulation of coincidence detection timing we report here. For example, the MSO receives GABAergic input, which activates presynaptic GABA<sub>B</sub> receptors on MSO inputs<sup>47,48</sup>. However, in contrast to phasic glycinergic inhibition, GABA<sub>B</sub> signalling enforces a gain control mechanism to adapt ITD sensitivity in dynamic auditory environments<sup>43</sup>. Furthermore, phasic<sup>49,50</sup> and sustained<sup>51</sup> inhibition are also prominent in nucleus laminaris (NL), the functionally equivalent avian analogue to the mammalian MSO<sup>52</sup>. In contrast to the MSO, inhibition in NL is predominantly GABAergic and imposes a shunting and depolarizing effect on NL neurons<sup>48,49</sup>. Here phasic and tonic inhibition work in concert to maintain ITD sensitivity at different frequencies and intensities<sup>53,54</sup>. The inhibitory shunt sharpens the coincidence detection time window<sup>55</sup> in a frequency region-specific manner, but it does not influence the peak timing of incoming excitatory signals<sup>50–52</sup>. Thus, both mammals and birds have evolved diverse inhibitory mechanisms to modulate ITD processing.

## Methods

**Tissue preparation.** All experiments were performed in accordance with protocols approved by the Deutsche Tierschutzgesetz. Male and female Mongolian gerbils (*Meriones unguiculatus*) aged P60–P90 or P17 (Supplementary Fig. 4) were anaesthetized with isoflurane [2-chloro-2-(difluoromethoxy)-1,1,1-trifluoroethane] and decapitated. Brains were removed and placed in a warmed (~35 °C, P60–90) or ice-cold (~4 °C, P17) dissecting solution containing the following (in mM): 200 sucrose, 25 glucose, 25 NaCl, 25 NaHCO<sub>3</sub>, 3 MgCl<sub>2</sub>, 3 myo-inositol, 2.5 KCl, 2 Na-pyruvate, 1.25 NaH<sub>2</sub>PO<sub>4</sub>, 0.4 ascorbic acid and 0.1 CaCl<sub>2</sub> (pH 7.4 when bubbled with 95% O<sub>2</sub> and 5% CO<sub>2</sub>). Horizontal (110 µm thick, P60–90) or coronal (250 µm thick, P17) slices were made from the brainstem using a VT1200S vibratome (Leica). Slices were then incubated for 30–45 min at 35 °C in a perfusion saline containing the following (in mM): 125 NaCl, 25 NaHCO<sub>3</sub>, 25 glucose, 3 myo-inositol, 2.5 KCl, 2 Na-pyruvate, 2 CaCl<sub>2</sub>, 1.25 NaH<sub>2</sub>PO<sub>4</sub>, 1 MgCl<sub>2</sub> and 0.4 ascorbic acid (pH 7.4 when bubbled with 95% O<sub>2</sub> and 5% CO<sub>2</sub>).

**Electrophysiology.** All experiments were performed in perfused saline (1 ml min<sup>-1</sup> and bubbled with 95% O<sub>2</sub> and 5% CO<sub>2</sub>), except that CaCl<sub>2</sub> was reduced to 1.2 mM. Recording temperature was measured near the slice and maintained at 35 ± 1 °C by an SF-28 in-line heater (Warner Instruments) and PH-1 bath chamber heater (Biomedical Instruments). Tissue was visualized under a BX50WI upright microscope (Olympus) equipped with infrared Dodt Gradient Contrast optics (Luigs & Neumann), a Polychrome V monochromator (Till Photonics) and an Imago camera (TILL Photonics). Whole-cell recordings of morphologically identified MSO neurons (Fig. 1a) were obtained with borosilicate glass electrodes using an EPC10/2 patch-clamp amplifier (HEKA Elektronik).

**Voltage-clamp experiments.** For voltage-clamp experiments (Supplementary Fig. 1), the internal solution contained the following (in mM): 130 Cs-gluconate, 20 TEA-Cl (tetraethylammonium chloride), 15 HEPES [4-(2-hydroxyethyl)-1-piperazineethanesulfonic acid], 5 Cs-EGTA (caesium ethylene glycol tetraacetic acid), 5 QX-314 [N-(2,6-dimethylphenylcarbamoylmethyl) triethylammonium chloride], 5 Na<sub>2</sub>-phosphocreatine, 3 Mg-ATP, 0.3 Na<sub>2</sub>-GTP, 0.05 Alexa Fluor 568 and 0.01 ZD 7288 (4-Ethylphenylamino-1,2-dimethyl-6-methylaminopyrimidinium chloride), adjusted to pH 7.25 and 320 m Osm. Electrodes had 2–3 MΩ tip resistances, and experiments were performed at -75 mV (after correcting for an estimated liquid junction potential for this internal solution of 15 mV). Series resistance was 4–7 MΩ and was compensated to a residual of 1.5–2 MΩ on the amplifier. Experiments were terminated if the uncompensated series resistance changed by >10%.

Synaptic inputs were stimulated with borosilicate glass electrodes (of 3–4 MΩ resistance) filled with saline and placed in the vicinity (50–150 µm) of the recorded neuron. Ipsilateral and contralateral glutamatergic (excitatory) inputs could be independently activated because they are well segregated to the lateral and medial sides of the MSO, respectively, (Fig. 1b)<sup>55</sup>. As glycinergic (inhibitory) inputs are not well segregated in the slice, the population of inhibitory conductance waveforms likely reflects inputs from both the lateral and medial nucleus of the trapezoid body (lateral and medial nucleus of the trapezoid body)<sup>56</sup>. Axons were stimulated with brief (0.2 ms) 10–50 V bipolar pulses generated by a Model 2100-isolated pulse stimulator (A-M Systems). The stimulus voltage was adjusted such that putative single fibres were activated, as indicated by all-or-none threshold responses and <25% s.d. in amplitude<sup>1</sup>. Conductance values (Supplementary Fig. 1f) were calculated from the measured reversal potential for EPSCs (5 mV) and the calculated Nernst potential of chloride for IPSCs (-44 mV). All voltage-clamp experiments were performed in the presence of 10 µM R-CPP [3-[(R)-2-Carboxypiperazin-4-yl]-propyl-1-phosphonic acid] and 10 µM SR 95531 [6-Imino-3-(4-methoxyphenyl)-1(6H)-pyridazinebutanoic acid hydrobromide] to block NMDA receptors and GABA<sub>A</sub> receptors, respectively. Glutamatergic and glycinergic inputs were isolated with 0.5 µM strychnine and 20 µM DNQX (6,7-Dinitroquinoxaline-2,3-dione), respectively.

**Single-electrode conductance-clamp experiments.** For single-electrode conductance-clamp experiments (Figs 1, 2 and 4–7 and Supplementary Figs 2 and 5–8), the internal solution contained the following (in mM): 145 K-gluconate, 15 HEPES, 5 Na<sub>2</sub>-phosphocreatine, 3 Mg-ATP, 0.3 Na<sub>2</sub>-GTP and 0.05 Alexa Fluor 568, adjusted to pH 7.25 and 320 m Osm. Electrodes had 3.5–5 MΩ tip resistances, and series resistance (4–6 MΩ) was 100% balanced on the bridge of the amplifier (Supplementary Fig. 4a). The liquid junction potential was estimated to be 15 mV and compensated online. Selected synaptic conductance waveforms as measured in Supplementary Fig. 1 were delivered to an SM-1 conductance injection amplifier (Cambridge Conductance), which calculates instantaneous current commands  $I(t)$  by equation (1).

$$I(t) = G(t)[V(t) - E_{\text{rev}}] \quad (1)$$

This calculation was performed independently for excitatory (reversal potential  $E_{\text{rev}} = 5$  mV) and inhibitory ( $E_{\text{rev}} = -90$  mV)<sup>20</sup> synaptic conductance waveform templates  $G(t)$ , while simultaneously measuring the membrane potential  $V(t)$ . Although single inhibitory fibre conductance was roughly twice that of a single excitatory fibre (Supplementary Fig. 1b,f), previous studies have indicated that

there are also about only half the number of inhibitory inputs compared with excitatory inputs, and thus the effective inhibitory and excitatory synaptic strength is balanced<sup>1</sup>. Therefore, for subthreshold experiments EPSCs and IPSCs were injected with a peak conductance of 30 nS, yielding an E–I ratio of 1:1 (except for Fig. 2h, where the IPSC was reduced to 15 nS). To minimize recording time and maximize the number of parameters that could be tested in a single recording (typically <10 min)<sup>57</sup>, EPSC and IPSC template pairs were randomized and then injected at 50 Hz. Current test pulses were delivered directly before and after each acquisition epoch to ensure that  $I_h$  activity had not substantially changed<sup>56</sup>. Experiments were terminated if membrane input resistance changed by >1 MΩ.

EPSP peak shifts (Figs 1–3, 5 and 6 and Supplementary Figs 3 and 5–7) were calculated by comparing the peak EPSP time generated by an EPSC plus IPSC injection with that of an EPSC injection alone. Subthreshold PSP summation bias (Fig. 4b,d,f,h, Fig. 7, and Supplementary Fig. 8) was determined by Gaussian fitting of PSP summation functions. PSP summation functions were generated by presenting two identical EPSCs at different relative times ( $\Delta t_{\text{exc}}$  in 100 µs increments). The amplitude of the composite PSP was then normalized to a single EPSC, and the relationship between the normalized composite PSP amplitude and  $\Delta t_{\text{exc}}$  (an *in vitro* representation of an ITD in the absence of any other intrinsic delay mechanisms) was fitted with a Gaussian function. The peak of the function fit was defined as the best  $\Delta t_{\text{exc}}$ . Each timing condition was repeated six times in each recording, and analysis was performed on the average voltage responses.

For suprathreshold coincidence detection experiments (Fig. 4c,e,g,i), the timing convention was the same as for subthreshold PSP summation experiments, but  $\Delta t_{\text{exc}}$  was presented in 20 µs increments. Because action potential conductance thresholds in MSO neurons are extremely sensitive to changes in membrane potential, baseline current ( $192 \pm 66$  pA,  $n = 13$  recordings) was injected to maintain the membrane potential at -65 mV. Then two identical EPSCs were injected with a magnitude ( $\tau_{\text{EPSC}} = 0.3$  ms:  $43 \pm 2$  nS,  $n = 13$  recordings;  $\tau_{\text{EPSC}} = 0.5$  ms:  $32 \pm 2$  nS) that brought the neuron to threshold ( $G_t$ ), defined as 50% action potential probability at  $1 \Delta t_{\text{exc}}$ . The protocol was then repeated 10 times at 200 pS (~3%) above  $G_t$ , where action potential probability peaked near 100%. Repeating these experiments with the inclusion of the IPSC (60 nS,  $\tau_{\text{IPSC}} = 1.5$  ms) required an adjustment of EPSC magnitude to depolarize the neuron to  $G_t$ . Adjustments for each  $\Delta t_{\text{inh}}$  using the average-speed EPSC ( $\tau_{\text{EPSC}} = 0.3$  ms) were as follows: 0.1 ms:  $50 \pm 1$  nS, -0.2 ms:  $61 \pm 2$  nS and -0.6 ms:  $48 \pm 1$  nS. Adjustments for each  $\Delta t_{\text{inh}}$  using the slow-speed EPSC ( $\tau_{\text{EPSC}} = 0.5$  ms) were as follows: 0.2 ms:  $51 \pm 2$  nS, -0.1 ms:  $56 \pm 2$  nS and -0.4 ms:  $50 \pm 3$  nS. Owing to the many trials for these experiments, only 1–3 inhibitory timing conditions were performed in each recording. The average action potential probability function from all 10 trials in each recording were then averaged for each inhibitory timing condition ( $n = 8$ –12 recordings per condition). For statistical analysis, the data were fitted with Gaussian functions as for subthreshold experiments (Fig. 4b,d,f,h).

For jitter experiments (Fig. 5), four EPSCs and IPSCs (10 nS each) were jittered randomly according to the gamma ( $\Gamma$ ) distribution generated by equation (2).

$$P(t+ab) = \frac{t^{a-1}e^{-t}}{b^a\Gamma(a)} \quad (2)$$

The function asymmetry variable  $a$  was 40 to mimic the shape of sound-evoked spiking output of AVCN neurons<sup>34</sup>, and the function width variable  $b$  was 20, 40, 80, 120 and 160 µs to evaluate different magnitudes of jitter. This generated function half-widths of 80, 160, 320, 480 and 640 µs. Iterations of the jittered four inputs were presented 100 times at each inhibitory timing condition in each recording.

For train experiments (Fig. 6 and Supplementary Figs 7 and 8), individual templates were compounded at 200, 333, 500 and 800 Hz for 16 pulses and then injected. Inhibition-enforced EPSP peak shifts (Fig. 6) were calculated relative to the excitation-only peak time for each pulse in the train. Analysis for subthreshold PSP summation bias (Supplementary Fig. 8) was performed as for single-pulse experiments (Figs 4 and 7). Although depression of synaptic currents has been reported<sup>1</sup>, recent observations indicate little if any depression of synaptic potentials during ongoing activity<sup>23</sup>. Therefore, the conductance amplitude was constant for each pulse in the train. This approach thus maximized the effect of summation at higher frequencies. Each timing condition was repeated six times in each recording.

**Fibre stimulation experiments.** For combined fibre stimulation and conductance-clamp experiments (Fig. 1c,f,h and Supplementary Fig. 2d,e), synaptic conductance was injected as for single-electrode conductance-clamp experiments, except that an extracellular stimulating electrode was placed on the medial fibre tract, and single-fibre stimulation was obtained in current-clamp. Then an EPSC was selected to match the decay kinetics of the stimulated EPSP, typically  $\tau_{\text{EPSC}} = 0.2$  or 0.3 ms. The strength of the EPSC template was then adjusted to produce an EPSP with equal amplitude to the synaptically evoked EPSP (Supplementary Fig. 2d). Then the IPSC template amplitude was matched to the EPSC template such that the conductance-clamp-simulated EPSP and fibre-stimulated EPSP would have an equivalent influence of the IPSC (E–I ratio ~1:1). Trials were presented at 10 Hz. To eliminate the potential effects of short-term plasticity during the protocol<sup>1</sup>, each

trial was directly preceded by a 20 pulse, 10 Hz train such that the amplitude of fibre-stimulated EPSPs was securely at steady state<sup>1</sup>. Each timing condition was repeated 10 times in each recording. In separate experiments, single-fibre EPSPs and IPSPs were also synaptically evoked in current-clamp for a comparison with conductance-clamp-simulated PSPs (Supplementary Fig. 2b,c, blue).

**Dual-electrode conductance-clamp experiments.** MSO neuron somata were patched sequentially with two electrodes<sup>23</sup>, but otherwise performed as for single-electrode conductance-clamp experiments. To determine the potential influence of hardware errors introduced by injecting conductance and measuring voltage through the same electrode, synaptic conductance was always injected through the first electrode (E-1), but membrane voltage was measured using the same electrode or using the second (passive) electrode (E-2) and compared (Supplementary Fig. 3). Both directions were evaluated for each recording. Thus, the terms E-1 and E-2 are functionally and not physically defined.

**Data acquisition and analysis.** Data were acquired at 100 kHz. Voltage-clamp data were additionally filtered at 8 kHz using a shallow three-pole Bessel filter in the amplifier. Analysis was performed off-line using Igor Pro (Wavemetrics). Example conductance-clamp traces represent an average of 6–10 trials except for Fig. 4c,e,g,i and Fig. 5c,d, and Supplementary Fig. 5, which show individual raw traces. Example voltage-clamp (Supplementary Fig. 1b) and current-clamp (Supplementary Fig. 2b, blue) traces represent an average of 30 trials. Group averages are presented as mean  $\pm$  s.e.m., except for the results of Gaussian fittings, which are presented as peak time ( $t_0$ )  $\pm$  s.d. Sample sizes for each experiment were at least five per group, which generated normal distributions (determined by Kolmogorov–Smirnov normality tests,  $P < 0.05$ ). Statistical analysis of the data was determined using two-way ANOVA in Prism software (GraphPad). Dunnett's *post hoc* tests were performed to determine statistical significance ( $P < 0.05$ ).

**Computational model.** A conductance-based point-neuron model was generated to explain subthreshold postsynaptic integration (Fig. 3). The dynamics of the membrane voltage  $V$  was simulated by current-balance equation (3).

$$C_m \frac{dV}{dt} = -(I_h + I_{K_{LTA}} + I_{syn} + I_{leak}) \quad (3)$$

$C_m$  denotes the measured individual cell capacitance (24.6 pF on average). Ohmic currents were assumed in equation (4).

$$I_x(V) = g_x a_x^m b_x^n (V - E_x) \quad (4)$$

$g_x$  denotes the peak conductance,  $a_x$  and  $b_x$  were gating functions with cooperativities of  $m$  and  $n$ , respectively, and  $E_x$  was the reversal potential. The gating functions adhere to first order kinetics (equations 5 and 6).

$$\frac{da}{dt} = \frac{a_\infty - a}{\tau_a} \quad \frac{db}{dt} = \frac{b_\infty - b}{\tau_b} \quad (5, 6)$$

$a_\infty$  and  $b_\infty$  are the steady-state activation, and  $\tau_a$  and  $\tau_b$  are the voltage-dependent time constants. The leak current  $I_{leak}$  was passive (that is,  $m = n = 0$ ) with a reversal potential  $E_{leak} = -90$  mV and a conductance  $G_{leak} = 0.8$  pS  $\mu\text{m}^{-2}$ , estimated from the measured remaining input resistance (on average 280 M $\Omega$ ) at  $-90$  mV when  $K_{LTA}$  and  $I_h$  channels were blocked with dendrotoxin-k and ZD 7288, respectively. The  $K_{LTA}$  current was modelled with a reversal potential of  $-105$  mV (ref. 37), an average half-activation voltage ( $V_{0.5}$ ) of  $-72.9$  mV, and an average activation time constant scaling factor ( $q$ ) of 0.77. This resulted in kinetics for the  $K_{LTA}$  channels in equations (7–10) ( $V$  in mV,  $\tau$  in ms,  $m = 4$ ,  $n = 1$ ).

$$a_\infty(V) = \left(1 + e^{\frac{V+92.74}{-11.7}}\right)^{-1} \quad (7, 8)$$

$$\tau_a(V) = q^{-1} \left( \frac{21.5}{6e^{\frac{V+95.4}{7}} + 24e^{\frac{V+95.4}{30.6}}} \right) + 0.35$$

$$b_\infty(V) = \frac{1 - 0.27}{1 + e^{\frac{V+102.4}{6.16}}} + 0.27 \quad (9, 10)$$

$$\tau_b(V) = \frac{170}{5e^{\frac{V+95.4}{10}} + e^{\frac{V+105.4}{8}}} + 10.7$$

These equations are, apart from the scaling factor  $q$ , the same as given by Mathews *et al.*<sup>39</sup> with 35.4 mV added to all voltages.

The kinetics of the  $I_h$  current were modelled by equations 11 and 12.

$$a_\infty(V) = \left(1 + e^{0.1536(V+73.97)}\right)^{-1} \quad (11, 12)$$

$$\tau_a(V) = 7 \cdot \frac{28.17 + 100.9e^{-\frac{(V+93.2)^2}{364.8}}}{3^{(39-32)/10}}$$

This is similar to the  $I_h$  current of Rothman and Manis<sup>58</sup>, but about three times slower. The cooperativity was set to  $m = 1$ , and the reversal potential was set to  $-50$  mV.

The synaptic conductance templates were the same as those used for conductance-clamp experiments in Fig. 2 ( $\tau_{EPSC} = 0.3$ ,  $\tau_{IPSC} = 1.5$  ms,  $n = 16$ ;  $\tau_{EPSC} = 0.5$  ms,  $n = 5$ ). Conductance-clamp-simulated voltage traces were fitted

using the following four parameters:  $V_{0.5}$  and  $q$  of  $K_{LTA}$  (Fig. 3b), and the peak conductances of  $I_h$  and  $K_{LTA}$  currents. These parameters were adjusted to fit the cell-specific PSP kinetics, resting potential and input resistance according to conductance-clamp measurements.

## References

- Couchman, K., Grothe, B. & Felmy, F. Medial superior olivary neurons receive surprisingly few excitatory and inhibitory inputs with balanced strength and short-term dynamics. *J. Neurosci.* **30**, 17111–17121 (2010).
- Klumpp, R. G. & Eady, H. R. Some measurements of interaural time difference thresholds. *J. Acoust. Soc. Am.* **28**, 859–860 (1956).
- Grothe, B., Pecka, M. & McAlpine, D. Mechanisms of sound localization in mammals. *Physiol. Rev.* **90**, 983–1012 (2010).
- Goldberg, J. M. & Brown, P. B. Response of binaural neurons of dog superior olivary complex to dichotic tonal stimuli: some physiological mechanisms of sound localization. *J. Neurophysiol.* **32**, 613–636 (1969).
- Yin, T. C. & Chan, J. C. Interaural time sensitivity in medial superior olive of cat. *J. Neurophysiol.* **64**, 465–488 (1990).
- Pecka, M., Brand, A., Behrend, O. & Grothe, B. Interaural time difference processing in the mammalian medial superior olive: the role of glycinergic inhibition. *J. Neurosci.* **28**, 6914–6925 (2008).
- Brand, A., Behrend, O., Marquardt, T., McAlpine, D. & Grothe, B. Precise inhibition is essential for microsecond interaural time difference coding. *Nature* **417**, 543–547 (2002).
- Van der Heijden, M. *et al.* Directional hearing by linear summation of binaural inputs at the medial superior olive. *Neuron* **78**, 936–948 (2013).
- Jeffress, L. A. A place theory of sound localization. *J. Comp. Physiol. Psychol.* **41**, 35–39 (1948).
- McAlpine, D., Jiang, D. & Palmer, A. R. A neural code for low-frequency sound localization in mammals. *Nat. Neurosci.* **4**, 396–401 (2001).
- Karino, S., Smith, P. H., Yin, T. C. T. & Joris, P. X. Axonal branching patterns as sources of delay in the mammalian auditory brainstem: a re-examination. *J. Neurosci.* **31**, 3016–3031 (2011).
- Van der Heijden, M., Louage, D. H. G. & Joris, P. X. Responses of auditory nerve and anteroventral cochlear nucleus fibers to broadband and narrowband noise: implications for the sensitivity to interaural delays. *J. Assoc. Res. Otolaryngol.* **12**, 485–502 (2011).
- Spitzer, M. W. & Semple, M. N. Neurons sensitive to interaural phase disparity in gerbil superior olive: diverse monaural and temporal response properties. *J. Neurophysiol.* **73**, 1668–1690 (1995).
- Jercog, P. E., Svirsksis, G., Kotak, V. C., Sanes, D. H. & Rinzel, J. Asymmetric excitatory synaptic dynamics underlie interaural time difference processing in the auditory system. *PLoS Biol.* **8**, e1000406 (2010).
- Zhou, Y., Carney, L. H. & Colburn, H. S. A model for interaural time difference sensitivity in the medial superior olive: interaction of excitatory and inhibitory synaptic inputs, channel dynamics, and cellular morphology. *J. Neurosci.* **25**, 3046–3058 (2005).
- Pena, J. L., Viète, S., Funabiki, K., Saberi, K. & Konishi, M. Cochlear and neural delays for coincidence detection in owls. *J. Neurosci.* **21**, 9455–9459 (2001).
- Leibold, C. & van Hemmen, J. L. Spiking neurons learning phase delays: how mammals may develop auditory time-difference sensitivity. *Phys. Rev. Lett.* **94**, 168102 (2005).
- McAlpine, D. & Grothe, B. Sound localization and delay lines—do mammals fit the model? *Trends Neurosci.* **26**, 347–350 (2003).
- Kadner, A. & Berrebi, A. S. Encoding of temporal features of auditory stimuli in the medial nucleus of the trapezoid body and superior paraolivary nucleus of the rat. *Neuroscience* **151**, 868–887 (2008).
- Magnusson, A. K., Kapfer, C., Grothe, B. & Koch, U. Maturation of glycinergic inhibition in the gerbil medial superior olive after hearing onset. *J. Physiol.* **568**, 497–512 (2005).
- Chirila, F. V., Rowland, K. C., Thompson, J. M. & Spirou, G. A. Development of gerbil medial superior olive: integration of temporally delayed excitation and inhibition at physiological temperature. *J. Physiol.* **584**, 167–190 (2007).
- Grothe, B. & Sanes, D. H. Bilateral inhibition by glycinergic afferents in the medial superior olive. *J. Neurophysiol.* **69**, 1192–1196 (1993).
- Grothe, B. & Sanes, D. H. Synaptic inhibition influences the temporal coding properties of medial superior olivary neurons: an in vitro study. *J. Neurosci.* **14**, 1701–1709 (1994).
- Leibold, C. Influence of inhibitory synaptic kinetics on the interaural time difference sensitivity in a linear model of binaural coincidence detection. *J. Acoust. Soc. Am.* **127**, 931–942 (2010).
- Lehnert, S. *et al.* Action potential generation in an anatomically constrained model of medial superior olive axons. *J. Neurosci.* **34**, 5370–5384 (2014).
- Roberts, M. T., Seeman, S. C. & Golding, N. L. A mechanistic understanding of the role of feedforward inhibition in the mammalian sound localization circuitry. *Neuron* **78**, 923–935 (2013).
- Portfors, C. V. & von Gersdorff, H. Macrocircuits for sound localization use leaky coincidence detectors and specialized synapses. *Neuron* **78**, 755–757 (2013).

28. Grothe, B. New roles for synaptic inhibition in sound localization. *Nat. Rev. Neurosci.* **4**, 540–550 (2003).
29. Joris, P. & Yin, T. C. T. A matter of time: internal delays in binaural processing. *Trends Neurosci.* **30**, 70–78 (2007).
30. Rautenberg, P. L., Grothe, B. & Felmy, F. Quantification of the three-dimensional morphology of coincidence detector neurons in the medial superior olive of gerbils during late postnatal development. *J. Comp. Neurol.* **517**, 385–396 (2009).
31. Kuwabara, N. & Zook, J. M. Projections to the medial superior olive from the medial and lateral nuclei of the trapezoid body in rodents and bats. *J. Comp. Neurol.* **324**, 522–538 (1992).
32. Scott, L. L., Mathews, P. J. & Golding, N. L. Posthearing developmental refinement of temporal processing in principal neurons of the medial superior olive. *J. Neurosci.* **25**, 7887–7895 (2005).
33. Borst, J. G. G. & Soria van Hoeve, J. The calyx of held synapse: from model synapse to auditory relay. *Annu. Rev. Physiol.* **74**, 199–224 (2012).
34. Joris, P. X., Carney, L. H., Smith, P. H. & Yin, T. C. Enhancement of neural synchronization in the anteroventral cochlear nucleus. I. Responses to tones at the characteristic frequency. *J. Neurophysiol.* **71**, 1022–1036 (1994).
35. Couchman, K., Grothe, B. & Felmy, F. Functional localization of neurotransmitter receptors and synaptic inputs to mature neurons of the medial superior olive. *J. Neurophysiol.* **107**, 1186–1198 (2012).
36. Kapfer, C., Seidl, A. H., Schweizer, H. & Grothe, B. Experience-dependent refinement of inhibitory inputs to auditory coincidence-detector neurons. *Nat. Neurosci.* **5**, 247–253 (2002).
37. Morest, D. K. The collateral system of the medial nucleus of the trapezoid body of the cat, its neuronal architecture and relation to the olivo-cochlear bundle. *Brain Res.* **9**, 288–311 (1968).
38. Mathews, P. J., Jercog, P. E., Rinzel, J., Scott, L. L. & Golding, N. L. Control of submillisecond synaptic timing in binaural coincidence detectors by K(v)1 channels. *Nat. Neurosci.* **13**, 601–609 (2010).
39. Baumann, V. J., Lehnert, S., Leibold, C. & Koch, U. Tonotopic organization of the hyperpolarization-activated current (I<sub>h</sub>) in the mammalian medial superior olive. *Front. Neural Circuits* **7**, 117 (2013).
40. Köppl, C. Phase locking to high frequencies in the auditory nerve and cochlear nucleus magno-cellularis of the barn owl, *Tyto alba*. *J. Neurosci.* **17**, 3312–3321 (1997).
41. Spirou, G. A., Rowland, K. C. & Berrebi, A. S. Ultrastructure of neurons and large synaptic terminals in the lateral nucleus of the trapezoid body of the cat. *J. Comp. Neurol.* **398**, 257–272 (1998).
42. Smith, P. H., Joris, P. X. & Yin, T. C. Projections of physiologically characterized spherical bushy cell axons from the cochlear nucleus of the cat: evidence for delay lines to the medial superior olive. *J. Comp. Neurol.* **331**, 245–260 (1993).
43. Stange, A. *et al.* Adaptation in sound localization: from GABA(B) receptor-mediated synaptic modulation to perception. *Nat. Neurosci.* **16**, 1840–1847 (2013).
44. Siveke, I., Leibold, C., Schiller, E. & Grothe, B. Adaptation of binaural processing in the adult brainstem induced by ambient noise. *J. Neurosci.* **32**, 462–473 (2012).
45. Park, T. J., Grothe, B., Pollak, G. D., Schuller, G. & Koch, U. Neural delays shape selectivity to interaural intensity differences in the lateral superior olive. *J. Neurosci.* **16**, 6554–6566 (1996).
46. Day, M. L. & Semple, M. N. Frequency-dependent interaural delays in the medial superior olive: implications for interaural cochlear delays. *J. Neurophysiol.* **106**, 1985–1999 (2011).
47. Hassfurth, B., Grothe, B. & Koch, U. The mammalian interaural time difference detection circuit is differentially controlled by GABAB receptors during development. *J. Neurosci.* **30**, 9715–9727 (2010).
48. Fischl, M. J., Combs, T. D., Klug, A., Grothe, B. & Burger, R. M. Modulation of synaptic input by GABAB receptors improves coincidence detection for computation of sound location. *J. Physiol.* **590**, 3047–3066 (2012).
49. Hyson, R. L., Reyes, A. D. & Rubel, E. W. A depolarizing inhibitory response to GABA in brainstem auditory neurons of the chick. *Brain Res.* **677**, 117–126 (1995).
50. Yang, L., Monsivais, P. & Rubel, E. W. The superior olivary nucleus and its influence on nucleus laminaris: a source of inhibitory feedback for coincidence detection in the avian auditory brainstem. *J. Neurosci.* **19**, 2313–2325 (1999).
51. Tang, Z.-Q., Dinh, E. H., Shi, W. & Lu, Y. Ambient GABA-activated tonic inhibition sharpens auditory coincidence detection via a depolarizing shunting mechanism. *J. Neurosci.* **31**, 6121–6131 (2011).
52. Köppl, C. Evolution of sound localisation in land vertebrates. *Curr. Biol.* **19**, R635–R639 (2009).
53. Yamada, R. *et al.* The cooperation of sustained and phasic inhibitions increases the contrast of ITD-tuning in low-frequency neurons of the chick nucleus laminaris. *J. Neurosci.* **33**, 3927–3938 (2013).
54. Tang, Z.-Q. & Lu, Y. Two GABAA responses with distinct kinetics in a sound localization circuit. *J. Physiol.* **590**, 3787–3805 (2012).
55. Kuba, H., Koyano, K. & Ohmori, H. Development of membrane conductance improves coincidence detection in the nucleus laminaris of the chicken. *J. Physiol.* **540**, 529–542 (2002).
56. Stotler, W. A. An experimental study of the cells and connections of the superior olivary complex of the cat. *J. Comp. Neurol.* **98**, 401–431 (1953).
57. Khurana, S. *et al.* An essential role for modulation of hyperpolarization-activated current in the development of binaural temporal precision. *J. Neurosci.* **32**, 2814–2823 (2012).
58. Rothman, J. S. & Manis, P. B. Kinetic analyses of three distinct potassium conductances in ventral cochlear nucleus neurons. *J. Neurophysiol.* **89**, 3083–3096 (2003).

## Acknowledgements

We wish to thank Michael Pecka, Nick Lesica and Michael Beierlein for their helpful comments on the manuscript. This work was supported by the German Science Foundation Collaborative Research Centre (CRC) 870 (to S.L., C.L., F.F. and B.G.), the Alexander von Humboldt Foundation (to M.H.M.), and the Elisabeth and Helmut Uhl Foundation (to F.F.).

## Author contributions

M.H.M. performed the electrophysiology experiments and analysis; S.L. generated the computational model; F.F., C.L. and B.G. provided intellectual guidance; and M.H.M., F.F., C.L. and B.G. wrote the manuscript.

## Additional information

**Supplementary Information** accompanies this paper at <http://www.nature.com/naturecommunications>

**Competing financial interests:** The authors declare no competing financial interests.

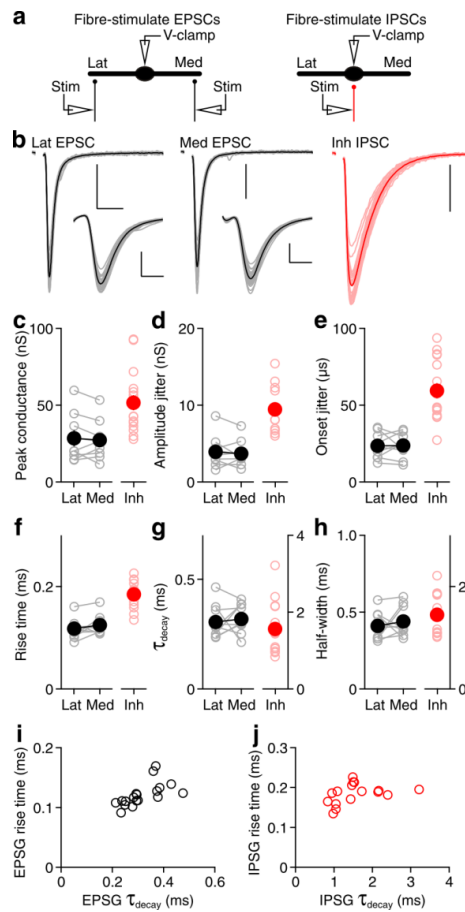
**Reprints and permission** information is available online at <http://npg.nature.com/reprintsandpermissions/>

**How to cite this article:** Myoga, M. H. *et al.* Glycinergic inhibition tunes coincidence detection in the auditory brainstem. *Nat. Commun.* **5**:3790 doi: 10.1038/ncomms4790 (2014).

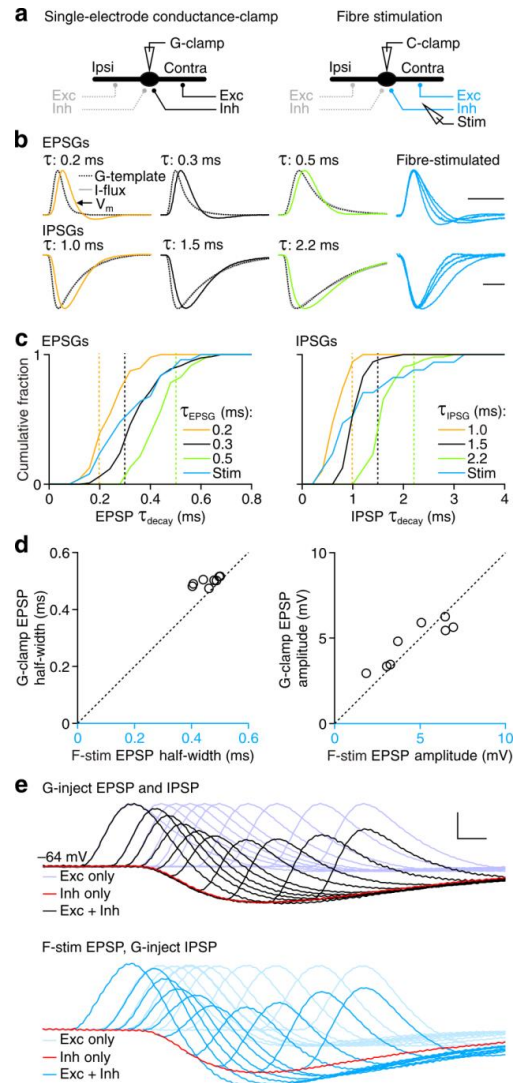


This work is licensed under a Creative Commons Attribution-NonCommercial-NoDerivs 3.0 Unported License. The images or other third party material in this article are included in the article's Creative Commons license, unless indicated otherwise in the credit line; if the material is not included under the Creative Commons license, users will need to obtain permission from the license holder to reproduce the material. To view a copy of this license, visit <http://creativecommons.org/licenses/by-nc-nd/3.0/>

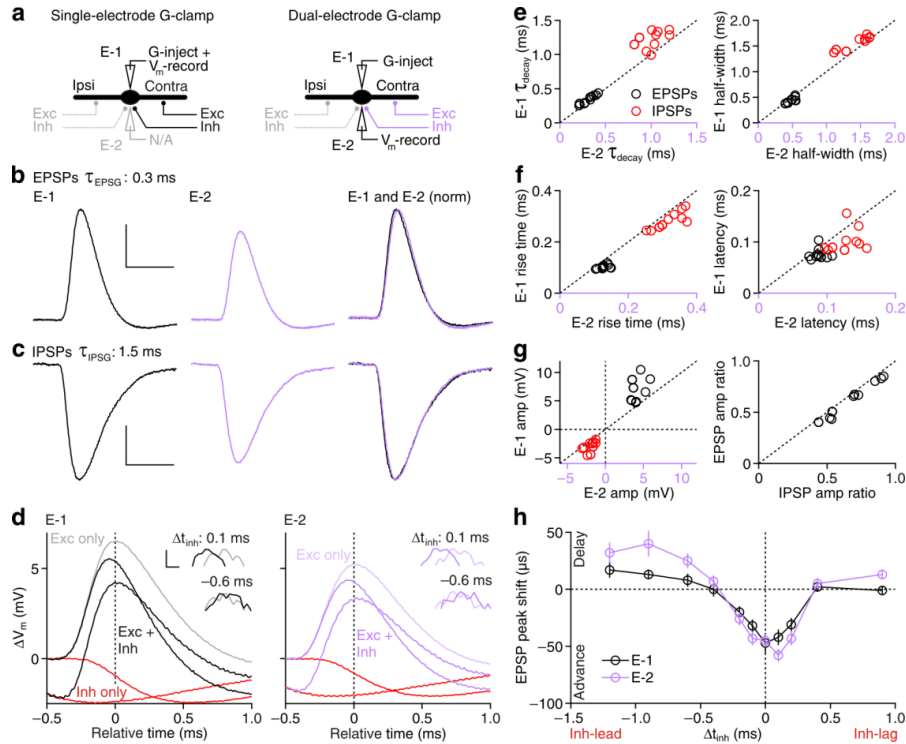




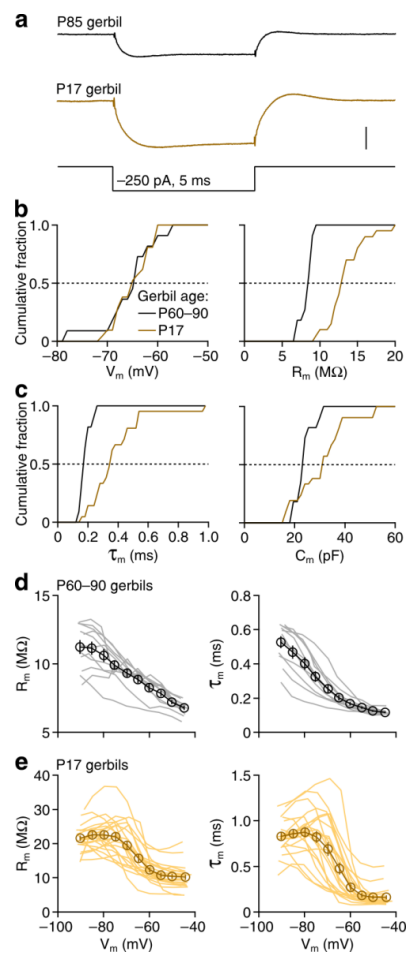
**Supplementary Figure 11 Properties of synaptic inputs to mature MSO neurons.** (a) Schematics of recording configurations for stimulating lateral (Lat, ipsilateral side) and medial (Med, contralateral side) excitatory inputs (left) and a mix of ipsilateral and contralateral inhibitory (Inh) inputs (right, see **Methods**). (b) Current traces for example recordings in response to single stimuli of lateral (left) and medial (centre) excitatory inputs (EPSCs) in one recording, as well as an inhibitory input (IPSCs, right) in a different recording.  $V_m$ :  $-75$  mV. Light and dark traces represent individual trials and the average response of 30 trials, respectively. Scale bar:  $0.5$  nA,  $2$  ms. Insets are zooms of the EPSCs. Inset scale bar:  $0.5$  nA,  $0.5$  ms. (c–h) Average ( $\pm$ s.e.m.) postsynaptic conductance waveforms, calculated from the reversal potential and peak current amplitude were analysed for lateral and medial excitatory inputs to the same neuron ( $n=9$  recordings,  $18$  inputs) and inhibitory inputs to different neurons ( $n=16$  recordings,  $16$  inputs) shown for individual recordings (light markers) and population averages (dark markers) as follows: peak conductance amplitude (c), peak amplitude jitter (d), conductance onset jitter (e),  $20$ – $80\%$  conductance rise-time (f), decay time constant ( $\tau_{\text{decay}}$ ) as determined by single exponential fitting (g), and conductance half-width (h). Note the additional vertical axis for IPSG analysis in g,h. (i,j) PSG rise time plotted against decay kinetics, shown for EPSGs (lateral and medial inputs pooled, i) and IPSGs (j). Although there was a greater diversity of decay kinetics, there was a small positive correlation between rise time and decay kinetics.



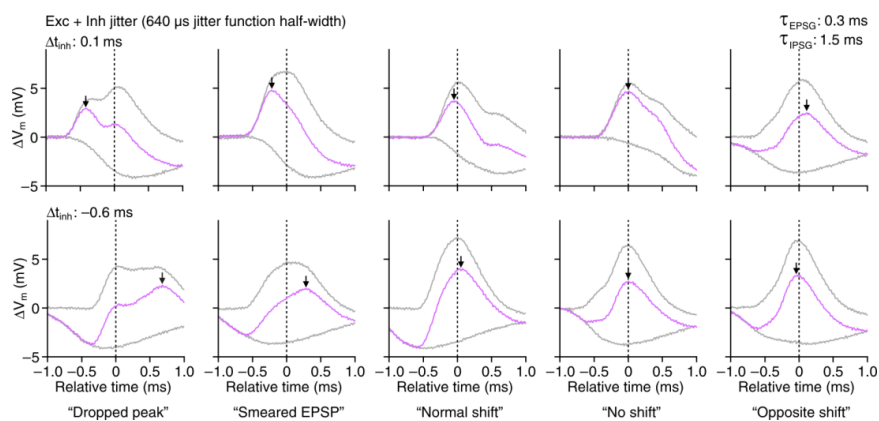
**Supplementary Figure 2 | Conductance-clamp simulation of EPSPs and IPSPs.** (a) Schematics of recording configurations for simulating PSPs with conductance-clamp (left) and fibre-stimulating PSPs in current-clamp (C-clamp, right). (b) Normalized traces for an example recording showing the transformation of selected excitatory (EPSP, top) and inhibitory (IPSP, bottom) conductance templates into EPSPs and IPSPs, respectively. The conductance command waveforms were measured in **Supplementary Figure 1** (G-command, dotted black traces) and were converted to a current injection command (I-flux, grey traces). Coloured traces indicate the membrane voltage ( $V_m$ ) from the current injection. Three EPSPs (top) and IPSPs (bottom) were selected from the population to represent fast [ $\tau_{EPSP}=0.2$  ms,  $\tau_{IPSP}=1.0$  ms (goldenrod)], average [ $\tau_{EPSP}=0.3$  ms,  $\tau_{IPSP}=1.5$  ms (black)], and slow [ $\tau_{EPSP}=0.5$  ms,  $\tau_{IPSP}=2.2$  ms (chartreuse)] decay kinetics and are used throughout the manuscript. Normalized example fibre-stimulated EPSPs and IPSPs from separate recordings are shown in blue. Scale bar: 1 ms. (c) Cumulative histograms of decay kinetics for PSPs generated by each EPSP (left,  $n=23-26$  recordings) and IPSP (right,  $n=24-30$  recordings) in the population. Dotted lines indicate the conductance command  $\tau_{decay}$ . The cumulative distribution of fibre-stimulated EPSPs ( $n=25$  recordings) and IPSPs ( $n=17$  recordings) are overlaid for comparison (blue). Note that the distributions of stimulated EPSPs and IPSPs cover the range of conductance-clamp-simulated events. (d) Comparison between conductance-clamp-simulated and fibre-stimulated EPSP half-width (left) and amplitude (right) measured in the same recording ( $n=7$  recordings, from **Fig. 1f-h**). (e) Voltage traces from the example recording in **Figure 1f,g** re-plotted, but aligned in time to the IPSP for conductance-clamp-simulated (top) and fibre-stimulated (bottom, stimulus artefacts removed) EPSPs. Although a larger afterhyperpolarization in fibre-stimulated EPSPs indicates a larger recruitment of voltage-gated potassium channels, this observation did not correspond to a significant influence on inhibition-enforced EPSP peak shifts (**Fig. 1h**). Scale bar: 5 mV, 0.5 ms.



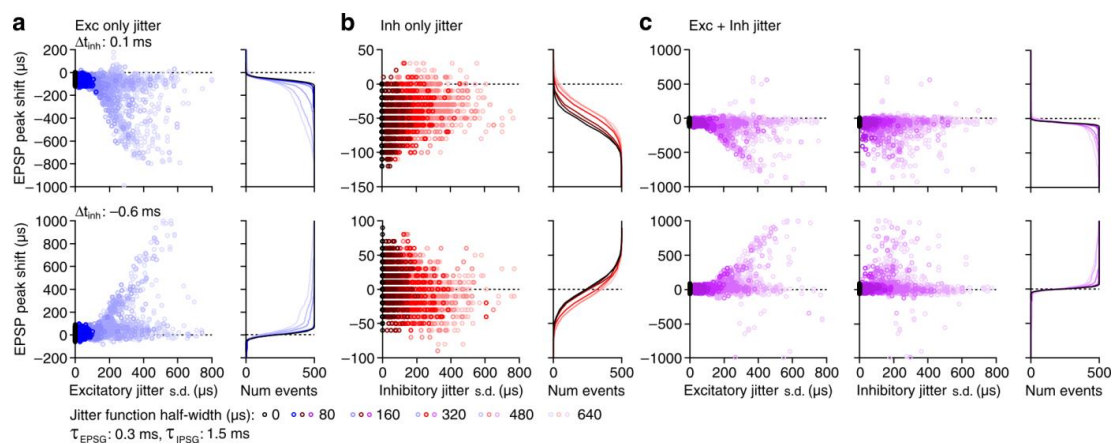
**Supplementary Figure 3| Single-electrode and dual-electrode conductance-clamp.** (a) Schematics of recording configurations for dual-electrode whole-cell recordings. In the same recording, the conductance was always delivered through one electrode (E-1), but the voltage was either measured ( $V_m$ -record) in the same electrode (left) or in the second electrode (E-2, right). (b,c) Voltage traces of EPSPs (b) and IPSPs (c) for an example recording, measured in E-1 (left) and E-2 (middle) and normalized (right).  $V_{rest}$ :  $-63$  mV. Scale bars: 2 mV, 1 ms (top) and 1 mV, 2 ms (bottom). (d) Voltage traces for the recording in b,c of inhibition-enforced EPSP peak shifts at timing conditions that advanced ( $\Delta t_{inh}=0.1$  ms) and delayed ( $\Delta t_{inh}=-0.6$  ms) EPSP peak timing, as recorded in E-1 (left) and E-2 (right). Insets are zooms of the peaks, aligned in amplitude. Inset scale bar: 0.2 mV, 50  $\mu$ s. (e-g) Analyses of EPSP (black) and IPSP (red) E-1 measurements plotted against E-2 measurements for the following parameters: (e) decay time constant (left) and half-width (right), (f) 20–80% rise time (left) and latency to 20% of peak amplitude (right), and (g) PSP amplitude (left). (right) The ratio of E-1:E-2 amplitude for EPSPs is plotted against IPSPs to indicate the linearity of the voltage drop across the electrodes. Note that although there was a consistent voltage drop, the kinetic profile was not altered. (h) Average ( $\pm$ s.e.m.) inhibition-enforced EPSP peak shifts plotted against  $\Delta t_{inh}$  for experiments as shown in d. For EPSP peak shifts recorded in E-1 and E-2,  $\Delta t_{inh}=0.1$  ms:  $-42\pm 7$  and  $-58\pm 6$   $\mu$ s, respectively ( $P=0.575$ ) and  $\Delta t_{inh}=-0.6$  ms:  $8\pm 6$  and  $25\pm 7$   $\mu$ s, respectively ( $P=0.485$ ). Two-way ANOVA,  $n=10$  comparisons from five recording pairs.



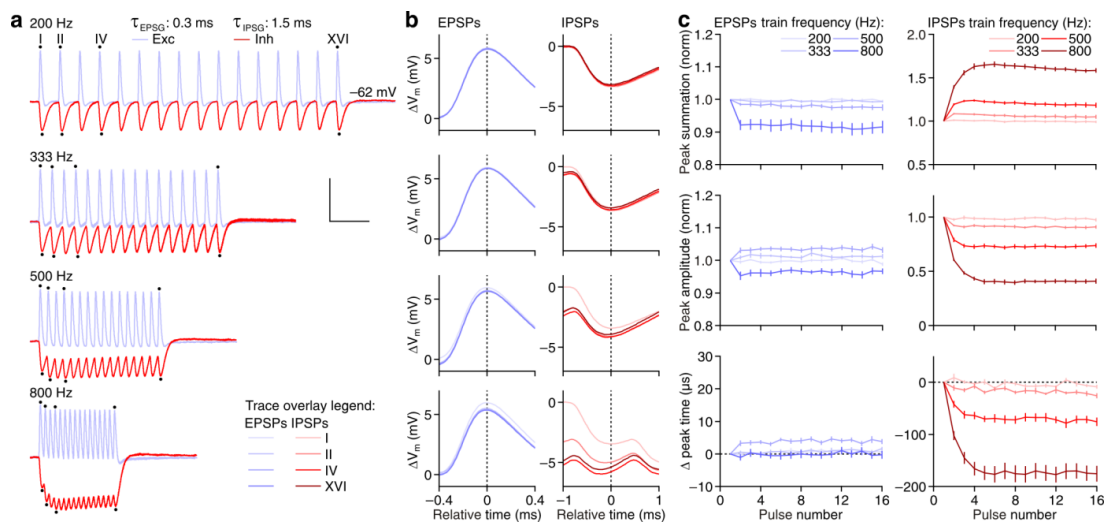
**Supplementary Figure 4| Intrinsic membrane properties of P60–90 and P17 MSO neurons. (a)** Voltage traces for example current-clamp recordings of MSO neurons from a P85 (top) and P17 (bottom) gerbil in response to a  $-250$  pA, 5 ms current step.  $V_{rest}$ :  $-65$  (P85) and  $-65$  mV (P17). Scale bar: 2 mV. **(b,c)** Cumulative histograms of resting membrane potential ( $V_m$ , **b**, left), membrane resistance ( $R_m$ , **b**, right), membrane time constant ( $\tau_m$ , **c**, left), and membrane capacitance ( $C_m$ , **c**, right) for P60–90 (black) and P17 (brown) gerbils. **(d,e)** The voltage-dependence of membrane input resistance (left) and time constant (right) for P60–90 gerbils ( $n=11$  recordings, **d**) and P17 gerbils ( $n=21$  recordings, **e**). Individual recordings and the population average ( $\pm$ s.e.m.) are presented as light lines and dark markers, respectively. Note that the input resistance of some neurons further increased between  $-80$  and  $-90$  mV in P60–90 gerbils, but had completely tapered off by  $-80$  mV in P17 gerbils.



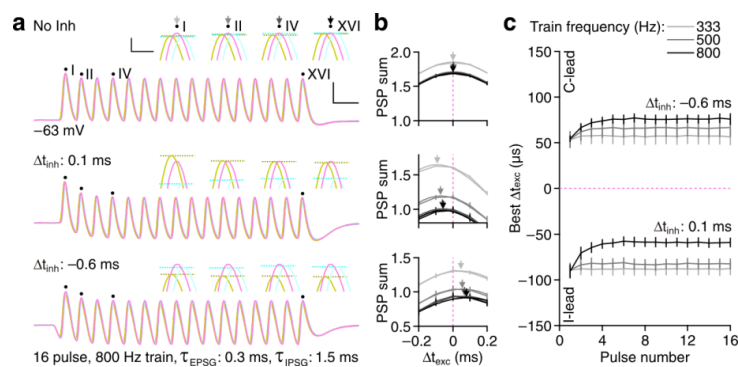
**Supplementary Figure 5I Example traces from individual jitter trials.** Traces from individual trials for the example recording in **Figure 5c,d**, shown for inhibitory timing conditions that generated an EPSP peak advance ( $\Delta t_{\text{inh}}=0.1$  ms, top) and delay ( $\Delta t_{\text{inh}}=-0.6$  ms, bottom), but with the excitatory plus inhibitory 640  $\mu\text{s}$  jitter function half-width (only voltage traces for the 320  $\mu\text{s}$  jitter function half-width are shown in **Fig. 5d**). Grey traces indicate the EPSP and IPSP alone, and magenta traces indicate the composite PSP. Arrows indicate peak shifts. Examples were chosen to illustrate the diversity of peak shifts observed with substantially jittered EPSPs and IPSPs. (from left to right) A “Dropped peak” occurred when inhibition hyperpolarized one of two distinguishable peaks. A “Smeared EPSP” was more sensitive to peak shifts, consistent with slower EPSPs (**Figs. 2c,e,i,j**, and **3g**). Stochastic timing could also produce a “Normal shift,” “No shift” at all, and even an “Opposite shift” of direction the timing condition normally enforced.  $V_{\text{rest}}: -64$  mV.



**Supplementary Figure 6I Analysis of all jitter trials.** All trials for experiments in **Figure 5** were pooled to illustrate the distribution of EPSP peak shifts for each excitatory (**a**), inhibitory (**b**), and excitatory plus inhibitory (**c**) jitter functions. Data are separated for inhibitory timing conditions that enforced an EPSP peak advance ( $\Delta t_{inh}=0.1$  ms, top) and delay ( $\Delta t_{inh}=-0.6$  ms, bottom). Data are colour-coded to indicate the amount of jitter for each condition (colour code is indicated below the plots). For each condition, EPSP peak shifts for individual trials are plotted against the s.d. of the four jittered input onset times for that specific trial (left). Note that for excitatory plus inhibitory jitter conditions (**c**) data are plotted independently against the excitatory jitter s.d. (left) as well as inhibitory jitter s.d. (centre). Cumulative histograms are also shown to illustrate the distributions of peak shifts for each jitter function half-width (**a–c**, right).



**Supplementary Figure 7I Analysis of independent EPSP and IPSP trains.** (a) Voltage traces for an example 16 pulse train recording of EPSPs ( $\tau_{EPSP}=0.3$  ms, blue) and IPSPs ( $\tau_{IPSP}=1.5$  ms, red) at (from top to bottom) 200, 333, 500, and 800 Hz. Dots and numerals above the traces indicate individual events that are further analysed in **b**. Scale bar: 5 mV, 10 ms. (b) The first, second, fourth, and 16<sup>th</sup> event for each train in **a** overlaid for EPSPs (left) and IPSPs (right), aligned to the predicted peak time based on the ISI. Traces are colour-coded to indicate their position in the train (colour code is indicated in **a**, bottom right). (c) Analysis of each event in EPSP (left) and IPSP (right) trains. (top) Absolute peak amplitude of each event is normalized to the first to indicate summation. At 800 Hz, EPSPs were depressed to  $92\pm 2\%$  at the 16<sup>th</sup> event. IPSP summation begins to develop at 333 Hz. At 800 Hz, IPSPs had summated to  $158\pm 2\%$  at the 16<sup>th</sup> event. (middle) Trough-to-peak amplitude of each event is normalized to the peak amplitude of the first event to indicate the relative voltage modulation throughout the train. At 800 Hz, modulation at the 16<sup>th</sup> EPSP was  $97\pm 1\%$  of the first. IPSP modulations began to deteriorate at frequencies above 333 Hz. At 800 Hz, modulation was reduced to  $41\pm 2\%$  at the 16<sup>th</sup> event. (bottom) Peak time relative to the ISI prediction is plotted to indicate changes in the relative timing of EPSPs and IPSPs. At 500 Hz, EPSPs were delayed by  $4\pm 1$   $\mu$ s at the 16<sup>th</sup> event. IPSPs during the train became advanced at frequencies above 333 Hz, thereby altering the effective  $\Delta t_{inh}$  during the train. At 800 Hz, IPSPs were advanced by  $176\pm 15$   $\mu$ s at the 16<sup>th</sup> event.  $n=8$  recordings.



**Supplementary Figure 8I Subthreshold PSP summation bias at high frequencies.** The protocol and analysis in **Figure 4b,d,h** was repeated, but for 16 pulse trains at 333, 500, and 800 Hz using the average speed EPSP and IPSP. **(a)** Voltage traces for an example recording at 800 Hz without inhibition (top) and with inhibition timed to bias PSP summation toward ipsilateral-leading ( $\Delta t_{inh}=0.1$  ms, middle) and contralateral-leading ( $\Delta t_{inh}=-0.6$  ms, bottom) excitation. Traces are colour-coded to reflect excitatory timing conditions as in **Figure 4a**. Dots and numerals above the traces indicate individual events zoomed in insets, as in **Figure 4b,d,f,h**. Scale bar: 5 mV, 2 ms. Inset scale bar: 0.5 mV, 0.1 ms. **(b)** Normalized PSP amplitudes plotted against  $\Delta t_{exc}$  and fitted with Gaussian functions for events indicated by the arrow greyscale tones of the insets in **a**. **(c)** Best  $\Delta t_{exc}$  ( $\pm$ s.d.) plotted against each event in the train at 333, 500, and 800 Hz. At high frequencies, Best  $\Delta t_{exc}$  changes during the train, similarly as for inhibition-enforced EPSP peak shifts (**Fig. 6**). At 800 Hz, the 16<sup>th</sup> event compared to the first,  $\Delta t_{inh}=0.1$  ms:  $-59\pm 5$  vs  $-90\pm 8$   $\mu$ s,  $P<0.001$ ;  $\Delta t_{inh}=-0.6$  ms:  $64\pm 5$  vs  $42\pm 4$   $\mu$ s,  $P<0.001$ , two-way ANOVA,  $n=8$  recordings. Note that the peak shifts during the train are consistent with an IPSP that becomes relatively advanced in time (**Supplementary Fig. 7**), altering the effective  $\Delta t_{inh}$  during the train.

## **4. Tonotopic organization of the hyperpolarization-activated current ( $I_h$ ) in the mammalian medial superior olive**

Published in Frontiers in Neural Circuits (2013).

**Reference:** Baumann VJ, Lehnert S, Leibold C, Koch U. Tonotopic organization of the hyperpolarization-activated current ( $I_h$ ) in the mammalian medial superior olive. Front Neural Circuits 7:117, 2013.

### **Author Contributions:**

List of authors: Veronika J Baumann (VJB), Simon Lehnert (SL), Christian Leibold (CL), Ursula Koch (UK).

Individual contributions: CL and UK, conception and design of the study; VJB performed the electrophysiological experiments and analyzed the data. VJB and UK interpreted the electrophysiological data. SL generated the computational model, performed the simulations and analyzed the resulting data, SL and CL interpreted the results of the modeling; VJB prepared all figures, except for Figure 7, which was prepared by SL. All authors contributed to the initial draft of the manuscript. All authors critically revised the manuscript. All authors approved the final version of the manuscript.





# Tonotopic organization of the hyperpolarization-activated current ( $I_h$ ) in the mammalian medial superior olive

Veronika J. Baumann<sup>1,2</sup>, Simon Lehnert<sup>1</sup>, Christian Leibold<sup>1</sup> and Ursula Koch<sup>1,2\*</sup>

<sup>1</sup> Division of Neurobiology, Department Biology II, Ludwig-Maximilians-Universität München, Munich, Germany

<sup>2</sup> Institute of Biology, Fachbereich Biologie, Chemie, Pharmazie, Freie Universität Berlin, Berlin, Germany

## Edited by:

Stephen R. Williams, University of Queensland, Australia

## Reviewed by:

Stephen R. Williams, University of Queensland, Australia

Deborah Baro, Georgia State University, USA

## \*Correspondence:

Ursula Koch, Institute of Biology, AG Neurophysiology, Freie Universität Berlin, Takustraße 6, 14195 Berlin, Germany  
e-mail: ursula.koch@fu-berlin.de

Neuronal membrane properties can largely vary even within distinct morphological cell classes. The mechanisms and functional consequences of this diversity, however, are little explored. In the medial superior olive (MSO), a brainstem nucleus that performs binaural coincidence detection, membrane properties at rest are largely governed by the hyperpolarization-activated inward current ( $I_h$ ) which enables the temporally precise integration of excitatory and inhibitory inputs. Here, we report that  $I_h$  density varies along the putative tonotopic axis of the MSO with  $I_h$  being largest in ventral, high-frequency (HF) processing neurons. Also  $I_h$  half-maximal activation voltage and time constant are differentially distributed such that  $I_h$  of the putative HF processing neurons activate faster and at more depolarized levels. Intracellular application of saturating concentrations of cyclic AMP removed the regional difference in hyperpolarization-activated cyclic nucleotide gated (HCN) channel activation, but not  $I_h$  density. Experimental data in conjunction with a computational model suggest that increased  $I_h$  levels are helpful in counteracting temporal summation of phase-locked inhibitory inputs which is particularly prominent in HF neurons.

**Keywords: HCN channel, medial superior olive, sound localization, tonotopy, coincidence detection**

## INTRODUCTION

Neuronal encoding of information in the time domain is enhanced by specific adjustments of membrane properties to the dynamics and temporal characteristics of the inputs (O'Donnell and Nolan, 2011). This is especially important for neurons in the medial superior olive (MSO), a binaural nucleus in the auditory brainstem that analyses interaural time differences (ITDs) of different input frequencies with extremely high temporal precision. This acuity primarily relies on the coincidence detection of precisely timed excitatory inputs from both ears onto MSO neurons (Grothe et al., 2010). In addition, two glycinergic inputs, originating from the ipsilateral medial and lateral nucleus of the trapezoid body, provide a prominent and phase-locked inhibition to MSO neurons, which fine-tunes the slope of the ITD function to occur within the physiological range (Brand et al., 2002; Pecka et al., 2008; Leibold, 2010). Equally important for the high temporal precision with which these neurons integrate their excitatory and inhibitory inputs are the large voltage-gated channels that are open around the resting potential of the membrane. Such exquisitely fine-tuned temporal processing crucially depends on the composition and the properties of voltage-gated ion channels. One of these voltage-gated currents is  $I_h$  (or HCN-current), a cationic current, which is activated upon hyperpolarization (Wahl-Schott and Biel, 2009).  $I_h$  is especially large in MSO neurons and is regulated by intrinsic modulators such as cAMP and PIP2 (Khurana et al., 2012). In addition, these neurons also express a large low voltage-activated  $K^+$ -channel ( $K_{LVA}$ ) that also opens around the resting potential (Barnes-Davies et al., 2004; Mathews et al., 2010; Khurana et al., 2011). The sophisticated

interplay between these channels reduces the input resistance and shortens the membrane time constant and thereby enhances the temporal acuity with which these neurons integrate their synaptic inputs (Barnes-Davies et al., 2004; Hassfurth et al., 2009; Mathews et al., 2010; Karcz et al., 2011; Khurana et al., 2011).

Like most nuclei in the auditory brainstem, the MSO is tonotopically organized: Low-frequency (LF) sounds are represented dorsally and higher frequencies are processed ventrally (Guinan et al., 1972; Müller, 1990). This spatial gradient of input frequencies enabled us to investigate the relationship between  $I_h$  properties, the integration of inhibitory inputs and its dependence on input frequency in the acute brain slice preparation using whole-cell patch-clamp recordings. We found that  $I_h$  is differentially distributed along the dorsoventral axis of the nucleus and that this spatial arrangement is paralleled by differential properties of synaptic integration.

Moreover, we explored the putative functional consequences of this relationship theoretically using a computational single-compartment model featuring HCN and  $K_{LVA}$  channels that was fitted to electrophysiological recordings: this model suggests that integration of inhibitory inputs in a frequency-dependent manner helps to maintain the neuron's membrane potential close to firing threshold.

## MATERIALS AND METHODS

All experiments were performed in accordance with the rules laid down by the EC Council Directive (86/89/ECC) and German animal welfare legislation and approved by the Regierung Oberbayern (AZ 55.2-1-54-2531-57-05, Bavaria, Germany).

All agents were purchased from Sigma-Aldrich (Germany) and Biotrend (Germany) unless otherwise indicated.

### SLICE PREPARATION

Patch-clamp recordings were performed from MSO neurons of gerbils (*Meriones unguiculatus*) at the age of postnatal day 17/18 (denoted P18) and 21/22/23 (denoted P22). The animals were decapitated under isoflurane anesthesia. The brain was removed in ice-cold oxygenated (95%  $O_2$ /5%  $CO_2$ ) sucrose replacement solution containing (in mM): 2.5 KCl, 1.25  $NaH_2PO_4$ , 26  $NaHCO_3$ , 0.25  $CaCl_2$ , 3  $MgCl_2$ , 12.5 glucose and 100 sucrose (pH 7.4). Transverse brainstem slices (180  $\mu m$ ) comprising the MSO were cut with a vibratome (VT1200S; Leica, Germany), incubated at 32°C for 15 min in oxygenated artificial cerebrospinal fluid (ACSF) containing (in mM) 125 NaCl, 2.5 KCl, 1.25  $NaH_2PO_4$ , 26  $NaHCO_3$ , 2  $CaCl_2$ , 1  $MgCl_2$  and 25 glucose and then maintained at room temperature. For recordings, slices were transferred to a recording chamber, which was perfused continuously with oxygenated ACSF at 32°C, and visualized with an upright microscope (Axioscope, Zeiss, Germany) using infrared-differential interference contrast optics.

### ELECTROPHYSIOLOGY

Current- and voltage-clamp recordings were made from visually identified MSO cells using a Multiclamp 700 A amplifier (Axon Instruments, USA) with standard electrode solution containing (in mM): 125 K-gluconate, 5 KCl, 10 HEPES, 1 EGTA, 2  $Na_2ATP$ , 2  $MgATP$ , 0.3  $Na_2GTP$  and 10 Na-phosphocreatine; adjusted to pH 7.25 with KOH. All experiments were performed at near-physiological temperature (32°C). Patch pipettes were pulled from borosilicate glass capillaries (BioMedical Instruments, Germany) on a DMZ Universal Puller (Zeitz Instruments, Germany). When filled with electrode solution, patch pipettes had a resistance of 2–4 M $\Omega$ . In some experiments Alexa-488 (100  $\mu M$ ) (Molecular Probes, Germany) was added to the electrode solution in order to verify the location of the neuron along the presumed tonotopic axis.

During voltage-clamp recordings, whole-cell capacitance was compensated and used as measure for cell surface. The series resistance (<10 M $\Omega$ ) was compensated to a residual of 2–2.5 M $\Omega$  and not allowed to change more than 20%. To isolate  $I_h$  pharmacologically we applied the following drugs (in mM): 1 3,4 diaminopyridine, 10 TEA-Cl, 0.2  $BaCl_2$ , 0.001 TTX, 0.05  $NiCl_2$ , 0.1  $CdCl_2$ , 0.01 DNQX, 0.025 DL-AP5 and 0.001 strychnine. NaCl was reduced to maintain iso-osmolarity.

We cannot exclude that our voltage-clamp recordings are distorted due to space-clamp errors which result in incomplete control of dendritic membrane potential. We minimize these errors by using an  $I_h$  isolation cocktail. Additionally, MSO neurons are anatomically compact cells with short dendrites (~150  $\mu m$ ) (Rautenberg et al., 2009) so that space-clamp errors should be small. Moreover, it is likely that the somatic voltage-clamp underestimates the HCN channel conductance.

During current-clamp experiments, the bridge-balance was adjusted to compensate for artifacts arising from electrode resistance. In some experiments,  $I_h$  was blocked with the HCN channel-selective inhibitor ZD7288 (20  $\mu M$ ).

Synaptic currents were evoked stimulating the slice with a glass electrode filled with 2 M NaCl. Stimulation electrodes were placed medial and lateral to the MSO. Inhibitory postsynaptic currents (IPSCs) were isolated by addition of 10  $\mu M$  DNQX and 25  $\mu M$  DL-AP5. IPSCs were evoked by brief pulses (100  $\mu s$ , intensities 10–40 V) triggered by an analogue stimulus isolation unit (BSI-950, Dagan Corporation, USA). Patch electrodes were filled with (in mM) 99 CsMeSO<sub>4</sub>, 41 CsCl, 10 HEPES, 10 EGTA, 2  $Na_2ATP$ , 2  $MgATP$ , 0.3  $Na_2GTP$ , 5 TEA-Cl and 1  $CaCl_2$ , and 5 QX314 to block postsynaptic  $Na^+$  channels; adjusted to pH 7.25 with CsOH.

In conductance-clamp experiments, simulated inhibitory conductances at 100 Hz were injected into MSO neurons with a SM-1 amplifier (Cambridge Conductance, UK). The simulated inhibitory conductance based upon recorded IPSCs (decay time: ~1.5 ms, 10–90% rise time: ~0.9 ms, reversal potential: -90 mV). The reversal potential was chosen according to data by Magnusson et al. (2005).

### DATA ACQUISITION AND ANALYSIS

Both voltage and current signals were low-pass filtered at 10 kHz with a four-pole Bessel filter and sampled at a rate of 20–50 kHz. Stimulus generation and recordings were done with pCLAMP (Axon Instruments, USA). All electrophysiological data were analysed in IGOR Pro (Wavemetrics, USA) using Neuromatic and custom-written routines, or in Clampfit (Axon Instruments, USA). A junction potential of -10.5 mV was corrected.

Steady-state current responses were evaluated at the end of the voltage pulse.  $I_h$  density was obtained by normalizing the amplitude to the compensated whole-cell capacitance. The voltage dependence of  $I_h$  activation was measured from the tail current. Values were fitted with a Boltzmann function to obtain the half-maximal activation voltage  $V_{0.5}$ :  $f(V) = 1/(1 + \exp[(V_{0.5} - V/k]))$ , where  $V$  is the membrane voltage and  $k$  is the slope factor. The membrane time constants were evaluated by fitting a double-exponential function to the current traces:  $f(t) = A_1 \exp(-t/\tau_{fast}) + A_2 \exp(-t/\tau_{slow})$  where  $\tau_{fast}$  and  $\tau_{slow}$  are the fast and slow time constant of  $I_h$  activation. The effective time constant of  $I_h$  activation,  $\tau_{weighted}$ , was calculated according to:  $\tau_{weighted} = (A_1 * \tau_{fast} + A_2 * \tau_{slow}) / (A_1 + A_2)$ .  $V_{0.5}$  and  $\tau_{weighted}$  were estimated for each experiment and averaged.

Input resistance was assessed from the peak hyperpolarization triggered by -100 pA current injection according to Ohm's law  $R = U/I$ . The membrane time constant was estimated from a single-exponential fit to the voltage response to -100 pA current injection.

To determine decay times of evoked IPSCs the decay was fitted with a single-exponential function. The time course of inhibitory postsynaptic potentials (IPSPs) was analyzed by averaging 30 traces, normalizing the resulting trace to the first IPSP amplitude, and then the 10–90% rise time, the 90–10% decay time and the half-width of the IPSPs were estimated.

Results are expressed as mean  $\pm$  standard error of the mean (SEM). Statistical significance was determined by a single-factor ANOVA test followed by a Scheffé's *post-hoc* test or by Student's unpaired *t*-test in Excel (Microsoft) with significance thresholds of  $P < 0.05$  (\*),  $P < 0.01$  (\*\*), and  $P < 0.001$  (\*\*\*)

## RECONSTRUCTION OF PATCHED NEURONS

Following recording, slices were fixed in 4% paraformaldehyde for 30 min. After extensive washing in phosphate-buffered saline (PBS) slices were exposed to blocking buffer (0.5% triton X-100/0.1% saponin/1% BSA in PBS) followed by incubation with the primary antibody (chicken anti-microtubule-associated protein 2, MAP2, 1:1000, Neuromics) in blocking buffer. Slices were then rinsed in washing buffer (0.5% Triton X-100/0.1% saponin in PBS) and immunoreactivity was visualized by incubating the slices with the Cy3-conjugated secondary antibody raised in donkey (1:300; Dianova). Finally, slices were washed and mounted on slides with vectashield mounting reagent (Vector Laboratories, USA).

## MODELING

A Hodgkin-Huxley-type single-compartment model was implemented separately for prototypic P22 dorsal and ventral cells. The temporal evolution of membrane potential  $V$  followed the differential equation

$$C_m \frac{dV}{dt} = - (I_h + I_{KLT} + I_{syn} + I_{leak})$$

with membrane capacitance  $C_m$  and Ohmic currents

$$I_x(V) = g_x a_x^m b_x^n (V - E_x).$$

The parameter  $g_x$  describes the peak conductance,  $a_x$  and  $b_x$  are the gating variables for activation and inactivation, respectively, and  $E_x$  denotes the reversal potential. The gating variables follow first order kinetics

$$\frac{da}{dt} = \frac{a_\infty - a}{\tau_a} \text{ and } \frac{db}{dt} = \frac{b_\infty - b}{\tau_b}$$

with the steady-state activation  $a/b_\infty$  and the voltage-dependent time constants  $\tau_a/b$ .

The low-threshold potassium channel (KLT) was modeled according to Mathews et al. (2010) with  $E_K = -90$  mV. The kinetics of the hyperpolarization-activated cation current ( $I_h$ ) was fitted to the data of voltage-clamp experiments from **Figure 5**, which resulted in the steady-state activation and the activation time constant (see **Figure 7A**)

$$a_\infty(V) = \left(1 + e^{0.1(V + 80.4)}\right)^{-1} \text{ and } \tau_a = 79 + 417e^{-(V + 61.5)^2/800}$$

for dorsal cells, and

$$a_\infty(V) = \left(1 + e^{0.095(V + 75.5)}\right)^{-1} \text{ and } \tau_a = 65 + 292e^{-(V + 62.5)^2/722}$$

for ventral cells, respectively ( $V$  in mV). Since HCN channels do not spontaneously inactivate,  $b$  was set to 1. As reversal potential we used  $E_h = -35$  mV.

The model has been adapted to the different mean values of the membrane properties of the ventral (HF) and dorsal (LF) population by using the following channel peak conductances (in nS/ $\mu\text{m}^2$ ):  $g_{KLT}^{\text{dorsal}} = 0.0531$ ,  $g_{HCN}^{\text{dorsal}} = 0.01025$ ,

$g_{KLT}^{\text{ventral}} = g_{KLT}^{\text{dorsal}} * 5.4$  and  $g_{HCN}^{\text{ventral}} = g_{HCN}^{\text{dorsal}} * 3.15$ . These settings yield a resting potential of around  $-60$  mV for both model types and input resistances of  $R_{in} = 23.94$  M $\Omega$  for the dorsal and  $R_{in} = 3.77$  M $\Omega$  for the ventral model corresponding to membrane time constants of  $\tau_m$  of 1.64 ms and 0.45 ms, respectively. Using a specific membrane capacitance of 1  $\mu\text{F}/\text{cm}^2$  these correspond to a modeled cell surface of 6839  $\mu\text{m}^2$  (dorsal) and 12064  $\mu\text{m}^2$  (ventral) with membrane capacities of 68.39 pF and 120.64 pF, respectively.

For both cell models the passive leak conductance was set to  $g_{leak} = 33.3$  fS/ $\mu\text{m}^2$  and the reversal potential was set to  $-70$  mV.

The fitting procedure described above implicates that the model parameters (specifically the HCN conductances) are adjusted according to our current-clamp data. This was done on purpose, since we assume the voltage-clamp data to be less accurate due to the above mentioned incomplete voltage-clamp control especially in the dendrites.

The inhibitory input to the model was implemented as a conductance with reversal potential of  $-90$  mV. The IPSP kinetics were fitted with a double-exponential ( $t$  in ms) to resemble measurements from Couchman et al. (2010):

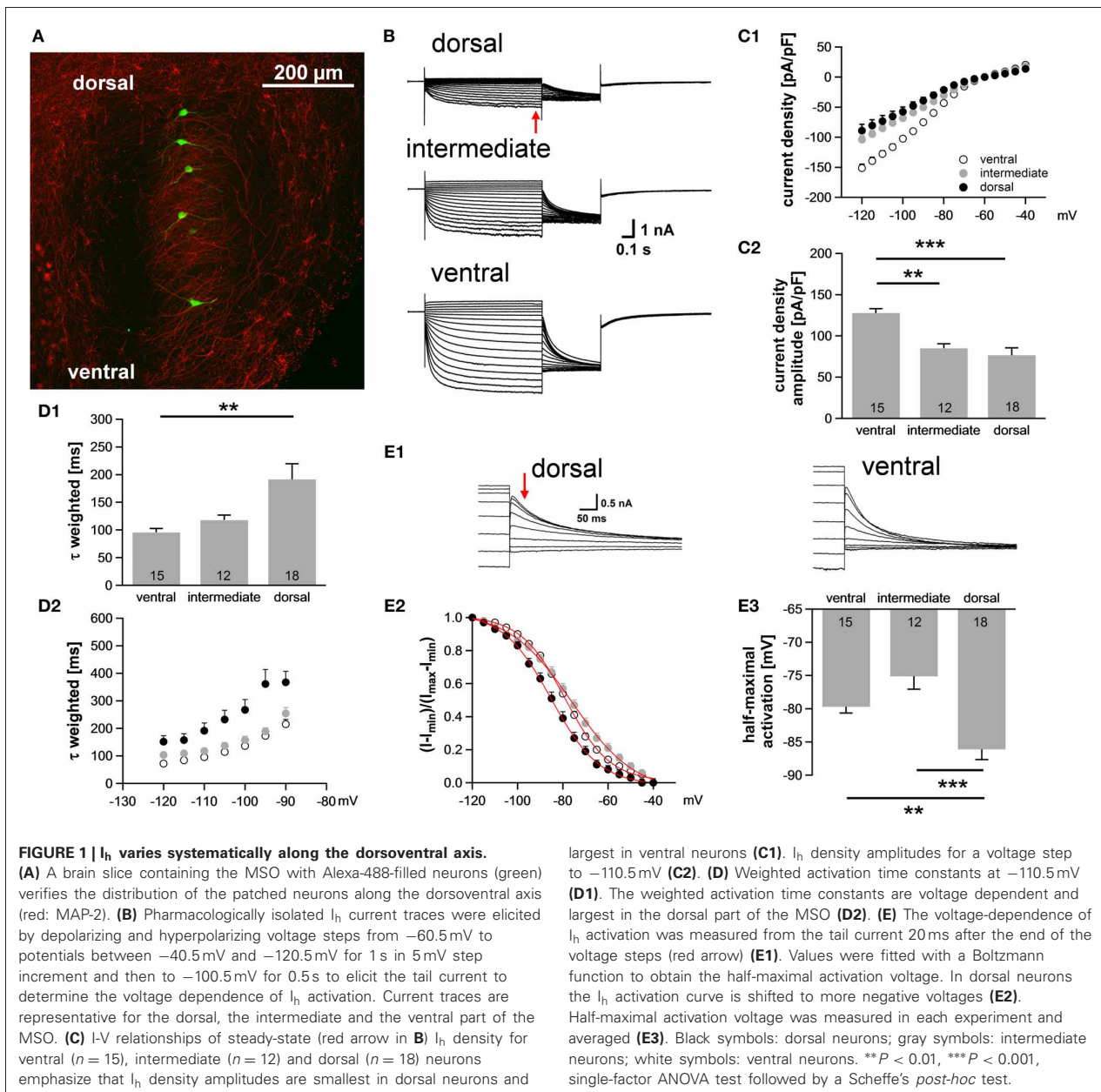
$$G(t) = g_{inh} \frac{(1 - e^{-t/0.4}) e^{-t/1.6}}{\max((1 - e^{-t/0.4}) e^{-t/1.6})}$$

For simulations to investigate the IPSP half-widths inhibitory 100 Hz input stimuli of 20.5 nS (dorsal) and 90 nS (ventral) were applied to the models to roughly fit the membrane potential deflection seen in the corresponding current clamp experiments. The stimulus train was kept up for 800 ms to show the influence of the slowly activating HCN current.

## RESULTS

### $I_h$ VARIES ALONG THE DORSOVENTRAL AXIS IN THE MSO

Neuronal processing in the auditory system is tonotopically organized such that frequencies are orderly represented across most auditory nuclei. In the MSO, low frequency sounds are supposed to be encoded in the dorsal part of the MSO and higher frequency sounds are presumably represented in the ventral part (Guinan et al., 1972). In general, best frequencies of MSO neurons are lower compared to neurons in the LSO, but can occasionally still be above 2 kHz (Pecka et al., 2008). Here, we investigated in a brain slice preparation of P18 gerbils the biophysical properties of MSO neurons along this putative tonotopic axis. The MSO was subdivided into three regions, a ventral region, which we refer to as high-frequency (HF), a dorsal region, which we refer to as low-frequency (LF) and an intermediate middle-frequency (MF) region. MSO neurons were identified on the basis of their bipolar shape and their arrangement in a parasagittal plane. In some experiments, 100  $\mu\text{M}$  Alexa-488 was included in the pipette solution to verify the visually determined location of the neurons along the dorsoventral axis (**Figure 1A**). The properties of  $I_h$  between the regions were analyzed using voltage-clamp experiments. In all cells hyperpolarizing voltage pulses triggered slowly activating, large inward currents.  $I_h$  amplitude was 57% larger in ventral (presumably HF) neurons compared with dorsal (presumably



LF) neurons [at  $-110.5$  mV: ventral:  $-3006 \pm 165$  pA; intermediate:  $-2388 \pm 123$  pA; dorsal:  $-1910 \pm 278$  pA; ANOVA:  $F_{(2, 42)} = 6.60$ ,  $P = 0.003$ ; **Figure 1B**]. Also,  $I_h$  density was significantly larger in the ventral part of the MSO compared with the dorsal and intermediate part [at  $-110.5$  mV: ventral:  $-127.7 \pm 5.3$  pA/pF; intermediate:  $-85.1 \pm 5.4$  pA/pF; dorsal:  $-73.4 \pm 9.3$  pA/pF; ANOVA:  $F_{(2, 42)} = 14.86$ ,  $P < 0.001$ ; **Figure 1C**]. Dorsal neurons not only exhibited the smallest  $I_h$  amplitude but also  $I_h$  that activated slowest. The calculated weighted activation time constant was two-fold larger in dorsal neurons compared with ventral neurons [at  $-110.5$  mV: ventral:  $95.6 \pm 7.0$  ms; intermediate:  $117.9 \pm 9.2$  ms; dorsal:  $191.3 \pm 28.1$  ms;

ANOVA:  $F_{(2, 42)} = 6.62$ ,  $P = 0.003$ ; **Figure 1D1**]. For all three regions, the weighted activation time constants were voltage-dependent with  $\tau_{\text{weighted}} = 72 \pm 5$  ms at  $-120.5$  mV increasing to  $\tau_{\text{weighted}} = 215 \pm 17$  ms at  $-90.5$  mV in the ventral part of the MSO (Student's paired  $t$ -test:  $P < 0.001$ ) and with  $\tau_{\text{weighted}} = 152 \pm 22$  ms at  $-120.5$  mV increasing to  $\tau_{\text{weighted}} = 367 \pm 40$  ms at  $-90.5$  mV in the dorsal part (Student's paired  $t$ -test:  $P < 0.001$ ) (**Figure 1D2**). Analyzing the amplitude of the tail current revealed that  $I_h$  voltage dependence was negatively shifted in dorsal neurons compared with ventral and intermediate neurons (**Figure 1E**). Consequently, the half-maximal activation voltage was most negative in dorsal neurons [ventral:  $-79 \pm$

1 mV; intermediate:  $-76 \pm 2$  mV; dorsal:  $-87 \pm 2$  mV; ANOVA:  $F_{(2, 42)} = 13.51, P < 0.001$ ; **Figure 1E**]. On average, our measurements are in line with recently published data (Khurana et al., 2012).

Taken together, we observed a large difference in  $I_h$  properties between the ventral and the dorsal part of the MSO. Dorsal neurons exhibited smaller  $I_h$  amplitude, slower activation kinetics and more negative half-maximal activation voltage as compared to ventral neurons.

**cAMP MODULATION OF  $I_h$  DIFFERS ALONG THE DORSOVENTRAL AXIS**

HCN channel properties depend largely on the intracellular concentration of cAMP. The extent by which cAMP is able to regulate the gating of HCN channels is determined by the HCN subunits (Wahl-Schott and Biel, 2009). HCN1, which is

less sensitive to cAMP, is the main subunit in MSO neurons (Koch et al., 2004; Khurana et al., 2012). Nevertheless, cAMP modulates the gating of HCN channels in the MSO probably due to a co-assembly of HCN1 and HCN4 to heteromeric HCN channels (Khurana et al., 2012). To test whether a cAMP-dependent modulation underlies the differences in  $I_h$  properties across the dorsoventral axis, we included  $25 \mu\text{M}$  cAMP in the pipette solution, which induces maximal cAMP modulation (Ludwig et al., 1998). As expected,  $I_h$  density amplitude was still significantly larger in ventral neurons compared with dorsal neurons (at  $-110.5$  mV: ventral:  $-99.9 \pm 6.6$  pA/pF; dorsal:  $-74.6 \pm 6.8$  pA/pF; Student's unpaired  $t$ -test,  $P = 0.014$ ; **Figures 2A,B**). Moreover, cAMP accelerated the activation kinetics (**Figures 2C,E**) and positively shifted the activation curves in the two regions such that the activation curves overlapped for all

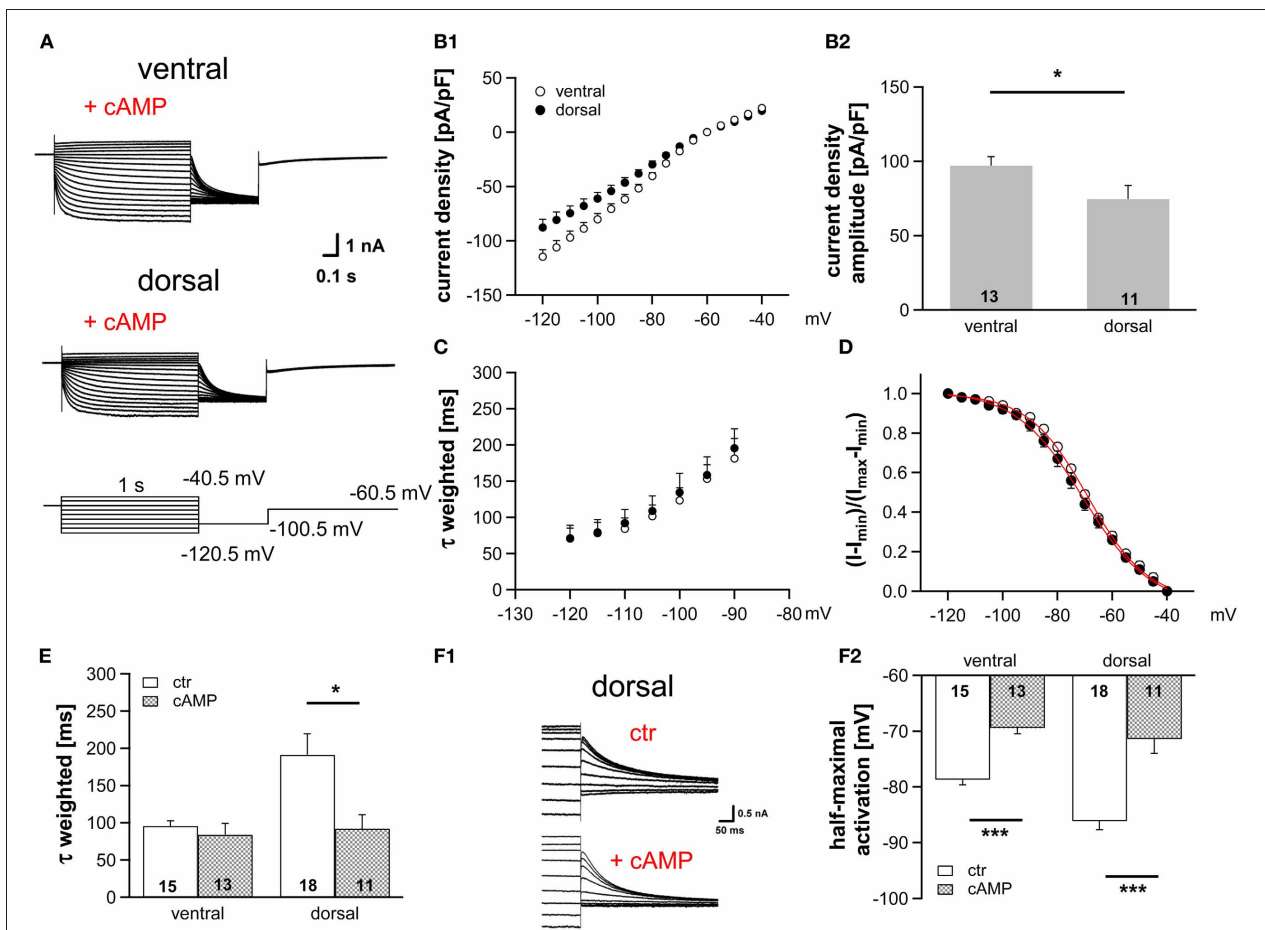


**FIGURE 2 | Modulation of  $I_h$  by cAMP differs along the dorsoventral axis.**

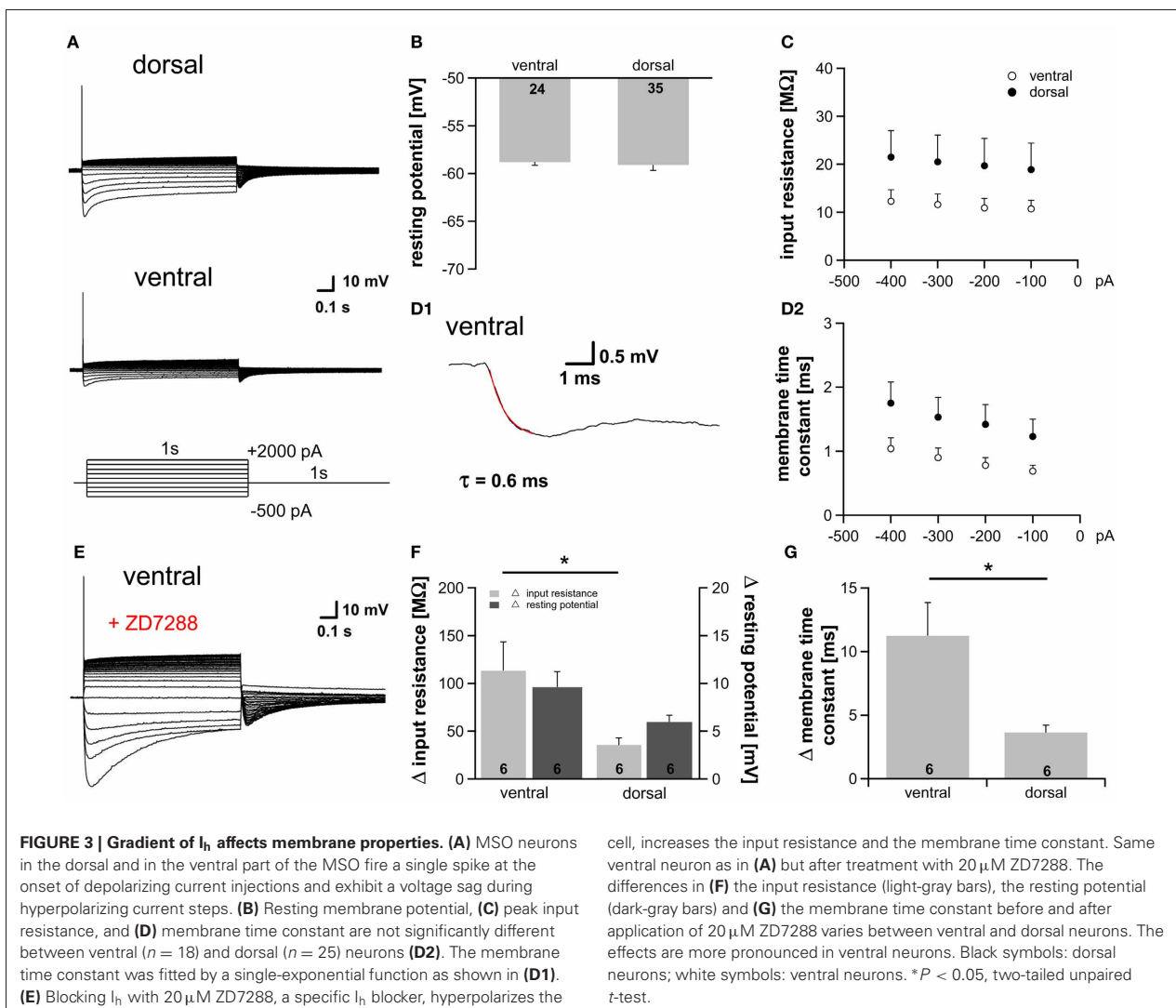
(A) Current responses to depolarizing and hyperpolarizing voltage steps were recorded from MSO neurons in the ventral and dorsal part of the MSO with  $25 \mu\text{M}$  cAMP in the pipette solution. (B)  $I_h$  density gradient persists in the presence of cAMP as illustrated by the current-voltage relationships for ventral ( $n = 13$ ) and dorsal ( $n = 11$ ) neurons (B1) and their  $I_h$  density amplitudes for a  $-110.5$  mV voltage step (B2). (C) The weighted activation time constants and (D), the voltage dependence of  $I_h$  activation overlap in the

presence of cAMP. Comparison of (E) the weighted activation time constants and (F) the half-maximal activation voltages in the absence and presence of  $25 \mu\text{M}$  cAMP reveals that dorsal neurons are more sensitive to cAMP than ventral neurons (F2). (F1) In the upper panel, tail currents were elicited using standard pipette solution. In the lower panel, a different, dorsal neuron is illustrated using standard pipette solution supplemented with  $25 \mu\text{M}$  cAMP. Black symbols: dorsal neurons; white symbols: ventral neurons. \* $P < 0.05$ , \*\*\* $P < 0.001$ , two-tailed, unpaired  $t$ -test.

neurons (Figures 2D,F), with the largest shift observed in dorsal neurons. Here,  $\tau_{\text{weighted}}$  decreased more than two-fold from  $191.3 \pm 28.1$  ms ( $n = 18$ ) to  $92.1 \pm 18.8$  ms ( $n = 11$ ) at  $110.5$  mV (Student's unpaired  $t$ -test:  $P = 0.012$ , Figure 2E) and half-maximal activation voltage increased by  $15$  mV from  $-87 \pm 2$  mV ( $n = 18$ ) to  $-72 \pm 3$  mV ( $n = 11$ ) (Student's unpaired  $t$ -test:  $P < 0.001$ ). In ventral neurons, no shift of  $\tau_{\text{weighted}}$  was observed and half-maximal activation voltage was only shifted by about  $9$  mV (from  $-79 \pm 1$  mV ( $n = 15$ ) to  $-70 \pm 1$  mV ( $n = 13$ ); Student's unpaired  $t$ -test:  $P < 0.001$ ; Figure 2F2). Hence, in the presence of saturating concentrations of cAMP the  $I_h$  activation kinetics and the dependence of  $I_h$  activation are similar whereas the dorsoventral difference of  $I_h$  amplitude persists. We, therefore, assume that the spatial arrangement of  $I_h$  density originates from differences in HCN channel density, whereas distinct basal intracellular cAMP levels cause the dorsoventral organization of the half-maximal activation voltage and the activation time constants.

### $I_h$ DIFFERENCES AFFECT MEMBRANE PROPERTIES

At rest a fraction of HCN channels is open in the dorsal part ( $\sim 9\%$ ) as well as in the ventral part ( $\sim 15\%$ ) of the MSO (Figure 1E2). This is in accordance with studies showing that  $I_h$  plays a critical role in determining the membrane properties in auditory brainstem neurons (Golding et al., 1995; Adam et al., 2001; Koch and Grothe, 2003; Golding and Oertel, 2012). To test whether the observed differences in  $I_h$  result in diverse membrane properties we applied depolarizing as well as hyperpolarizing current injections and recorded the voltage responses from 59 neurons. As previously reported, depolarization of the cells elicited a single action potential at the onset of the current injection, whereas hyperpolarization induced a depolarizing voltage sag, which can be attributed to the activation of HCN channels (Figure 3A, Magnusson et al., 2005; Scott et al., 2005). Despite the different open probability of HCN channels at rest, the resting potential was nearly identical in all parts of the MSO (ventral:  $-58.8 \pm 0.3$  mV; dorsal:  $-59.1 \pm$



0.6 mV; Student's unpaired  $t$ -test:  $P = 0.692$ ; **Figure 3B**) indicating compensatory gradient of outward currents. The peak input resistance and the membrane time constant did not differ significantly between the frequency regions, however, both showed clear trends. Ventral neurons tended to exhibit the lowest input resistance (at  $-100$  pA: ventral:  $10.7 \pm 1.8$  M $\Omega$ ; dorsal:  $18.9 \pm 5.5$  M $\Omega$ ; Student's unpaired  $t$ -test:  $P = 0.240$ ; **Figure 3C**). The membrane time constants were determined by fitting a single exponential function to the voltage traces (**Figure 3D1**). Ventral neurons tended to display the smallest membrane time constant (at  $-100$  pA: ventral:  $0.69 \pm 0.09$  ms; dorsal:  $1.23 \pm 0.27$  ms; Student's unpaired  $t$ -test:  $P = 0.108$ ; **Figure 3D2**). To solidify the observed trends, we repeated the experiments under bath application of  $20 \mu\text{M}$  ZD7288, which selectively inhibits HCN channels. In all neurons, irrespective of their location along the dorsoventral axis, HCN channel blockade hyperpolarized the membrane potential and increased the input resistance and the membrane time constant (**Figure 3E**). This difference in input resistance and membrane time constant between control condition and HCN channel blockade varied significantly between dorsal and ventral neurons (**Figures 3E,G**). Thus, the fractional contribution of  $I_h$  is significantly different between dorsal and ventral neurons. The effects of  $20 \mu\text{M}$  ZD7288 were more pronounced in the ventral part of the MSO (**Figures 3E,G**) demonstrating that  $I_h$  contribution to the membrane properties is larger in ventral neurons, and confirming that the distinct membrane properties along the dorsoventral axis can be attributed to the observed differences in  $I_h$ .

#### INTEGRATION OF SIMULATED INHIBITORY INPUTS VARIES ALONG THE DORSOVENTRAL AXIS

Assuming the MSO receives inputs that are phase-locked to the fine structure of a sound, the temporal summation of IPSP should vary between the regions, being most prominent in ventral neurons that presumably receive HF inputs and least in dorsal neurons that presumably receive LF inputs. This summation would lead to a stronger hyperpolarization in ventral neurons and thereby reduce their excitability. In this case the observed dorsoventral difference of  $I_h$ , which activates upon hyperpolarization, would compensate for the putatively increased hyperpolarization. To test our hypothesis, we simulated inhibitory inputs at 100 Hz and recorded the voltage responses from neurons in the dorsal and ventral part of the MSO. The simulated inhibitory conductance, which was injected into MSO neurons, was based upon recorded IPSCs (decay time:  $\sim 1.5$  ms, 10–90% rise time:  $\sim 0.9$  ms, amplitude:  $\sim 2$  nA). We also confirmed that decay times of IPSCs did not differ significantly between the regions (ventral:  $2.2 \pm 0.1$  ms,  $n = 9$ ; dorsal:  $2.7 \pm 0.3$  ms,  $n = 12$ ; Student's unpaired  $t$ -test:  $P = 0.215$ ; **Figure 4B**). These results are in line with data by Magnusson et al. (2005) showing that the IPSCs decay with time constants of around 1.5–3 ms in P18 gerbils (Magnusson et al., 2005).

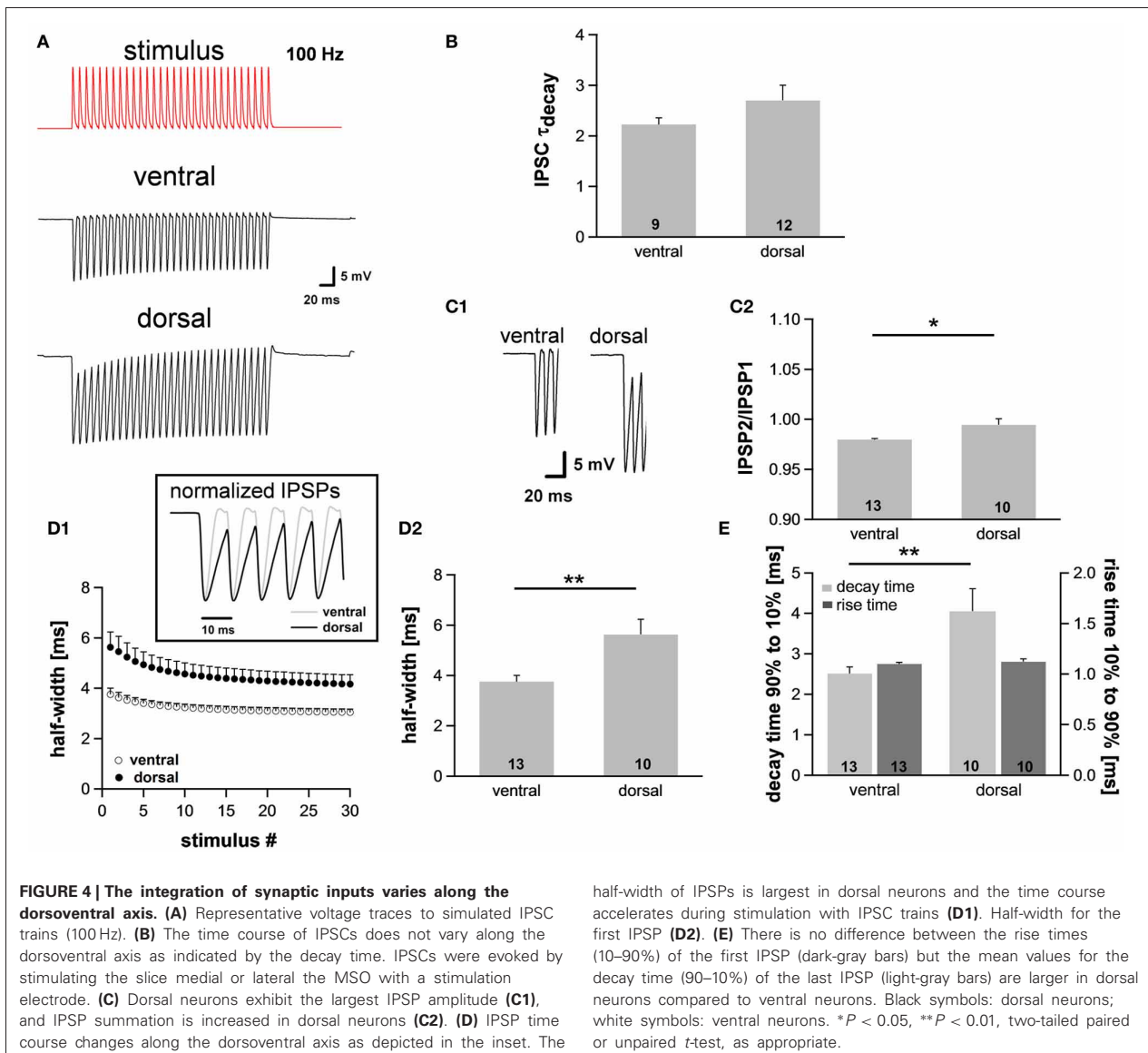
As expected, the membrane potential response to the simulated IPSC trains varied as a function of the neuron's location along the dorsoventral axis (**Figure 4A**). The amplitude of the evoked IPSPs was significantly larger in neurons of the dorsal part compared with neurons of the ventral part (ventral:

$18.3 \pm 0.8$  mV,  $n = 13$ ; dorsal:  $21.1 \pm 0.9$  mV,  $n = 10$ ; Student's unpaired  $t$ -test:  $P = 0.035$ ; **Figure 4C1**), also indicative for a larger input resistance in dorsal cells. Moreover, ventral neurons showed less summation than dorsal neurons (IPSP2/IPSP1: ventral:  $0.980 \pm 0.001$ ,  $n = 13$ ; dorsal:  $0.995 \pm 0.006$ ,  $n = 10$ ; Student's unpaired  $t$ -test:  $P = 0.011$ ; **Figure 4C2**). To facilitate comparison of the time course, IPSPs were amplitude-normalized (**Figure 4D1**, inset) illustrating that the time course of IPSPs changed along the dorsoventral axis. The half-width of the IPSPs was largest in the dorsal part of the MSO and became smaller in the ventral part (ventral:  $3.76 \pm 0.25$  ms,  $n = 13$ ; dorsal:  $5.63 \pm 0.60$  ms,  $n = 10$ ; Student's unpaired  $t$ -test:  $P = 0.005$ ; **Figure 4D**). There was no difference in 10–90% rise time of the first IPSP between the frequency regions (ventral:  $1.10 \pm 0.01$  ms; dorsal:  $1.12 \pm 0.03$  ms; Student's unpaired  $t$ -test:  $P = 0.450$ ; **Figure 4E**), but the 90–10% decay time of the last IPSP was smallest in the ventral part (ventral:  $2.51 \pm 0.16$  ms,  $n = 13$ ; dorsal:  $4.05 \pm 0.56$  ms,  $n = 10$ ; Student's unpaired  $t$ -test:  $P = 0.008$ ; **Figure 4E**). Taken together, the time course of the IPSPs is faster in ventral neurons than in dorsal neurons. We speculate that these effects can be attributed to the dorsoventral organization of  $I_h$  as HCN channels are the main channel subtypes that open upon hyperpolarization.

#### DORSOVENTRAL ORGANIZATION IS PRESERVED IN MORE MATURE ANIMALS

There is evidence that HCN channels in the superior olivary complex undergo drastic developmental changes during the first three postnatal weeks (Leao et al., 2006; Hassfurth et al., 2009; Khurana et al., 2012). To rule out that these developmental refinements have implications on the observed dorsoventral organization, we repeated experiments at P22, which is more at the end of this developmental period. Compared with P18, P22 MSO neurons exhibited slightly increased  $I_h$  amplitudes, the activation curves were shifted to more positive half-maximal activation voltages and the activation kinetics were accelerated (**Table 1**). Nevertheless,  $I_h$  still varied systematically along the dorsoventral axis, such that ventral neurons exhibited significantly larger  $I_h$  amplitudes than dorsal neurons (at  $-110.5$  mV: ventral:  $-3304 \pm 1.5$  pA,  $n = 8$ ; dorsal:  $-2560 \pm 238$  pA,  $n = 9$ ; Student's unpaired  $t$ -test:  $P = 0.019$ ; **Figure 5A**). Accordingly,  $I_h$  density also varied significantly (at  $-110.5$  mV: ventral:  $-122.4 \pm 9.6$  pA/pF,  $n = 8$ ; dorsal:  $-92.7 \pm 5.0$  pA/pF,  $n = 9$ ; Student's unpaired  $t$ -test:  $P = 0.012$ ; **Figure 5B**). Also, the activation kinetics and the half-maximal activation voltage differed between the ventral part and the dorsal part of the MSO ( $\tau_{\text{weighted}}$  at  $-110.5$  mV: ventral:  $78.0 \pm 3.6$  ms,  $n = 8$ ; dorsal:  $109.6 \pm 18.7$  ms,  $n = 9$ ; Student's unpaired  $t$ -test:  $P = 0.138$ ; **Figure 5C**;  $V_{0.5}$ : ventral:  $-76 \pm 3$  mV,  $n = 8$ ; dorsal:  $-81 \pm 2$  mV,  $n = 9$ ; Student's unpaired  $t$ -test:  $P = 0.160$ ; **Figure 5D**). In P22 animals,  $I_h$  still was organized along the dorsoventral axis. However, these differences between ventral and dorsal neurons were less pronounced as compared to P18 gerbils.

To assess to what extent these subtle changes in HCN properties between P18 and P22 neurons affect the neurons' membrane properties, we also measured voltage changes in response to current injections in P22 animals. During depolarization neurons in the ventral part of the MSO fired a single spike at the beginning



of the current injection (**Figure 6A**). In most ventral neurons, only for strong hyperpolarizing current injections the depolarizing voltage sag was obvious which is due to the extremely large  $I_h$ . This is also reflected in the very low input resistance (at  $-100$  pA: ventral:  $3.7 \pm 0.7$  M $\Omega$ ,  $n = 10$ ; dorsal:  $24.0 \pm 6.4$  M $\Omega$ ,  $n = 12$ ; Student's unpaired  $t$ -test:  $P = 0.016$ ; **Figure 6B**) and in the very small time constant of ventral neurons (at  $-100$  pA: ventral:  $0.45 \pm 0.07$  ms,  $n = 10$ ; dorsal:  $1.64 \pm 0.45$ ,  $n = 12$ ; Student's unpaired  $t$ -test:  $P = 0.047$ ; **Figure 6C**). Compared with P18 gerbils, the differences in the membrane time constant and in the input resistance between ventral and dorsal neurons were larger which resulted in significant differences along the dorsoventral axis (**Figures 6B,C; Table 1**).

We evaluated the integration of inhibitory postsynaptic inputs by injecting currents with stimulus amplitudes adjusted to evoke

physiological IPSPs of similar sizes ( $-8.1 \pm 0.3$  mV in the ventral part,  $n = 10$ , and  $-8.4 \pm 0.3$  mV in the dorsal part of the MSO,  $n = 12$ ; Student's unpaired  $t$ -test:  $P = 0.493$ ). Similar to P18, the voltage response to the simulated IPSC trains varied along the dorsoventral axis. The half-width of the first IPSP (ventral:  $2.73 \pm 0.06$  ms,  $n = 10$ ; dorsal:  $4.29 \pm 0.51$  ms,  $n = 13$ ; Student's unpaired  $t$ -test:  $P = 0.014$ ; **Figure 6D**), the 10–90% rise time of the first IPSP (ventral:  $1.14 \pm 0.03$  ms,  $n = 10$ ; dorsal:  $1.37 \pm 0.07$  ms,  $n = 6$ ; Student's unpaired  $t$ -test:  $P = 0.007$ ; **Figure 6E**) as well as the 90–10% decay time of the last IPSP (ventral:  $1.84 \pm 0.08$  ms,  $n = 10$ ; dorsal:  $3.08 \pm 0.39$  ms,  $n = 13$ ;  $P = 0.013$ ; **Figure 6E**) were largest in the dorsal part of the MSO and became smaller in the ventral part. By comparing the time course of P18 and P22 neurons (**Figure 6F**, example for ventral neurons) we can demonstrate that consistent with an increase

**Table 1 | Summary of HCN channel properties, membrane properties and synaptic properties of dorsal and ventral neurons for P18 and P22.**

	P18			P22		
	Ventral	Dorsal	<i>P</i>	Ventral	Dorsal	<i>P</i>
<b>HCN CHANNEL PROPERTIES (AT -110.5 mV)</b>						
Current [pA]	-3006 ± 165 (15)	-1909 ± 277 (18)	**	-3303 ± 134 (8)	-2559 ± 238 (9)	*
Current density [pA/pF]	-127.7 ± 5.3 (15)	-73.4 ± 9.3 (18)	***	122.4 ± 4.9 (6)	92.7 ± 5.0 (9)	*
Half-maximal activation voltage [mV]	-79 ± 1 (15)	-87 ± 2 (18)	**	-76 ± 3 (8)	-81 ± 2 (9)	n.s.
$\tau_{\text{weighted}}$ [ms]	95.6 ± 7.0 (15)	191.3 ± 28.1 (18)	**	78.0 ± 3.6 (8)	109.6 ± 18.7 (9)	n.s.
<b>MEMBRANE PROPERTIES (AT -100 pA)</b>						
Resting potential [mV]	-58.8 ± 0.3 (24)	-59.1 ± 0.6 (35)	n.s.	-60.0 ± 0.7 (10)	-60.1 ± 0.9 (12)	n.s.
Input resistance [M $\Omega$ ]	10.7 ± 1.8 (24)	18.9 ± 5.5 (35)	n.s.	3.7 ± 7.0 (10)	24.0 ± 6.4 (12)	*
Membrane time constant [ms]	0.69 ± 0.09 (24)	1.23 ± 0.27 (35)	n.s.	0.45 ± 0.07 (10)	1.64 ± 0.45 (12)	*
<b>SYNAPTIC PROPERTIES</b>						
IPSP half-width [ms]	3.76 ± 0.25 (13)	5.63 ± 0.60 (10)	**	2.72 ± 0.06 (10)	4.29 ± 0.51 (13)	*
Rise time 10–90% [ms]	1.10 ± 0.01 (13)	1.12 ± 0.03 (10)	n.s.	1.14 ± 0.03 (10)	1.37 ± 0.07 (13)	*
Decay time 90–10% [ms]	2.51 ± 0.16 (13)	4.05 ± 0.56 (10)	**	1.84 ± 0.08 (10)	3.08 ± 0.39 (13)	**

Values are mean ± SEM. The level of significance between ventral and dorsal was determined by using Student's unpaired *t*-test except for HCN channel properties of P18, where Scheffe's post-hoc test was employed following a single-factor ANOVA test (\**P* < 0.05, \*\**P* < 0.01, \*\*\**P* < 0.001, n.s. not significant). The *n*-values for each group are stated in brackets.

in  $I_h$  the half-width of the IPSPs is decreased in P22 neurons (Figure 6G). This emphasizes our hypothesis that  $I_h$  accelerates the time course of the IPSP and thereby decreases the temporal summation of IPSP. In addition,  $I_h$  compensates the summated hyperpolarization induced by the temporal summation of HF inhibitory inputs.

Taken together, these data provide evidence that also in mature animals the integration of synaptic inputs varies as a function of the neuron's location along the dorsoventral axis and that a tonotopic organization of  $I_h$  may at least partially account for the observed gradient in synaptic integration.

#### TONOTOPIC ORGANIZATION OF $I_h$ ACCOUNTS FOR THE DORSOVENTRAL DIFFERENCES IN SYNAPTIC INTEGRATION

To gain further mechanistic understanding and to assess the functional consequences of the dorsoventral  $I_h$  gradient in a computational model of a MSO cell, we first fitted activation profiles and channel time constants of  $I_h$  (from Figure 5) as described in the Materials and Methods section (Figure 7A). In addition to  $I_h$ , the model also included a low-voltage activated potassium current  $I_{K-LVA}$  to counteract  $I_h$  induced depolarization (Svirskis et al., 2002; see Materials and Methods). The peak conductances of  $I_h$  and  $I_{K-LVA}$  were used as free parameters to adjust the neuron models to a given input resistance and resting potential. Whereas the former was taken to be 3.77 M $\Omega$  for ventral (putative HF) neurons and 23.94 M $\Omega$  for dorsal (putative LF) neurons, the latter was assumed identical (-60 mV) in both populations.

We first validated our models by reproducing the current clamp experiments from Figure 6F (Figures 7B,C). Applying a stimulus of 100 Hz, we measured the half-width of the inhibitory potentials for cell models with both dorsal and ventral characteristics. The simulated IPSP half-widths are in very good agreement with the experimental data.

Following the idea that the dorsoventral differences parallel the tonotopic axis, we simulated the response of the model neuron to periodic inhibitory inputs with different frequencies (Figure 7D). The kinetics of the individual IPSPs was modeled to fit those measured experimentally (Couchman et al., 2010 and Materials and Methods). The decay constant  $\tau = 1.6$  ms of these IPSPs is so slow that there is temporal summation of the IPSPs, which produces a significant hyperpolarizing voltage offset (dark lines in Figure 7D). This offset increased for higher stimulation frequencies (200 Hz vs. 600 Hz in the example of Figure 7D). The increase of the hyperpolarizing voltage offset for HF inputs can, however, be mitigated, if we assume that only the ventral neurons process HF inputs: In those neurons this offset is smaller because of the lower input resistance that results from larger  $I_h$  and  $I_{K-LVA}$  conductances (Figure 7D).

The kinetics of  $I_h$  are much slower than the time constants that are typical for fast auditory processing. Therefore,  $I_h$  is generally assumed not to be suited to directly interact with neuronal processing of sound information on a fast time scale. However, the interplay between  $I_h$  and  $I_{K-LVA}$  may play an important role in temporal sharpening of the PSPs (Khurana et al., 2011). In contrast to  $I_h$ , the  $I_{K-LVA}$  does possess fast kinetics and thus has been proposed to contribute to fast temporal processing of MSO neurons in several studies (Svirskis et al., 2002; Jercog et al., 2010). To specifically evaluate the interaction between  $I_h$  and  $I_{K-LVA}$  channel kinetics in the present context of IPSP trains, we also simulated a model in which the  $I_{K-LVA}$  kinetics had been slowed down such that the kinetics were comparable to the  $I_h$  kinetics, while leaving the input resistance unchanged. Comparing both models (fast  $I_{K-LVA}$  kinetics, Figure 7C and slow  $I_{K-LVA}$  kinetics, Figure 7E) we found a clear effect on temporal precision as measured by an increase in IPSP half-width. This increase was stronger for the model of the ventral MSO neuron

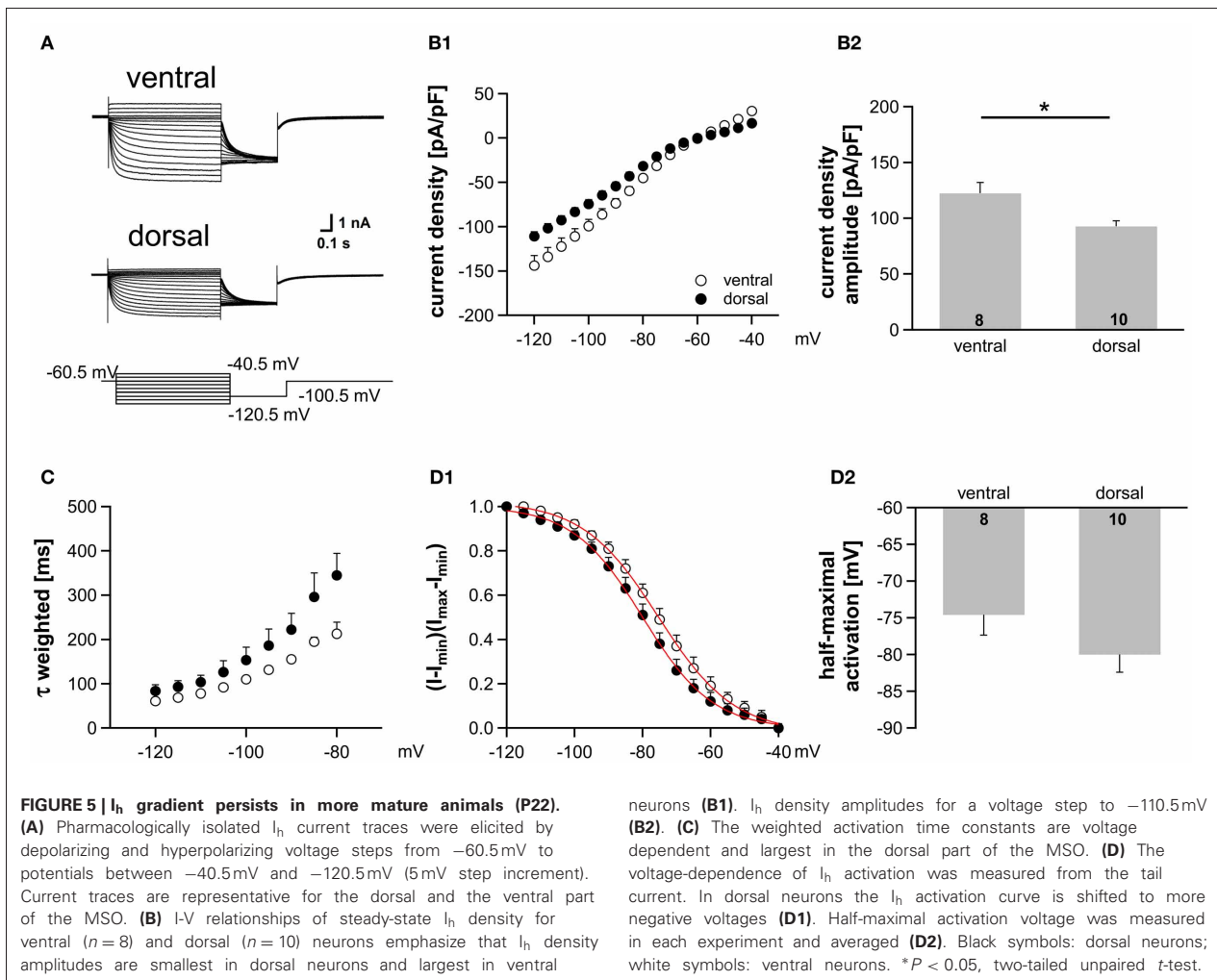


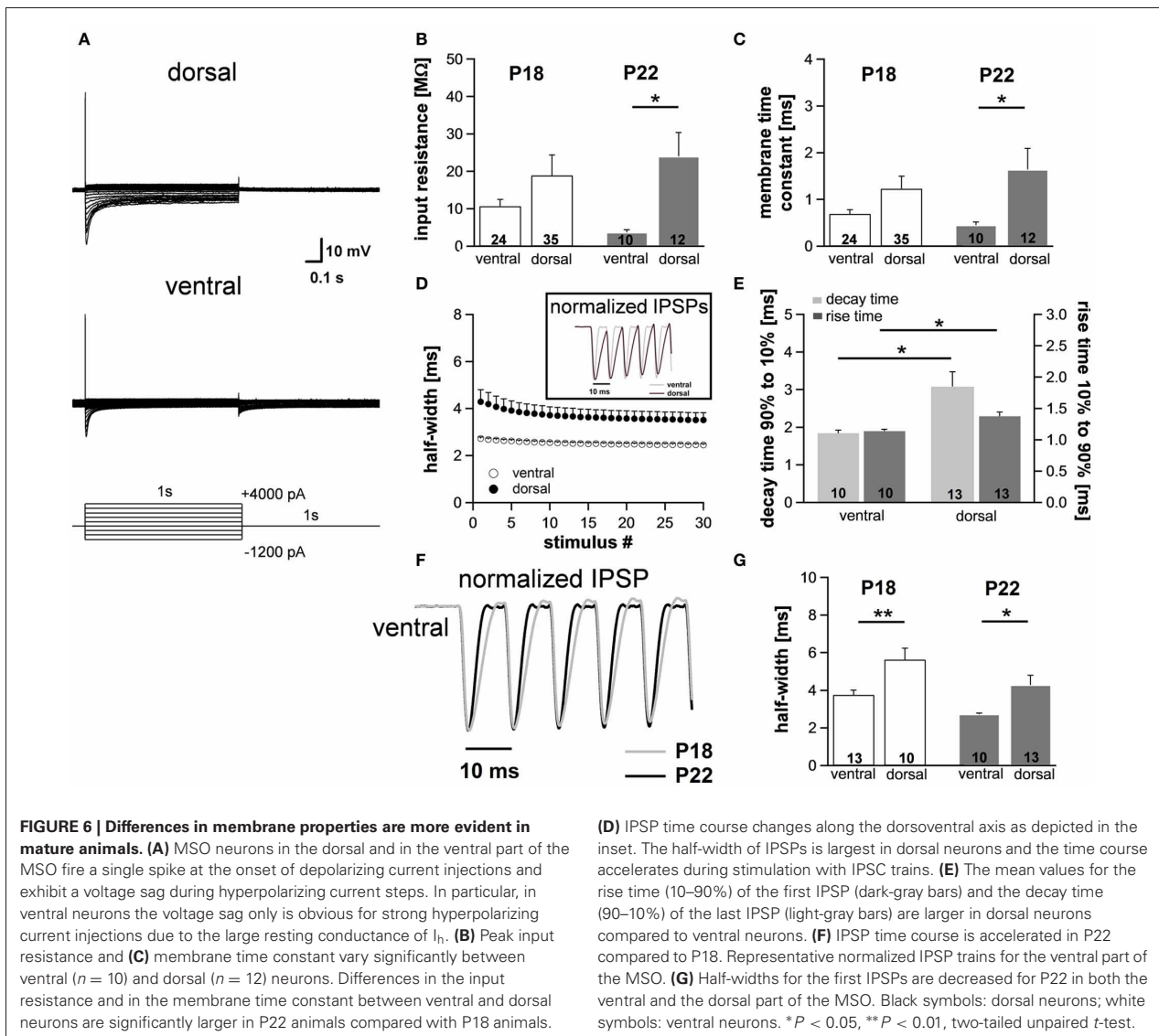
(Figure 7E), i.e., a putative HF processing neuron, although the input resistance was the same for both  $I_{K-LVA}$  kinetics. This shows that for high frequencies neurons with large  $I_h$  the temporal precision of the hyperpolarizing IPSPs is considerably enhanced by the active properties of the fast  $K_{LVA}$  channels, whereas for low frequency neurons this temporal integration is mostly explained by the differences in input resistance. Mechanistically, the  $I_h$ -dependent sharpening of IPSPs can be understood as follows: During the hyperpolarizing flank of the IPSPs the  $I_{K-LVA}$  channels – which are open at rest – close very rapidly and thereby effectively set a new equilibrium potential of the whole cell at a depolarized level close to the reversal of  $I_h$ . The resulting huge driving force massively speeds up the depolarizing flank of the IPSP and thereby accounts for the temporal sharpening. As the membrane potential approaches the old equilibrium potential, the  $K_{LVA}$  channels quickly open again and they restore the original equilibrium potential with only little overshoot as witnessed by the small amplitude of the voltage fluctuation after the IPSPs in Figure 7C. To test the above hypothesis, we conducted simulations with different reversal potentials of  $I_h$ . As

expected, a reduction of the driving force broadened the IPSPs (Figures 7E,G).

In summary, we conclude that fast  $K_{LVA}$  channels in interaction with  $I_h$  may predominantly sharpen the IPSPs (particularly in HF neurons with large  $I_h$ ), whereas  $I_h$  in MSO neurons alone balances out the hyperpolarizing voltage offset induced by the temporal summation of phase-locked inhibitory synaptic currents.

## DISCUSSION

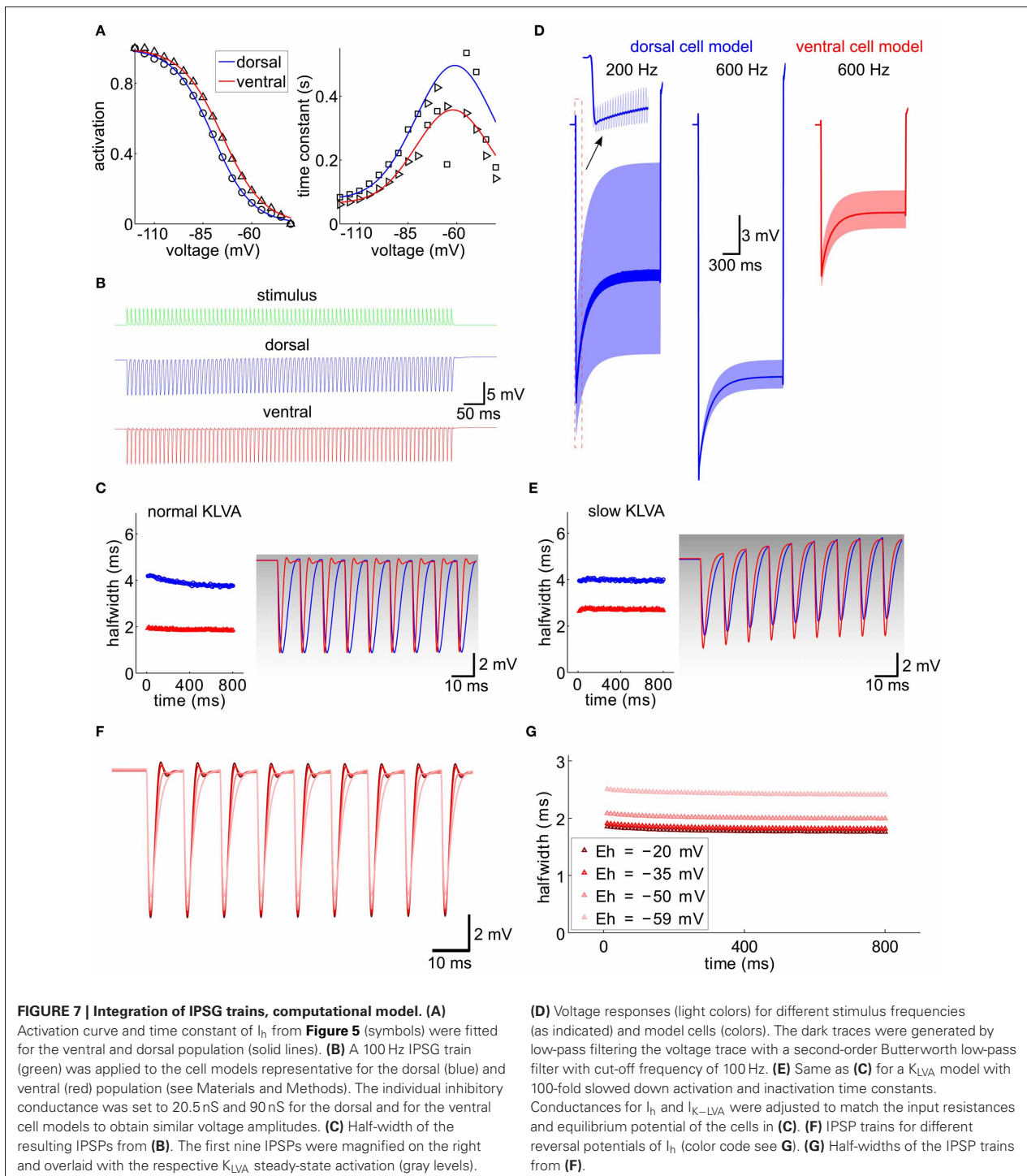
In the present study we demonstrate that  $I_h$  amplitude systematically varies along the dorsoventral axis of the MSO, being largest in ventral neurons and smallest in dorsal neurons. Consistent with this dorsoventral organization of membrane properties, the integration of inhibitory inputs systematically varies as a function of the neuron's location in both experiments and the model indicating that MSO neurons are tuned differentially along the presumed tonotopic axis. Tonotopic gradients of  $I_h$  have been previously observed in auditory brainstem nuclei. For example, in the lateral superior olive (LSO)  $I_h$  is larger in the LF region of



the nucleus compared to the HF region (Hassfurth et al., 2009). This opposite gradient might be due to the fact that in general LSO processes much higher input frequencies compared to MSO neurons (Sanes et al., 1989; Tolnai et al., 2008). The  $I_h$  gradient is also opposite in the nucleus laminaris (NL) (Yamada et al., 2005), the bird's MSO analogue ITD processing stage. Whether this difference is due to the diverse function of inhibitory inputs in mammals and birds or to different ITD processing strategies in the two animal classes is not clear. However, these results suggest that tuning of biophysical membrane properties through differential expression of HCN channels along the tonotopic axis in general optimizes the processing of different inputs frequencies (Kuba et al., 2005; Slee et al., 2010).

In mammals,  $I_h$  (or HCN) channels can derive from four different genes (HCN1-4) and assemble into homo-

heterotetramers with distinct electrophysiological properties in terms of their activation kinetics, their activation dependence, and their sensitivity to cAMP. In contrast, single-channel conductance is very similar for the different HCN isoforms (Brandt et al., 2009) and maximal  $I_h$  amplitude depends only very little on intracellular modulators (Ludwig et al., 1998; Wahl-Schott and Biel, 2009). This suggests that the observed dorsoventral gradient of  $I_h$  density in the MSO most likely relies on differences in the number of HCN channels and is independent of subunit variation. Our experiments also show that  $I_h$  activation kinetics accelerates and half-maximal activation voltage increases from the dorsal to the ventral part of the MSO. A distinct distribution of the isoforms along the dorsoventral axis might provide an explanation for the differences in biophysical properties of  $I_h$  (Yamada et al., 2005). MSO neurons mainly express HCN1 and HCN4 subunits



which both possess distinct physiological properties (Khurana et al., 2012). Among all different HCN subunits, HCN4 possesses the slowest kinetics and the most negative half-maximal activation voltage, whereas HCN1 possesses the fastest kinetics and the most positive half-maximal activation voltage (Santoro

et al., 2000; Moosmang et al., 2001). Thus, an increased contribution of HCN1 towards ventral neurons could result in faster activation kinetics and more positive half-maximal activation voltage. Conversely, our data suggest that different basal levels of intracellular cAMP cause the observed dorsoventral gradient in  $I_h$

properties. The gating of HCN channels in MSO neurons is very sensitive to cAMP, since most likely HCN1 and HCN4 isoforms co-assemble to form fast-activating but cAMP-sensitive HCN heteromers (Khurana et al., 2012). We show that dialyzing neurons with a saturating cAMP concentration resulted in nearly identical activation kinetics and half-maximal activation voltages in all MSO neurons. This opens the possibility that differential activation or expression of receptors that modulate intracellular cAMP levels could modify  $I_h$  properties along the presumed tonotopic axis of the MSO (Yamada et al., 2005) and regulate processing of various input frequencies in an activity dependent manner.

Functionally,  $I_h$  strongly influences basic membrane properties such as resting potential, input resistance and membrane time constant of neurons. These properties determine cellular excitability and synaptic integration. More specifically,  $I_h$  depolarizes the resting potential toward spike threshold, decreases the membrane time constant and lowers the input resistance at and below the resting potential, when the membrane potential is hyperpolarized in response to inhibitory inputs. Consistent with this idea we found that ventral neurons had a lower input resistance and a faster membrane time constant than dorsal neurons. In addition, postsynaptic integration of inhibitory inputs differed dependent on  $I_h$  amplitude and properties.

But what are the functional implications for the diversity of  $I_h$  of different neuron types for information processing in a small network? This and the relation to  $I_h$  has been extensively studied in both the entorhinal cortex and the hippocampus where  $I_h$  properties and HCN channels are as well distributed along a dorsoventral gradient (Garden et al., 2008; Giocomo and Hasselmo, 2008; Marcelin et al., 2012a,b). In these structures,  $I_h$  has been hypothesized to contribute to the observed gradient in grid field spacing in the entorhinal cortex (Giocomo et al., 2011; Hussaini et al., 2011). This mostly relates to the fact that  $I_h$  accelerates resonance frequency in those neurons. In these neurons  $I_h$  also tunes the membrane properties to the slow oscillatory activity of the inputs they receive, which is crucial for the specific function of these neurons. In auditory brainstem neurons and especially in the MSO, input frequencies (up to 1.5 kHz) are a magnitude higher than the activation and deactivation kinetics of  $I_h$  and thus an active contribution to temporal processing is unlikely.

One possible explanation why  $I_h$  distribution is tonotopically organized is suggested by our model and our experimental data. Neurons in the MSO not only receive two precisely timed excitatory but also two prominent inhibitory inputs from the medial

and lateral nucleus of the trapezoid body (Grothe et al., 2010), which are phase-locked to the fine-structure of the sound. Due to the relatively slow time constants of the inhibitory inputs (Magnusson et al., 2005; Couchman et al., 2010), the inhibition summates and strongly hyperpolarizes the neuron. Since  $I_h$  is rapidly activated during hyperpolarization we propose that  $I_h$  reduces the integration of synaptic inputs during periods of prolonged hyperpolarization. Indeed, both our experimental data and our model show that  $I_h$  decreases the temporal summation of IPSPs by gradually activating and thereby opposing the summated hyperpolarization induced by the temporal summation of HF inhibitory inputs. Functionally such a hyperpolarizing offset is problematic, since it effectively increases the spike threshold and thereby strongly reduces or even completely prohibits neuronal spiking in response to these input frequencies. The additional  $I_h$  activated in the ventral MSO region prevents this excessive hyperpolarization and keeps the neurons in an operating regime for binaural coincidence detection. In MSO neurons both  $I_h$  and  $I_{K-LVA}$  are open at rest (Khurana et al., 2011) and both contribute to the extremely low membrane time constants. The balance between the hyperpolarizing  $I_{K-LVA}$  and the depolarizing  $I_h$  determines the resting potential and together lowers the membrane time constants in both the hyperpolarizing and the depolarizing range. This decrease in time constant also in the depolarizing range would then improve coincidence detection of inputs thereby optimizing ITD analysis in these neurons. In addition, a higher expression level of  $I_h$  also indirectly enhances  $I_{K-LVA}$ -induced sharpening of inhibitory synaptic potentials by modulating the speed of depolarization via the driving force of  $I_h$  (Figures 7C,E). Conversely, two recent studies suggest that increasing  $I_h$  in the MSO and the NL, the bird's analogue structure of the MSO, sharpens the time window for coincidence detection also of excitatory inputs (Yamada et al., 2005; Khurana et al., 2012). This all implies that MSO neurons that respond best to higher frequency sounds and have thus larger  $I_h$  should have sharper time windows for ITD detection compared to neurons responding best to low frequency sounds. This phenomenon can indeed be observed for ITD functions of MSO neurons that are tuned to different best frequencies (Yin and Chan, 1990; Brand et al., 2002).

## ACKNOWLEDGMENTS

This work was supported by Deutsche Forschungsgemeinschaft (SFB 870).

## REFERENCES

- Adam, T. J., Finlayson, P. G., and Schwarz, D. W. F. (2001). Membrane properties of principal neurons of the lateral superior olive. *J. Neurophysiol.* 86, 922–934.
- Barnes-Davies, M., Barker, M. C., Osmani, F., and Forsythe, I. D. (2004). Kv1 currents mediate a gradient of principal neuron excitability across the tonotopic axis in the rat lateral superior olive. *Eur. J. Neurosci.* 19, 325–333. doi: 10.1111/j.0953816X.2003.03133.x
- Brand, A., Behrend, O., Marquardt, T., McAlpine, D., and Grothe, B. (2002). Precise inhibition is essential for microsecond interaural time difference coding. *Nature* 417, 543–547. doi: 10.1038/417543a
- Brandt, M. C., Endres-Becker, J., Zagidullin, N., Motloch, L. J., Er, F., Rottlaender, D., et al. (2009). Effects of KCNE2 on HCN isoforms: distinct modulation of membrane expression and single channel properties. *Am. J. Physiol. Heart Circ. Physiol.* 297, H355–H363. doi: 10.1152/ajpheart.00154.2009
- Couchman, K., Grothe, B., and Felmy, F. (2010). Medial superior olivary neurons receive surprisingly few excitatory and inhibitory inputs with balanced strength and short-term dynamics. *J. Neurosci.* 30, 17111–17121. doi: 10.1523/JNEUROSCI.1760-10.2010
- Garden, D. L. F., Dodson, P. D., O'Donnell, C., White, M. D., and Nolan, M. F. (2008). Tuning of synaptic integration in the medial entorhinal cortex to the organization of grid cell firing fields. *Neuron* 60, 875–889.
- Giocomo, L. M., and Hasselmo, M. E. (2008). Time constants of h current in layer II stellate cells differ along the dorsal to ventral axis of medial entorhinal cortex. *J. Neurosci.* 28, 9414–9425. doi: 10.1523/JNEUROSCI.3196-08.2008
- Giocomo, L. M., Hussaini, S. A., Zheng, F., Kandel, E. R., Moser, M.-B., and Moser, E. I. (2011). Grid cells use HCN1 channels for spatial scaling.

- Cell* 147, 1159–1170. doi: 10.1016/j.cell.2011.08.051
- Golding, N. L., and Oertel, D. (2012). Synaptic integration in dendrites: exceptional need for speed. *J. Physiol.* 590, 5563–5569. doi: 10.1113/jphysiol.2012.229328
- Golding, N. L., Robertson, D., and Oertel, D. (1995). Recordings from slices indicate that octopus cells of the cochlear nucleus detect coincident firing of auditory nerve fibers with temporal precision. *J. Neurosci.* 15, 3138–3153.
- Grothe, B., Pecka, M., and McAlpine, D. (2010). Mechanisms of sound localization in mammals. *Physiol. Rev.* 90, 983–1012. doi: 10.1152/physrev.00026.2009
- Guinan, J. J., Norris, B. E., and Guinan, S. S. (1972). Single auditory units in the superior olivary complex: II: locations of unit categories and tonotopic organization. *Int. J. Neurosci.* 4, 147–166. doi: 10.3109/00207457209164756
- Hassfurth, B., Magnusson, A. K., Grothe, B., and Koch, U. (2009). Sensory deprivation regulates the development of the hyperpolarization activated current in auditory brainstem neurons. *Eur. J. Neurosci.* 30, 1227–1238. doi: 10.1111/j.1460-9568.2009.06925.x
- Hussaini, S. A., Kempadoo, K. A., Thuault, S. J., Siegelbaum, S. A., and Kandel, E. R. (2011). Increased size and stability of CA1 and CA3 place fields in HCN1 knockout mice. *Neuron* 72, 643–653. doi: 10.1016/j.neuron.2011.09.007
- Jercog, P. E., Svirskis, G., Kotak, V. C., Sanes, D. H., and Rinzel, J. (2010). Asymmetric excitatory synaptic dynamics underlie interaural time difference processing in the auditory system. *PLoS Biol.* 8:e1000406. doi: 10.1371/journal.pbio.1000406
- Karcz, A., Hennig, M. H., Robbins, C. A., Tempel, B. L., Rübsamen, R., and Kopp-Scheinpflug, C. (2011). Low-voltage activated Kv1.1 subunits are crucial for the processing of sound source location in the lateral superior olive in mice. *J. Physiol.* 589, 1143–1157. doi: 10.1113/jphysiol.2010.203331
- Khurana, S., Liu, Z., Lewis, A. S., Rosa, K., Chetkovich, D., and Golding, N. L. (2012). An essential role for modulation of hyperpolarization-activated current in the development of binaural temporal precision. *J. Neurosci.* 32, 2814–2823. doi: 10.1523/JNEUROSCI.388211.2012
- Khurana, S., Remme, M. W. H., Rinzel, J., and Golding, N. L. (2011). Dynamic interaction of  $I_h$  and  $I_{kva}$  during trains of synaptic potentials in principal neurons of the medial superior olive. *J. Neurosci.* 31, 8936–8947.
- Koch, U., Braun, M., Kapfer, C., and Grothe, B. (2004). Distribution of HCN1 and HCN2 in rat auditory brainstem nuclei. *Eur. J. Neurosci.* 20, 79–91. doi: 10.1111/j.0953816X.2004.03456.x
- Koch, U., and Grothe, B. (2003). Hyperpolarization-activated current ( $I_h$ ) in the inferior colliculus: distribution and contribution to temporal processing. *J. Neurophysiol.* 90, 3679–3687. doi: 10.1152/jn.00375.2003
- Kuba, H., Yamada, R., Fukui, I., and Ohmori, H. (2005). Tonotopic specialization of auditory coincidence detection in nucleus laminaris of the chick. *J. Neurosci.* 25, 1924–1934. doi: 10.1523/JNEUROSCI.4428-04.2005
- Leao, R. N., Sun, H., Svahn, K., Bernston, A., Youssoufian, M., Paolini, A. G., et al. (2006). Topographic organization in the auditory brainstem of juvenile mice is disrupted in congenital deafness. *J. Physiol.* 571, 563–578. doi: 10.1113/jphysiol.2005.098780
- Leibold, C. (2010). Influence of inhibitory synaptic kinetics on the interaural time difference sensitivity in a linear model of binaural coincidence detection. *J. Acoust. Soc. Am.* 127, 931–942. doi: 10.1121/1.3282997
- Ludwig, A., Zong, X., Jeglitsch, M., Hofmann, F., and Biel, M. (1998). A family of hyperpolarization-activated mammalian cation channels. *Nature* 393, 587–591. doi: 10.1038/31255
- Magnusson, A. K., Kapfer, C., Grothe, B., and Koch, U. (2005). Maturation of glycinergic inhibition in the gerbil medial superior olive after hearing onset. *J. Physiol. (Lond.)* 568, 497–512. doi: 10.1113/jphysiol.2005.094763
- Marcelin, B., Liu, Z., Chen, Y., Lewis, A. S., Becker, A., McClelland, S., et al. (2012a). Dorsoventral differences in intrinsic properties in developing ca1 pyramidal cells. *J. Neurosci.* 32, 3736–3747. doi: 10.1523/JNEUROSCI.5870-11.2012
- Marcelin, B., Lugo, J. N., Brewster, A. L., Liu, Z., Lewis, A. S., McClelland, S., et al. (2012b). Differential dorsoventral distributions of Kv4.2 and HCN proteins confer distinct integrative properties to hippocampal CA1 pyramidal cell distal dendrites. *J. Biol. Chem.* 287, 17656–17661. doi: 10.1074/jbc.C112.367110
- Mathews, P. J., Jercog, P. E., Rinzel, J., Scott, L. L., and Golding, N. L. (2010). Control of submillisecond synaptic timing in binaural coincidence detectors by K(v)1 channels. *Nat. Neurosci.* 13, 601–609. doi: 10.1038/nn.2530
- Moosmang, S., Stieber, J., Zong, X., Biel, M., Hofmann, F., and Ludwig, A. (2001). Cellular expression and functional characterization of four hyperpolarization-activated pacemaker channels in cardiac and neuronal tissues. *Eur. J. Biochem.* 268, 1646–1652. doi: 10.1046/j.1432-1327.2001.02036.x
- Müller, M. (1990). Quantitative comparison of frequency representation in the auditory brainstem nuclei of the gerbil, *Pachyuromys duprasi*. *Exp. Brain Res.* 81, 140–149. doi: 10.1007/BF00230110
- O'Donnell, C., and Nolan, M. F. (2011). Tuning of synaptic responses: an organizing principle for optimization of neural circuits. *Trends Neurosci.* 34, 51–60.
- Pecka, M., Brand, A., Behrend, O., and Grothe, B. (2008). Interaural time difference processing in the mammalian medial superior olive: the role of glycinergic inhibition. *J. Neurosci.* 28, 6914–6925. doi: 10.1523/JNEUROSCI.1660-08.2008
- Rautenberg, P. L., Grothe, B., and Felmy, F. (2009). Quantification of the three-dimensional morphology of coincidence detector neurons in the medial superior olive of gerbils during late postnatal development. *J. Comp. Neurol.* 517, 385–396. doi: 10.1002/cne.22166
- Sanes, D. H., Merickel, M., and Rubel, E. W. (1989). Evidence for an alteration of the tonotopic map in the gerbil cochlea during development. *J. Comp. Neurol.* 279, 436–444. doi: 10.1002/cne.902790308
- Santoro, B., Chen, S., Lüthi, A., Pavlidis, P., Shumyatsky, G. P., Tibbs, G. R., et al. (2000). Molecular and functional heterogeneity of hyperpolarization-activated pacemaker channels in the mouse CNS. *J. Neurosci.* 20, 5264–5275.
- Scott, L. L., Mathews, P. J., and Golding, N. L. (2005). Posthearing developmental refinement of temporal processing in principal neurons of the medial superior olive. *J. Neurosci.* 25, 7887–7895.
- Slee, S. J., Higgs, M. H., Fairhall, A. L., and Spain, W. J. (2010). Tonotopic tuning in a sound localization circuit. *J. Neurophysiol.* 103, 2857–2875. doi: 10.1152/jn.00678.2009
- Svirskis, G., Kotak, V., Sanes, D. H., and Rinzel, J. (2002). Enhancement of signal-to-noise ratio and phase locking for small inputs by a low-threshold outward current in auditory neurons. *J. Neurosci.* 22, 11019–11025.
- Tolnai, S., Hernandez, O., Englitz, B., Rübsamen, R., and Malmierca, M. S. (2008). The medial nucleus of the trapezoid body in rat: spectral and temporal properties vary with anatomical location of the units. *Eur. J. Neurosci.* 27, 2587–2598. doi: 10.1111/j.1460-9568.2008.06228.x
- Wahl-Schott, C., and Biel, M. (2009). HCN channels: structure, cellular regulation and physiological function. *Cell. Mol. Life Sci.* 66, 470–494. doi: 10.1007/s00018-0088525-0
- Yamada, R., Kuba, H., Ishii, T. M., and Ohmori, H. (2005). Hyperpolarization-activated cyclic nucleotide-gated cation channels regulate auditory coincidence detection in nucleus laminaris of the chick. *J. Neurosci.* 25, 8867–8877. doi: 10.1523/JNEUROSCI.2541-05.2005
- Yin, T. C., and Chan, J. C. (1990). Interaural time sensitivity in medial superior olive of cat. *J. Neurophysiol.* 64, 465–488.

**Conflict of Interest Statement:** The authors declare that the research was conducted in the absence of any commercial or financial relationships that could be construed as a potential conflict of interest.

Received: 15 February 2013; paper pending published: 19 April 2013; accepted: 19 June 2013; published online: 11 July 2013.

Citation: Baumann VJ, Lehnert S, Leibold C and Koch U (2013) Tonotopic organization of the hyperpolarization-activated current ( $I_h$ ) in the mammalian medial superior olive. *Front. Neural Circuits* 7:117. doi: 10.3389/fncir.2013.00117

Copyright © 2013 Baumann, Lehnert, Leibold and Koch. This is an open-access article distributed under the terms of the Creative Commons Attribution License, which permits use, distribution and reproduction in other forums, provided the original authors and source are credited and subject to any copyright notices concerning any third-party graphics etc.

## 5. Discussion

In three individual studies, presented in Chapter 2, 3, and 4, the excitability and action potential generation, the role of the glycinergic inhibition in the tuning of coincidence detection, as well as channel properties and synaptic integration along the tonotopic axis in the principal cells of the MSO were investigated. Each of these studies is comprised of an experimental and a computational part. The author of this thesis contributed to the computational part of the studies; the experiments were performed by experimental collaborators (see Author Contributions). A detailed statement of the author's contributions to the individual studies can be found at the end of the thesis (see Author Contributions).

In Chapter 2, we investigated the excitability and action potential generation in MSO neurons. An anatomically constrained multi-compartmental biophysical model of an MSO cell and its axon was created based on data acquired in a morphometric analysis of MSO axons. Using naturalistic synaptic inputs trains at different rates, our simulations indicate that the MSO's excitability is substantially modulated by morphological and electrical properties of the soma and axon. Furthermore, in patch-clamp experiments *in vitro*, as well as in our model simulations, we found that MSO neurons exhibit a frequency-dependent firing threshold. Strikingly, our simulations indicated that the site of action potential initiation in MSO neurons is modulated by the rate and intensity of their synaptic inputs. While in general we showed that the AP initiation takes place in the axon initial segment (AIS), in line with present knowledge of other cell types, we also demonstrated that, especially at firing threshold and for high-frequency inputs, a growing portion of action potentials is initiated in the first nodes of Ranvier. We identified two main mechanisms for these transient changes of the AP initiation site in MSO neurons. First, the extraordinarily leaky somatodendritic area constitutes a strong current sink to the AIS, thereby impairing its excitability, while the nodes of Ranvier are much less affected due to better electrotonic isolation. And second, the temporal summation of high-frequency excitatory inputs causes a depolarized baseline in the somatodendritic compartment, which primarily invades the

proximal axon and causes the inactivation of sodium channels, and thus a loss of excitability.

In Chapter 3 we studied the role of glycinergic inhibition in the coincidence detection of MSO neurons. To elucidate the impact of the phase-locked inhibitory afferents to MSO neurons on coincidence detection, *in vitro* recordings in acute auditory brainstem slices of adult gerbils as well as computational modeling were performed. We found that inhibition shifts the peak timing of excitation depending on its relative timing. As a consequence of these peak shifts the ITD sensitivity of the cell is modulated, which underlines the crucial role of inhibition in the ITD tuning of MSO neurons. The magnitude of the peak shifts was modulated by the excitatory and inhibitory input kinetics, the balance of excitation and inhibition, as well as the temporal jitter of the inputs. The inhibition-enforced effects were robust with respect to synaptic jitter and maintained efficacy during input trains at high frequencies. Using a well-constrained point model of an MSO neuron, we showed that an active low-threshold potassium conductance, mediated by Kv1 channels, substantially facilitated the peak shifts.

In Chapter 4 the properties of hyperpolarization-activated cyclic nucleotide-gated channels (HCN) along the dorsoventral (tonotopic) axis of the MSO are investigated. For this purpose *in vitro* voltage-clamp recordings of dorsal and ventral MSO neurons were performed. These recordings revealed that in the ventral (high-frequency) portion of the MSO, HCN channels show a larger current density compared to channels in the dorsal (low-frequency) part. Also, HCN currents in the ventral MSO activated faster and for more depolarized voltages. These systematic differences of HCN currents affect the membrane resting properties, and thus the integration of synaptic inputs in MSO neurons on the dorsoventral axis. Ventral MSO neurons show a faster membrane time constant and a lower input resistance compared to dorsal cells, resulting in substantially smaller half-widths of inhibitory postsynaptic potentials (IPSPs) evoked during current-clamp. Using two biophysical models, each based on the average of HCN channel data and membrane properties of dorsal and ventral MSO neurons, respectively, we could reproduce the results obtained in our current-clamp experiments. Our simulations suggest that the increased level of HCN currents helps to counteract the temporal summation of high-frequency inhibitory inputs to MSO cells in the ventral part of the MSO nucleus. Finally, the computational modeling allowed us to show that the

observed sharpening of IPSPs is mediated by an interplay of HCN channels with the fast-activating Kv1 channels expressed in MSO neurons.

We now continue discussing three selected topics based on the findings in Chapter 2,3, and 4, as well as related literature. The first topic (Subchapter 5.1.) is dedicated to the site of action potential generation in central neurons. In this topic we want to elucidate reasons why the otherwise generally accepted notion of one singular AP initiation site (the AIS) might not apply to MSO neurons, as we have demonstrated in Chapter 2. In the second topic (Subchapter 5.2.) the role of Kv1 channels in MSO neurons is discussed. Here, we illustrate the various functions Kv1 channels perform in MSO neurons showing their importance for coincidence detection. Also, our own results concerning Kv1 channels that we found in Chapter 3 and 4 are added to this list, further expanding the significance of Kv1 channels in the MSO. The third topic (Subchapter 5.3.) regards the biological function of MSO neurons, the encoding of ITDs, and examines the role of glycinergic inhibition. Since the role of glycinergic inhibition is strongly debated, we highlight the current arguments against and in favor of glycinergic inhibition tuning the MSO's coincidence detection, in the light of recent studies and the results in Chapter 2 and 3. The discussion is concluded with a brief outlook (Subchapter 5.4.) covering yet unanswered questions in the context of our studies in Chapters 2, 3, and 4.

## **5.1. The site of action potential initiation in central neurons**

The determination of the action potential initiation site (sometimes also called the trigger zone) in neurons has been a subject of intense study for many decades. During the course of these studies the site of AP initiation was narrowed down from the unspecific proximal axon in early works in spinal motoneurons (Coombs et al., 1957; Fatt, 1957; Fuortes et al., 1957), to the distal part of the AIS (20-40 microns from the soma) in most of the recent studies investigating neurons with myelinated axons (Palmer et al., 2006; Shu et al., 2007; Yu et al., 2008; Palmer et al., 2010; Foust et al., 2010; Popovic et al., 2011). Also for neurons with unmyelinated axons APs were

reported to initiate in the proximal axon<sup>4</sup>, within 20 to 30 microns from the soma (Schmidt-Hieber et al., 2008; Kress et al., 2008; Scott et al., 2014).

The study presented in Chapter 2 of this thesis investigates the action potential initiation in principal neurons of the medial superior olive. Our findings are in line with the existing literature as we also show that APs are initiated in the AIS. However, in contrast to most findings in other neuronal types, we also demonstrate, that the site of AP initiation might not be restricted to the AIS only, but – under specific circumstances – can also occur in more distal axonal structures, like the first nodes of Ranvier. This result, of course, raises the question as to why our results differ from the present literature in this particular point. This subchapter is dedicated to answering this question by hinting at the potential differences between our study and existing works in this field. Furthermore, the major factors that control the site of AP initiation, as well as the first insights into plasticity of the AP initiation site are discussed.

Compared to the very leaky coincidence detector neurons of the MSO, the vast majority of research investigating the site of AP initiation in central neurons was carried out in more excitable neuron types, like layer 5 pyramidal cells (Stuart and Sakmann, 1994; Stuart et al., 1997a; Palmer et al., 2006; Shu et al., 2007; Yu et al., 2008; Popovic et al., 2011), Purkinje cells (Stuart and Häusser, 1994; Khaliq and Raman, 2006; Palmer et al., 2010; Foust et al., 2010) or neurons of the subthalamic nucleus (Atherton et al., 2008). The input resistance of these neurons ranges between around 15 to 200 M $\Omega$  at rest (Crepel and Penit-Soria, 1986; McCormick and Prince, 1987; Beurrier et al., 1999; Zhu et al., 2000; McKay and Turner, 2005). The current threshold to evoke an AP in these neurons typically does not exceed a couple of hundred of picoamperes (pA). With membrane time constants ranging from several to tens of milliseconds (Crepel and Penit-Soria, 1986; McCormick and Prince, 1987; Kasper et al., 1994; Roth and Häusser, 2001) the somata of these cell types can provide a stable current source for their respective axons. For MSO neurons the situation is quite different (see Introduction, Section 1.1.7). Owing to the exceptionally high expression of sub-threshold activated

<sup>4</sup> In neurons with unmyelinated axons, the axon initial segment is often defined as the segment in the proximal axon that exhibits a high density of sodium channels and associated proteins, such as the scaffolding protein Ankyrin-G (Kress et al., 2008; Hu et al., 2009; also see Bender and Trussell, 2012; Kole and Stuart, 2012).

channels, mature MSO cells exhibit an input resistance of around 5 M $\Omega$  and a membrane time constant of merely  $\sim$ 350  $\mu$ s at rest (Scott et al., 2005; Couchman et al., 2010). To elicit an AP at rest a current pulse of 4 to 7 nA (depending on the shape and duration) is needed (Couchman et al., 2010). Under *in vivo* conditions, i.e. under the heavy synaptic bombardment MSO neurons receive, it is well conceivable that due to the massive additional leak, the input resistance even falls below the mark of 1 M $\Omega$ . The soma of MSO neurons therefore cannot provide a stable current source for AP initiation but, on the contrary, establishes a particularly strong current sink to the comparatively short AIS of only 20 microns (see Chapter 2, Figure 2). While for Purkinje cells equally short initial segments were reported (Clark et al., 2005), layer 5 pyramidal cells have the advantage of exhibiting AIS's of around 40 microns (Palmer et al., 2006; Shu et al., 2007), which results in a better electrotonic isolation for the distal parts of the AIS from the somatodendritic segments.

A second major difference between our study and the existing literature in this field is the nature of stimulation used to evoke the APs to be investigated. The stimulation methods include the somatic or axonal applications of current pulses (Palmer et al., 2006; Shu et al., 2007; Yu et al., 2008; Foust et al., 2010; Popovic et al., 2011) and fiber stimulation (Stuart et al., 1997a; Palmer et al. 2006; Palmer et al., 2010; Foust et al., 2010; Popovic et al., 2011). Furthermore, in some studies spontaneously elicited APs were analyzed (Atherton et al., 2008; Palmer et al., 2010). Most studies are restricted to the investigation of singular action potentials evoked by a brief singular current pulse. Only few studies systematically investigate the trigger zone of all APs evoked by a train of consecutive current pulses (Foust et al., 2010; Popovic et al., 2011), in situations of spontaneous or pharmacologically evoked up-states (Shu et al., 2007), or mimicked ongoing synaptic input via dynamic-clamp (Shu et al., 2007). In Chapter 2 we used temporally extended synaptic input trains in our model to assess the AP initiation site in *in vivo*-like situations. We systematically analyzed every AP evoked during such a train and, since our input trains are based on bandpass-filtered noise, we therefore could examine APs evoked by a great variety of stimuli with different amplitudes, kinetics and activity histories. The stimulus trains were presented at various intensities and, since MSO neurons receive synaptic inputs phase-locked, at various center frequencies

up to 1 kHz mimicking the periodicity of a cochlear channel. An investigation of the AP initiation site using stimulation most comparable to ours in Chapter 2 is provided by Shu et al (2007). In this *in vitro* study simultaneous whole-cell recordings from cortical pyramidal neurons during spontaneous up-states and up-states emulated by a dynamic-clamp procedure are performed. Up-states are thereby defined as synaptic barrages with a balanced proportion of excitatory and inhibitory activity up to 1 second in length. AP initiation was also analyzed during pharmacologically evoked epileptiform discharges and simple current injections. Regardless of the stimulation paradigm used, the AP initiation site was consistently found in the distal portion of the AIS.

In summary, it can be stated that the anatomical and physiological differences of MSO cells compared to the cell types typically studied in this context demonstrate that the AP initiation in MSO cells does take place under different means and thus might occur differently. Moreover, in Chapter 2 we provide one of the few studies that systematically investigates all action potentials during a train of heavy synaptic barrages at different frequencies and intensities, which gives us an insight into action potential initiation under more *in vivo*-like circumstances.

The site of AP initiation is typically studied by means of a latency analysis of the AP timing in different neuronal segments in order to obtain a spatiotemporal profile. Since normally the somatic AP functions as the reference, the segment with the largest negative latency with respect to the somatic AP time is considered to be the initiation site of the AP.

Before a latency analysis can be performed, simultaneous recordings of an action potential at different locations along the axon are needed. In a computational model this is a comparatively simple task; however, *in vitro* it is challenging due to the very small axonal diameter of central neurons (0.5 to 1.5 microns) making direct recordings difficult. While simultaneous whole-cell recordings from the soma and AIS have been established (Kole et al., 2007), myelinated parts of the axons seem to be completely inaccessible for patch-clamping methods unless loose-patch methods are employed (Clark et al., 2005; Meeks et al., 2005; Atherton et al., 2008). One recording technique,

however, allows to obtain whole-cell recordings from more distal axonal sites: the axon bleb recording (Hu and Shu, 2012). The axon bleb is an enlarged unmyelinated structure at the cut end of an axon which forms after the slicing procedure. Several studies made use of simultaneous whole-cell recordings from the soma and the axon bleb (Shu et al., 2007; Kole et al., 2007; Schmidt-Hieber et al., 2008). However, since the axon (without counting collaterals) exhibits only one axon bleb at an a-priori uncontrollable distance from the axon hillock, data from many neurons with axon blebs at different distances from the axon hillock has to be acquired and pooled such that a spatiotemporal profile of AP initiation emerges.

This problem can be overcome by employing optical recording and voltage-sensitive dyes (VSD). The usage of VSD imaging has the advantage that a large number of sites along a neuronal membrane can be recorded at the same time. To investigate the AP initiation site using VSD the neuron is filled with the VSD through a patch pipette attached to the soma in a whole-cell configuration. A camera mounted to a camera port of the microscope, which is set up to illuminate individual neurons in slices by excitation light in epi-fluorescence, records the voltage-changes (Popovic et al., 2012). The maximum amount of distinct optical recording sites using VSD imaging coincides with the resolution of the camera used. Since for the investigation of the AP initiation site an extraordinary temporal resolution is necessary, a high-speed CCD camera is used. Current high-speed CCD cameras used for this purpose provide a resolution of 80x12 pixels at a maximum frame rate of 10 kHz (for example Redshirt Imaging NeuroCCD-SM(Q); Foust et al., 2010; Popovic et al., 2011). Despite the relatively low spatial resolution compared to other (not high-speed) digital cameras, these high-speed CCD cameras still provide a tremendous improvement over conventional electrical recording methods, by allowing a much larger number of recording sites corresponding to their pixel amount.

Having acquired a data set of AP time courses at different locations along the axon a latency analysis is performed. Different points in the time course of the action potential were used to reference its timing: for example, the peak amplitude (Shu et al., 2007), voltage derivative criteria (Kole et al., 2007, Atherton et al., 2008) or the half-maximum

amplitude (Palmer et al., 2006; Palmer et al., 2010; Foust et al., 2010; Popovic et al., 2011).

In Chapter 2 we used the peak amplitude of the APs as the time reference to perform a latency analysis in order to identify the AP initiation site. The determination of this AP peak time for the APs in the soma and every segment of the axon, that occurred during a train of synaptic inputs was, however, a difficult task. Since we used inputs at different intensities and frequencies which resulted in a huge variety of response characteristics, a simple amplitude or derivative criterion was impossible to acquire. Furthermore, the very fast voltage deflections of MSO neurons, caused by the extreme leakiness, especially under synaptic bombardment, impedes the distinction of APs from sub-threshold responses in the soma and proximal axonal segments. We therefore identified APs in the distal axon, where this distinction is easy (Scott et al., 2007). From the peak in this distal segment onward, we acquired the voltage peaks of antidromic segments within a distinct time window (see Chapter 2, Figure 1F and Materials and Methods). This approach gave us a robust algorithm to acquire the trigger zone of action potentials throughout a vast number of different stimulus and cell-related parameters. However, we also came to the conclusion that the AP initiation is not necessarily a matter of a distinct segment of the membrane (especially for high stimulation frequencies), but rather a complex interplay of several neighboring compartments (Chapter 2, Figure 9).

A method which does not use latency analysis to determine the AP initiation site is the local application of tetrodotoxin (TTX) to block sodium channels in putative trigger zones in order to evaluate their significance for AP generation (Colbert and Johnston, 1996; Khaliq and Raman, 2006). Blocking sodium channels in the first node of Ranvier led to evidence that the first node of Ranvier might not be the site of AP initiation in Purkinje neurons (Khaliq and Raman, 2006), even though it was suggested otherwise using simultaneous loose-patch cell-attached recordings (Clark et al., 2005).

To further elaborate on the question, why the site of AP initiation in MSO neurons might not be restricted to the AIS only, it is important to understand why, in general, action potentials are preferentially initiated in the AIS.

Kole and Stuart (2012) highlighted three reasons why the AIS is a favorable site of AP initiation. First, the axon generally emerges from the soma and is therefore in a good position to follow the changes of the somatic membrane potential that are caused by the integration of synaptic inputs. Second, the axon exhibits a much smaller diameter compared to the soma resulting in a smaller surface and smaller capacitance. As a consequence, less inward current is necessary for the AIS to depolarize and accordingly a lower sodium channel density is needed. Therefore, AP initiation in the AIS is also energetically advantageous. Furthermore, the small capacitance facilitates fast changes of the membrane potential occurring during action potentials. Finally, the third reason emphasizes the circumstance that a singular AP initiation site establishes a single location where inhibition could efficiently influence AP generation.

These arguments can be extended further. For example: the small diameter of the AIS does not only lower the capacitance of the membrane, but also makes the AIS into a thin cable, enabling the electrotonic isolation of the AP initiation site in the axon from the somatic current sink (see Chapter 2). Moreover, the small local capacitance of the AIS is also facilitated by the proximity to the low-capacitance myelin sheath (Baranauskas et al., 2013). Please also note that, interestingly, the majority of these arguments also holds true for the nodes of Ranvier.

Combining these arguments with the knowledge that sodium ion influx is mediating action potentials (Hodgkin and Huxley, 1952d, see Section 1.2.1.), two major factors for the AP initiation site can be identified: (1) the specialized anatomical and electrical properties of the proximal axon (i.e. the cable properties), and (2) the sodium channels. Being experimentally comparably easy to access, a majority of AP initiation studies has focused a lot of attention on the role of sodium channels in AP initiation. Several approaches, including antibody staining, sodium imaging, patch-clamp experiments, and modeling suggest that the sodium channel density in the AIS is substantially higher than in the soma (Kole et al., 2008; Hu et al., 2009; Lorincz and Nusser, 2010, review: Kole and Stuart, 2012). Moreover, it has been demonstrated that axonal sodium channels exhibit a lower half-activation (Colbert et al., 1996; Colbert et al., 2002, Hu et al., 2009) and a faster activation time constant (Schmidt-Hieber et al., 2010). As a consequence of the considerable number of studies, the role of sodium channels has so

far dominated the discussion of AP initiation in central neurons. Interestingly, a recent study shows that the site of the largest sodium influx and the AP trigger zone do not coincide in layer 5 pyramidal neurons (Baranauskas et al., 2013). Using high-speed sodium imaging in combination with simultaneous axo-somatic recordings and computational modeling, Baranauskas et al. (2013) demonstrate that the largest sodium ion influx is located in the central portion of the AIS, whereas the AP trigger zone is in the distal part. Moreover, in a computational model Baranauskas et al. (2013) show that the electrical isolation of the actual AP trigger zone from the somatodendritic compartment is crucial for AP initiation. In conclusion, these results indicate that the cable properties of the axon play an important role in determining the AP initiation site (Baranauskas et al., 2013; also see the commentary: Ma and Huguenard, 2013). Unfortunately, the influences of the axonal cable properties on the initiation of APs are hard to assess experimentally. Computational modeling studies, however, make these properties accessible and therefore have pointed out early that not only the sodium channels but also the cable properties play a crucial role in AP initiation (Moore et al., 1983; Mainen et al., 1995).

In line with these observations, our results in Chapter 2 suggest that both, the sodium channel density and the cable properties, play a key role in the determination of the AP initiation site and AP generation in general. On the one hand, we show that an overall increase of the axonal sodium channel density facilitates firing (Chapter 2, Figure 3G). Increasing only the nodal sodium channel density, the model additionally exhibits an increase of distal AP initiation probability (Chapter 2, Figures 3H and 5K). On the other hand, decreasing the influence of the somatic current sink on the axon directly by decreasing the prominent somatic leak (induced by a reduction of Kv1 and HCN channel density) strongly facilitated firing (Chapter 2, Figure 3J). Furthermore, our results demonstrate the delicate interplay of cable properties and sodium channel density in AP initiation. When decreasing the overall axonal diameter, which, since we kept the sodium density fixed, goes along with a decrease of total sodium conductance, the AP probability dropped (Chapter 2, Figure 3E). At this point, the sodium channel density dominated the influence on AP initiation over the better electric isolation from the soma. However, only decreasing the diameter of the axon's base, resulted in a

facilitation of firing (Chapter 2, Figure 3I). In this situation, the better isolation from the somatic current sink and thus the cable properties prevailed over the (lesser) sodium channel decrease.

Analyzing the locus of AP initiation, we found that in our computational model a certain extent (depending on cell- and stimulus parameters) of action potentials is not initiated in the AIS, but in the nodes of Ranvier (Chapter 2, Figure 5). The prevalence of these distally initiated APs is particularly pronounced at firing threshold for low-frequency stimulations (250 Hz) and for high-frequency stimulations at high intensities (1000Hz; Chapter 2, Figure 7G, H). These phenomena can be explained by the influence of cable properties and sodium channels on AP initiation.

Due to the leaky soma and high axial resistance (induced by the very thin MSO axon, see Chapter 2, Figure 2), the comparatively distal parts of the axon, like the nodes of Ranvier, receive the inputs with strongly attenuated amplitudes (Chapter 5, Figure 5B). However, the good electrotonic isolation from the soma also induces a much better excitability (indicated by a higher input resistance) of the nodes of Ranvier compared to the more proximally located AIS (Chapter 2, Figure 5A). A direct consequence of the larger input resistance is the substantially lower current threshold, which then shows in the higher probability of action potential initiation at the nodes of Ranvier.

The higher prevalence of distally initiated APs at high-frequency stimuli is again most likely based on a synergy of cable properties and sodium channel influence. First, the high-frequency excitatory synaptic inputs induce an increase of the somatic leak and thus the intensification of the somatic current sink, since more current flows especially through the low-voltage activated potassium channels. Second, a depolarized baseline, caused by the temporal summation of the excitatory inputs, is tapped by the axonal membrane and causes the inactivation of sodium channels, particularly in the soma and proximal axonal segments, again leaving the nodes of Ranvier with an excitability advantage. Increasing the intensity of high-frequency stimuli successively even renders the nodes of Ranvier to be the main AP generating sites, helping to control excitability and to stabilize neuronal output (Chapter 2, Figure 7H).

To keep the influence of cable properties and sodium channels on AP initiation at balance, the sodium channel density of the AIS and the nodes of Ranvier were set to the same value in the standard model. Increasing the sodium channel density in the nodes reinforces their excitability advantage over the AIS even further and consequently raises the probability of APs being initiated at the nodes of Ranvier (Chapter 2, Figure 5K). Interestingly, immunogold-stainings of pyramidal cells showed an even twice as high sodium channel density in the nodes compared to the AIS (Lorincz and Nusser, 2010), hinting that our reported probability of distally initiated APs might even be underestimated.

A shift of the AP initiation site towards distal due to the partial inactivation of sodium channels particularly in the proximal axon has also been observed in a very recent study (Scott et al., 2014). In the present literature regarding the identification of the AP initiation site, Scott et al. (2014) is arguably the most comparable to our research presented in Chapter 2. In their study, AP initiation in the unmyelinated axons of hippocampal dentate granule cells was investigated using dual patch-clamp recordings from the soma and axon, sodium imaging and computational modeling. Employing latency analysis of APs recorded at different locations along the axon, the study confirms that the AP initiation site of dentate gyrus granule cells is located in the axon around 20 to 25 microns away from the soma (Schmidt-Hieber et al., 2008; Kress et al., 2008). However, Scott and colleagues also report an activity-dependent expansion of the AP initiation site away from the soma. The broadening of the AP initiation site was witnessed when comparing the first and the third spike in a spike train evoked by a sustained current injection, as well as for APs evoked by slow depolarizations. In the latter case also a substantial raise of voltage-threshold was observed. In line with our observations for high-frequency inputs, the mechanism behind this depolarization-dependent broadening of the AP initiation site was reported to be mediated by the inactivation of sodium channels following the invasion of somatic depolarization into particularly the proximal axon (Scott et al., 2014). In our simulations the shift of the trigger zone from the AIS to the nodes of Ranvier and back occurs during a train of stimuli (sometimes on a stimulus-to-stimulus basis) and thus constitutes a control

mechanism of neuronal excitability on a millisecond timescale (Chapter 2, Figure 5). Thus, similar to our findings in Chapter 2, the work of Scott et al. (2014) shows the capability of a neuron to rapidly adapt its AP generation in response to specific stimulus characteristics and their corresponding effects. Furthermore, the influence of sodium channel inactivation on action potential initiation is emphasized (Chapter 2, Figure 6; Scott et al., 2014).

The transient changes of the AP initiation site discussed up to this point are mediated by cell and cable properties in concert with sodium channel inactivation, and thus are not based on structural changes of the corresponding neuronal tissue. The question arises whether neurons that regularly receive inputs of a certain frequency and strength morphologically adjust their action potential generating sites to optimize neuronal output. In the nucleus laminaris (NL), the avian counterpart of the MSO, this question can be answered in the affirmative (Kuba et al., 2006). Patch-clamp recordings and immunohistochemical stainings in acute brainstem slices showed that the length of the AP initiation site (the hotspot, defined as a clustering of sodium channels) and its distance from the soma, depends on the characteristic frequency<sup>5</sup> (CF) of the neuron (Kuba et al., 2006). High-CF (around 3 kHz) and medium-CF (1-2.5 kHz) neurons exhibit a high expression of sodium channels within a short segment of the AIS comparatively distant from the soma, whereas for low-CF neurons (0.4-1 kHz) the sodium channel expression is distributed on a longer portion of the AIS. Computational modeling further indicates that these structural changes of the AP initiation site reduces the neuron's threshold and improves the sensitivity to ITDs (Kuba et al., 2006). *In vitro* studies deliver striking evidence on how initial segments of neurons undergo plastic changes (referred to as homeostatic plasticity) in response to input deprivation or increase (Kuba et al., 2010; Grubb and Burrone, 2010; also see Gründemann and Häusser, 2010). In one study, one day after hatch (i.e. 10 days after hearing onset) the cochlea of chicks was unilaterally removed, then over the course of two weeks acute brainstem slices incorporating the NL were cut and investigated using patch-clamp recordings and immunohistochemical labeling (Kuba et al., 2010). The withdrawal of inputs to NL neurons due to the cochlea removal resulted in a substantial increase of the

---

<sup>5</sup> The characteristic frequency is typically defined as the stimulation frequency to which the neuron responds at the lowest threshold.

length of the sodium channel and ankyrin-G cluster in NL axons on the deprived side. Alongside this rearrangement of the AIS, which saturated 7 days after cochlea removal, an increase of sodium current and decrease of current threshold (thus the increase of excitability) was observed. Another study investigated the effects of chronic depolarization on the axons of dissociated hippocampal neurons (Grubb and Burrone, 2010). Using high extracellular concentration of potassium ions mimicking increased neuronal activity, caused several components of the AIS, including sodium channels, to move distally over the course of 12 to 14 days. Here, the structural rearrangement of the AIS, was accompanied by a decrease of neuronal excitability witnessed by the increase of current threshold and membrane conductance. In sum, these two studies (Kuba et al., 2010; Grubb and Burrone, 2010) not only show that the AIS undergoes plastic changes, but also that these changes stabilize neuronal output by reducing excitability for more inputs and increasing excitability for less inputs. Strikingly, similar to our findings, on higher input load the site of AP initiation moves in distal direction.

### *Summary*

In the last ten years the research of the AP initiation site in central neurons has taken a major step forward. Experimental techniques like simultaneous patch-clamp recordings and optical recording methods like the use of voltage-sensitive dyes or high-speed sodium imaging allowed to precisely pinpoint the site of AP initiation in the axon. For neurons with myelinated axons, like layer 5 pyramidal cells or Purkinje neurons, the site of AP initiation is typically found at the distal end of the AIS in close proximity to the onset of myelination. The site of AP initiation for neurons with unmyelinated axons, like hippocampal dentate gyrus granule cells, is located in the proximal axon, approximately 20 to 25 microns distal to the soma. In Chapter 2 we found the distal AIS to be the site of AP initiation in principal neurons of the MSO. However, in contrast to existing work we also found that the AIS is not the only site of AP initiation in these cells, but, especially at the firing threshold or for high-frequency inputs, can also be found in the first few nodes of Ranvier. The reason for this discrepancy can be found in the consilience of two comparably unusual properties of MSO neurons. First, due to the particularly high expression of sub-threshold activated channels MSO neurons are much

leakier than neurons typically investigated in this field. Thus, the somatodendritic compartments of MSO cells establish an exceptionally strong current sink to the AIS. Second, MSO neurons receive strong synaptic inputs at frequencies of up to 1.5 kHz which activate even more transmembrane current flow that further intensifies the current sink, and which also cause a depolarized membrane potential baseline. These two properties have direct influence on the key factors that determine the AP initiation site: voltage-gated sodium channels and cable properties of the axon. We found that high-frequency excitatory synaptic inputs inactivate sodium channels preferentially in the proximal axon, thus increasing the excitability advantage of the first nodes of Ranvier compared to the AIS even further. Despite the addition of the first nodes of Ranvier to the possible locations of AP initiation, our results do not stand isolated in the recent literature. The tendency of the AP initiation site moving towards distal on higher input activity has also been observed in other works. A depolarization-dependent transient broadening of the AP initiation site away from the soma was observed in dentate gyrus granule neurons (Scott et al., 2014). Also structural changes of the proximal axon over the course of days based on input deprivation or chronic depolarization have been found in neurons of the NL and dissociated hippocampal granule neurons, respectively (Kuba et al., 2010; Grubb and Burrone, 2010). In NL neurons, which are the most comparable to MSO neurons in the field of AP initiation site research, high-frequency neurons exhibit a more distal AP initiation site compared to low-frequency neurons (Kuba et al., 2006). Summarized, the site of AP initiation of neurons under *in vivo*-like situations does not seem to be a rigid spot somewhere in the axon, but subject to activity-dependent rapid changes during input trains or even plastic changes over the course of days. It is striking that most studies confining the AP initiation site to one rigid locus in the axon typically focused their stimulation regime on singular current pulses or pulses in low-frequency succession.

## **5.2. The role of Kv1 channels in the context of coincidence detection in the MSO**

The Kv1 channel is a fast-activating low-threshold potassium channel encoded by the KCNA gene subfamily (see Introduction). A substantial expression of these low-threshold activated potassium channels is a common scheme in auditory brainstem neurons processing temporally sensitive information. Kv1 channels can, for example, be found in the VCN (Manis and Marx, 1991), the MNTB (Forsythe and Barnes-Davies, 1993), the LSO (Barnes-Davies et al., 2004) and the MSO (Smith et al., 1995). Over the past years the properties and functional roles of Kv1 channels in auditory brainstem neurons were investigated. In the following the effects of the strong Kv1-expression, and the role of Kv1 channels in the MSO's high-resolution coincidence detection are discussed.

On activation, Kv1 channels mediate an outward current that persists over hundreds of milliseconds given a long enough depolarizing stimulus. As a consequence, neurons with a substantial expression of Kv1 channels exhibit a strong outward rectification, which leads to a response profile called phasic firing. A neuron showing phasic firing elicits a singular (or very few) action potential(s) only at the onset of a depolarizing current injection. Apart from MSO neurons (Smith, 1995; Svirskis et al., 2002; Scott et al., 2005; Couchman et al., 2010), this characteristic firing profile has also been observed in upstream neurons of the MSO, for example, in cells of the VCN (Oertel, 1983; Manis and Marx, 1991; Isaacson and Walmsley, 1995; Golding et al., 1995) and in the MNTB (Wu and Kelly, 1991; Banks and Smith, 1992; Forsythe and Barnes-Davies, 1993; Scott et al., 2005; Roberts et al., 2014). In LNTB neurons a Kv1 expression seems to be less pronounced or less influential as these neurons generate a tonic firing pattern in response to a depolarizing current step – however, they show a larger inter-spike-interval between the first and the second action potential (Roberts et al., 2014).

Kv1 channels in interaction with hyperpolarization-activated cation channels (HCN) are the main contributors to the resting conductance of MSO neurons (Khurana et al.,

2011). Indeed, blocking Kv1 channels by the application of dendrotoxin (DTX) substantially increases the membrane time constant and decreases the current threshold, showing that Kv1 channels are already open at rest (Scott et al., 2005; Mathews et al., 2010). These two parameters are of major importance for the high-resolution coincidence detection performed by MSO neurons: if the membrane time constant is increased, the membrane potential repolarizes more slowly which broadens the time window in which synaptic inputs are being integrated (Scott et al., 2005). As a consequence, less coincident synaptic inputs would be able to drive the cell to firing threshold which is equivalent to a loss of temporal resolution. The same result can be expected for a lower current threshold, as it would allow less synchronous synaptic inputs to evoke an AP.

Another consequence of the increased membrane conductance induced by Kv1 channels is that action potentials of MSO neurons recorded at the soma are very small (in mature gerbils around 10-15 mV; Scott et al., 2005 and 2007; also see Chapter 2, Figure 4D, E). Axonal loose-patch recordings showed that in the axons of MSO neurons, beyond the initial segment, action potentials are all-or-nothing responses, whereas they are graded at the soma (Scott et al., 2007). Since action potentials of MSO neurons are generated in the axon, the APs observed in the soma are the result of backpropagation (Scott et al., 2005 and 2007; also see Chapter 2). Blocking Kv1 channels substantially increases the AP amplitude to around 40 mV (Scott et al., 2005). Although this value is still small for an action potential (compared to the 100 mV or more in pyramidal cells; Palmer et al., 2006; Popovic et al., 2011), it shows that Kv1 channels have a significant part in controlling the AP amplitude in MSO neurons. Other mechanisms that keep the AP amplitude small are most likely the considerable capacitive load of the MSO's somatodendritic membrane and the additional leak imposed by HCN channels. Considering the MSO neuron's task is coincidence detection, a small somatodendritic AP amplitude is highly desirable, since a massive invasion of APs to the somatodendritic membrane would disturb the temporally delicate integration of synaptic inputs.

Aside from the additional leak, also the fast activation time constant of Kv1 currents

shows to have a substantial impact on the processing of inputs in the MSO (Scott et al., 2005; Jercog et al., 2010). Due to the rapid activation kinetics<sup>6</sup>, cells expressing Kv1 channels show a filtering property regarding the synaptic inputs in that they inhibit AP firing for slow depolarizing slopes (Jercog et al., 2010). Recordings *in vitro* and computational modeling suggests that MSO neurons often do not elicit an AP when stimulated with slow input currents, whereas currents with a steeper slope evoke an AP with higher likelihood (Svirskis et al., 2002; Svirskis et al., 2004). In Chapter 2, *in vitro* recordings yielded results that corroborate the preference for fast depolarizations (Chapter 2; Figure 4B-E). Computational modeling of MSO neurons also demonstrated the preference for steep excitatory inputs in temporally extended naturalistic input trains (Jercog et al., 2010 and Chapter 2, Figure 4A). The bias towards steep slopes owing to a low-threshold potassium current was also observed in other auditory brainstem neurons, like the bushy and octopus cells of the VCN (Ferragamo and Oertel, 2002; McGinley and Oertel, 2006), and for neurons of the vestibular pathway (Beraneck et al., 2007). In the sound localization circuitry of the auditory brainstem, the reason for such a slope preference can most likely be found in the need for temporal precision and synchronicity of the signaling. Asynchronous inputs with a comparably large temporal jitter are most likely to produce a summed input which is too slow to evoke an AP, since the Kv1 channels would rapidly open, raise the AP threshold and thus inhibit firing. On the other hand, synchronous synaptic inputs result in a steep summed EPSP which rapidly drives the membrane potential to threshold, not giving Kv1 channels enough time to open up (Jercog et al., 2010). Consequently, a neuron with a significant Kv1 channel expression elicits action potentials with a short latency with respect to the arrival time of the synaptic input and thus ensures the temporal precision in the auditory pathway (for review, see Trussell, 1999).

With decay time constants of around 0.3 milliseconds for excitatory and around 1.5 milliseconds for inhibitory synaptic inputs, the inputs to the MSO (and the auditory brainstem in general) are some of the fastest in the central nervous system (Trussell, 1999; Couchman et al., 2010; also see Chapter 3, Supplementary Figure 1). Nevertheless, the fast activation kinetics enable Kv1 channels to have a strong impact

---

<sup>6</sup> Mathews et al. (2010) report an activation time constant of the currents mediated by Kv1 channels of roughly 1 millisecond at 35 °C.

on shaping the membrane responses to even these brief synaptic inputs (Svirskis et al., 2004; Scott et al., 2005; Mathews et al., 2010). *In vitro* recordings of MSO neurons have shown that blocking Kv1 channels broadens the half-width of excitatory postsynaptic potentials (Scott et al., 2005; Mathews et al., 2010). Thus, Kv1 channels contribute to the sharpening of EPSPs thus facilitating the temporal resolution of coincidence detection in MSO neurons (Scott et al., 2005).

Apart from the EPSPs, also IPSPs are influenced by Kv1 channels (Roberts et al., 2013; also see Chapter 3, Figure 3 and Chapter 4, Figure 7). In Chapter 3 we found that an active Kv1 channel accelerates the decaying phase of IPSPs, thereby facilitating the peak shift of the net EPSP particularly for leading inhibitory inputs (Chapter 3, Figure 3f,g,j). A plausible mechanism underlying this sharpening of IPSPs is based on the interplay of Kv1 and HCN channels in MSO neurons which is presented in Chapter 4 (Figure 7). Since the Kv1 kinetics are fast enough to follow the time course of IPSPs, Kv1 channels are closing during the hyperpolarizing phase of the IPSP. The successive closing of Kv1 channels induces membrane equilibrium potential to move towards the much more depolarized reversal potential of HCN currents<sup>7</sup>, thereby dramatically increasing the driving force during the decaying phase of the IPSP. As a consequence, the decay of the IPSP is substantially accelerated, resulting in a decrease of the IPSP half-width (Chapter 4, Figure 7F, G). Removing the fast kinetics of Kv1 channels by dramatically increasing the activation time constant, or by strongly hyperpolarizing the Kv1 activation, such that it does not significantly close during an IPSP, strongly impedes the effect of IPSP sharpening (Chapter 3, Figure 3f,g,j). The same happens when making the shift of the equilibrium potential impossible by moving the HCN reversal close to the resting potential of the neuron – which also demonstrates the importance of HCN channels keeping Kv1 channels within their optimum working range (Chapter 4, Figure 7F, G).

The interplay of Kv1 and HCN channels has also been investigated in another

---

<sup>7</sup> The resting potential of MSO neurons of around -64 mV is mainly induced by two sub-threshold channels expressed in MSO neurons, Kv1 and HCN. The current mediated by Kv1 channels is estimated to reverse at more hyperpolarized potentials (around -100 mV) compared to the resting potential. On the other hand, the HCN current, which apart from potassium ions, is mediated by sodium ions, reverses at much more depolarized membrane potentials (around -35 mV).

interesting study combining patch-clamp recordings and computational modeling (Khurana et al., 2011). Khurana et al. (2011) show that the interplay of Kv1 and HCN channels helps to stabilize the shape and amplitude of individual EPSPs in synaptic input trains of up to several seconds. Moreover, assuming short-term depression of synaptic inputs (Couchman et al., 2010), they demonstrate that an interaction of Kv1 and HCN channels helps to maintain the temporal resolution of MSO neurons during synaptic input trains. This prediction, however, assumes the input resistance to increase over time during the input trains, which Khurana et al. (2011) indeed found to occur in their experiments and modeling. In the light of the synaptic bombardment of strong excitatory and inhibitory inputs of MSO neurons *in vivo*, however, an increase as opposed to a decrease of input resistance seems to be rather controversial. Indeed, Khurana et al. (2011) stimulated with currents instead of synaptic inputs, which would have induced an additional (synaptic) leak to the membrane counteracting the input resistance increase. Furthermore, the prominent inhibitory inputs that MSO neurons receive were not included in neither the experiment nor in the computational model. The omission of inhibitory inputs poses two intertwined problems. First, the comparably slow time course of the MSO's glycinergic inhibitory synaptic inputs would result in temporal summation, thus imposing a steady transmembrane current flow (causing an input resistance decrease). Second, without inhibition, HCN channels progressively close during the purely excitatory (thus depolarizing) input trains, which possibly contributed to the increase of the input resistance. In sum, the exclusion of inhibitory inputs might be a problematic choice to investigate the evolution of input resistance as well as the interaction of Kv1 and HCN channels in MSO neurons *in vivo*.

### *Summary*

Kv1 channels strongly contribute to provide the basis for the exceptional temporal precision of coincidence detection in the MSO. Being already open at rest, Kv1 channels add to the particularly large membrane conductance of MSO neurons, which in turn facilitates the MSO neuron's temporal fidelity by lowering the membrane time constant, increasing the current threshold, and restricting the impact of backpropagating action potentials to the somatodendritic membrane. Due to the fast activation time

constant, the strong outward current mediated by Kv1 channels ensures low-latency firing and furthermore induces the sharpening of excitatory and inhibitory postsynaptic potentials. To perform its task, an interaction of Kv1 and HCN channels is of particular importance. The counteracting nature of these two channels is especially well-suited considering the excitatory and inhibitory synaptic bombardment MSO neurons receive. On synaptic activity, Kv1 channels act on a short time scale shaping individual responses, while HCN channels counterbalance the high-frequency (and temporally summing) glycinergic inhibition, thus keeping Kv1 channels within their optimum operating range.

### **5.3. The role of glycinergic inhibition in mammalian ITD processing**

One of the key arguments against the Jeffress model to be applicable to mammalian ITD processing is the vast occurrence of non-zero characteristic phases (CPs) obtained for the coincidence detectors of the MSO (see Introduction). In the gerbil MSO, for example, CPs are uniformly distributed between  $\pm 1/4^{\text{th}}$  of a cycle (Pecka et al., 2008), rather than to concentrate around zero as the Jeffress model would imply. Candidate mechanisms generating non-zero CPs could, for example, be based on an asymmetry of the kinetics of ipsi- and contralateral inputs, or asymmetries in the anatomy or electrical properties of the ipsi- and contralateral dendrites (Zhou et al., 2005; Jercog et al., 2010, but see van der Heijden et al., 2013 and Franken et al., 2015). However, to date no evidences for such asymmetries exist. Moreover, in a thorough study of the MSO's dendritic anatomy no significant differences between the medial and the lateral dendrite could be found (Rautenberg, et al., 2009). Another candidate which could evoke non-zero CPs is the theory of stereausis (Schroeder, 1977; Shamma et al., 1989) which introduces the possibility that inputs from one ear are evoked at a slightly different locus along the cochlea than the inputs from the other ear. In theory, such small differences could indeed take account for the CPs measured *in vivo* (Shamma et al., 1989; Joris et al., 2006; Day and Semple, 2011). Up to this point, experimental evidence supporting this proposition is lacking and, regarding the difficulties tracking individual

MSO inputs back to a specific position alongside the cochlea, is not to be expected soon. A further candidate to produce non-zero CPs which *is* corroborated by numerous experimental results, is the phase-locked glycinergic inhibition to the principal cells of the MSO. MSO neurons receive glycinergic phase-locked inhibitory inputs from the ipsi- and the contralateral ear, mediated by the lateral and medial nucleus of the trapezoid body, respectively (see Introduction). The role of this feedforward inhibition for ITD processing in the MSO is a topic of intense debate. This subchapter discusses the recent developments of this debate.

*In vivo* measurements of the ITD sensitivity of MSO neurons show a preference for positive (i.e. contra-leading) ITDs (McAlpine et al., 2001; Brand et al., 2002; Pecka et al., 2008; van der Heijden et al., 2013). Direct evidence for the influence of glycinergic inhibition on the MSO's ITD sensitivity was provided by applying the glycine-antagonist strychnine *in vivo*, which shifted the best ITD towards zero (Brand et al., 2002; Pecka et al., 2008). This result gave rise to the development of the inhibition model that provides a possible mechanism underlying the shift of ITD sensitivity towards positive ITDs (Grothe, 2003) as well as the generation of non-zero CPs (Grothe et al., 2010; Leibold, 2010). The inhibition model states that apart from the mere presence of phase-locked inhibition, also its timing relative to the excitatory input from the same side is imperative to explain the *in vivo* data (Grothe, 2003; Pecka et al., 2008). To account for the bias towards positive ITDs seen in most MSO cells, the contralateral inhibition has to precede the contralateral excitation by a couple of hundred microseconds and/or the ipsilateral inhibition must arrive at the same time or slightly after the ipsilateral excitation. This temporal arrangement of the inhibitory inputs would lead to a lag or advance of the net EPSP peak from the contralateral and ipsilateral side, respectively (Grothe, 2003). In Chapter 3, the mechanism behind the net EPSP peak shifts is explained assuming MSO cells integrate linearly (Chapter 3, Figure 2i,j; Roberts et al., 2013; van der Heijden et al., 2013). As a result of the EPSP peak shifts, the best coincidence of the ipsi- and contralateral net EPSPs is obtained for contra-leading (hence positive) ITDs. Furthermore, the asymmetry of the net inputs from both sides gives rise to a non-zero CP (Grothe et al., 2010; Leibold, 2010).

Evidence that feedforward inhibition is indeed a plausible candidate mechanism to mediate non-zero CPs observed *in vivo* is provided by a recent study of neurons in the dorsal nucleus of the lateral lemniscus (DNLL; Siveke et al., 2012). As a direct target of the binaural nuclei in the SOC, the neurons of the DNLL inherit the ITD and ILD sensitivity generated in the MSO and LSO (see Introduction). Performing extracellular recordings from single neurons in the DNLL *in vivo*, Siveke et al. (2012) found that, compared to a control group, the sensitivity to ITDs and ILDs is significantly changed after the animals are exposed to omnidirectional ambient noise for two weeks. The changes in binaural sensitivity, that involve a significant rise of the CP, are reversible, as they were not present after a recovery period of two weeks in a normal acoustical environment. Using a computational modeling approach it was found that an upregulation of inhibition in the MSO and LSO is capable of explaining the observed changes in binaural sensitivity. The study of Siveke et al. (2012) thus provides important indications in support of the hypothesis of feedforward inhibition tuning ITD processing. Considering the time scales involved, the control of the synaptic efficacy of feedforward inhibition presents a conceivable and efficient mechanism underlying the observed plasticity of CPs.

An interesting problem which the inhibition model has to face is that even though the ipsi- and contralateral inhibition has to pass an extra nucleus (and thus an extra synapse imposing a time delay) compared to the excitatory inputs, it is supposed to arrive earlier or only slightly later than the corresponding excitatory input. Remarkably, the mammalian ITD circuitry seems to be prepared for exactly this. The MNTB, mediating the contralateral inhibition, receives its inputs from the contralateral GBCs via particularly large fibers and the largest, fastest and most secure synapse in the mammalian brain (the calyx of Held; Harrison and Warr, 1962; Morest, 1968; von Gersdorff and Borst, 2002; Borst and Soria van Hoeve, 2012). The less investigated LNTB, mediating the ipsilateral inhibition, receives large synapses from the ipsilateral GBCs (albeit not as large as the calices of Held) and has shown to also be capable of providing rapid and temporally precise inhibition to the MSO (Roberts et al., 2014). Interestingly, despite the longer contralateral inhibitory pathway, both inhibitory inputs arrive with the same delay. Using a thick slice preparation (1 to 1.5 millimeters) which

leaves the ITD circuitry from the auditory nerve to the MSO intact, it was found that the latency and jitter of IPSPs at the MSO evoked by stimulating the auditory nerve on either side, is not significantly different (Roberts et al., 2014). In an earlier study, employing the same thick slice setup and providing the first study in which IPSPs in the MSO could be evoked by stimulating the auditory nerve, it was shown that inhibitory inputs from either side arrives around 0.3 to 0.4 milliseconds earlier than the corresponding excitatory input (Roberts et al., 2013). Consequently, Roberts et al. (2013) used conventional slices (200  $\mu\text{m}$ , horizontal cut) to perform coincidence detection experiments evoking EPSPs by activating afferent fibers (while inhibition was blocked) and simulating inhibitory inputs with a dynamic-clamp setup. Applying the measured inhibition timing profile, no significant shift of the best ITD was found (Roberts et al., 2013; also see the Supplementary Figure S2). This is in line with the results in Chapter 3, employing a similar inhibitory timing (Chapter 3, Figure 4f,g). However, one has to stress the fact that the *in vivo* timing of inhibition is still unclear. Also, the thick slice *in vitro* experiments in Roberts et al. (2013 and 2014) were performed with tissue of P15-P20 animals, amidst a developmental period of, for example, membrane and inhibitory input properties, and thus might not represent the inhibitory timing of a matured circuitry (Magnusson et al., 2005; Scott et al., 2005). Finally, the subsequent coincidence detection experiments were restricted to the average timing of inhibition, and thus did not do justice to the diversity of the measured inhibitory timings (preceding the excitation by 0.15 to 0.54 milliseconds) which is likely to be even larger *in vivo*.

Despite the original inhibition model (Grothe, 2003) already incorporated the ipsi- and contralateral inhibition, it was assumed that the contralateral inhibition is the predominant factor that tunes coincidence detection in the MSO. This assumption was mainly based on the circumstance that the contralateral inhibitory pathway via the MNTB is much more investigated and admits extraordinary anatomical and physiological features with respect to its reliability, speed and accuracy (von Gersdorff and Borst, 2002; Borst and Soria van Hove, 2012; also see Introduction). In the seminal paper demonstrating glycinergic inhibition to influence coincidence detection in the MSO, a computational model was generated to explain the *in vivo* findings (Brand et

al., 2002). And indeed, this model featured contralateral inhibition only, with an inhibitory decay time constant of only 0.1 milliseconds, which is much faster than the value later found in *in vitro* measurements (1-2.5 milliseconds; Magnusson et al., 2005; Couchman et al., 2010; also see Chapter 3, Supplementary Figure 1). Consequently, it has been argued that inhibition is not capable of producing large enough shifts (or any shift at all) of the best ITD to explain *in vivo* results due to its (too) slow kinetics (Jercog et al., 2010; Day and Semple, 2011; Roberts et al., 2013). In Chapter 3, the time courses of excitatory and inhibitory synaptic conductances (ESPGs and IPSGs) were extracted in voltage-clamp experiments. To assess the magnitude of the inhibition-enforced peak shifts, these EPSGs and IPSGs were used as templates to inject them into the soma in conductance-clamp using a broad parameter space of arrival times of inhibitory inputs relative to the excitatory inputs. It was found that despite the slow IPSG decay (around 1.5 milliseconds) a leading inhibitory input is capable of tuning the coincidence detection provided a lead of at least 0.4 milliseconds<sup>8</sup> (Chapter 3, Figure 4). However, it was also found that the contralateral inhibition alone is indeed not sufficient to generate large enough shifts to explain *in vivo* data of MSO ITD sensitivity. Instead it was observed that IPSGs arriving at the same time or slightly after (0 to 0.2 milliseconds) the EPSGs are capable of creating a larger shift of the net EPSP peak compared to leading inhibition. Hence, a slightly lagging ipsilateral inhibitory input would strongly facilitate the preference of positive (contra-leading) ITDs, and thus, together with the contralateral (leading) inhibition, would be capable of generating the best ITD shift witnessed *in vivo*. Regarding the results in Chapter 3 we conclude that albeit the ipsilateral inhibition already has been a part of the original inhibition model (Grothe, 2003), its importance for the tuning of coincidence detection was underestimated so far. A very recent study provided the first thorough assessment of the intrinsic physiology of LNTB neurons showing that they indeed are capable of providing rapid and precise inhibition to the MSO, which corroborates our result assigning a key role of ipsilateral inhibition in coincidence detection (Roberts et al., 2014).

---

<sup>8</sup> This number depends on the decay time constant of the excitatory inputs. Using fiber stimulation a diversity of EPSP kinetics with decay time constants ranging from 0.2 to 0.5 milliseconds was observed (Chapter 3, Supplementary Figure 1).

Up to this point in time, the very most of studies investigating the physiology and the synaptic inputs of MSO neurons have been performed *in vitro*. Only recently, using a ventral approach to the low-frequency part of the MSO, van der Heijden et al. (2013) were able to perform the first *in vivo* whole-cell recordings of (three) MSO neurons. Furthermore, several MSO neurons were recorded with a loose-patch (juxtacellular) setting. Examining raw traces obtained in both recording modes no evidence for a well-timed inhibition was found (van der Heijden et al., 2013). It was concluded that inhibition does not play a role in tuning MSO coincidence detection because it could not be detected. In Chapter 2 we used naturalistic synaptic input trains to drive our MSO model. And indeed, due to the comparably slow time course of IPSPs, inhibitory inputs are hardly noticeable in somatic membrane potential traces (Chapter 2, Figure 1E). Similarly, in Chapter 3, conductance trains of up to 800 Hz were used to assess the maintenance of inhibition efficacy in ongoing stimulation regimes. Especially during high frequency input trains, inhibitory timing was impossible to assess, hinting why inhibitory events might be hard to distinguish *in vivo*. However, in both, simulations and *in vitro* dynamic clamp experiments, inhibitory events still substantially modulated the net EPSP peak timing (Chapter 3, Figure 6) and best ITD (Chapter 2, Figure 8), despite being hard to detect. Furthermore, simulating synaptic jitter in dynamic-clamp experiments, a putative lowered precision of synaptic timing showed to facilitate peak shifts (Chapter 3, Figure 5), instead of impeding them as has been suggested before (Roberts et al., 2013; van der Heijden et al., 2013). Finally, a very recent study performing whole-cell recordings of MSO cells *in vivo* was published challenging (among other models) the role of glycinergic inhibition in the tuning of ITD sensitivity (Franken et al., 2015). In this study, Franken et al. (2015) hypothesize that the application of strychnine using iontophoresis generates unwanted side-effects and can not be used to find specific effects of the blocking of inhibitory inputs only. Although Franken et al. also observe ITD peak shifts along with a raise in firing rate, when reproducing the experiments of Brand et al. (2002) and Pecka et al. (2008), they report that this effect changed over time after strychnine application, eventually leading to an overall decrease of firing rate and even loss of ITD sensitivity of the cell. The loss of ITD sensitivity was attributed to a steady build up of strychnine levels (caused by the iontophoretic application of the drug) up to a point where unspecific effects manifest.

To prevent this, pressure application of a much smaller dose of strychnine (2  $\mu$ M for 18 minutes) was used (compared to 10 mM used in iontophoresis), which showed the same amount of firing rate increase. In this setup, however, no significant shift of ITD sensitivity could be observed. As a consequence, Franken et al. (2015) conclude, that glycinergic inhibition can not account for the tuning of coincidence detection in MSO neurons. Following the argument of Franken et al. (2015), that a build up of strychnine over time to harmful levels ensues when applying the drug using iontophoresis, as well as considering their own results, that during the time window of increased firing rate a shift of ITD sensitivity *was* observed, this conclusion is somewhat surprising.

Nonetheless, the inhibitory model *does* show limitations to explain *in vivo* best ITD data. Both, the computational modeling approach as well as the electrophysiological experiments performed in Chapter 2 and 3, demonstrated that phase-locked inhibitory inputs are capable of tuning coincidence detection of MSO neurons for low and medium frequency inputs. For higher frequency inputs (> 600 Hz) the induced phase shifts of the net EPSP peaks are substantial, although not large enough to enforce best ITD outside of the physiological range. Therefore, it is possible that to explain *in vivo* results for frequencies around 800-1500 Hz, an interaction of phase-locked inhibition with other mechanisms is necessary.

### *Summary*

A well-timed glycinergic inhibition to MSO neurons has shown to be capable of explaining *in vivo* ITD sensitivity data, as well as the generation and plasticity of non-zero CPs found in MSO neurons and their direct targets, the neurons of the DNLL. Despite constituting a plausible, theoretically and experimentally corroborated model, the role of glycinergic inhibition in the MSO is a topic of intense debate. The main points of criticism, such as (1) the inhibitory inputs being temporally not precise enough, (2) IPSPs mostly being undetectable in traces, and (3) IPSPs being too slow to account for a sufficient shift, are opposed by a variety of electrophysiological, anatomical and theoretical results demonstrating (1) the exceptional temporal accuracy of the inhibitory pathway, (2) the efficacy of well-timed inhibition tuning the ITD

sensitivity despite being hard to detect in the trace (shown in Chapter 2 and 3), and (3) the underestimated importance of the ipsilateral inhibition (shown in Chapter 3). For high-frequencies ( $> 600$  Hz), the inhibition model, however, shows its limitations, suggesting that an interaction of well-timed inhibition and other mechanisms could be necessary to explain *in vivo* data. In conclusion, the developments of the past few years, including our article in Chapter 3, demonstrate that the debate on how ITD sensitivity is tuned in MSO neurons in general, and in particular on the role of well-timed inhibition, is still in full swing and ready for another round.

#### **5.4. Concluding remarks and outlook**

In this thesis we gained new insights on biophysical, physiological and functional properties of MSO neurons. In three peer-reviewed articles, the author of this thesis performed computational modeling of MSO neurons to gain the major proportion of the results (Chapter 2) or to aid answering experimentally-intractable questions in electrophysiological studies (Chapter 3 and 4). This last section is dedicated to briefly review the yet unanswered questions in the context of these three articles.

In Chapter 2, using a multi-compartment model of an MSO neuron and its axon we show that despite the extraordinarily leaky MSO soma the axon maintains the excitability of the neuron. We found that, unlike the general assumption of the AIS being the singular AP initiation site in central neurons, APs were also initiated in more distal axonal site, such as the first nodes of Ranvier, especially at threshold and for high-frequency inputs. Even though the model was morphologically and physiologically well-constrained, this is purely a theoretical result and thus can merely yield a prediction concerning MSO cell firing. To test the predictions made regarding the AP initiation site in MSO neurons, as a next step, *in vitro* recordings and the usage of voltage-sensitive dye (VSD) combined with fast imaging would be desirable. This method was already successfully employed to investigate the AP initiation site in pyramidal and Purkinje neurons (Palmer et al., 2006; Foust et al., 2010; Palmer et al., 2010; Popovic et al., 2011; also see Section 5.1). Following the results in our theoretical study, the hypothesis should be tested in situations in which we found the highest

prevalence of distal AP initiation, with a particular focus on mimicking strong (and high-frequency) synaptic bombardment. Our study also raises the question of whether the predictions are restricted to MSO neurons only. Although the site of AP initiation has been scrutinized in other neuronal types using VSD, mostly only singular current pulses or low-frequency trains of current pulses were used to stimulate the neuron. Using VSD in another neuronal type, such as Purkinje neurons or layer 5 pyramidal cells, combined with mimicking naturalistic synaptic activity at an up-state (Shu et al., 2007) and evaluating the initiation site for every single AP generated could possibly show similar effects as proposed in our study.

Conducting dynamic-clamp recordings in MSO slices, in Chapter 3 it was demonstrated that a well-timed inhibition can account for the best ITD bias towards contra-leading stimuli observed in MSO neurons (Brand et al., 2002; Pecka et al., 2008; Leibold, 2010; van der Heijden et al., 2013). Following the result of the study, we extended the existing inhibition model (Grothe, 2003) by strongly emphasizing the importance of the ipsilateral inhibition, as well as presenting timing conditions for the inhibitory inputs that provide highest efficacy in tuning the ITD sensitivity. The relative timing of inhibitory inputs with respect to the excitatory inputs from the same side *in vivo*, is, however, still elusive. Although first *in vivo* whole-cell recordings of MSO neurons were established (van der Heijden et al., 2013; Franken et al., 2015), it is very hard to separate excitatory and inhibitory events to measure latencies, and thus remains a hard, nonetheless important, problem to solve in the future.

Finally, in the paper in Chapter 4, performing *in vitro* patch-clamp recordings, it was found that the properties of HCN currents ( $I_h$ ) systematically change along the tonotopical (dorsoventral) axis of the MSO. In the putative high-frequency (ventral) part  $I_h$  is larger and faster than in the low-frequency (dorsal) part of the MSO. Using a computational model of an MSO neuron we show that the larger  $I_h$  facilitates the processing of high-frequency inputs in ventral neurons. As ventral neurons showed to have a substantially lower input resistance and time constant, but a similar resting potential *in vitro*, we had to adjust the Kv1 conductance in the model accordingly to the HCN gradient as a counterbalance. Consequently, as a future study it would be of interest to test our assumption of a Kv1 gradient along the dorsoventral axis of the MSO.



## References

- Adams JC Ascending projections to the inferior colliculus. *J Comp Neurol* 183:519-538, 1979.
- Adams JC and Mugnaini E. Dorsal nucleus of the lateral lemniscus: a nucleus of GABAergic projection neurons. *Brain Res Bull* 13:585-590, 1984.
- Adams JC and Mugnaini E. Immunocytochemical evidence for inhibitory and disinhibitory circuits in the superior olive. *Hear. Res.* 49, 281–298, 1990.
- Aitkin L and Shuck D. Low frequency neurons in the lateral central nucleus of the cat inferior colliculus receive their input predominantly from the medial superior olive. *Hear Res* 17:87-93, 1985.
- Atherton JF, Wokosin DL, Ramanathan S, Bevan MD. Autonomous initiation and propagation of action potentials in neurons of the subthalamic nucleus. *J Physiol* 586: 5679-5700, 2008.
- Banks MI and Smith PH. Intracellular recordings from neurobiotin-labeled cells in brain slices of the rat medial nucleus of the trapezoid body. *J. Neurosci.* 12, 2819–2837, 1992.
- Baranauskas G, David Y, Fleidervish IA. Spatial mismatch between the Na<sup>+</sup> flux and spike initiation in axon initial segment. *Proc Natl Acad Sci USA* 110:4051–4056, 2013.

- Barnes-Davies M, Barker MC, Osmani F, Forsythe ID. Kv1 currents mediate a gradient of principal neuron excitability across the tonotopic axis in the rat lateral superior olive. *Eur. J. Neurosci.*, 19, 325–333, 2004.
- Batra R, Kuwada S, Fitzpatrick DC. Sensitivity to interaural temporal disparities of low- and high-frequency neurons in the superior olivary complex. I. Heterogeneity of responses. *J Neurophysiol* 78:1222–1236, 1997a.
- Batra R, Kuwada S, Fitzpatrick DC. Sensitivity to interaural temporal disparities of low- and high-frequency neurons in the superior olivary complex. II. Coincidence detection. *J Neurophysiol* 78:1237–1247, 1997b.
- Bean BP. The action potential in mammalian central neurons. *Nat Rev Neurosci* 8: 451–465, 2007.
- Beckius GE, Batra R, Oliver DL. Axons from anteroventral cochlear nucleus that terminate in medial superior olive of cat: Observations related to delay lines. *Journal of Neuroscience* 19:3146- 3161, 1999.
- Bender KJ, Trussell LO. Axon initial segment  $Ca^{2+}$  channels influence action potential generation and timing. *Neuron* 61: 259-271, 2009.
- Bender KJ, Trussell LO. The physiology of the Axon Initial Segment. *Annu Rev Neurosci* 35:249-265, 2012.
- Beraneck M, Pfanzelt S, Vassias I, Rohregger M, Vibert N, Vidal PP, Moore LE, Straka H. Differential intrinsic response dynamics determine synaptic signal processing in frog vestibular neurons. *J Neurosci* 27:4283– 4296, 2007.

- Bernstein J. Untersuchungen zur Thermodynamik der bioelektrischen Ströme. Pflügers Arch 92:521–562, 1902.
- Bernstein J. Elektrobiologie. Die Lehre von den elektrischen Vorgängen im Organismus auf moderner Grundlage dargestellt. Vieweg & Sohn, Braunschweig, 1912.
- Bernstein LR. Auditory processing of interaural timing information: new insights. J Neurosci Res 66:1035-1046, 2001.
- Beurrier C, Congar P, Bioulac B, Hammond C. Subthalamic nucleus neurons switch from single spike activity to burst-firing mode. J Neurosci 19:599–609, 1999.
- Biel M, Wahl-Schott C, Michalakis S, Zong X. Hyperpolarization-Activated Cation Channels: From Genes to Function. Physiol Rev 89:847-885, 2009.
- Bischofberger J, Jonas P. Action potential propagation into the presynaptic dendrites of rat mitral cells. J Physiol 504: 359-365, 1997.
- Borst JGG, and Soria van Hoeve J. The calyx of held synapse: from model synapse to auditory relay. Annu Rev Physiol 74, 199–224, 2012.
- Boudreau JC, Tsuchiani C. Binaural interaction in the cat superior olive S segment. J Neurophysiol 31:442-454, 1968.
- Boudkazi S, Carlier E, Ankri N, Caillard O, Giraud P, Fronzaroli-Molinieres L, Debanne D. Release-dependent variations in synaptic latency: a putative code

for short- and long-term synaptic dynamics. *Neuron* 56: 1048–1060, 2007.

Brand A, Behrend O, Marquardt T, McAlpine D, Grothe B. Precise inhibition is essential for microsecond interaural time difference coding. *Nature* 417:543-547, 2002.

Brew HM, Forsythe ID. Two voltage-dependent K<sup>+</sup> conductances with complementary functions in postsynaptic integration at a central auditory synapse. *J Neurosci* 15:8011–8022, 1995.

Brugge JF, Anderson DJ, Aitkin LM. Responses of neurons in the dorsal nucleus of the lateral lemniscus of cat to binaural tonal stimulation. *J Neurophysiol* 33: 441-458, 1970.

Brugge JF, Dubrovsky NA, Aitkin LM, Anderson DJ. Sensitivity of single neurons in auditory cortex of cat to binaural tonal stimulation: effects of varying interaural time and intensity. *J Neurophysiol* 32: 1005-1024, 1969.

Brugge JF, Merzenich MM. Responses of neurons in auditory cortex of the macaque monkey to monaural and binaural stimulation. *J Neurophysiol* 36: 1138-1158, 1973.

Brungart DS, Rabinowitz WM. Auditory localization of nearby sources. Head-related transfer functions. *J Acoust Soc Am* 106:1465-1479, 1999.

Brunso-Bechtold JK, Thompson GC, Masterton RB. HRP study of the organization of auditory afferents ascending to central nucleus of inferior colliculus in cat. *J Comp Neurol* 197:705-722, 1981.

- Caird D, and Klinke R. Processing of binaural stimuli by cat superior olivary complex neurons. *Exp Brain Res* 52:385–399, 1983.
- Caird D, Klinke R. Processing of interaural time and intensity differences in the cat inferior colliculus. *Exp Brain Res* 68:379–392, 1987.
- Cant NB. Projections to the lateral and medial superior olivary nuclei from the spherical and globular bushy cells of the anteroventral cochlear nucleus. In: *Neurobiology of hearing: The central auditory system* (Altschuler RA, Bobbin RP, Clopton BM, Hoffman DW, eds), pp 99-119. New York: Raven Press, 1991.
- Cant NB, Casseday JH. Projections from the anteroventral cochlear nucleus to the lateral and medial superior olivary nuclei. *J Comp Neurol* 247:457-476, 1986.
- Cant NB, Hyson RL. Projections from the lateral nucleus of the trapezoid body to the medial superior olivary nucleus in the gerbil. *Hear Res* 58:26-34, 1992.
- Carr CE, Konishi M. A circuit for detection of interaural time differences in the brain stem of the barn owl. *J Neurosci* 10:3227-3246, 1990.
- Clark BA, Monsivais P, Branco T, London M, Hausser M. The site of action potential initiation in cerebellar Purkinje neurons. *Nat Neurosci* 8: 137–139, 2005.
- Clark GM. Vesicle shape versus type of synapse in the nerve endings of the cat medial superior olive. *Brain Research* 15:548-551, 1969.

- Colbert CM, Johnston D. Axonal action-potential initiation and Na<sup>+</sup> channel densities in the soma and axon initial segment of subicular pyramidal neurons. *J Neurosci* 16:6676–6686, 1996.
- Colbert CM, Pan E. Ion channel properties underlying axonal action potential initiation in pyramidal neurons. *Nat Neurosci* 5:533–538, 2002.
- Cole KS, Curtis HJ. Electrical impedance of the squid giant axon during activity. *J Gen Physiol* 22 (5): 649–670, 1939.
- Conlee JW, Parks TN, Romero C, Creel DJ. Auditory brainstem anomalies in albino cats: II. Neuronal atrophy in the superior olive. *J Comp Neurol* 225:141-148, 1984.
- Conlee JW, Parks TN, Creel DJ. Reduced neuronal size and dendritic length in the medial superior olivary nucleus of albino rabbits. *Brain Res* 363:28-37, 1986.
- Coombs JS, Curtis DR, Eccles JC. The interpretation of spike potentials of motoneurons. *J Physiol* 139: 198–231, 1957.
- Couchman K, Grothe B, Felix F. Medial superior olivary neurons receive surprisingly few excitatory and inhibitory inputs with balanced strength and short-term dynamics. *J Neurosci* 30:17111-17121, 2010.
- Covey E, Casseday JH. The monaural nuclei of the lateral lemniscus in an echolocating bat: parallel pathways for analyzing temporal features of sound. *J Neurosci* 11:3456–3470, 1991.

- Crepel F, Penit-Soria J. Inward rectification and low threshold calcium conductance in rat cerebellar Purkinje cells. An in vitro study. *J Physiol* 372:1-23, 1986.
- Crow G, Rupert AL, Moushegian G. Phase locking in monaural and binaural medullary neurons: implications for binaural phenomena. *J Acoust Soc Am* 64:493-501, 1978.
- Day ML, Semple MN. Frequency-dependent interaural delays in the medial superior olive: implications for interaural cochlear delays. *J Neurophysiol* 106:1985-1999, 2011.
- Debanne D. Information processing in the axon. *Nat Rev Neurosci* 5:304-316, 2004.
- Debanne D, Campanac E, Bialowas A, Carlier E, Alcaraz G. Axon physiology. *Physiol Rev* 91: 555–602, 2011.
- Du Bois-Reymond E. Vorläufiger Abriß einer Untersuchung über den sogenannten Froschstrom und über die elektromotorischen Fische. *Annalen der Physik und Chemie* 58: 1–30, 1843.
- Du Bois-Reymond E. Untersuchungen über thierische Elektrizität. G.Reimer Verlag, Berlin, 1848. [this is the first version of the first of two volumes, the second volume was published in 1884]
- Eccles JC. *The physiology of synapses*. Springer-Verlag, Berlin, 1964.
- Englitz B, Tolnai S, Typlt M, Jost J, and Rübsamen R. Reliability of synaptic transmission at the synapses of held in vivo under acoustic stimulation. *PLoS*

One 4:e7014. doi: 10.1371/journal.pone.0007014, 2009.

Fatt P. Sequence of events in synaptic activation of a motoneurone. *J Neurophysiol* 20: 61– 80, 1957.

Ferragamo MJ, Oertel D. Octopus cells of the mammalian ventral cochlear nucleus sense the rate of depolarization. *J Neurophysiol* 87:2262–2270, 2002.

Fleidervish IA, Lasser-Ross N, Gutnick MJ, Ross WN. Na<sup>+</sup> imaging reveals little difference in action potential-evoked Na<sup>+</sup> influx between axon and soma. *Nat Neurosci* 2010.

Forsythe ID, Barnes-Davies M. The binaural auditory pathway: membrane currents limiting multiple action potential generation in the rat medial nucleus of the trapezoid body. *Proc Biol Sci* 251:143-150, 1993.

Foust A, Popovic M, Zecevic D, McCormick DA. Action potentials initiate in the axon initial segment and propagate through axon collaterals reliably in cerebellar Purkinje neurons. *J Neurosci* 30: 6891– 6902, 2010.

Franken TP, Roberts MT, Wei L, Golding NL, Joris PX. In vivo coincidence detection in mammalian sound localization generates phase delays. *Nat Neurosci* 18:444-452, 2015.

Friauf E, Ostwald J. Divergent projections of physiologically characterized rat ventral cochlear nucleus neurons as shown by intra-axonal injection of horseradish peroxidase. *Exp Brain Res* 73:263-284, 1988.

- Fuortes MG, Frank K, Becker MC. Steps in the production of motoneuron spikes. *J Gen Physiol* 40: 735–752, 1957.
- Galambos R, Davis H. The response of single auditory-nerve fibers to acoustic stimulation. *Journal of Neurophysiology* 6:39-57, 1943.
- Galambos R, Schwartzkopf J, Rupert A. Microelectrode study of superior olivary nuclei. *Am J Physiol* 197, 527–536, 1959.
- Galvani LA. De viribus electricitatis in motu musculari, commentarius. *Bononiensi scientiarum et artium instituto atque academia commentarii* 7. 364-415, 1791.
- Geiger JR, Jonas P. Dynamic control of presynaptic Ca<sup>2+</sup> inflow by fast-inactivating K<sup>+</sup> channels in hippocampal mossy fiber boutons. *Neuron* 28:927–39, 2000.
- Geisler CD, Rhode WS, Hazelton DW. Responses of inferior colliculus neurons in the cat to binaural acoustic stimuli having wide-band spectra. *J Neurophysiol* 32:960-974, 1969.
- Glendenning KK, Baker BN, Hutson KA, Masterton RB. Acoustic Chiasm V: inhibition and excitation in the ipsilateral and contralateral projections of LSO. *Journal of Comp Neurol* 319:100-122, 1992.
- Glendenning KK, Brunso-Bechtold JK, Thompson GC, Masterton RB. Ascending auditory afferents to the nuclei of the lateral lemniscus. *J Comp Neurol* 197:673-703, 1981.
- Glendenning KK, Masterton RB. Acoustic chiasm: efferent projections of the lateral

superior olive. *J Neurosci* 3: 1521-1537, 1983.

Goldberg JM, Brown PB. Response of binaural neurons of dog superior olivary complex to dichotic tonal stimuli: some physiological mechanisms of sound localization. *J Neurophysiol* 32:613- 636, 1969.

Golding NL, Robertson D, and Oertel D. Recordings from slices indicate that octopus cells of the cochlear nucleus detect coincident firing of auditory nerve fibers with temporal precision. *J Neurosci* 15:3138–3153, 1995.

Golding NL, Spruston N. Dendritic sodium spikes are variable triggers of axonal action potentials in hippocampal CA1 pyramidal neurons. *Neuron* 21:1189-1200, 1998.

Griffin SJ, Bernstein LR, Ingham NJ, McAlpine D. Neural sensitivity to interaural envelope delays in the inferior colliculus of the guinea pig. *J Neurophysiol* 93:3463-3478, 2005.

Grothe B. The evolution of temporal processing in the medial superior olive, an auditory brainstem structure. *Prog Neurobiol* 61:581-610, 2000.

Grothe B. New roles for synaptic inhibition in sound localization. *Nat Rev Neurosci* 4:540-550, 2003.

Grothe B, Pecka M. The natural history of sound localization in mammals – a story of neuronal inhibition. *Front Neural Circuits* 8:116, 2014.

Grothe B, Pecka M and McAlpine D. Mechanisms of sound localization in mammals.

Physiol Rev 90:983-1012, 2010.

Grubb MS, Burrone J. Activity-dependent relocation of the axon initial segment fine-tunes neuronal excitability. *Nature* 465:1070–1074, 2010.

Gründemann, J, Häusser M. Neuroscience: a plastic axonal hotspot. *Nature* 465:1022–1023, 2010.

Hancock KE, Delgutte B. A physiologically based model of interaural time difference discrimination. *J Neurosci* 24:7110-7117, 2004.

Harrison JM, Warr WB. A study of the cochlear nuclei and ascending auditory pathways of the medulla. *J Comp Neurol* 119:341–379, 1962.

Hartmann WM, Macaulay EJ. Anatomical limits on interaural time differences: an ecological perspective. *Front Neurosci* 8:34, 2014.

Häusser M, Stuart G, Racca C, Sakmann B. Axonal initiation and active dendritic propagation of action potentials in substantia nigra neurons. *Neuron* 15: 637–647, 1995.

Heffner RS, Heffner HE. Auditory function in albino cats. *Assoc Res Otolaryngol Abstr* 1987.

Hermann J, Pecka M, von Gersdorff H, Grothe B, Klug A. Synaptic transmission at the calyx of Held under in vivo-like activity levels. *J Neurophysiol* 98:807–820, 2007.

Hodgkin AL, Huxley AF, Katz B. Measurement of current-voltage relations in the membrane of the giant axon of *Loligo*. *J Physiol* 116:424-448, 1952.

Hodgkin AL, Huxley AF. Currents carried by sodium and potassium ions through the membrane of the giant axon of *Loligo*. *J Physiol* 116:449-472, 1952a.

Hodgkin AL, Huxley AF. The components of membrane conductance in the giant axon of *Loligo*. *J Physiol* 116:473-496, 1952b.

Hodgkin AL, Huxley AF. The dual effect of membrane potential on sodium conductance in the giant axon of *Loligo*. *J Physiol* 116:497-506, 1952c.

Hodgkin AL, Huxley AF. A quantitative description of membrane current and its application to conduction and excitation in nerve. *J Physiol* 117:500-544, 1952d.

Hodgkin AL, Katz B. The effect of sodium ions on the electrical activity of the giant axon of the squid. *J Physiol* 108: 37-77, 1949.

Hoff HE. Galvani and the pre-Galvanian electrophysiologists. *Annals of Science*, 1:2, 157-172, 1936.

Hoff HE, Geddes LA. Ballistics and the Instrumentation of Physiology: The Velocity of the Projectile and of the Nerve Impulse. *Journal of the History of Medicine and Allied Sciences* 15/2: 133-146, 1960.

- Hu W, Shu Y. Axonal bleb recording. *Neurosci Bull* 28:342-350, 2012.
- Hu W, Tian C, Li T, Yang M, Hou H, Shu Y. Distinct contributions of Na(v)1.6 and Na(v)1.2 in action potential initiation and backpropagation. *Nat Neurosci* 12:996-1002, 2009.
- Isaacson JS, Walmsley B. Receptors underlying excitatory synaptic transmission in slices of the rat anteroventral cochlear nucleus. *Journal of Neurophysiology* 73:964–973, 1995.
- Izhikevich EM. *Dynamical Systems in Neuroscience: The Geometry of Excitability and Bursting*. MIT Press, Cambridge, Massachusetts, 2007.
- Jeffress LA. A place theory of sound localization. *J Comp Physiol Psychol* 41:35-39, 1948.
- Jercog PE, Svirskis G, Kotak VC, Sanes DH, Rinzel J. Asymmetric excitatory synaptic dynamics underlie interaural time difference processing in the auditory system. *PLoS Biol* 8:e1000406, 2010.
- Joris PX, Carney LH, Smith PH, Yin TC. Enhancement of neural synchronization in the anteroventral cochlear nucleus. I. Responses to tones at the characteristic frequency. *J Neurophysiol* 71:1022–1036, 1994.
- Joris PX, Smith PH, Yin TC. Enhancement of neural synchronization in the anteroventral cochlear nucleus. II. Responses in the tuning curve tail. *J Neurophysiol* 71:1037–1051, 1994.

- Joris PX, Van de Sande B, Louage DH, van der Heijden M. Binaural and cochlear disparities. *Proc Natl Acad Sci USA* 103:12917–12922, 2006.
- Karino S, Smith PH, Yin TCT, Joris PX. Axonal delay lines from bushy cells to the medial superior olive: a reexamination. *Assoc Res Otolaryngol Abstr*, 2010.
- Kasper EM, Larkman AU, Lübke J, Blakemore C. Pyramidal neurons in layer 5 of the rat visual cortex. II. Development of electrophysiological properties. *J Comp Neurol* 339:475-494, 1994.
- Khaliq ZM, Raman IM. Axonal propagation of simple and complex spikes in cerebellar Purkinje neurons. *J Neurosci* 25: 454 – 463, 2005.
- Khaliq ZM, Raman IM. Relative contributions of axonal and somatic Na channels to action potential initiation in cerebellar Purkinje neurons. *J Neurosci* 26: 1935–1944, 2006.
- Khurana S, Liu Z, Lewis AS, Rosa K, Chetkovich D, Golding NL. An essential role for modulation of hyperpolarization-activated current in the development of binaural temporal precision. *J Neurosci* 32:2814–2823, 2012.
- Khurana S, Remme MWH, Rinzel J, Golding NL. Dynamic interaction of  $I_h$  and  $I_{K-LVA}$  during trains of synaptic potentials in principal neurons of the medial superior olive. *J Neurosci* 31:8936–8947, 2011.
- Kiang NY, Watanabe T, Thomas C, Clark LF. Discharge patterns of single fibres in the cat's auditory nerve. MIT Press, Cambridge, 1965.

- Koch C. Biophysics of computation: information processing in single neurons. Oxford University Press, New York, 1999.
- Koch U, Braun M, Kapfer C, Grothe B. Distribution of HCN1 and HCN2 in rat auditory brainstem nuclei. *Eur J Neurosci* 20:79-91, 2004.
- Kole MH, Ilshner SU, Kampa BM, Williams SR, Ruben PC, Stuart GJ. Action potential generation requires a high sodium channel density in the axon initial segment. *Nat Neurosci* 11: 178 –186, 2008.
- Kole MH, Letzkus JJ, Stuart GJ. Axon initial segment Kv1 channels control axonal action potential waveform and synaptic efficacy. *Neuron* 55:633-647, 2007.
- Kole MH, Stuart GJ. Signal processing in the axon initial segment. *Neuron* 73:235-247, 2012.
- Kopp-Scheinflug C, Lippe WR, Dorrscheidt GJ, Rubsamen R. The medial nucleus of the trapezoid body in the gerbil is more than a relay: comparison of pre- and postsynaptic activity. *J Assoc Res Otolaryngol* 4:1–23, 2003.
- Kopp-Scheinflug C, Steinert JR, Forsythe ID. Modulation and control of synaptic transmission across the MNTB. *Hear Res* 279:22-31, 2011.
- Kress GJ, Dowling MJ, Meeks JP, Mennerick S. High threshold, proximal initiation, and slow conduction velocity of action potentials in dentate granule neuron mossy fibers. *J Neurophysiol* 100:281–291, 2008.
- Kuba H, Ishii TM, Ohmori H. Axonal site of spike initiation enhances auditory

coincidence detection. *Nature* 444:1069–1072, 2006.

Kuba H, Oichi Y, Ohmori H. Presynaptic activity regulates Na<sup>+</sup> channel distribution at the axon initial segment. *Nature* 465:1075–1078, 2010.

Kuwabara N, DiCaprio RA, Zook JM. Afferents to the medial nucleus of the trapezoid body and their collateral projections. *J Comp Neurol* 314:684–706, 1991.

Kuwabara N, Zook JM. Projections to the medial superior olive from the medial and lateral nuclei of the trapezoid body in rodents and bats. *J. Comp. Neurol.* 324, 522–538, 1992.

Kuwada S, Yin TCT. Binaural interaction in low-frequency neurons in inferior colliculus of the cat. I. Effects of long interaural delays, intensity, and repetition rate on interaural delay function. *J Neurophysiol* 50:981–999, 1983.

Leibold C. Influence of inhibitory synaptic kinetics on the interaural time difference sensitivity in a linear model of binaural coincidence detection. *J Acoust Soc Am* 127:931-942, 2010.

Lesica NA, Lingner A, Grothe B. Population coding of interaural time differences in gerbils and barn owls. *J Neurosci* 30:11696–11702, 2010.

Lindsey BG. Fine structure and distribution of axon terminals from the cochlear nucleus on neurons in the medial superior olivary nucleus of the cat. *J Comp Neurol* 160:81-103, 1975.

Llinás RR. The intrinsic electrophysiological properties of mammalian neurons: insights

- into central nervous system function. *Science* 242:1654-1664, 1988.
- Lorincz A, Nusser Z. Molecular identity of dendritic voltage-gated sodium channels. *Science* 328:906-909, 2010.
- Lorteije JAM, Rusu SI, Kushmerick C, Borst JG. Reliability and precision of the mouse calyx of Held synapse. *J Neurosci* 29:13770-13784, 2009.
- Ma Y, Huguenard JR. Reemerging role of cable properties in action potential initiation. *Proc Natl Acad Sci USA* 110:3715–3716, 2013.
- Magnusson AK, Kapfer C, Grothe B, Koch U. Maturation of glycinergic inhibition in the gerbil medial superior olive after hearing onset. *J Physiol* 568:497-512, 2005.
- Mainen ZF, Joerges J, Huguenard JR, Sejnowski TJ. A model of spike initiation in neocortical pyramidal neurons. *Neuron* 15:1427–1439, 1995.
- Maki K, Furukawa S. Acoustical cues for sound localization by the Mongolian gerbil, *Meriones unguiculatus*. *Journal of the Acoustical Society of America* 118:872-886, 2005.
- Manis PB, Marx SO. Outward currents in isolated ventral cochlear nucleus neurons. *J Neurosci* 11:2865–2880, 1991.
- Mathews PJ, Jercog PE, Rinzel J, Scott LL, Golding NL. Control of submillisecond synaptic timing in binaural coincidence detectors by K(v)1 channels. *Nat Neurosci* 13:601-609, 2010.

- Matsubara JA. Calbindin D-28K immunoreactivity in the cat's superior olivary complex. *Brain Res* 508:353-357, 1990.
- McAlpine D, Jiang D, Palmer AR. A neural code for low-frequency sound localization in mammals. *Nat Neurosci* 4:396-401, 2001.
- McAlpine D, Jiang D, Shackleton TM, Palmer AR. Convergent input from brainstem coincidence detectors onto delay-sensitive neurons in the inferior colliculus. *J Neurosci* 18:6026-6039, 1998.
- McCormick DA, Prince DA. Post-natal development of electrophysiological properties of rat cerebral cortical pyramidal neurones. *J Physiol* 393:743-762, 1987.
- McGinley MJ, Oertel D. Rate thresholds determine the precision of temporal integration in principal cells of the ventral cochlear nucleus. *Hear Res* 216-217:52-63, 2006.
- McKay BE, and Turner RW. Physiological and morphological development of the rat cerebellar Purkinje cell. *J Physiol* 567:829-850, 2005.
- McLaughlin M, van der Heijden M, Joris PX. How secure is *in vivo* synaptic transmission at the calyx of Held? *J Neurosci* 28:10206-10219, 2008.
- Meeks JP, Jiang X, Mennerick S. Action potential fidelity during normal and epileptiform activity in paired soma-axon recordings from rat hippocampus. *J Physiol* 566:425-441, 2005.

- Moore BCJ. *An Introduction to the Psychology of Hearing* (Sixth edition). Emerald Publishing Group Limited, ISBN: 978-1-78052-038-4, 2012.
- Moore, RY, Goldberg JM. Ascending projections of the inferior colliculus in the cat. *J Comp Neurol* 121: 109-135, 1963.
- Moore JW, Stockbridge N, Westerfield M. On the site of impulse initiation in a neurone. *J Physiol* 336:301–311, 1983.
- Moore JK, Moore RY. Glutamic acid decarboxylase-like immunoreactivity in brainstem auditory nuclei of the rat. *J Comp Neurol* 260:157-174, 1987.
- Morest DK. The collateral system of the medial nucleus of the trapezoid body of the cat, its neuronal architecture and relation to the olivo-cochlear bundle. *Brain Res* 9:288–311, 1968.
- Moruzzi G. The electrophysiological work of Carlo Matteucci. *Brain Res. Bull.* 40:69-91, 1996 (translated by M. Piccolino, P. Witkovsky and A. Fiorentini; original (Italian) in “*Physis*” 4:101–140; 1964).
- Moushegian G, Rupert AL, Gidda JS. Functional characteristics of superior olivary neurons to binaural stimuli. *J Neurophysiol* 38:1037-1048, 1975.
- Neher E and Sakmann B. Single-channel currents recorded from membrane of denervated frog muscle fibers. *Nature* 260:799-802, 1976.
- Neher E, Sakmann B and Steinbach JH. *The Extracellular Patch Clamp: A Method for Resolving Currents through Individual Open Channels in Biological*

Membranes. *Pflügers Arch* 375:219-228, 1978.

Neher E and Sakmann B. The patch clamp technique. *Sci Am* 266(3):44-51, 1992.

Oertel D. Synaptic responses and electrical properties of cells in brain slices of the mouse anteroventral cochlear nucleus. *J Neurosci* 3:2043-2053, 1983.

Palmer LM, Clark BA, Grundemann J, Roth A, Stuart GJ, Häusser M. Initiation of simple and complex spikes in cerebellar Purkinje cells. *J Physiol* 588: 1709 – 1717, 2010.

Palmer LM, Stuart GJ. Site of action potential initiation in layer 5 pyramidal neurons. *J Neurosci* 26: 1854 –1863, 2006.

Pecka M, Brand A, Behrend O, Grothe B. Interaural time difference processing in the mammalian medial superior olive: the role of glycinergic inhibition. *J Neurosci* 28:6914 – 6925, 2008.

Paolini AG, FitzGerald JV, Burkitt AN, Clark GM. Temporal processing from the auditory nerve to the medial nucleus of the trapezoid body in the rat. *Hear Res* 159:101–116, 2001

Pape HC. Queer current and pacemaker: the hyperpolarization-activated cation current in neurons. *Annu Rev Physiol* 58: 299–327, 1996.

Perkins RE. An electron microscopic study of synaptic organization in the medial superior olive of normal and experimental chinchillas. *J Comp Neurol* 148:387-415, 1973.

- Piccolino M. Luigi Galvani and animal electricity: two centuries after the foundation of electrophysiology. *Trends in Neuroscience* 20 (10): 443–448, 1997.
- Piccolino M. Animal electricity and the birth of electrophysiology: The legacy of Luigi Galvani. *Brain Res Bull* 46(5): 381-407, 1998.
- Piccolino M. The bicentennial of the Voltaic battery (1800–2000): the artificial electric organ. *Trends in Neuroscience* 23 (4): 147–151, 2000.
- Pockberger H. Electrophysiological and morphological properties of rat motor cortex neurons in vivo. *Brain Res* 539:181-190, 1991.
- Popovic MA, Foust AJ, McCormick DA, Zecevic D. The spatio-temporal characteristics of action potential initiation in layer 5 pyramidal neurons: a voltage imaging study. *J Physiol* 589:4167–4187, 2011.
- Popovic MA, Gao X, Zecevic D. Voltage-sensitive Dye Recording from Axons, Dendrites and Dendritic Spines of Individual Neurons in Brain Slices. *J Vis Exp* (69), e4261, doi:10.3791/4261, 2012.
- Raastad M, Shepherd GM. Single-axon action potentials in the rat hippocampal cortex. *J Physiol* 548: 745–752, 2003.
- Ramón y Cajal, S. *Histologie du système nerveux de l'homme & des vertébrés*. A. Maloine, Paris, 1909.

- Rancz EA, Hausser M. Dendritic calcium spikes are tunable triggers of cannabinoid release and short-term synaptic plasticity in cerebellar Purkinje neurons. *J Neurosci* 26: 5428–5437, 2006.
- Rautenberg PL, Grothe B, Felmy F. Quantification of the three-dimensional morphology of coincidence detector neurons in the medial superior olive of gerbils during late postnatal development. *J Comp Neurol* 517:385-396, 2009.
- Rayleigh L, On our perception of sound direction. *Philos Mag* 13: 214-232, 1907.
- Recio-Spinoso A. Enhancement and distortion in the temporal representation of sounds in the ventral cochlear nucleus of chinchillas and cats. *PLoS One* 7:e44286, 2012.
- Regehr W, Kehoe J, Ascher, P, Armstrong C. Synaptically triggered action potentials in dendrites. *Neuron* 77:145-151, 1993.
- Regehr WC, Konnerth A, Armstrong, CM. Sodium action potentials in the dendrites of cerebellar Purkinje cells. *Proc Natl Acad Sci USA* 89:5492-5496, 1992.
- Rhode WS. Response patterns to sound associated with labeled globular/bushy cells in cat. *Neuroscience* 154: 87–98, 2008.
- Roberts MT, Seeman SC, Golding NL. A mechanistic understanding of the role of feedforward inhibition in the mammalian sound localization circuitry. *Neuron* 78:923–935, 2013.
- Roberts MT, Seeman SC, Golding NL. The relative contributions of MNTB and LNTB

neurons to inhibition in the medial superior olive assessed through single and paired recordings. *Front. Neural Circuits* 8:49. doi:10.3389/fncir.2014.00049, 2014.

Rose JE, Brugge JF, Anderson DJ, Hind JE. Phase-locked response to low-frequency tones in single auditory nerve fibers of the squirrel monkey. *J Neurophysiol* 30:769–793, 1967.

Rose JE, Gross NB, Geisler CD, Hind JE (1966) Some neural mechanisms in the inferior colliculus of the cat which may be relevant to localization of a sound source. *J Neurophysiol* 29:288-314.

Roth A, Häusser M. Compartmental models of rat cerebellar Purkinje cells based on simultaneous somatic and dendritic patch-clamp recordings. *J Physiol* 535:445–472, 2001.

Rubel EW, Parks TN. Organization and development of brain stem auditory nuclei of the chicken: tonotopic organization of n. magnocellularis and n. laminaris. *J Comp Neurol* 164:411-433, 1975.

Sakmann B and Neher E (Eds). *Single channel recording* (2<sup>nd</sup> edition). Plenum Press (New York), 1995.

Sandel TT, Teas DC, Feddersen WE, Jeffress LA. Localization of sound from single and paired sources. *J Acoust Soc Am* 27:842-852, 1955.

Saint Marie RL, Ostapoff EM, Morest DK, Wenthold RJ. Glycine-immunoreactive projection of the cat lateral superior olive: possible role in midbrain ear

dominance. *J Comp Neurol* 279:382-396, 1989.

Saint Marie RL, Baker RA. Neurotransmitter-specific uptake and retrograde transport of [3H]glycine from the inferior colliculus by ipsilateral projections of the superior olivary complex and nuclei of the lateral lemniscus. *Brain Res* 524:244-253, 1990.

Sanes DH. An in vitro analysis of sound localization mechanisms in the gerbil lateral superior olive. *J Neurosci* 10:3494–3506, 1990.

Schmidgen H. Passagenwerk 1850. Bild und Zahl in den physiologischen Zeitexperimenten von Hermann von Helmholtz. *Berichte zur Wissenschaftsgeschichte* 34:139-155, 2011.

Schmidt-Hieber C, Jonas P, Bischofberger J. Action potential initiation and propagation in hippocampal mossy fibre axons. *J Physiol* 586: 1849 –1857, 2008.

Schmidt-Hieber C, Bischofberger J. Fast sodium channel gating supports localized and efficient axonal action potential initiation. *J Neurosci* 30:10233–10242, 2010.

Schroeder MR. New viewpoints in binaural interactions. In: *Psychophysics and physiology of hearing* (Evans EF, Wilson JP, eds), pp 455– 467. New York: Academic, 1977.

Schwartz IR. The superior olivary complex and lateral lemniscal nuclei. In: *The mammalian auditory pathway: Neuroanatomy* (eds: Webster DB, Popper AN, Fay RR), Springer, New York, 1992.

- Scott LL, Mathews PJ, Golding NL. Posthearing developmental refinement of temporal processing in principal neurons of the medial superior olive. *J Neurosci* 25:7887–7895, 2005.
- Scott LL, Hage TA, Golding NL. Weak action potential backpropagation is associated with high-frequency axonal firing capability in principal neurons of the gerbil medial superior olive. *J Physiol* 583:647–661, 2007.
- Scott RS, Henneberger C, Padmashri R, Anders S, Jensen TP, Rusakov DA. Neuronal adaptation involves rapid expansion of the action potential initiation site. *Nat Commun* 5:3817, 2014.
- Seyfarth, EA. Julius Bernstein (1839-1917): pioneer neurobiologist and biophysicist. *Biol Cybern* 94: 2-8, 2006.
- Shamma SA, Shen NM, Gopaldaswamy P. Stereausis: binaural processing without neural delays. *J Acoust Soc Am* 86:989–1006, 1989.
- Shinn-Cunningham BG, Santarelli S, Kopco N. Tori of confusion: binaural localization cues for sources within reach of a listener. *J Acoust Soc Am* 107: 1627-1636, 2000.
- Shneiderman A, Oliver DL, Henkel CK. Connections of the dorsal nucleus of the lateral lemniscus: an inhibitory parallel pathway in the ascending auditory system? *J Comp Neurol* 276:188- 208, 1988.
- Shu Y, Hasenstaub A, Duque A, Yu Y, McCormick DA. Modulation of intracortical synaptic potentials by presynaptic somatic membrane potential. *Nature* 441:

761–765, 2006.

Shu Y, Duque A, Yu Y, Haider B, McCormick DA. Modulation of intracortical synaptic potentials in neocortical pyramidal cells: evidence from whole cell axon recordings. *J Neurophysiol* 97: 746-760, 2007.

Siveke I, Pecka M, Seidl AH, Baudoux S, Grothe B. Binaural response properties of low- frequency neurons in the gerbil dorsal nucleus of the lateral lemniscus. *J Neurophysiol* 96:1425-1440, 2006.

Siveke I, Leibold C, Grothe B. Spectral composition of concurrent noise affects neuronal sensitivity to interaural time differences of tones in the dorsal nucleus of the lateral lemniscus. *J Neurophysiol* 98:2705–2715, 2007.

Siveke I, Leibold C, Schiller E, Grothe B. Adaptation of binaural processing in the adult brainstem induced by ambient noise. *J Neurosci* 32:462-473, 2012.

Smith PH. Structural and functional differences distinguish principal from nonprincipal cells in the guinea pig MSO slice. *J Neurophysiol* 73:1653–1667, 1995.

Smith PH, Joris PX, Carney LH, Yin TC (1991) Projections of physiologically characterized globular bushy cell axons from the cochlear nucleus of the cat. *J Comp Neurol* 304:387-407, 1991.

Smith PH, Joris PX, Yin TC (1993) Projections of physiologically characterized spherical bushy cell axons from the cochlear nucleus of the cat: evidence for delay lines to the medial superior olive. *J Comp Neurol* 331:245-260, 1993.

- Smith PH, Joris PX, Yin TC (1998) Anatomy and physiology of principal cells of the medial nucleus of the trapezoid body (MNTB) of the cat. *Journal of Neurophysiology* 79:3127-3142, 1998.
- Spangler KM, Warr WB and Henkel CK. The projections of principal cells of the medial nucleus of the trapezoid body in the cat. *J. Comp. Neurol.* 238, 249–262, 1985.
- Spencer WA, Kandel ER. Electrophysiology of hippocampal neurons IV. Fast prepotentials. *J Neurophysiol* 24:272-285, 1961.
- Spirou GA, Brownell WE, Zidanic M. Recording from the cat trapezoid body and HRP labeling of globular bushy cell axons. *J Neurophysiol* 63:1169–1190, 1990.
- Spirou GA, and Berrebi AS. Organization of ventrolateral periolivary cells of the cat superior olive as revealed by PEP-19 immunocytochemistry and Nissl stain. *J. Comp. Neurol.* 368, 100–120, 1996.
- Spirou GA, and Berrebi AS. Glycine immunoreactivity in the lateral nucleus of the trapezoid body of the cat. *J. Comp. Neurol.* 383, 473–488, 1997.
- Spitzer MW, Semple MN. Neurons sensitive to interaural phase disparity in gerbil superior olive: diverse monaural and temporal response properties. *J Neurophysiol* 73:1668-1690, 1995.
- Spruston N, Schiller Y, Stuart G, Sakmann B. Activity-dependent action potential invasion and calcium influx into hippocampal CA1 dendrites. *Science* 268: 297–300, 1995.

- Stange A, Myoga MH, Lingner A, Ford MC, Alexandrova O, Felmy F, Pecka M, Siveke I, Grothe B. Adaptation in sound localization: from GABA(B) receptor-mediated synaptic modulation to perception. *Nat Neurosci* 16:1840–1847, 2013.
- Stillman RD. Characteristic delay neurons in the inferior colliculus of the kangaroo rat. *Exp Neurol* 32: 404-412, 1971.
- Stotler WA. An experimental study of the cells and connections of the superior olivary complex of the cat. *Journal of Comparative Neurology* 98:401-432, 1953.
- Stuart G, Häusser M. Initiation and spread of sodium action potentials in cerebellar Purkinje cells. *Neuron* 13: 703–712, 1994.
- Stuart GJ, Sakmann B. Active propagation of somatic action potentials into neocortical pyramidal cell dendrites. *Nature* 367:69 –72, 1994.
- Stuart G, Schiller J, Sakmann B. Action potential initiation and propagation in rat neocortical pyramidal neurons. *J Physiol* 505: 617– 632, 1997a.
- Stuart G, Spruston N, Sakmann B, Häusser M. Action potential initiation and backpropagation in neurons of the mammalian CNS. *Trends Neurosci* 20:125–131, 1997b.
- Sullivan WE, Konishi M. Neural map of interaural phase difference in the owl's brainstem. *Proc Natl Acad Sci USA* 83:8400-8404, 1986.

- Svirskis G, Kotak V, Sanes DH, Rinzel J. Enhancement of signal-to-noise ratio and phase locking for small inputs by a low-threshold outward current in auditory neurons. *J Neurosci* 22:11019–11025, 2002.
- Svirskis G, Kotak V, Sanes DH, Rinzel J. Sodium along with low-threshold potassium currents enhance coincidence detection of subthreshold noisy signals in MSO neurons. *J Neurophysiol* 91:2465–2473, 2004.
- Thompson AM, Schofield BR. Afferent projections of the superior olivary complex. *Microsc Res Tech* 51:330–354, 2000.
- Thompson GC, Cortez AM, Lam DM. Localization of GABA immunoreactivity in the auditory brainstem of guinea pigs. *Brain Res* 339:119-122, 1985.
- Tolbert LP, Morest DK, Yurgelun-Todd DA. The neuronal architecture of the anteroventral cochlear nucleus of the cat in the region of the cochlear nerve root: horseradish peroxidase labelling of identified cell types. *Neuroscience* 7, 3031–3052, 1982.
- Tollin DJ. The lateral superior olive: a functional role in sound source localization. *Neuroscientist* 9:127–143, 2003.
- Tollin DJ, Yin TCT. Interaural phase and level difference sensitivity in low-frequency neurons in the lateral superior olive. *Journal of Neuroscience* 25:10648-10657, 2005.
- Trussell LO. Synaptic mechanisms for coding timing in auditory neurons. *Annu Rev Physiol* 61:477–496, 1999.

- Turner RW, Meyers DER, Barker JL. Localization of tetrodotoxin-sensitive field potentials of CA1 pyramidal cells in the rat hippocampus. *J Neurophysiol* 62:1375-1387, 1989.
- van der Heijden M, Lorteije JA, Plauška A, Roberts MT, Golding NL, Borst JG. Directional hearing by linear summation of binaural inputs at the medial superior olive. *Neuron* 78:936–948, 2013.
- Volta, A. On the electricity excited by the mere contact of conducting substances of different species. *Philos. Trans. Roy. Soc.* 90, 403–431, 1800.
- von Békésy G. The variations of phase along the basilar membrane with sinusoidal vibrations. *J Acoust Soc Am* 19:452-460, 1947.
- von Gersdorff H, Borst JG. Short-term plasticity at the calyx of held. *Nat Rev Neurosci* 3:53–64, 2002.
- von Helmholtz H. Vorläufiger Bericht über die Fortpflanzungsgeschwindigkeit der Nervenreizung, *Archiv für Anatomie, Physiologie und wissenschaftliche Medizin* 17:71–73, 1850.
- Wahl-Schott C, Biel M. HCN channels: structure, cellular regulation and physiological function. *Cell Mol Life Sci* 66:470–494, 2009.
- Warr WB. Fiber degeneration following lesions in the anterior ventral cochlear nucleus of the cat. *Experimental Neurology* 14:453-474, 1966.

- Webster, DB. An Overview of Mammalian Auditory Pathways with an Emphasis on Humans. In: The mammalian auditory pathway: Neuroanatomy (eds: Webster DB, Popper AN, Fay RR), Springer, New York, 1992.
- Wenthold RJ, Huie D, Altschuler RA, Reeks KA. Glycine immunoreactivity localized in the cochlear nucleus and superior olivary complex. *Neuroscience* 22:897-912, 1987.
- Williams SR, Stuart GJ. Mechanisms and consequences of action potential burst firing in rat neocortical pyramidal neurons. *J Physiol* 521: 467– 482, 1999.
- Wong RKS, Prince DA, Basbaum AI. Intradendritic recordings from hippocampal pyramidal neurons. *Proc Natl Acad Sci USA* 76:986-990, 1979.
- Wu SH, Kelly JB. Physiological properties of neurons in the mouse superior olive: membrane characteristics and postsynaptic responses studied *in vitro*. *J Neurophysiol* 65:230–246, 1991.
- Yavuzoglu A, Schofield BR, Wenstrup JJ. Substrates of auditory frequency integration in a nucleus of the lateral lemniscus. *Neuroscience* 169:906-919, 2010.
- Yin TC, Carney LH, Joris PX. Interaural time sensitivity in the inferior colliculus of the albino cat. *J Comp Neurol* 295:438–448, 1990.
- Yin TC, Chan JC. Interaural time sensitivity in medial superior olive of cat. *J Neurophysiol* 64:465-488, 1990.
- Yin TC, Kuwada S. Binaural interaction in low-frequency neurons in inferior colliculus

of the cat. II. Effects of changing rate and direction of interaural phase. *J Neurophysiol* 50:1000–1019, 1983a.

Yin TC, Kuwada S. Binaural interaction in low-frequency neurons in inferior colliculus of the cat. III. Effects of changing frequency. *J Neurophysiol* 50:1020–1042, 1983b.

Yu Y, Shu Y, McCormick DA. Cortical action potential backpropagation explains spike threshold variability and rapid-onset kinetics. *J Neurosci* 28: 7260 –7272, 2008.

Zhou Y, Carney LH, Colburn HS. A model for interaural time difference sensitivity in the medial superior olive: interaction of excitatory and inhibitory synaptic inputs, channel dynamics, and cellular morphology. *J Neurosci* 25:3046 –3058, 2005.

Zhu JJ Maturation of layer 5 neocortical pyramidal neurons: amplifying salient layer 1 and layer 4 inputs by Ca<sup>2+</sup> action potentials in adult rat tuft dendrites. *J Physiol* 526: 571–587, 2000.

## List of abbreviations

AIS	axon initial segment
ANF	auditory nerve fiber
AP	action potential
AVCN	anterior ventral cochlear nucleus
BF	best frequency
CCD	charge-coupled device
CD	characteristic delay
CF	characteristic frequency
CP	characteristic phase
DCN	dorsal cochlear nucleus
DNLL	dorsal nucleus of the lateral lemniscus
DTX	dendrotoxin
EE	excitatory-excitatory
EI	excitatory-inhibitory
EPSC	excitatory postsynaptic conductance
EPSP	excitatory postsynaptic potential
GABA	gamma-Aminobutyric acid
GBC	globular bushy cell
HCN	hyperpolarization-activated cyclic nucleotide-gated channel
Hz	Hertz
IC	inferior colliculus
ICC	central nucleus of the inferior colliculus
$I_h$	HCN current
IHC	inner hair cell
ILD	interaural level difference
$I_{Kv1}$	Kv1 current
INLL	intermediate nucleus of the lateral lemniscus
IPD	interaural phase difference
IPSC	inhibitory postsynaptic conductance
IPSP	inhibitory postsynaptic potential
ITD	interaural time difference
KCNA	voltage-gated potassium channel subfamily A
Kv1	low-threshold activated potassium channel
LL	lateral lemniscus
LNTB	lateral nucleus of the trapezoid body
LSO	lateral superior olive
MNTB	medial nucleus of the trapezoid body
MSO	medial superior olive
M $\Omega$	megaohm
NL	nucleus laminaris
P<n>	postnatal day <n>
PVCN	posterior ventral nucleus

SBC	spherical bushy cell
SOC	superior olivary complex
SPN	superior periolivary nucleus
TTX	tetrodotoxin
VCN	ventral cochlear nucleus
VNLL	ventral nucleus of the lateral lemniscus
VSD	voltage-sensitive dye

## List of publications

Baumann VJ, **Lehnert S**, Leibold C, Koch U. Tonotopic organization of the hyperpolarization-activated current (I<sub>h</sub>) in the mammalian medial superior olive. *Front Neural Circuits* 7:117, 2013.

**Lehnert S**, Ford MC, Alexandrova O, Hellmundt F, Felmy F, Grothe B, Leibold C. Action potential generation in an anatomically constrained model of medial superior olive axons. *J Neurosci* 34: 5370–5384, 2014.

Myoga MH, **Lehnert S**, Leibold C, Felmy, F, and Grothe B. Glycinergic inhibition tunes coincidence detection in the auditory brainstem. *Nat Commun* 5: 3790. doi: 10.1038/ncomms4790.

### Conference contributions:

**Lehnert S**, Leibold C. The spike initiation in neurons with low input resistance. *Front. Comput. Neurosci. Conference Abstract: BC11 : Computational Neuroscience & Neurotechnology Bernstein Conference & Neurex Annual Meeting, Freiburg, Germany, 2011.*

**Lehnert S**, Leibold C. Model of Spike Initiation in the Medial Superior Olive. *Assoc Res Otolaryngol Abstr, 35<sup>th</sup> Annual Midwinter Meeting of the Association for Research in Otolaryngology, San Diego, California, USA, 2012.*

Auer V, **Lehnert S**, Leibold C, Koch U. Tonotopic Organization of the Hyperpolarization-Activated Current (I<sub>h</sub>) in the Mammalian Medial Superior Olive. *Assoc Res Otolaryngol Abstr, 35<sup>th</sup> Annual Midwinter Meeting of the Association for Research in Otolaryngology, San Diego, California, USA, 2012.*

**Lehnert S**, Leibold C. Site of spike initiation changes with functional context in coincidence detector neurons. Front. Comput. Neurosci. Conference Abstract: Bernstein Conference, München, Germany, 2012.

Myoga MH, **Lehnert S**, Leibold C, Felmy F, Grothe B. Glycinergic Inhibition Controls Synaptic Integration in the Medial Superior Olive. Assoc Res Otolaryngol Abstr, 36<sup>th</sup> Annual Midwinter Meeting of the Association for Research in Otolaryngology, Baltimore, Maryland, USA, 2013.

**Lehnert S**, Ford M, Alexandrova O, Hellmundt F, Felmy F, Grothe B, Leibold C. Action potential generation in coincidence detector neurons of the medial superior olive. Bernstein Conference, Tübingen, Germany, 2013.

**Lehnert S**, Leibold C. Asymmetric excitatory amplitudes modulate ITD sensitivity in a model of principal cells of the medial superior olive. Bernstein Conference, Göttingen, Germany, 2014.

## Acknowledgments

First and foremost, I thank my supervisor Prof. Dr. Christian Leibold for accepting me as a PhD student in his lab and introducing me to the world of biophysical modeling. I thank Christian for his guidance and support over the years, for giving me much free rein in my research, for his patience when I got lost into details, and for disentangling my ideas numerous times, teaching me how to transform them into actual science.

I thank all the people I had the honor to collaborate with: Dr. Olga Alexandrova, Dr. Veronika Baumann, Prof. Dr. Felix Felmy, Dr. Marc Ford, Prof. Dr. Benedikt Grothe, Franziska Hellmundt, Prof. Dr. Ursula Koch, and Dr. Michael Myoga.

I thank Prof. Dr. Felix Felmy, PD Dr. Conny Kopp-Scheinflug, and Dr. Michael Pecka for always taking the time to share their expertise with me.

I thank Dr. Kay Thurley for his consistent support and helpful consultation over the last few years.

I thank Axel Kammerer and Dr. Chun-Wei Yuan for proofreading my thesis.

I thank the current and former members of the computational and experimental neuroscience labs at the LMU Biozentrum, as well as the members of the SFB 870, for inspiring discussions and fun meetings.

Last, but certainly not least, I would like to express my deepest gratitude to Moni: I couldn't have made it without your loving support. And, of course special thanks goes to our son Maxi, who always manages to put a smile on my face.





## **Eidesstattliche Erklärung**

Ich versichere hiermit an Eides statt, dass die vorgelegte Dissertation von mir selbständig und ohne unerlaubte Hilfe angefertigt ist.

München, den 30.06.2015

Simon Lehnert

## **Erklärung**

Hiermit erkläre ich, dass die Dissertation nicht ganz oder in wesentlichen Teilen einer anderen Prüfungskommission vorgelegt worden ist. Des Weiteren erkläre ich, dass ich mich anderweitig einer Doktorprüfung ohne Erfolg nicht unterzogen habe.

München, den 30.06.2015

Simon Lehnert



# Author contributions

## **Paper 1 (Chapter 2):**

*Action potential generation in an anatomically constrained model of medial superior olive axons*

**List of authors:** Simon Lehnert (SL), Marc C. Ford (MCF), Olga Alexandrova (OA), Franziska Hellmundt (FH), Felix Felmy (FF), Benedikt Grothe (BG), and Christian Leibold (CL).

**Individual contributions:** SL and CL, conception and design of the study, SL designed and generated the computational model, performed all simulations and analyzed the resulting data, SL and CL interpreted the results of the modeling; MCF and OA, designed and performed the immunohistochemical experiments, MCF and OA analyzed the immunohistochemical data; FF designed the electrophysiological experiments, FH and FF performed the electrophysiological experiment and analyzed the data; SL prepared all figures, except Figure 2, which was made by MCF. SL wrote the initial draft of the manuscript, MCF wrote the immunohistochemical part of the manuscript. FF, BG, and CL contributed to various parts of the manuscript. SL, MCF, FF, BG, and CL critically revised the manuscript. All authors approved the final version of the manuscript.

## **Paper 2 (Chapter 3):**

*Glycinergic inhibition tunes coincidence detection in the auditory brainstem*

**List of authors:** Michael H. Myoga (MHM), Simon Lehnert (SL), Christian Leibold (CL), Felix Felmy (FF), and Benedikt Grothe (BG).

**Individual contributions:** MHM, CL, FF and BG, conception and design of the study; MHM performed the electrophysiological experiments and analyzed the data. SL generated the computational model, performed the simulations and analyzed the resulting data, SL and CL interpreted the results of the modeling; MHM prepared all figures. MHM, CL, FF and BG wrote the initial draft of the manuscript. All authors critically revised the manuscript. All authors approved the final version of the manuscript.

## **Paper 3 (Chapter 4):**

*Tonotopic organization of the hyperpolarization-activated current (I<sub>h</sub>) in the mammalian medial superior olive*

**List of authors:** Veronika J Baumann (VJB), Simon Lehnert (SL), Christian Leibold (CL), Ursula Koch (UK).

**Individual contributions:** CL and UK, conception and design of the study; VJB performed the electrophysiological experiments and analyzed the data. VJB and UK interpreted the electrophysiological data. SL generated the computational model, performed the simulations and analyzed the resulting data, SL and CL interpreted the results of the modeling; VJB prepared all figures, except for Figure 7, which was prepared by SL. All authors contributed to the initial draft of the manuscript. All authors critically revised the manuscript. All authors approved the final version of the manuscript.

